Internal erosion and piping failure of landslide dams

OKEKE, Chukwueloka Austin Udechukwu

Department of Geoscience
Interdisciplinary Graduate School of Science and Engineering
Shimane University, Japan

September, 2016

ABSTRACT

Landslide dams are formed in valley-confined settings where favourable geomorphological and hydro-climatic factors result in the downslope movement of weathered slope materials, causing the blockage of river valleys and the creation of barrier lakes. Landslide dams are potentially dangerous natural phenomena, which are made up of heterogeneous masses of unconsolidated or poorly consolidated sediments, and thus may fail by seepage or piping. Failure of landslide dams could trigger catastrophic outburst floods and debris flows, which could inundate the downstream areas, causing loss of lives and infrastructural damage. Therefore, timely evaluation of landslide dams is important for prevention of catastrophic dam failures and mitigation of disasters caused by downstream flooding of the released water masses. This research performs a series of field investigations, flume experiments and large-scale physical experiments to study the potentials for internal erosion and piping failure of landslide dams.

An integrated geophysical approach comprising the microtremor chain array and self-potential surveys were successfully used to characterize the internal structure of landslide dams and delineate potential seepage zones. The microtremor chain array survey results revealed the internal structure of the landslide dams while the self-potential survey results indicated areas of anomalous seepage or zones of high water saturation. In most of the surveyed sites, the presence of an anomalous seepage was confirmed by a very good correlation between the areas of low phase velocities (80 to 200 m/s) and high negative SP anomalies.

A series of experiments were performed to study the hydromechanical constraints for landslide dam failure by piping. The experiments were conducted in a 2m*0.45m*0.45m flume, with a flume bed slope of 5°. Uniform dams of height 0.25 m

were built with either mixed or homogeneous silica sands. Two laser displacement sensors were used to monitor the behaviour of the dams during the internal erosion process while a linear displacement transducer and a water-level probe were deployed to monitor the onset of internal erosion and the hydrological trend of the upstream lake. Five major phases of the breach evolution process were observed: pipe evolution, pipe enlargement, crest settlement, hydraulic fracturing and progressive sloughing. Two major failure modes were observed: seepage and piping-induced collapse. It is found that an increase in soil density and homogeneity of the dam materials reduced the potential to form a continuous piping hole through the dams. The rate of pipe enlargement is related to the erodibility of the soil, which itself is inversely proportional to the soil density.

Extensive laboratory experiments were performed to evaluate the critical hydraulic and geometrical conditions for seepage-induced failure of landslide dams. The experiments were conducted in a flume tank specifically designed to monitor time-dependent transient changes in pore-water pressures within the unsaturated dam materials under steady-state seepage. Two critical hydraulic gradients corresponding to the onset of seepage erosion initiation and collapse of the dam crest were determined for different upstream inflow rates, antecedent moisture contents, compactive efforts, grain size ranges, and dam geometries. The deformation behaviour of the dams was significantly influenced by particle density, pore geometry, hydraulic conductivity, and the amount of gravel and pebbles present in the materials. The results indicate that the critical seepage velocity for failure of the dams decreased with an increase in downstream slope angle, but increased with an increase in pore geometry, dam height, dam crest width, upstream inflow rate, and antecedent moisture content.

Large-scale (outdoor) physical experiments were conducted to evaluate the premonitory factors for internal erosion and piping failure of landslide dams. Several

monitoring sensors comprising pore-water pressure sensors, linear displacement transducers, and turbidity sensors were installed at different parts of the dam to monitor the hydrodynamic changes that occur during the internal erosion and piping. Furthermore, self-potential measurements were made during the experiments by installing several electrodes on the dam crest. The experimental results indicated that the emergence of a high turbidity (300~450 NTU) effluent seepage at the downstream face of the dam coincided with a very high negative self-potential anomaly. This was also found to correlate with the development of high pore-water pressures (4~8 kPa) which subsequently led to a gradual decrease in the dam height (settlement). These large-scale (outdoor) physical experiments provide important information regarding the premonitory factors for piping failure of landslide dams.

The integration of the geophysical surveys, flume experiments, and large-scale (outdoor) physical experiments provides a framework for a better understanding of the likelihood of piping-induced failure of landslide dams. The results of this comprehensive research would aid in the development of accurate dam breach models for the prediction of the breaching time, flood hydrograph and an early warning system for disaster risk reduction.

ACKNOWLEDGEMENTS

LIST OF FIGURES

CHAPTER 3

CHAPTER 4

CHAPTER 5

CHAPTER 6

LIST OF TABLES

CHAPTER 7

TABLE OF CONTENTS

REFERENCES

CHAPTER 1

INTRODUCTION

1.1 Background

The impacts of climate change and global warming have triggered many natural disasters in numerous mountainous regions of the world. A large number of environmental changes have continued to modify the hydrogeologic system as a result of global warming. Every year, tens of thousands of fatalities are being recorded and several billions of dollars are lost due to damage caused by the prevalence of floods, river-damming landslides, debris flows, earthquakes, glacier outburst floods (GLOFs) and other hydroclimatologically-related disasters. The last two decades have witnessed an increasing trend in the frequency and intensity of precipitation and extremely high temperatures. These effects, in combination with rapid urbanization and deforestation, have triggered several natural disasters including landslides and associated disasters such as catastrophic outburst floods from the failure of landslide dams and glacier-ice dams. The relationships between climate change and the initiation of several geomorphological processes that trigger landslides and other mass movements have been documented in the literature (Bo et al 2008; Jakob and Lambert 2009; Crozier 2010; Stoffel and Huggel 2012). These processes are caused by a change in equilibrium between precipitation and evapotranspiration which alters the hydrologic regime of mountain slopes, triggering landslides that occasionally form secondary hazards such as landslide dams. For these reasons, an interdisciplinary research scheme comprising geomorphology, hydrogeology, hydroclimatology, and

disaster risk management needs to be developed and sustained for accurate evaluation and mitigation of natural dam hazards.

Landslide dams represent a significant geomorphic hazard that occurs in many mountainous regions of the world. High frequency of river-damming events has been observed in tectonically active regions of high seismic activity. These regions are usually characterized by favourable topographic boundaries such as oversteepened slopes and narrow valleys. Landslide dams are complex and composite in nature; their origin can be attributed to the blockage of stream-channels in confined valley settings by rock falls, landslides, rock avalanches and debris flows. The major factors controlling the formation of landslide dams are the geometry of the stream-channel, the velocity of the landslide and the volume of the displaced material (sediment budget). A few examples of the earliest historic records of landslide dam formation and failure in the European Alps include the 1219 damming of the Romanche River in France and subsequent failure which led to the downstream flooding that claimed thousands of lives (Bonnard 2011); the 1419 Ganderberg-Passeier Wildsee (Passer Valley, Italy) rockslide dam failure and outburst flood that claimed at least 400 lives; and the 1515 Val Blenio (Switzerland) rock avalanche dam failure and outburst flood that took about 600 lives (Li 1990). In China, two notable records of river-damming events are: (1) the 1737 BC earthquake-triggered landslide dam in the Yi and Lo Rivers in Hunan Province of central China (Xue-Cai and An-ning 1986); and (2) the 1786 M=7.75 earthquake-triggered landslide in Sichuan Province, southwest China, which dammed the Dadu River and breached ten days later, leading to catastrophic flooding of the downstream areas that claimed over 100,000 lives (Dai et al. 2005).

Not much has been reported on the immense contributions of landslide dams in the socioeconomic development of the human society. Rapid urbanization and industrialization witnessed in the 19th and 20th Centuries resulted in the stabilization and utilization of several landslide dams for various purposes such as flood control,

navigation, recreational activities, water supply, aquaculture and hydropower generation (Heim 1932; Terzaghi 1960; Schuster 2006; Coppola and Bromhead 2008). For instance, the Waikaremoana Lake, located on the east coast of the Northern Island of New Zealand, was formed ca. 2,200 years ago, by a rockslide dam with an estimated dam volume of 5.2 billion m³ (Adams 1981; Davies et al. 2006). This scenic lake which generates a total output of 124 Megawatts of electricity remains one of the many cases where upstream waters are being utilized for hydroelectric power generation (Read et al. 1992). Other important examples are: (1) the 30 m high Rhodannenberg Dam built on the Klontalersee rockslide dam in Switzerland, which impounds a reservoir with a total volume of 56.4×10^6 m³. This hydropower dam was completed in 2010, with a capacity of generating 60 Megawatts of electricity; and (2) the 80 m high Zavoj (Pirot) Dam built on the 1963 rockslide dam that dammed the Visocica River in Serbia (Evans et al. 2011).

Landslide dams pose enormous risks because of the potentially catastrophic outburst floods that could be triggered by the sudden release of stored water masses from the failure of the blockage. These floods, upon surging downstream, transform into debris flows and hyperconcentrated flows with peak discharges most times greater than 10,000 m³/s, thereby, threatening the lives of people living in the downstream areas (O'Connor and Costa 2004). For example, the Diexi landslide dams (Dahaizi, Xiaohaizi and Diexi), formed by deep-seated mass movements triggered by the August 25, 1933, M=7.5 earthquake in northwestern Sichuan Province of China, claimed about 2,423 lives from outburst floods (that travelled with an average velocity of 20~25 km/hr) generated from the breaching of the dams (Chai et al. 2000). Peak discharges are controlled by several factors including dam geometry, downstream topography, failure mode, the internal structure of the blockage and lake volume. Therefore, a good knowledge of the complex processes involved in the evolution and

failure of river-damming landslides, coupled with the hydraulics of the outburst floods, is imperative for disaster risks assessment and mitigation.

Internal erosion and piping are common phenomena occurring in landslide dams and other water-retaining structures such as embankment dams and artificial levees. The prevalence of these processes in landslide dams has been attributed to the anisotropic and heterogeneous nature of landslide dam deposits which are mostly unconsolidated or poorly consolidated. This ultimately increases the probability of initiation of seepage and piping which sometimes results in dam breaching and failure. Seepage erosion triggers slope instability through three major interrelated mechanisms: (1) increase in pore-water pressure and its effects on the shear strength of the soil, (2) increase in seepage gradient forces that reduce the effective stress of the soil, and (3) mobilization and downstream entrainment of the eroded particles.

Internal erosion and piping occur in many geologic materials including clay, silt, fine sand, volcanic ash, tuff, loess, colluvium, alluvium, claystone, siltstone and mudstone (Parker 1964). The development of internal erosion and piping in landslide dams has been attributed to the interplay between the internal structure of the dam and the discharge rate through the impoundment. Internal erosion and piping are usually favored by a coarse blocky carapace with large void spaces where anomalous seepage has the potential to form subsurface conduits or tunnels which acts as channels for the release of the lake waters impounded behind the dam. A typical example is the relatively stable Usoi landslide dam, where the rate of discharge through the dam has equaled the inflow rate into the upstream lake, thus maintaining a static water level which has contributed to the stability of the dam (Strom 2013).

Failure of landslide dams and earthen dams involves a complex, sporadic, nonlinear and homogeneous process (Singh et al. 1988). Hence, a good knowledge of sediment transport processes, including the hydraulics and hydrodynamics is needful for a

better understanding of the complex processes that lead to the initiation and development of internal erosion and piping. In general, piping failure of landslide dams has been ascribed to three major interrelated mechanisms: (1) initiation of internal erosion and piping; (2) progressive erosion and removal of sediments at the downstream face under steady-state seepage conditions; and (3) formation of an initial breach at the crest and subsequent enlargement by erosion (Singh et al. 1988). A lot of difficulties have been reported by researchers while simulating the internal erosion process which has been recognized as an important factor for the determination of the extent, magnitude and duration of the flood hydrograph. Timely assessment of landslide dams and prediction of the potential flood hydrograph are essential for effective planning and implementation of disaster management schemes. Similarly, a large number of results abound on numerical models developed for the simulation of piping in earthen dams and landslide dams (Singh et al. 1988; Gattinoni and Francani 2009). Yet, none of these methods have investigated the influence of hydromechanical properties of landslide dams on their potential failure mechanisms as relates to internal erosion and piping.

One major problem in dam engineering is the monitoring of seepage, especially in heterogeneous and anisotropic materials. Information on seepage processes (seepage velocity, seepage forces, seepage paths and hydraulic conductivity) are essential for predicting the hydraulic behaviour and the failure mechanism of landslide dams. The internal structure and the hydraulic behaviour of landslide dams can be assessed by the application of several geophysical exploration techniques. The microtremor (MTM) chain array survey and the self-potential (SP) measurement are two non-invasive geophysical techniques that are sensitive to soil and fluid properties. These techniques can be used to evaluate contrasting specific subsurface properties that can be attributed to varying seepage conditions. Hence, data acquired from the application of these geophysical techniques can be used wholly or in part to produce

a representative image of the hydraulic conditions and the internal structure of the impoundment.

1.2 Objectives and thesis outline

The purpose of the present research is to study the mechanisms of internal erosion and piping in landslide dams. This thesis is focused on the following four main objectives.

1. To determine the apparent phase velocity structure of landslide dams and evaluate their internal structure, stability and the potential for failure by piping. This is achieved through carrying out microtremor chain array surveys on selected landslide dams using a set of seismometers, 3 reels of connecting wires, a data logging device, portable batteries and laptop computers installed with a data logging software.

2. To identify zones of anomalous seepage that could likely develop into internal erosion, and provide information on the subsurface geologic structures influencing groundwater flow and seepage conditions. This is achieved through the conduction of self-potential investigations using Copper-Copper Sulphate (half-cell) reference electrodes.

3. To identify the various failure mechanisms of landslide dams under varying hydromechanical properties of the materials forming the dams, and to evaluate the geometric and hydraulic factors governing the onset of internal erosion and piping. This is achieved by performing a series of experiments in a flume tank equipped with monitoring sensors and transducers, using materials of differing physical properties.

4. To determine the critical hydraulic gradients for the onset of internal erosion and failure of landslide dams under differing hydraulic and geometrical conditions. This is achieved by using several precision sensors to track the

transient hydraulic conditions in dam models of varying geometrical and physical properties subjected to steady-state seepage conditions.

5. To investigate the premonitory conditions for internal erosion and piping in landslide dams, and to examine the relationship between the transient deformation behaviour of the dams and turbidity of the seepage water. This task is accomplished by performing large-scale (outdoor) model tests using strain gauges and laser displacement sensors to monitor the internal and external deformations that occur during internal erosion. Furthermore, turbidity sensors and pore-water pressure transducers will be used to track the onset of internal erosion and the dynamic behaviour of the dam models during piping.

The main body of this thesis comprises eight chapters. Chapter 1 introduces the research topic, states the major research objectives and discusses the geomorphic settings for landslide dams, including the triggering mechanisms of river-damming landslides and the failure modes of landslide dams.

Chapter 2 presents a comprehensive review of the literature on internal erosion and piping processes in landslide dams and soil slopes. This chapter comprises detailed definitions and nomenclature of the piping process; the various classifications of piping and mechanisms of internal erosion and piping are discussed. Furthermore, the mechanisms of seepage-induced failure of landslide dams and soil slopes are summarized, including the effects of pore-water pressures on the destabilization of soil slopes. The effects of seepage gradient forces on soil materials and the internal structure of landslide dams, considering its implications on the initiation of piping are presented as well.

In Chapter 3, an integrated geophysical approach is employed to characterize the internal structure of selected landslide dams and to study the variations in specific physical properties of the soil that could provide information on the potential zones

of anomalous seepage. Field investigation results using the microtremor chain array and the self-potential techniques are presented and discussed. Analysis of the results involves a detailed description of the internal structure of the dams based on variations in phase velocities and the identification of likely seepage zones in the dams.

Chapter 4 presents the results of a series of laboratory experiments on the hydromechanical constraints on the piping failure of landslide dams. The experimental programme, including the apparatus, materials and procedure are described. The test results, including the various breach evolution processes, the effect of density on erodibility of the materials and the characteristic failure mechanisms under differing materials are discussed.

Chapter 5 presents a series of experiments performed to determine the critical hydraulic gradients for the seepage-induced failure of landslide dams under varying physical properties of the dam materials. In addition, the details of the modified flume tank used in the investigation, including the soil characteristics, experimental procedure, and method adopted for the determination of critical hydraulic gradients are described.

Chapter 6 presents the results of the experimental investigation reported in Chapter 5. The variations in critical hydraulic gradients for the initiation of internal erosion and collapse of the dam crests under differing hydromechanical and geometrical conditions are described. In addition, the hydraulic behaviour of the dam models under steady-state seepage conditions, and the effects and variation of pore-water pressures and seepage velocities are discussed.

Chapter 7 presents the results of a series of large-scale (outdoor) experimental investigations performed to study the premonitory conditions for internal erosion and piping failure of landslide dams. The variations in turbidity of the seepage water with respect to the deformation behaviour of the dam models are discussed. Finally,

Chapter 8 presents the present research findings and recommendations for further research.

1.3 Geomorphic settings for landslide dams

A lot of studies have been done on the relationships between fluvial processes and the frequency of landslide damming events in connection with sediment delivery processes and the development of drainage networks (Whitehouse and Griffiths 1983; Hammack and Wohl 1996; Cenderelli and Kite 1998; Hewitt 1998; Hovius et al. 1997, 1998). Landslide dams are formed by the partial or complete blockage of stream-channels by displaced earth or rock materials. The phenomenon can occur in several kinds of geomorphic settings. These settings are usually characterized by steep-walled narrow valleys bordered by high rugged mountains; a feature commonly found in geologically active regions where uplift or mountain building associated with active tectonic activities increases the likelihood of initiation of river-damming landslides (Costa and Schuster 1988). Also, these regions are characterized by highly weathered and unstable source materials, including fractured and hydrothermally altered bedrock, and thick Quaternary sediments. The majority of the inherent factors that trigger landslide damming events in these regions include increases in local relief and hillslope gradient, and incessant weathering that reduce the shear strength of hillslope materials. These overarching factors are exacerbated by high orographic precipitations or snowmelts, coupled with active tectonic activities including earthquakes and volcanic eruptions.

The probability of formation of landslide dams is determined by several factors including the volume of the displaced material (sediment budget), the type of landslide, the velocity of the displaced material, and morphology of the stream-channel. Schuster et al. (1998) enumerated four kinds of factors that govern the spatial distribution of landslide dams based on the study of the landslide dams

formed by the 1989 Loma Prieta earthquake in California (USA). These factors are (1) seismic intensity (peak acceleration, duration of strong motion), (2) topography and high slope gradient, (3) lithology and weathering, and (4) soil moisture and groundwater content.

Geodynamically active regions where landslide dams form are characterized by orogenic processes (mountain building), which evolve from crustal shortening, vertical thickening, and denudation processes. These processes are augmented by other essential factors such as earthquakes and orographically enhanced precipitation on steep narrow gorges. The evolution of mountain belts at tectonic boundaries results in the development of narrow stream-channels and gorges which are bordered by steep hillslopes. Most significantly, a large number of these gorges and stream-channels are V-shaped, implying the effects of strong tectonic activity on river incision, which obviously leads to the geomorphological alteration of the postglacial terrain (Korup 2005). From past historical records, notable geomorphic regions where landslide dams are prevalent include the Andes of South America (Porter and Savigny 2002; Schuster et al. 2002), the European Alps (Huggel et al. 2002; Casagli et al. 2003; Crosta et al. 2013), the Himalayas (Hewitt 1998; Richardson and Reynolds 2000), the Canadian Cordillera (Clague and Evans 1994; Geertsema et al. 2006), the mountains of Central Asia (Strom 2010, 2013), the mountainous margin of the Tibetan Plateau (China) (Ouimet 2007; Korup and Montgomery 2008), and the Southern Alps of New Zealand (Korup et al. 2004, 2006). A brief summary of the tectonic evolution of some of these regions is given below.

1.3.1 The European Alps

The European Alps are the highest and largest mountain belts in Europe, extending more than 1000 km from the French and Italian Mediterranean coasts across Switzerland, northern Italy, and Austria into the central parts of the European

continent. Numerous catastrophic events associated with rock avalanche processes, landslide dams, glacier-ice dams and moraine dams have been recorded in many parts of the European Alps (Allen et al. 2011; Huggel et al. 2012; Stoffel and Huggel 2012; Crosta et al. 2013). These have been related to the orogenic processes that lead to mass accretion into the mountains, followed by isostatic uplifts, hillslope erosion processes that lead to high sediment yield, and the evolution of relief. Historical records of events predating the 13th Century indicate that several catastrophic disasters such as glacial lake outburst floods (GLOFs), were triggered from the failure of many natural dams formed by deep-seated landslides, ice, snow and rock avalanches, and sturzstroms in many parts of the Western European (Swiss) Alps (Costa and Schuster 1988; Wassmer et al. 2004; Pollet and Schneider 2004; Gutiérrez 2005, pp. 548~550).

The tectonic style of the European Alps is characterized by a complex pattern of overthrusted nappes (Fitzsimons and Veit 2001; Kühni and Pfiffner 2001). The Alps evolved from continental convergence and collision between the Adriatic microplate (the smaller part of the African Plate) and the European Plate. The collision resulted in the southward subduction of the Penninic Ocean and subsequent intra-plate (continent-continent) collision during the Tertiary (Schmid and Kissling 2000). These orogenic processes resulted in the overthrust of the European continental margin (Helvetic domain) by the African continental margin (Australoalpine domain) (Figure 1.1). The orogenic processes that led to the evolution of the entire Alps into a high mountain range are as a result of isostatic compression and exhumation of the lighter continental crust (Bernet et al. 2001). Consequently, the topography of the Alps is roughly symmetrical, with the highest mountain summits in the central region. The mountain range of the Alps is characterized by a crystalline core comprised of pre-Alpine magmatic rocks and polymetamorphic sediments overlain by Mesozoic and Cenozoic metasedimentary sequences, both of which constitute the Penninic and

Helvetic thrust nappes (Wittmann et al. 2007). Other major tectonic units in the Alps include the Jura Mountains, the Molasse Basin, the nappe complexes of the Austroalpine and Southalpine zones, and the Po Basin (Kühni and Pfiffner 2001). The Southern Alps are separated from the Central Alps by the Tonale Line, which is an E-W trending portion of the Insubric Line (Schmid et al. 2004). Due to strong tectonic compression and deep incision of the Lepontine area, the mountain range of the Western (Swiss) Alps is narrower with higher elevations (4,807 m at Mont Blanc) than the Eastern Alps (Fitzsimons and Veit 2001). The prevalence of many catastrophic geomorphic processes in the Alps has been linked to several large-scale European climate patterns, coupled with the steep relief and elevation of the Alps (Frei and Schär 1998; Auer et al. 2005). All these have been included in the predisposing factors for the high frequency of occurrence of deep-seated landslides and landslide dams, glacier-ice dams and moraine dams in the Alps.
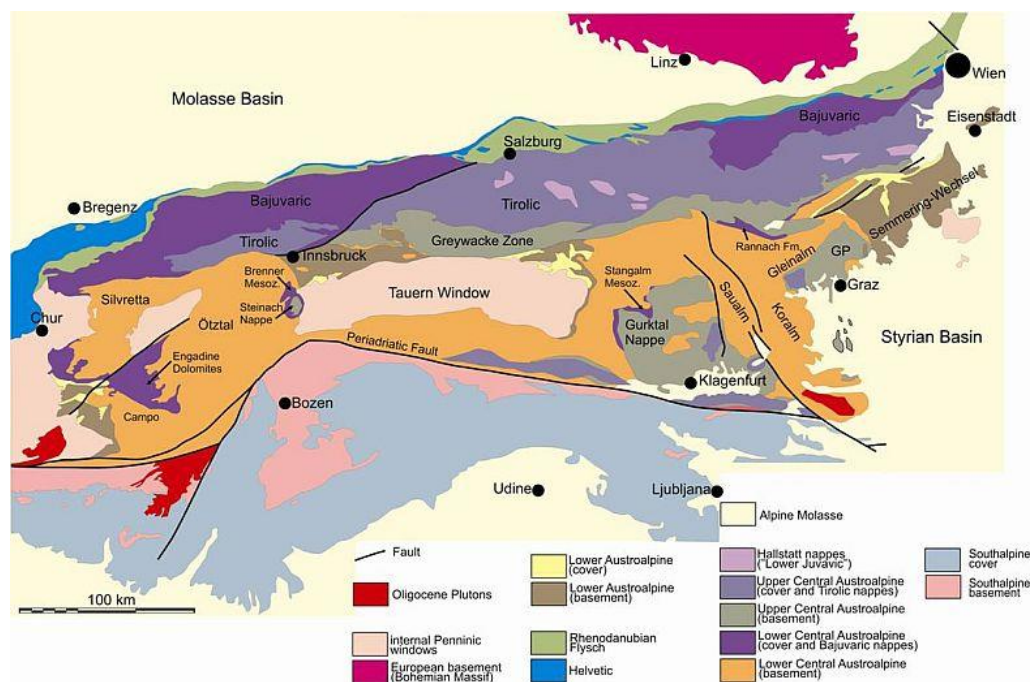
Figure 1.1 Geologic map of the European Alps (http://erdwissenschaften.uni-graz.at)

1.3.2 The Himalayas

The Himalayas are a geodynamically active region which is susceptible to extreme crustal activity that causes earthquakes. For this reason, denudation processes and natural damming of stream-channels and gorges are common phenomena in the region. The resultant effects have triggered several catastrophic outburst floods released from the breaching of landslide dams, glacier-ice dams and neoglacial moraine dams (Richardson and Reynolds 2000; Mool et al. 2001; Hewitt 2011). Most significant among these natural disasters are glacial lake outburst floods (GLOFs), which commonly occur in many river basins of the Nepal Himalaya, at altitudes of 4500~5500 m a.s.l. (Kattelmann 2003).

The evolution of the Himalayan mountain range began around 65 Ma as a result of the intra-plate (continent-continent) collision between the Indian and Eurasian Plates, along the Indus-Zangbo Suture Zone (Korup et al. 2006). For this reason, the Himalayan mountain range is characterized by a complex aggregate of structurally deformed and highly metamorphosed lithologic units which bear imprints of various stages of tectonic occurrences (Figure 1.2; Yin 2006). Partly forming the summits of the highest peaks on earth (Mt. Everest, 8848 m a.s.l.), is a 10~17 km thick unmetamorphosed parautochthonous sedimentary sequence of the Tibetan Himalaya (Proterozoic-Eocene) (Korup et al. 2006; Weidinger 2011). Further south abounds crustal thrust planes formed within the Indian Plate at 20~25 Ma (Weidinger 2011). The Main Central Fault (MCT), which is a longitudinal thrust fault characterized by mylonitization and retrograde metamorphic assemblages, delineates the boundary between the Higher Himalayas and the Lesser Himalayas (Yin 2006; Webb et al. 2007). The Higher Himalayas (or Greater Himalayan Crystalline Complex) mark the axis of orogenic uplift and signify a multiphase deformational event, which is mainly composed of ductily deformed metamorphic rocks including quartzite, migmatite, paragneiss and mica schists (Gehrels 2003; Wang et al. 2013). The Main Boundary

Thrust (MBT) marks the southernmost tectonic boundary where the unmetamorphosed clastic rocks of the Miocene-Pliocene Himalayan foredeep comprising the molasse-type Siwalik Formation are overthrust by the nappe systems (comprised of metasedimentary rocks) of the Lesser Himalayas (Meigs et al. 1995; Robinson et al. 2006). The southern end of the Himalayan foredeep (Sub-Himalayan sequence) is bordered by the Main Frontal Thrust (MFT), which uplifts sediments of the Siwalik Group southward over the Indo-Ganjetic plain (Baker et al. 1988; Wesnousky et al. 1999; DeCelles et al. 2001; Yin 2006).

The principal factors that favour the occurrence of natural dams in many parts of the Himalayas stem from the high rate of exhumation of about 1~15 mm/year and the high topographic relief (Korup et al. 2006). This is exacerbated by the summer monsoon rainfall (1500 mm/yr~6000 mm/yr) that results in high fluvial processes and sediment yield of $10^2 - 10^4$ t km^{-2}/yr (Korup et al. 2006). Most noteworthy is the fact that the duration and intensity of precipitation are orographically controlled by the barrier formed by the Himalayan mountain chain (Bookhagen et al. 2005; Wulf et al. 2010). The occurrence of deep-seated slope deformations and giant rock flows within pre-existing fissures and joints have continued to modify the Himalayan postglacial terrain (Figure 1.3; Korup et al. 2006). Similarly, the high frequency of formation of glacier dams and moraine dams in many parts of the Himalayas (Delany and Evans 2011; Weidinger 2011), and in the headwaters of the Indus and Tsangpo rivers have been attributed to a dynamic coupling between the rate of erosion and exhumation in the cores of the Himalayan Syntaxes (Korup et al. 2010; Hewitt 2009, 2011).
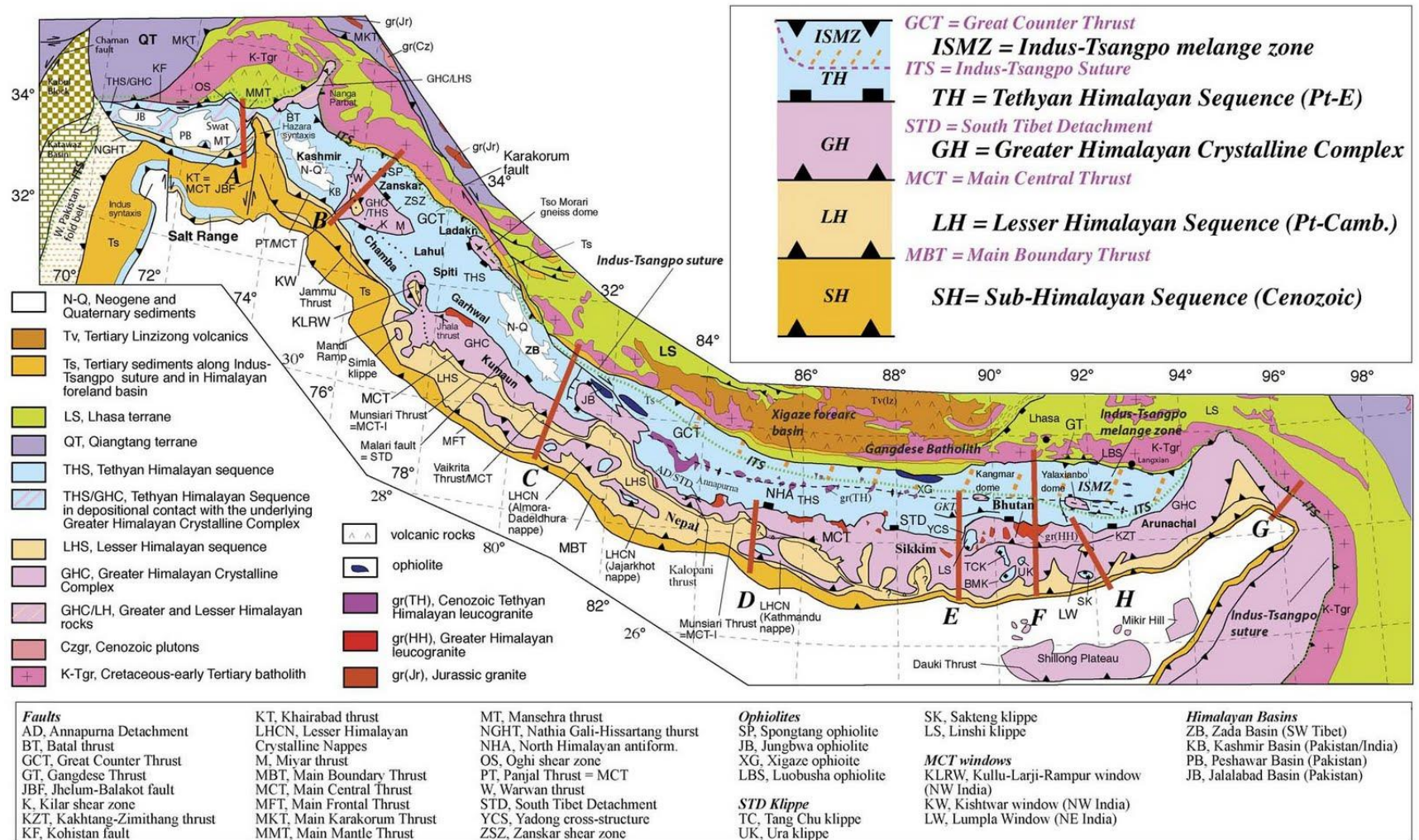
Figure 1.2 Regional geologic map of the Himalayan orogen (Yin 2006)

Figure 1.3 Source area of the May 2012 rock fall and avalanche into the Seti River Gorge in the Nepal Himalaya. The rocks in the source area are highly tilted metamorphosed sedimentary rocks which are covered with snow (Image source: NASA earth observatory file image)

1.3.3 The Southern Alps of New Zealand

Historical records of landslide dam formation in New Zealand show that a large number of these events occur in the Southern Alps. The types of landslides that form these dams are predominantly deep-seated block slides and rock avalanche processes (Whitehouse and Griffiths 1983; Korup 2005; Allen et al. 2009, 2011). The southern part of New Zealand is straddled by a 500 km-long mountain range of the Southern Alps, which evolved from an oblique continental collision of the Indo-Australian Plate and the Pacific Plate, primarily along a 600 km Alpine Fault (Figure 1.4) (Kamp and Tippett 1993; Sutherland 1995). The collision resulted in the upturning and rapid exhumation of the leading edge of the Pacific Plate which is

comprised of partly metamorphosed greywacke of the Torlesse Terrane (Fitzsimons and Veit 2001; Herman et al. 2007). High rate of uplift (5~8 mm/yr) along the plate boundary resulted in the formation of a mountain range, which is characterized by an asymmetrical cross-section with sharp topographic expressions, deeply dissected valleys and peak summits higher than 3000 m a.s.l., a few kilometers from the Tasman Sea (Fitzsimons and Veit 2001).
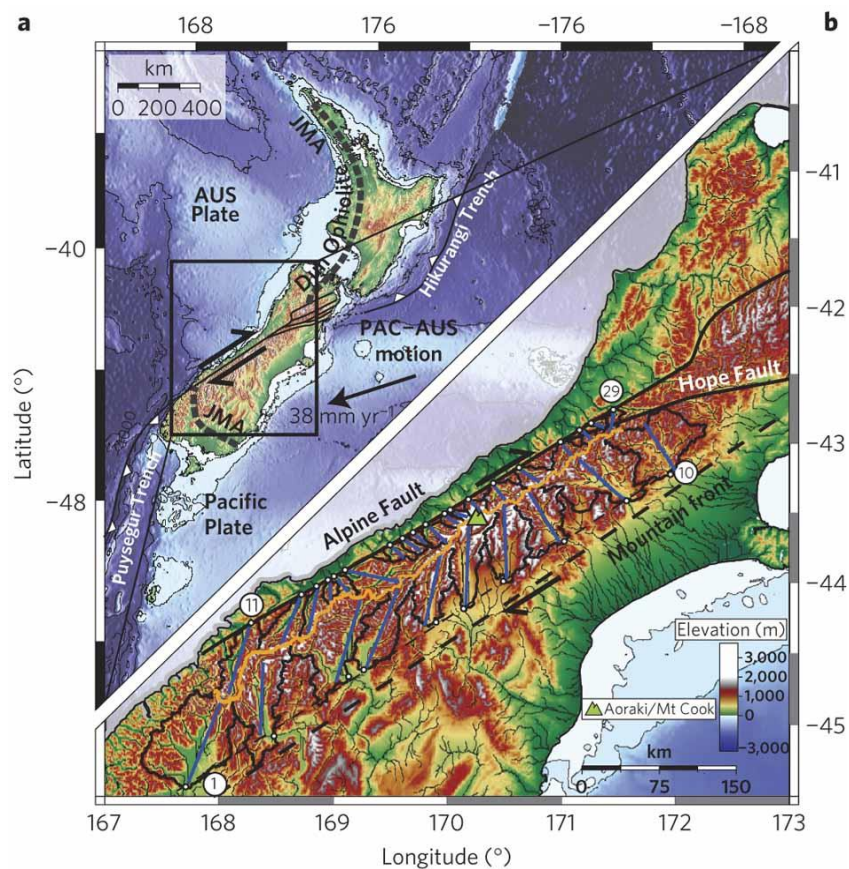
Figure 1.4 Tectonic and topographic map of the South Island of New Zealand (Castelltort et al. 2012)

The mountain range of the Southern Alps is considerably young and is being modified by high uplift forces and denudation processes. High fluvial sediment yield of $10^2 \sim 10^4$ t/km²/y from the western Southern Alps (WSA) has been related to the

extremely steep and intensely dissected slopes that are being modified by high fluvial erosion and debris avalanche processes (Whitehouse 1988; Korup et al. 2006). This is because precipitation is orographically enhanced, especially at the steeper faces of the western divide where up to 14,000 mm/y of rainfall has been recorded (Henderson and Thompson 1999). Highly glaciated landforms dominate the axial Southern Alps (ASA), while the eastern divide (ESA) are predominated by intermontane basins and broad valleys where huge volumes of glacigenic deposits are preserved (Korup 2011).

1.4 Occurrence of Landslide Dams in China and Japan

1.4.1 Landslide Dams in China

Several forms of natural disasters frequently occur in China, most times resulting in an untold number of deaths and infrastructural damage worth several billions of Chinese RMB. High frequency of occurrence of landslides and river-damming events in most parts of China has been attributed to the complex geological structure of many Chinese mountain regions including the Loess Plateau area, the Hengduan mountain areas of Southwest China, as well as in the Provinces of Hubei Xizang, Guizhou, Sichuan, Gansu, Shaanxi, Yunnan and Shanxi (Li 1990). These rugged mountains are characterized by high rates of rock weathering and mass shattering, coupled with orographically enhanced precipitation of high intensity and frequent earthquakes which make up the predisposing factors for the occurrence of landslides and landslide dams (Li 1990).

Historical records of geomorphic disasters in China indicate that the occurrence of landslides and landslide dams predates the 11th Century BC (Table 1.1). The June 11, 1786, landslide dam disaster which occurred in Luding area, Sichuan Province of China, remains the worst recorded landslide dam disaster in the world. This

landslide dam was triggered on June 1, 1786, by the Mw 7.75 earthquake in the Kangding-Luding area. The landslide dammed the Dadu River and failed ten days later resulting in catastrophic outburst floods that traveled downstream, claiming about 100,000 lives (Dai et al. 2005).

Table 1.1: Selected historical cases of landslide dam disasters in China

No	Year	Province/Region	Affected Area	No. of Fatalities	Source
1	1786	Sichuan	Luding	100,000	Dai et al. 2005
2	1933	Sichuan	Maowen	2,429	Li 1990
3	1951	Taiwan	Tsao-Ling	154	Li 1990
4	1965	Sichuan	Zepozhu	-	Costa and Schuster 1991
5	1967	Sichuan	Tanggudong	none	Dai et al. 2005
6	2000	Tibet	Bomi	30	Shang et al. 2003
7	2008	Sichuan	Beichuan*	-	Xu et al. 2009
8	2008	Sichuan	Tianchi*	-	Wang et al. 2013
9	2014	Yunnan	Ludian*	-	Zhang et al. 2014

On April 9, 2000, a huge landslide with a volume of 3×10^8 m³ occurred in the Zhamu Creek, in Bomi county, the southeastern region of Tibet (Shang et al. 2003). The entire drainage area of the Zhamu Creek is 20.2 km², with length, width and mean longitudinal slope of 9.7 km, 50~200 m, and 52.6%, respectively. The high occurrence of landslides in the area has been attributed to the collision between the Indian plate and the Eurasian plate, resulting in an uplift- and slip rate of 3 mm/year and 10 mm/year, respectively. The landslide evolved as a wedge failure and entrained colluvial materials downstream before transforming into a debris flow that subsequently blocked the Yigong River (Figure 1.5b). The landslide dam occupied an area of 2.5 km², with minimum and maximum heights of 60 and 100 m, respectively, and minimum and maximum bottom widths of 2200 and 2500 m, respectively. The upstream and downstream slope angles of the impoundment were 5° and 8°, respectively. Prior to the breaching of the landslide dam, remote sensing images

analyzed by Shang et al. (2003) provided evidence of the likely occurrence of piping and seepage at the downstream end of the blockage. However, the landslide dam was overtopped by the upstream lake 62 days after its formation resulting in about 30 deaths and causing a large number of damage to infrastructures (Figure 1.5c).

The devastating effects of the Ms 8.0 Wenchuan earthquake resulted in a large number of landslide dams in the Sichuan Province of China. The earthquake occurred in the Longmenshan mountain range at exactly 14:28 (Beijing time) on May 12, 2008 (Figure 1.6). The epicenter was located on the north-east trending Longmenshan thrust fault zone (LTFZ) at a focal depth of 14~19 km (an active crustal region) (Fan et al. 2012), as a result of the collision between the Indian plate and the Eurasian plate (Dai et al. 2011). Data analysis revealed that a total number of 828 river-damming landslides were triggered by the earthquake (Fan et al. 2012); 61% of these resulted in complete blockage of rivers, while 39% caused partial blockage and stream-channel diversion. Although a good number of these natural blockages had not failed as at the time the database was generated, studies carried out by Xu et al. (2009) indicated that some of these dams could potentially fail by seepage and piping, considering the nature of the materials composing them.

1.4.2 Landslide Dams in Japan

The Japanese archipelago is located within the *Pacific Ring of Fire* where frequent crustal movements (tectonic activities) have resulted in a large number of earthquakes and volcanic eruptions. The geologic and geomorphic features of the Japanese Islands are being modified by the subduction of the Pacific Plate and the Philippine Sea Plate. These have triggered several natural disasters including earthquakes, volcanic eruptions, typhoon-induced landslides and debris flows, and catastrophic outburst floods (Sassa 1998, 2005; Chigira and Yagi 2006; Hayashi et al. 2013).
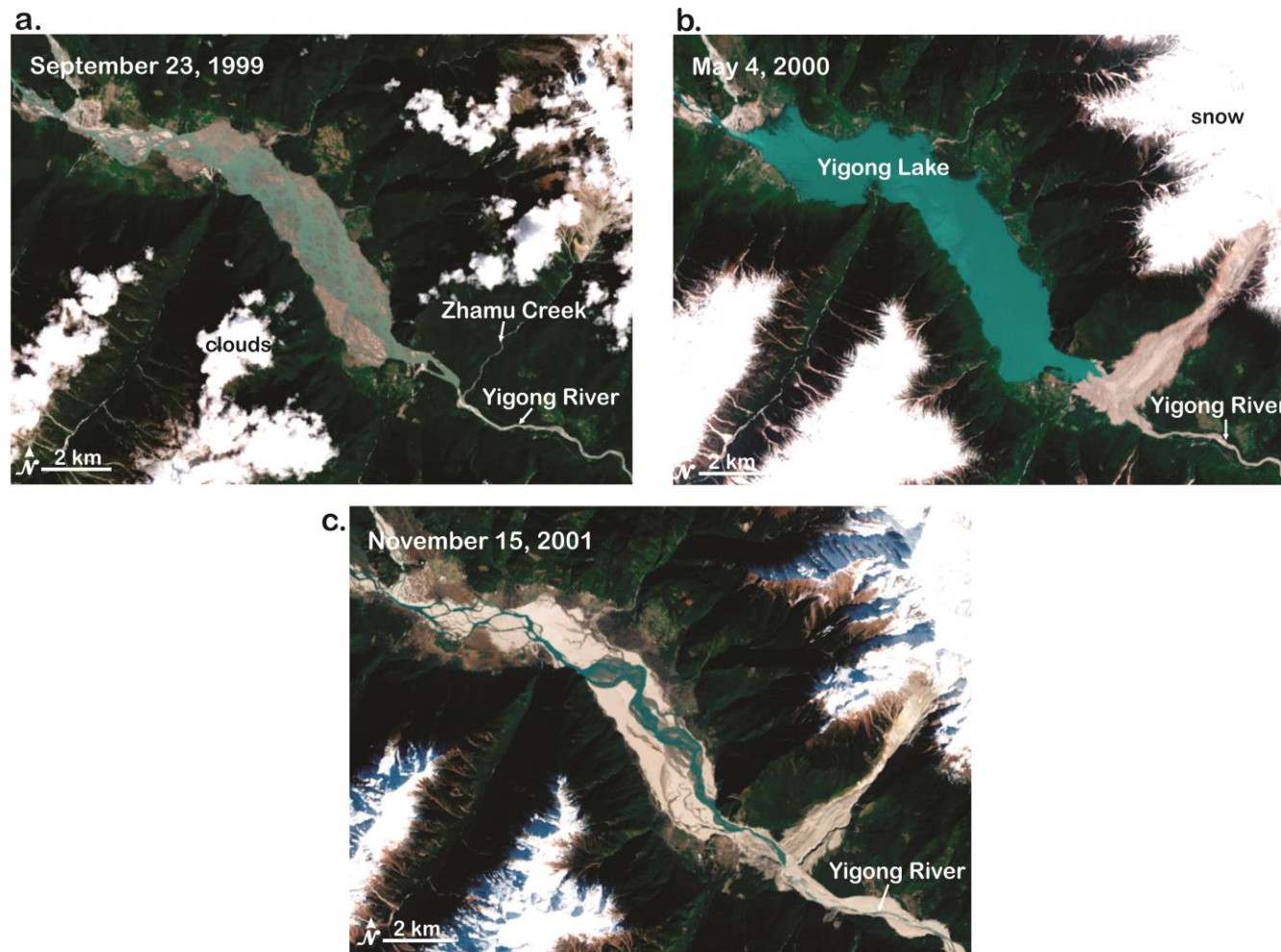
Figure 1.5 Time history of formation and failure of the Yigong landslide dam. **a.** Yigong River before the damming event **b.** Post-damming setting of the Yigong River **c.** Post-failure setting of the Yigong River (Image credit: NASA Earth Observatory)
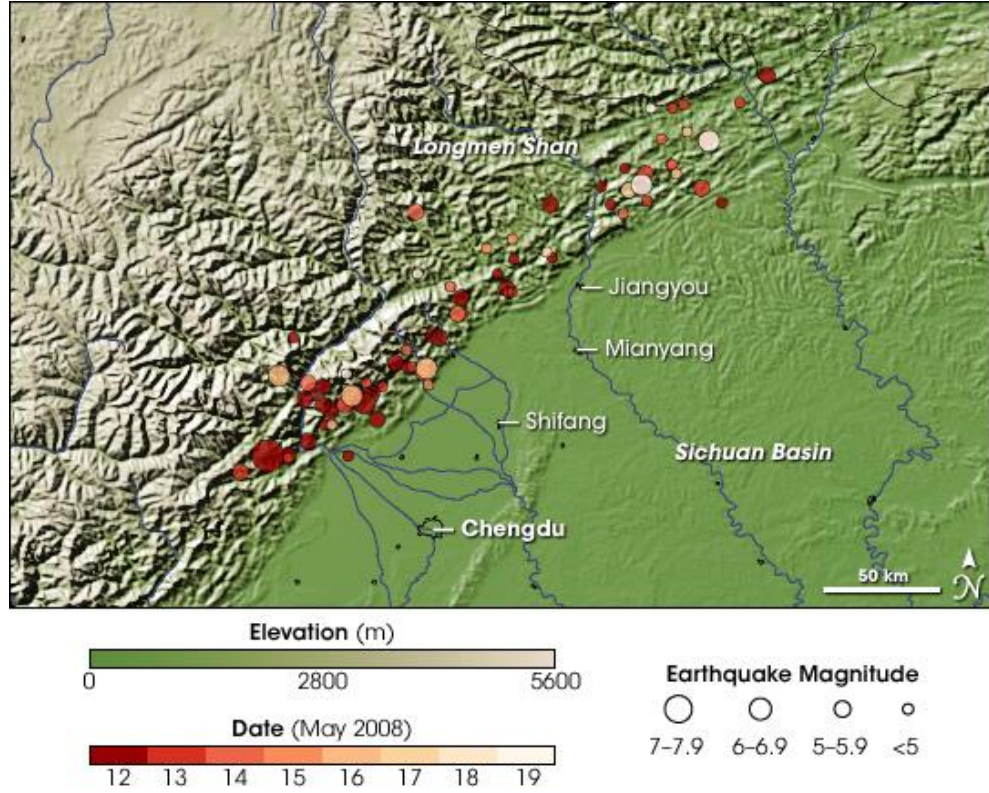
Figure 1.6 Topographic map of the Longmenshan mountain range and surrounding region showing the distribution of main shocks and aftershocks of the 2008 Wenchuan earthquake (Image: NASA Earth Observatory)

The Japanese Islands are characterized by steep and rugged watersheds coupled with high-intensity rainfall and snowmelts. These characteristic features have resulted in high fluvial processes in many mountain slopes which initially, have been destabilized by repeated earthquake ground motions. Oguchi et al. (2001) identified 6(six) major geomorphological and hydrological variables influencing the rate of fluvial processes in Japan. These include high-intensity precipitation, catastrophic hydro-geomorphological events associated with earthquakes and volcanic eruptions, high sediment yield, steep watersheds, large flood discharge and efficient transport, and frequent slope failures and landslides.

The occurrence of landslide dams in several part of the Japanese Islands has been attributed to the abundance of steep and unstable mountain slopes with average modal angle of 35° (Katsube and Oguchi 1999), high-gradient streams, narrow gorges, coupled with frequent hydrologic and seismic events (Swanson et al. 1986; Oguchi et al. 2001). Historical data from Tabata et al. (2002) and Inoue et al. (2013) indicated that the occurrence of landslide dams in Japan predates the 9th Century BC, and occurred mostly in active tectonic boundaries. A typical example is the high distribution of landslide dams in Northern Nagano Prefecture, Japan (Table 1.2). The occurrence of landslide dams in this region has been attributed to the geomorphic history of the area which is located in the great central belt of Japan (*the Fossa Magna*) (Mizuyama et al. 2011; Inoue et al. 2013).

The 1847 Zenkoji Earthquake (M_s 7.4) and the 1858 Hietsu Earthquake (M_s 7.1) triggered two mass movements that dammed the Sai River and the Joganji River. The high sediment (ca. 1.3 to 2×10^8 m³) yielded from the latter event resulted in the failure of the landslide dam and consequently caused several damages due to the release of the impounded waters which resulted in catastrophic outburst floods.

Table 1.2: Historical data of landslide dams in Northern Nagano Prefecture, Japan (Mizuyama et al. 2011)

No	Landslide Dam	Date Formed	Causative factor	Longevity	Dammed River
1	Aoki Lake	30,000 years ago	Unknown	Still existing	R. Takase
2	Old Chikuma	22-8-887	Goki Shichido Earthquake	303 days	R. Chikuma
3	Old Aiki	20-6-888	Secondary debris avalanche	600 years	R. Aiki
4	Kashima River	7-1441	Heavy rain	3 days	R. Kashima
5	Mt. Manaita	28-1-1502?	Essa Earthquake	Unknown	R. Hime
6	Mt. Shimizu	28-1-1502?	Essa Earthquake	Unknown	R. Nakatani
7	Mt. Iwato	28-4-1714	Shinshu Otari Earthquake	3 days	R. Hime

8	Tobata	24-6-1757	Heavy Rain	54 hours	R. Azusa
9	Mt. Iwakura	08-5-1847	Zenkoji Earthquake	19 days	R. Sai
10	Kiriake	08-5-1847	Zenkoji Earthquake	Failed gradually	R. Nakatsu
11	Mt. Amamizu	08-5-1847	Zenkoji Earthquake	A few days	R. Shinano
12	Yanakubo Lake	08-5-1847	Zenkoji Earthquake	Still existing	R. Yanakubo
13	Ikari	08-5-1847	Zenkoji Earthquake	16 days	R. Dojiri
14	Somuro	08-5-1847	Zenkoji Earthquake	Failed gradually	R. Somuro
15	Oyasawa	08-5-1847	Zenkoji Earthquake	Unknown	R. Susobana
16	Garagara Sawa	16-6-1891	Heavy Rain	Failed gradually	R. Matsu
17	Mt. Hieda	08-8-1911	Heavy Rain	3 days	R. Hime
18	Taisho Lake	06-6-1915	Volcanic Eruption	Still existing	R. Azusa
19	Mt. Kazahari	21-4-1939	Snowmelt - Flood	Failed gradually	R. Hime
20	Mt. Akahage	04-5-1967	Snowmelt - Flood	101 days	R. Odokoro
21	Mt. Kozuchi	16-7-1971	Heavy Rain	Failed gradually	R. Hime
22	Oku Susobana	05-5-1997	Snowmelt - Flood	Still existing due to engineered spillway	R. Susobana

The October 23, 2004, Mid Niigata Prefecture earthquake ($M_w = 6.8$) triggered thousands of all kinds of landslides. As many as 30 small-scale landslide dams were formed in the Imogawa River and adjoining tributaries (Chigira and Yagi 2006). The data excludes those formed by deep-seated mass movements that created huge blockages in the Imogawa River, especially in Higashi-Takezawa and Terano districts. Many of the small-scale landslide dams breached several hours after their formation. Their short lifespan has been related to the materials forming the dams which were mostly comprised of highly weathered bedrock and regolith (Wang et al. 2007). However, emergency countermeasure works (construction of spillways, water diversion pipes/tunnels, and installation of drainage 12 pumps) were carried out on the Terano and Higashi-Takezawa landslide dams to avert potential dam breaching

and the release of water from the impounded lakes upstream of the dams (Sassa 2005).

The passage of a severe tropical cyclone, Typhoon Talas (named Typhoon No. 12 in Japan), over the Japanese archipelago in September 2011 brought cumulative precipitation of 1,000 to 1,500 mm in the southern part of the Kii Peninsula, and 2,436 mm in 5 days in some districts in Nara Prefecture. The Kii Peninsula of Japan has been considered as one of the regions prone to deep catastrophic landslides and associated mass movements (SABO 2010). The arrival of the cyclone destroyed inhabited areas and affected municipal buildings, leading to a severe infrastructural damage worth close to $600 million USD. Data obtained from erosion and sediment control division of the Ministry of Land, Infrastructure, Transport and Tourism showed that in Nara Prefecture alone, 14 fatalities were recorded while 10 people were declared missing. About 13 houses were inundated by debris flows and floods, 50 houses were completely destroyed while 70 houses were partially destroyed. Wakayama Prefecture recorded 52 deaths with 5 people declared missing. A total of 1,985 houses were partially destroyed, and a record 2,642 buildings were flooded, with the complete destruction of 365 buildings (Fujita 2012). About 207 landslides, landslide dams, debris flows and other sediment-related disasters were triggered in 21 prefectures with Mie, Nara and Wakayama Prefectures recording the highest number of cases. The volume of sediments produced by the effect of the cyclone was estimated to be about 100 million m³ (Hayashi et al. 2013). Field investigations carried out immediately after the disaster confirmed that deep catastrophic landslides were triggered in 72 locations and 17 landslide dams were formed in different locations as a result of these deep-seated movements, five of which were discovered to be at risk of failure due to the rate of increase in the level of the barrier lakes created by the impoundments (Figure 1.7 and 1.8; Hayashi et al. 2013).
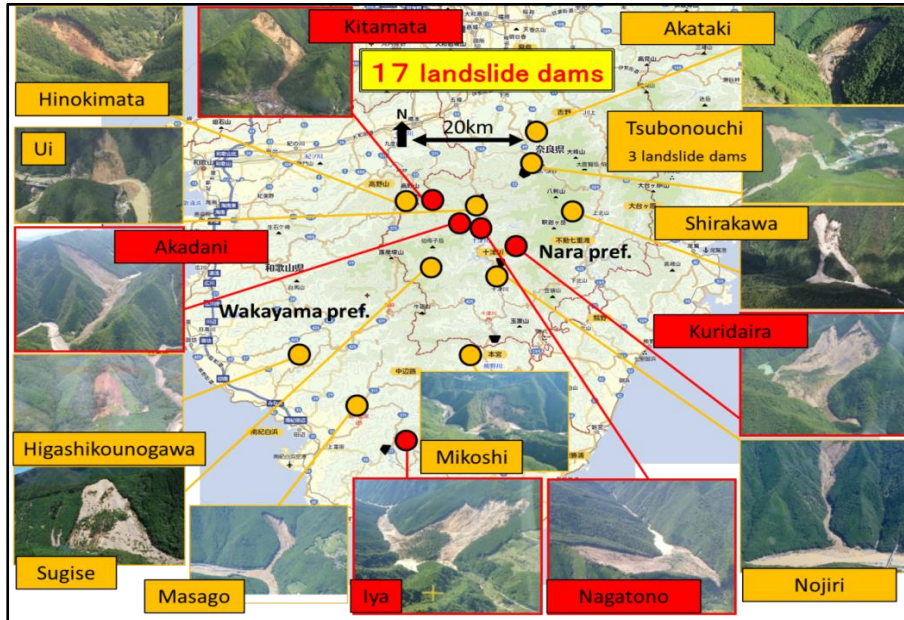
Figure 1.7 Distribution of 17 landslide dams triggered by Typhoon Talas in the Kii Peninsula. The images in red borders represent dams where emergency investigations were carried out (Hayashi et al. 2013).
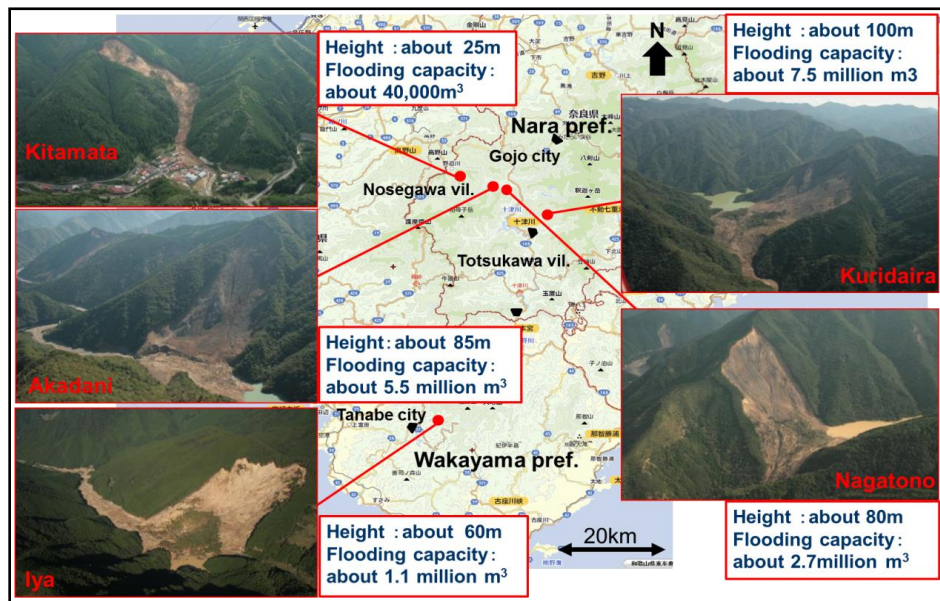
Figure 1.8 Locations of the 5 landslide dams selected for emergency investigations and countermeasure works (Hayashi et al. 2013)

1.5 Classification of river-damming landslides

Many river-damming landslides have been classified based on the general classification scheme proposed by Cruden and Varnes (1996) in their classification of landslides, with emphasis on the type of movement and the material involved (Table 1.3). Notable research on the classification of river-damming landslides has been completed by Costa and Schuster (1988), who identified a wide variety of mass movements that cause river-damming events. Costa and Schuster found that a large number of landslide dams were caused by avalanches, slumps, and slides, and flows. Similarly, the dataset of more than 500 landslide dam cases collected from around the world by Costa and Schuster (1991), and Schuster (1993) found that more than 50% of the dams were formed from earth slumps and slides; ca. 25% by debris, mud or earth flows; ca. 19% by rock or debris avalanche; and ca. 6% shared by sensitive-clay failures and by rock and earth falls. The results above were corroborated by a more recent study by Peng and Zhang (2012), using a dataset of 1,239 landslide dam cases.

Table 1.3: Classification of landslides based on the type of movement and material (Cruden and Varnes 1996)

Type of Movement	Type of Material		
	Bedrock	Engineering Soils	
		Predominantly Coarse	Predominantly Fine
Fall	Rock Fall	Debris Fall	Earth Fall
Topple	Rock Topple	Debris Topple	Earth Topple
Slide	Rock Slide	Debris Slide	Earth Slide
Spread	Rock Spread	Debris Spread	Earth Spread
Flow	Rock Flow	Debris Flow	Earth Flow

The authors found that a total of 469 landslide dam cases (37.9%) were caused by rock and soil slides or slumps; 396 (32.0%) by unknown causes; 180 (14.5%) by rock and debris avalanches; 164 (13.2%) by mud, debris and earth flows; 19 (1.5%) by rock

and debris falls; and 11 (0.9%) by other types of mass-movements such as lateral spreads and volcanic eruptions (Figure 1.9). Costa and Schuster (1988) noted that the insignificant number of landslide dams formed from falls can be attributed to the volume of the material representing this type of landslide damming mechanism.
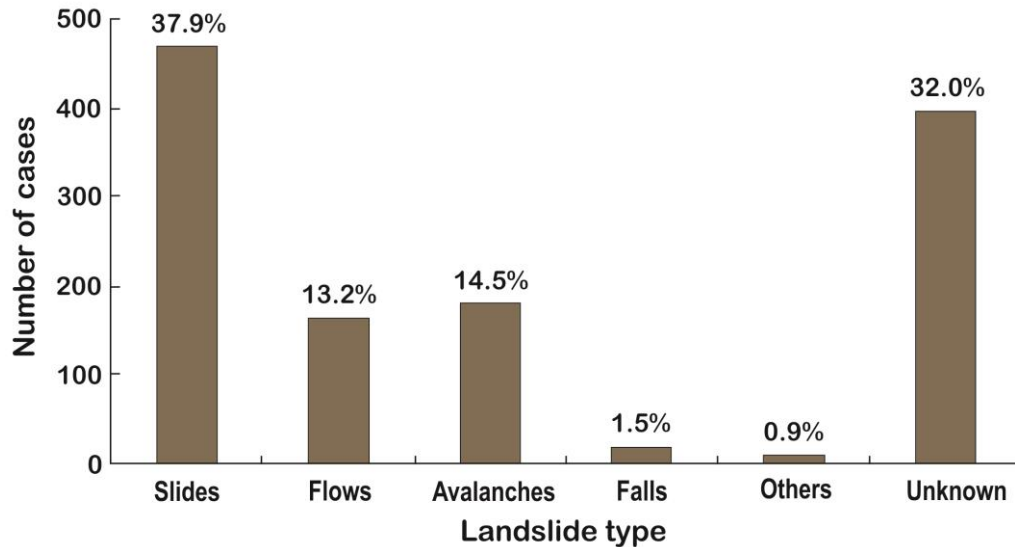
Figure 1.9 Types of landslides that have formed landslide dams based on 1,239 cases histories inventoried by Peng and Zhang (2012)

1.6 Triggering mechanisms of river-damming landslides

The triggering of mass movements involves an external stimulus which causes an abrupt increase in stress or reduction in strength resulting in a near immediate response in the form of a landslide (Wieczorek 1996). The three most significant triggering mechanisms of landslide dams are high-intensity rainstorms, snowmelt, and earthquakes. Schuster et al. (1998) identified four groups of factors that control the spatial distribution of landslide dams formed by the 1989 Loma Prieta (California) earthquake. These include (1) seismic intensity, (2) hillslope gradient and topography, (3) lithology and weathering properties of the rock material, and (4)

soil moisture and groundwater. In some cases, the unavailability of data on triggering mechanisms and types of river-damming landslides emphasize the discrepancies associated with documentation of landslide dam inventory. For instance, the examination of $n = 232$ landslide dams from New Zealand inventoried by Korup (2004) indicated that 59% of the triggering mechanisms remained unknown, 28% were triggered by earthquakes, 11% by coseismic ground motions, 3% by high-intensity rainstorms (tropical cyclones), and 3% from fluvial undercutting, anthropogenic activities, or less obvious mechanisms.

There seems to be a strong link between the temporal occurrence of landslide dams and climatic and/or seasonal rainfall patterns. This assertion has been observed from the datasets of 353 case histories of landslide dams mostly from Italy, Japan, Canada, USA and New Zealand (Figure 1.10). The result showed that 47% of the inventoried dams were triggered by rainfall events, while 34% were triggered by earthquakes (Ermini and Casagli 2003). Similarly, the database of 1,239 cases of landslide dams revealed that rainfall (42%, 517 cases) and earthquakes (40%, 500 cases) were the most dominant causes of landslide dams (Figure 1.11; Peng and Zhang 2012).
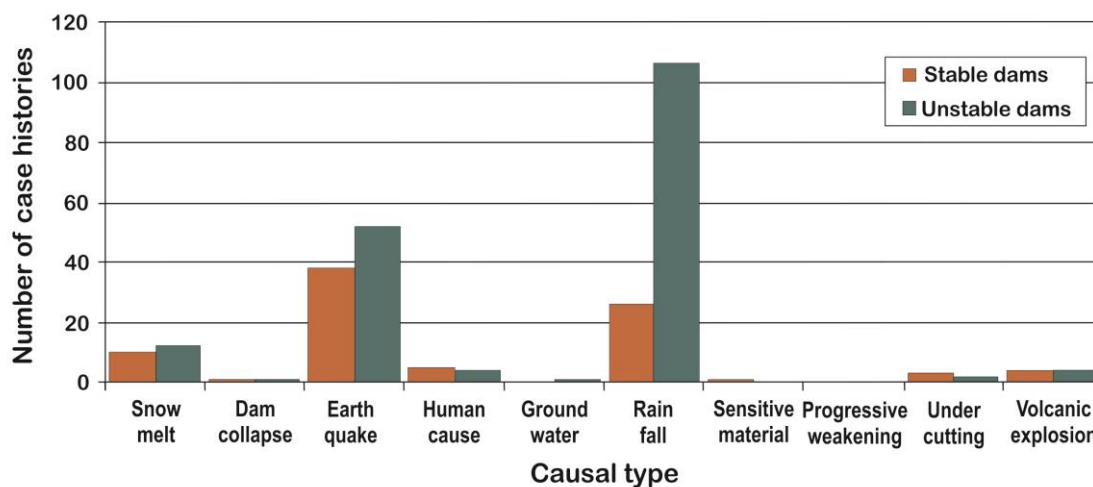
Figure 1.10 Subdivision of the 353 inventoried landslide dam cases according to the cause that triggered the movements (Ermini and Casagli 2003)
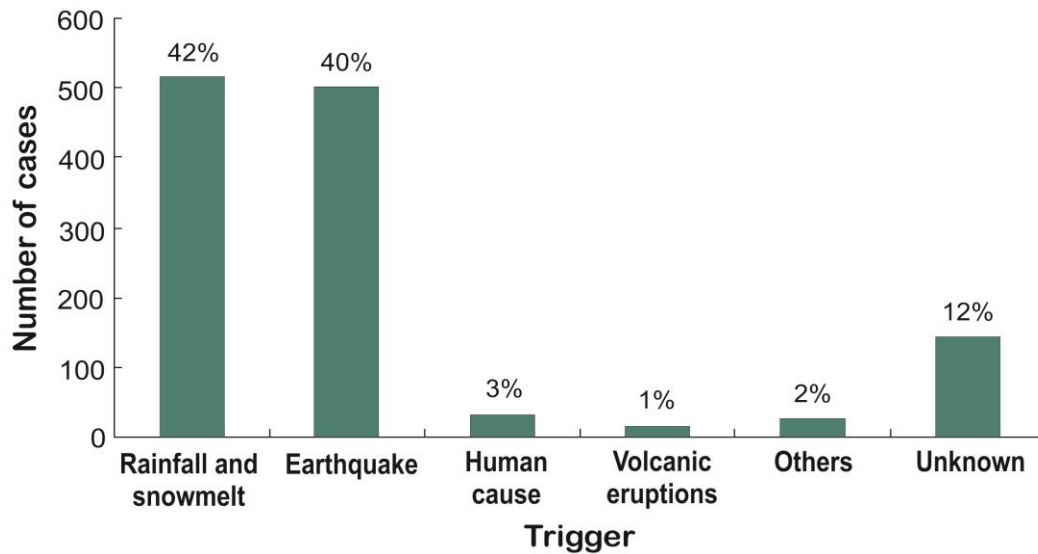
Figure 1.11 Triggering mechanisms of river-damming landslides based on 1.239 cases inventoried by Peng and Zhang (2012)

1.6.1 Implications for longevity and stability of landslide dams

The longevity of landslide dams has been a principal subject in many natural dam hazard evaluation studies. The internal structure of landslide dams has been regarded as the major factor controlling the longevity and stability of landslide dams (Costa and Schuster 1988; Dunning and Armitage 2011). The time of failure of landslide dams and the magnitude of the outburst floods depends on the internal characteristics of the impoundment, such as the grain size distribution, grain shape, degree of consolidation, presence of subsurface discontinuities, erodibility, and percentage clay content (Schuster 1995; Bromhead et al. 1996). Landslide dams composed of large-sized angular boulders or cohesive clays are less likely to fail than less consolidated or highly permeable impoundment materials. Of all the existing landslide dams in the world, the Usoi landslide dam in southeast Tajikistan remains the highest known natural dam, with a lifespan of 104 years. The dam was formed by the 1911 Ms 7.4 Sarez earthquake, which triggered rockslides that inundated the

Murghab Valley in Tajik Pamir. Seepage and piping were observed in the dam, but these have been regarded as of no threat to the downstream area (Schuster and Alford 2004). The short lifespan of many landslide dams, unlike constructed embankment dams, has been attributed to the absence of breach prevention measures such as filter zones and water barriers to prevent piping, and drain zones to control pore-water pressures. Also, the absence of channelized spillways in landslide dams leads to overtopping, which is the predominant failure mode of natural dams (Costa and Schuster 1988). However, some landslide dams do not fail quickly, lasting for months or years. For example, the longevity of 204 cases of landslide dams inventoried by Peng and Zhang (2012) indicated that 34% of the cases lasted less than 1 day while 87% lasted less than 1 year (Figure 1.12).
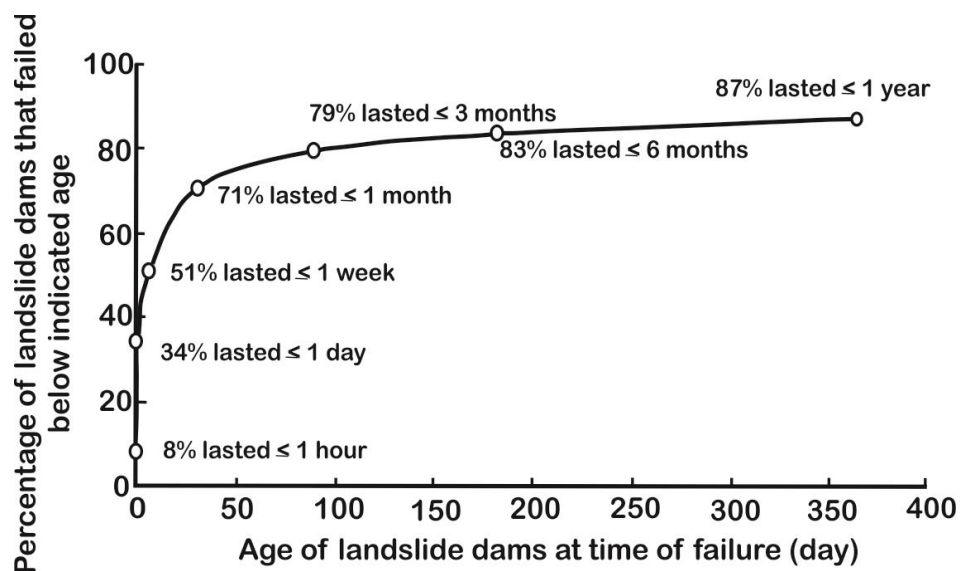
Figure 1.12 Length of time before failure of landslide dams based on 204 cases (Peng and Zhang 2012)

The longevity and stability of landslide dams can be related to the type of landslide that formed the dam and the triggering mechanism that initiated the movement. The dataset of 353 landslide dams cases inventoried by Ermini and Casagli (2003)

revealed that landslide dams formed as a result of earthquakes (57% unstable; 43% stable) and snowmelt (54% unstable; 46% stable) were more stable than those triggered by rainfall events (80% unstable; 20% stable). Similarly, landslide dams formed by translational movements were more stable than those formed by rock avalanche processes (Figures 1.10 and 1.13).
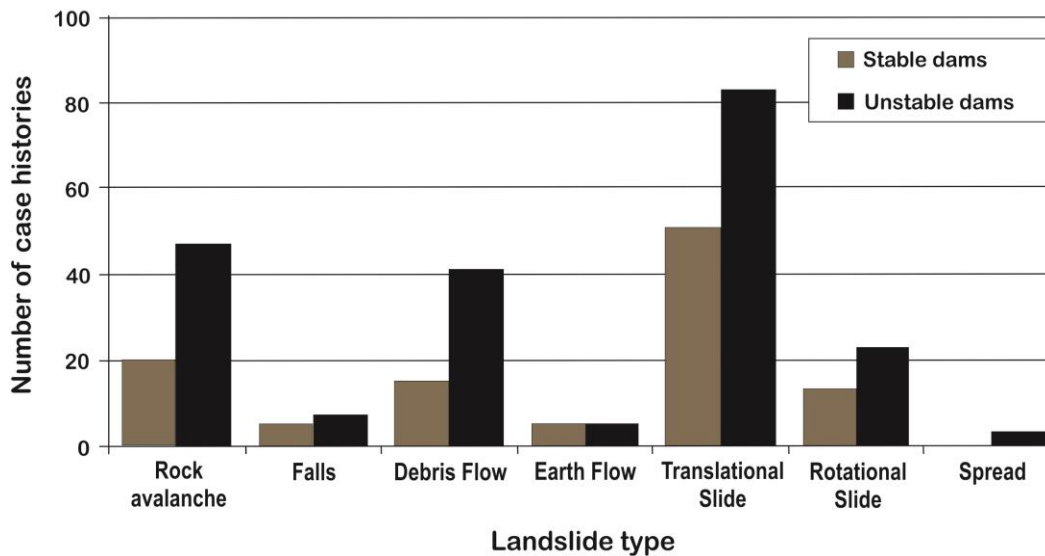
Figure 1.13 Types of landslides that have created landslide dams based on 353 cases histories documented by Ermini and Casagli (2003)

1.7 Failure Modes of Landslide Dams

Landslide dams are mostly made up of large volumes of displaced materials which sometimes vary between $10^6 \sim 10^8$ m³ (Evans 2011). For this reason, the failure of landslide dams involves the initial release of sediments and debris before the development of a complete breach. There are three major modes of failure of landslide dams. These are overtopping, piping and slope failure (Costa and Schuster 1988). The failure modes of landslide dams share similar characteristics to those observed in man-made earth and rockfill dams. Peng and Zhang (2012) made a

comparison of failure modes of landslide dams and earth and rockfill dams using the datasets of 144 landslide dam failures and 176 earth and rockfill dam failures. The result of their analysis indicated that 37% of piping cases were recorded in man-made earth and rockfill dams while 8% were recorded in landslide dams (Figure 1.14).
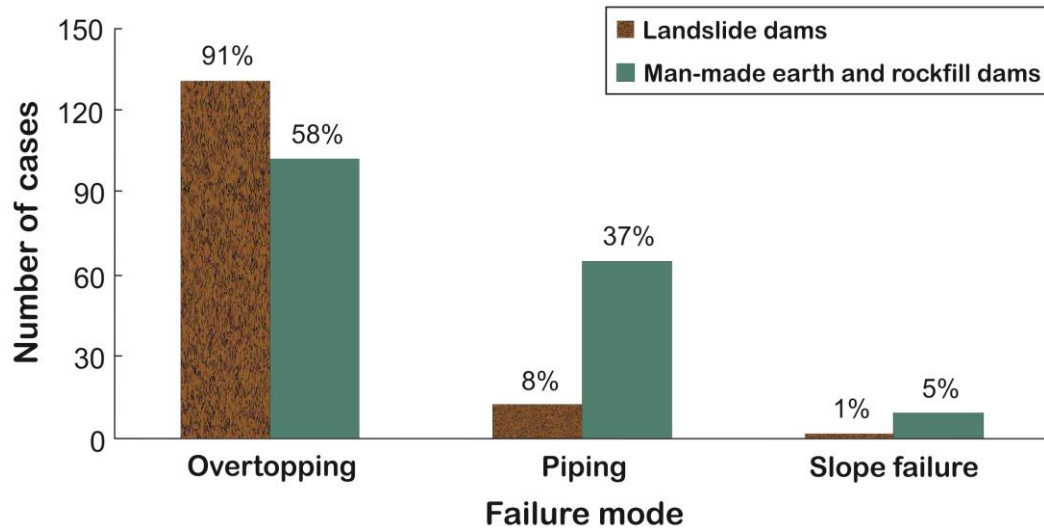
Figure 1.14 Comparison of failure modes of landslide dams (144 cases) and man-made earth and rockfill dams (176 cases) based on historical cases inventoried by Peng and Zhang (2012)

1.7.1 Piping

Piping is one of the failure modes of landslide dams. The phenomena involve pressure-driven flows which remove subsurface soils in pipe-like erosional channels towards an unprotected exit at the downstream face. In general, the development of internal erosion and piping in their early stages is not usually visible, but manifests when the internal erosion process has progressed towards an unprotected exit. The vulnerability of landslide dams to internal erosion and piping has been attributed to their heterogeneous nature, unlike engineered earthen dams which have undergone systematic compaction or have seepage barriers to reduce the potentials for internal

erosion and piping. The likelihood of initiation of internal erosion and piping in landslide dams has been attributed to their internal structure and material properties. The most important factors that influence the initiation and development of piping in several materials are the erodibility of the soil in the periphery of the seepage path and the hydraulic shear stress (McCook 2004; Hanson et al. 2010). Internal erosion and piping are common in landslide dams and earthen dams composed of dispersive soil (Figure 1.15). This is due to the high erodibility of dispersive soils arising from their low to medium plasticity and poor interlocking bonds.

Figure 1.15 The May 1937 piping failure of a dam in Arizona (USA) comprised of dispersive soil (Image source: USDA NEH 633.13)

1.7.2 Overtopping

Overtopping is one of the primary modes of failure of landslide dams. The mechanism of breach evolution due to overtopping begins as soon as the shear stress of the flowing water exceeds a critical value, after which the materials are entrained

and carried downstream. The erosion process progresses by initiating a headcut at the downstream toe which moves backward toward the upstream, resulting in the formation of an initial breach (or notch). The enlargement of the initial breach occurs through scouring of the breach sidewalls where the shear stress of the eroding medium is higher than in adjacent locations (Singh 1996). This process prevails until the depth of the breach channel reaches a competent layer or a non-erodible layer. Evidently, the scale and size of the breach are influenced by several factors including the erosive capacity of the flowing water, the shear strength of the dam material, and the area and volume of the upstream lake.

Powledge et al (1989a, 1989b) identified three flow regimes of overtopping erosion and three corresponding zones of erosion in embankment dams (Figure 1.16): (1) *Flow regime I* (subcritical flow over the dam crest) and *erosion zone I* are characterized by low flow velocities and reduced hydraulic stresses as a result of the low energy level of the flowing water. For this reason, tractive stress is usually low even though the flow depth may be reasonably high. Thus, erosion (scouring) rarely occurs except when the crests are composed of erodible materials; (2) *Flow regime II* (supercritical flow over the dam crest) and *erosion zone II* represents a transitional stage where the energy level increases from a low level to a significantly higher level, leading to an increase in the hydraulic stresses. This abrupt change in energy level over a short distance causes erosion to occur at the downstream margin of the crest; (3) *Flow regime III* (supercritical flow on the downstream slope) and *erosion zone III* describe the evolution of high-velocity conditions caused by the flow of water down the downstream slope. These conditions are enhanced by the gradient of the downstream slope which influences the development of high tractive stresses that ultimately lead to high erosion potential.
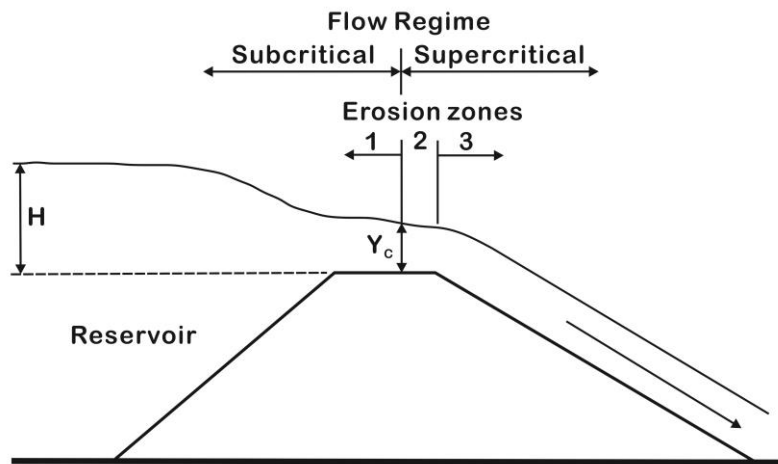
Figure 1.16 Hydraulic flow regimes and erosion zones during overtopping (after Powledge in Singh 1996)

1.7.3 Slope failure

According to Costa and Schuster (1988), slope failure occurs in landslide dams with steep upstream and downstream faces, and when pore-water pressures within the dams are above a critical value. This type of failure is sometimes related to progressive sloughing or unraveling of the downstream toe. This failure mode is initiated by undercutting erosion at the downstream toe, and results in minor slumps or slides, leaving relatively steep faces. Subsequently, small-scale slides occur intermittently at the steep faces as the hydraulic pressure exerted by the seepage causes the saturation of the downstream face. This gradual erosion process continues until the shear strength of the dam materials is reduced by the hydraulic pressure of the upstream lake, leading to instantaneous failure of the dam (Singh 1996).

CHAPTER 2

LITERATURE REVIEW ON SEEPAGE AND PIPING

2.1 Introduction

Seepage and piping are among the major subsurface erosion processes affecting the stability and long-term performance of landslide dams and other hydraulic structures. Historical records of performance of embankment dams have shown that besides overtopping, seepage and piping have triggered more catastrophic failure of embankment dams (Sherard et al. 1953; Foster et al. 2000). Internal erosion became an important field of study in the 19th and 20th Centuries when several catastrophic failures of earth dams were recorded. The phenomena naturally occur in all kinds of porous media wherever a difference in total head exists between two points. Hence, the existence of anomalous seepage in dams results in the formation of subsurface cavities or channels which trigger the uncontrolled release of impounded water, leading to instability and failure. The mechanisms of seepage and piping failure of landslide dams have not been fully understood, despite the wealth of research on internal erosion in earth dams and in other hydraulic structures. This chapter presents a critical review of internal erosion processes and the mechanisms of seepage- and piping-induced failure of dams and soil slopes, with emphasis on the critical hydraulic conditions that lead to failure of dams and soil slopes.

2.2 Definitions and nomenclature

A large amount of research has been completed on subsurface erosion in soils. However, confusion still exists between civil engineers and geomorphologists

regarding the definition and adoption of appropriate terminologies which describe these processes. Many references in the literature define these processes using several terms such as piping, tunnel erosion, soffosion, subcutaneous erosion, internal erosion, sapping, spring sapping, jugging, heave or blowout, sand boil, and tunnel scouring (Zasłavsky and Kassiff 1965; Jones 1981; Higgins 1982, 1984; Hutchinson 1982; Dunne 1990; Hagerty 1991; Wörman 1993; Terzaghi 1943; Terzaghi et al. 1996).

There have been challenges in adopting a unified model for the initiation of internal erosion and piping, considering the variety of environments that suggest the type of different initiation mechanisms (Jones 1981, 1990). Many authors have evaluated a combination of different conditions that contribute to piping erosion in different environments. These conditions include: the occurrence of a high permeable stratum underlain by impermeable strata (Bryan and Yair 1982); cyclic rainfall of high intensity (Jones 1981; Selby 1982); the existence of high hydraulic gradient within the soil layer (Parker and Jenne 1967); high pH (Heede 1971); high percentage of swelling clay (Parker and Jenne 1967); and high exchangeable sodium content (Parker and Jenne 1967).

Bryan and Jones (1997) identified two categories of subsurface erosion processes. The first occurs when water seeping through a porous medium produces sufficient drag forces required for particle entrainment at the outlet through liquefaction or Coulomb failure. The authors termed this process "*true piping*" following the work of Terzaghi and Peck (1968), as it can form a continuous piping hole that works back from the free unprotected exit towards the upstream reservoir. The second refers to the gradual enlargement of an existing conduit or macropore essentially caused by the shear stress of the flowing water.

The piping phenomenon has been related to the combined effects of seepage and flows through a porous medium. Fox and Wilson (2010) referred to seepage through or below an embankment as piping. The authors further stated that one remarkable distinction between piping by seepage and flow through a soil pipe lies in their erosion and hydraulic processes. In general, subsurface erosion involves all the processes that lead to the detachment and entrainment of finer soil particles through a porous medium under a hydraulic gradient caused by the seeping water. Cedergren (1977) listed two kinds of failures caused by internal erosion processes: (1) failures induced by the entrainment and transportation of soil particles towards a free unprotected exit or into a system of interconnected voids, and (2) failures resulting from uncontrolled saturation and seepage forces. Similarly, Dunne (1990) and Bryan and Jones (1997) presented two conditions for the occurrence of internal erosion in soils: (1) the development of sufficient drag force that entrains materials in water seeping through and out of a porous medium, resulting in liquefaction or Coulomb failure, (2) the gradual evolution of a macropore essentially caused by the effects of the shear stress exerted by the flowing water.

2.2.1 Internal erosion

This process involves the movement of water through a continuous crack or defect within a compacted fill, foundation, or at the contact between a fill and a foundation. Internal erosion can be initiated by concentrated leakage, backward erosion, and suffusion. Fell et al. (2003) divided the various processes of internal erosion and piping into four phases: initiation of erosion, continuation of erosion, progression to form a continuous piping hole and formation of a breach.

2.2.2 Piping

Piping is one of the internal erosion processes which is initiated by backward erosion, or concentrated leakage in a high permeable zone, and results in the development of a continuous tunnel called a "pipe" between the upstream and the downstream side of an earth dam or its foundation (Figure 2.1; Foster et al. 2000; Bonelli et al. 2007). A few of the processes that initiate piping in soils are described below.

- *Seepage-face erosion*: This process occurs mostly in saturated soils exposed on a sloping bed where concentrated seepage entrains fine particles at the free unprotected face and transports them downstream. This process creates a niche or re-entrant that gradually works back into the soil slope or dam to form a continuous piping hole.

- *Eluviation*: This phenomenon involves the selective erosion of finer particles through the interstitial voids of coarser materials thereby creating micropores which may form a continuous soil pipe. Eluviation also occurs where a discontinuous layer of sand or gravel is interbedded with finer sediment, and where the particles of the fine material are smaller than the interstitial voids of the sand or gravel. Hence, seeping water may entrain the fine particles and transport them through the sand, leading to the formation of soil pipes.

- *Tunneling* (or *jugging*): This process is a form of internal erosion triggered by rainfall in dispersive soils. Jugging commonly occur in the vadose zone as a result of chemical dispersion of clay soils from rainwater entering preexisting cracks or conduits that evolve as the surface dries. Parker (1964) distinguished tunneling from piping by noting that tunneling starts from the upstream face of dams and proceeds towards the downstream face. "Jugholes" are common features occurring in the crest of embankment dams (Figure 2.2). For tunneling or jugging to occur, the shear strength of the damp soils bordering the existing crack or conduit must be sufficient to support the vertical sides of the jughole so that the hole does not cave in.

- *Tunnel scour*: This process involves the concentrated flow of water through a developing pipe or conduit formed by any of the internal erosion processes such as tunneling, eluviation, seepage-face erosion or through biogenic activities such as animal burrows or decaying plant roots. The erosive action of the flowing water enlarges the pipe by scouring the pipe wall and transports the detached sediments downstream, forming a continuous piping hole.

Figure 2.1 The 2002 piping failure of the Lonesome Dove Reservoir levee in Louisiana, USA (Image source: USDA NEH 633.13)

Figure 2.2 Formation of jugholes in an auxiliary spillway of Diablo Arroyo Site 1, Hudspeth County, in the Trans-Pecos area of Chihuahua desert, USA (Image source: USDA NEH 633.13)

2.2.3 Backward erosion

Backward erosion involves the detachment and entrainment of soil particles when the seepage exits to a free surface such as the downstream face of a landslide dam or an embankment dam (Fell et al. 2003). This process gradually progresses backward towards the upstream side of the dam, forming a continuous pipe as the detached particles are carried downstream by the seeping water (Singh 1996). This kind of internal erosion generally occurs in cases where a roof a competent soil supports the evolution of a bridged opening.

2.2.4 Concentrated leak erosion

This process refers to the formation of a crack or concentrated leak in an embankment dam or its foundation which originates from the upstream face to an

exit point at the downstream face. This type of erosion is usually caused by freeze-thaw cycles, differential settlement, hydraulic cracking, desiccation and differential compressibilities in sediments resulting in the formation of large voids.

2.2.5 Heave (or blow out)

This phenomenon occurs in cohesionless soils due to the reduction of the effective stress of the soil by seepage pore pressures such that pore-water pressure equals total stress. Terzaghi (1943) reported that the phenomenon of heave occurs when a semi-permeable barrier is overlain by a pervious zone under a relatively high fluid pressure (Richards and Reddy 2007). In civil engineering, heave has been known to occur mainly during the filling of reservoirs behind dams and levees, or during the dewatering of deep, pumped excavations. Similarly, "boils" are attributed to the existence of large hydraulic head differentials which result in channelized subsurface flow leading to the erosion of the fluidized material. Instability caused by heave is usually initiated at a hydraulic boundary where the rate of movement of water through the barrier is smaller than the rate of increase in seepage pressure under steady state transient flow. Heave is characteristically different from seepage erosion or backward erosion in that backward erosion requires a critical seepage velocity sufficient for the detachment and entrainment of soil particles.

2.2.6 Suffusion (internal instability)

This process is a form of internal erosion involving the selective erosion of finer particles from the matrix of coarser particles that are in point-to-point contact, such that the finer particles are removed through the interstitial voids between the coarser particles by seepage flow, leaving behind an intact soil skeleton comprised mainly of the coarser particles. Materials which are susceptible to suffusion are

termed "internally unstable". These materials are mostly coarse widely graded or gap-graded soils (Figure 2.3). Suffusion results in an increase in seepage velocities, higher permeability, and potentially higher hydraulic gradients. Similarly, a related process known as *Suffosion* occurs when no point-to-point contact exists between the coarser particles resulting in a change in volume of the soils and thus, the development of sinkholes.
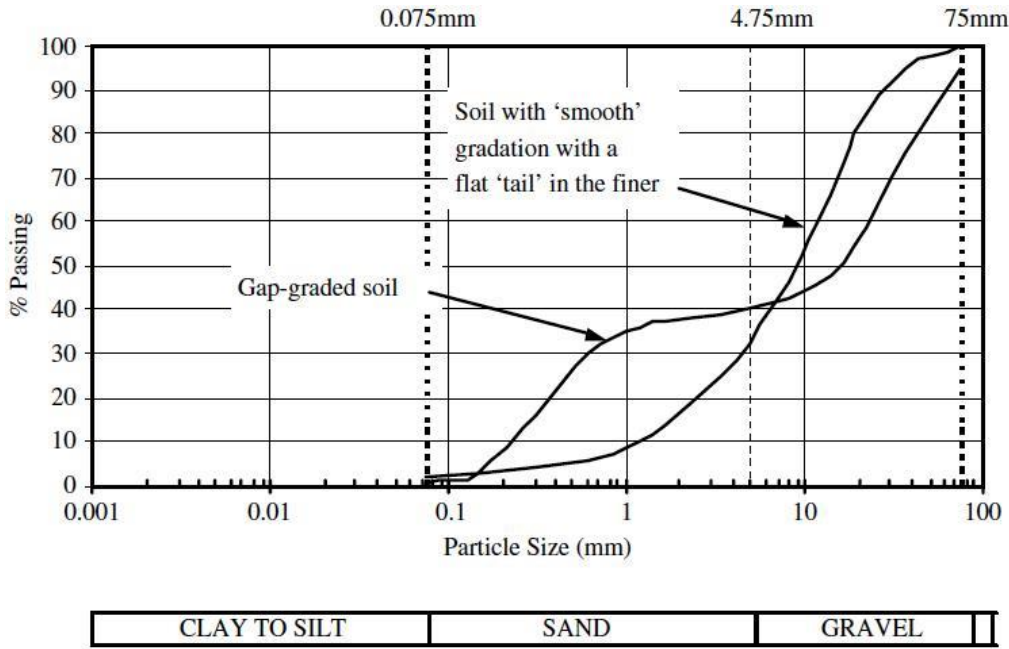
Figure 2.3 Grain size distribution curves of materials susceptible to suffusion or internal instability (Fell et al. 2005, pp. 347)

2.2.7 Internal migration (stoping)

This phenomenon refers to a scenario where the soil is not capable of forming a continuous piping hole or lacks the capability to support the pipe roof. In this case, the soil particles are transported downwards by gravity-driven movement, or may be distressed by intense seepage which causes the development of ephemeral voids in the periphery of the initiation zone until the pipe roof can no longer be supported,

thus resulting in the collapse of the void. This process may be repeated over time until the core is breached or the downstream slope is oversteepened leading to collapse. Stoping can occur in the central core of embankment dams constructed with broadly graded cohesionless materials (glacial till) due to suffusion and internal instability.

2.2.8 Contact erosion

Contact erosion involves the selective erosion of finer sediments from the contact with a coarse material due to intergranular flow through the coarse material parallel to the contact. This erosion process commonly occurs in zoned embankment dams, at the interface between different materials.

2.3 Mechanisms of internal erosion and piping

As water flows through a soil from a region of high total head to a region of low total head, the pressure head is dissipated in overcoming the viscous drag forces resisting the flow through the soil micropores. This dissipation is followed by the generation of high erosive forces which tend to weaken the interlocking bonds binding the soil particles together. If the seepage force becomes equal to or greater than the interlocking bonds (erosion resisting forces) binding the soil particles together, the soil loses its strength, leading to the initiation of internal erosion and piping. The erosion resisting forces depend on several factors including the plasticity index of the soil, the interlocking effect, gradation, cohesion, and the dispersive characteristics of any clay in the soil as well as the density of the soil particles (Singh 1996). The formation of a piping hole at the exit face of the dam has been attributed to high hydraulic gradients which must be high enough to cause internal instability in the soil. This development accentuates subsequent entrainment and erosion of

the soil at the periphery of the piping hole leading to the enlargement of the piping hole.

Fell and Wan (2005) divided the internal erosion and piping process in embankment dams into four phases: (1) initiation, (2) continuation, (3) progression, and breach/failure. The authors noted that internal erosion is initiated from the embankment into the foundation through pre-existing cracks and defects or coarse soils such as gravel in a soil foundation from which piping develops under seepage gradients. This kind of erosion involves backward erosion or suffusion but could also be initiated through concentrated leak as a result of a high hydraulic conductivity or poorly compacted zone such as the contact between the embankment and the foundation.

Fell et al. (2005, p 418) enumerated four important conditions which must exist for internal erosion and piping to occur through embankment dams or below their foundations. These conditions are:

1. There must be a seepage flow path and a water source.
2. There must be an erodible material within the flow path and this material must be able to be entrained and transported downstream by the seeping water.
3. There must be an unprotected exit (open and unfiltered), from which the eroded material may escape.
4. The material being piped or the material directly above must be able to form and support the "pipe roof".

Similarly, Parker (1964) listed four basic conditions for the occurrence of piping, irrespective of climatic and environmental conditions. These conditions are: (1) the presence of a significant amount of water to saturate the soil or bedrock above a base level; (2) hydraulic head to cause the water to flow through the subsurface

conduit; (3) the presence of a permeable, erodible soil or bedrock above a base level; and (4) an unprotected exit for outflow of the eroded sediments.

2.4 Seepage-induced failure of landslide dams and soil slopes

Seepage erosion involves the entrainment of soil particles due to the flow of water through soil micropores. When the seepage velocity is sufficiently large, particle mobilization caused by the drag forces exerted by the seepage flux causes undercutting and subsequently induces slope failure. Seepage can trigger erosion and instability in landslide dams and soil slopes through three interrelated mechanisms: (1) effects of pore-water pressure on the shear stress of the soil, (2) increase in hydraulic gradient forces acting on the soil, and (3) the detachment and entrainment of soil particles in the direction of the seepage flow (Fox and Wilson 2010).

One seepage process commonly occurring in landslide dams and soil slopes is sapping. The phenomenon involves the exfiltration of water from the exit face of landslide dams and streambanks under a sufficiently high hydraulic gradient induced by the seeping water (Hagerty 1991). Sapping is usually initiated when exfiltration occurs over a wide area such that multiple piping holes are formed or larger lenticular cavities appear at the exit point on the dam or soil slope. Under favourable conditions, the process can intensify causing an increase in hydraulic gradient and subsequent erosion of the soil materials, shortening the seepage paths. This could potentially lead to undermining of the downstream slope and breaching of the dams once there is a sufficient supply of water (Zhang and Chen 2006).

The conditions governing the mechanisms of seepage-induced transport in cohesionless sediments have been evaluated by Howard and McLane (1988). The authors carried out a series of experiments using a flume tank of dimension 2.5 m $\times$

$0.6\,m \times 0.051\,m$ (Figure 2.4). Results of their experiments showed that three distinct zones occurred at the sapping face: the *undermining zone*, the *sapping zone,* and the *fluvial zone*. The majority of the hydraulic erosion were found to concentrate in the sapping zone, mostly characterized by steep surface gradients, intermittent shallow bulk failures and rapid upward seepage. Howard (1988) observed that seepage gradients in the sapping zone are near the threshold of failure based on the balance of seepage and gravity moments and the internal friction angle of the material.
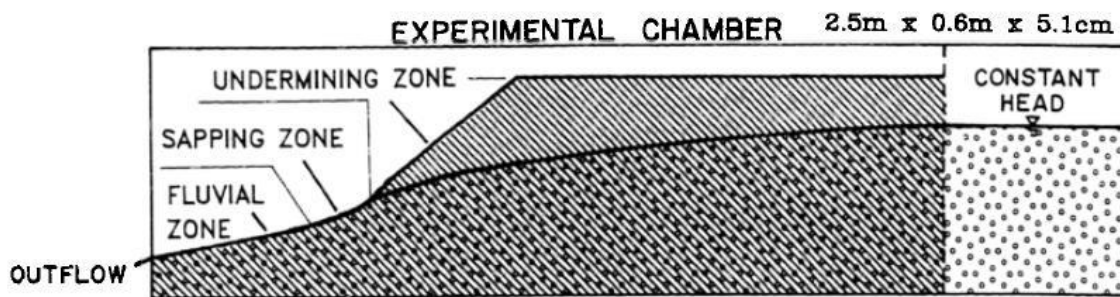
Figure 2.4 Experimental groundwater sapping chamber, showing the three major sapping zones. Ruled areas are sand, circles represent saturated zone. Permeable screen (dashed line) permits water to flow from constant head reservoir into sand (Howard and McLane 1988).

2.5 Effects of pore-water pressures on landslide dams and soil slopes

Landslide dams are generally comprised of heterogeneous and unconsolidated or poorly consolidated materials which are unsaturated in ambient conditions. The stability of landslide dams in unsaturated conditions depends on the presence of matric suction which increases the shear strength of the soil τ, as described in the equation proposed by Fredlund et al. (1978):

$$\tau = c' + (\sigma_n - u_a)\tan\phi' + (u_a - u_w)\tan\phi^b$$

(2.1)

where c' = effective cohesion of the soil, $(\sigma_n - u_a)$ = net normal stress on the failure plane, ϕ' = effective friction angle with respect to the net normal stress, $(u_a - u_w)$ = matric suction, ϕ^b = angle indicating increase in shear strength relative to matric suction. The shear stress term due to matric suction increases the stability of landslide dams and soil slopes (when the phreatic water level is significantly lower than a critical value) at an angle greater than the effective friction angle. Transient changes from unsaturated to saturated conditions under steady-state seepage causes the removal of negative pore-water pressures, and subsequent reduction of the shear strength of the soil leading to internal instability and mass failure.

The transient changes that occur under steady-state seepage in landslide dams, earth dams, soil slopes and riverbanks have been studied in detail by Talwani and Acree (1984), Fredlund et al. (1994), Rinaldi et al. (2004), and Zhang and Chen (2006). For instance, Budhu and Gobin (1995) proposed a simple model based on seepage that is parallel to an infinite, homogeneous, cohesionless soil to determine the limiting stable slope angle considering variations in river stage and peak discharge holding time. The authors reported that the materials deposited above the stable seepage slope will fail along a predefined failure plane from high pore-water pressure, gravitational forces and seepage forces. Matric suction in streambanks has been reported to vary through time due to the effects of transient variation in water stage, evapotranspiration, and rainfall. Hence, the factor of safety of the streambank and the geotechnical properties of the material vary on a seasonal scale and at the scale of a single flow event (Rinaldi and Casagli 1999).

2.6 Governing equations for seepage in saturated-unsaturated soils

The governing equations below were derived by Lam et al. (1987) on the basis of unsaturated flow theory which can be used to illustrate continuous flow in

saturated-unsaturated soil systems. In general, seepage flow through a soil mass can be described using Darcy's law:

$$q = ki \qquad (2.2)$$

where q = discharge per unit area, i = potential gradient, and k = coefficient of permeability. The governing equation for seepage through saturated-unsaturated soils can be obtained by introducing Darcy's law into the continuity equation. To describe the stress state of an unsaturated soil, Fredlund and Morgenstern (1977) suggested the use of two independent stress state variables: $(\sigma - u_a)$ and $(u_a - u_w)$. Taking h as the total hydraulic head, the net flow through a two-dimensional element of unsaturated soil can be expressed as

$$\Delta q = \frac{\partial \theta_w}{\partial t} = -\frac{\partial}{\partial x}\left(k_x \frac{\partial h}{\partial x}\right) - \frac{\partial}{\partial y}\left(k_y \frac{\partial h}{\partial y}\right) \qquad (2.3)$$

The constitutive equation for the water phase of an isotropic unsaturated soil is

$$d\theta_w = m_1^w d(\sigma - u_a) + m_2^w d(u_a - u_w) \qquad (2.4)$$

where σ = total stress in the x- and y-direction, u_a = pore-air pressure, u_w = pore-water pressure, m_1^w = slope of the $(\sigma - u_a)$ versus θ_w plot when $d(u_a - u_w)$ is zero, and m_2^w = slope of the $(u_a - u_w)$ versus θ_w plot when $d(u_a - u_w)$ is zero. Assuming m_1^w and m_2^w to be constant for a particular time step during the transient process, the time derivative of the constitutive equation are expressed as

$$\frac{\partial \theta_w}{\partial t} = m_1^w \frac{\partial(\sigma - u_a)}{\partial t} + m_2^w \frac{\partial(u_a - u_w)}{\partial t} \qquad (2.5)$$

(2.3) and (2.5) are combined to give

$$-\frac{\partial}{\partial x}\left(k_x\frac{\partial h}{\partial x}\right) - \frac{\partial}{\partial y}\left(k_y\frac{\partial h}{\partial y}\right) = m_1^w \frac{\partial(\sigma - u_a)}{\partial t} + m_2^w \frac{\partial(u_a - u_w)}{\partial t} \tag{2.6}$$

Assuming the air phase to be continuous in the unsaturated zone and that there are no external loads on the soil mass during the transient process, (2.6) can be simplified as follows:

$$\frac{\partial}{\partial x}\left(k_x\frac{\partial h}{\partial x}\right) - \frac{\partial}{\partial y}\left(k_y\frac{\partial h}{\partial y}\right) = m_2^w \frac{\partial u_w}{\partial t} \tag{2.7}$$

If the pore-water pressure term in (2.7) is expressed in terms of total head, the governing differential equation for transient seepage is then written as follows:

$$\frac{\partial}{\partial x}\left(k_x\frac{\partial h}{\partial x}\right) - \frac{\partial}{\partial y}\left(k_y\frac{\partial h}{\partial y}\right) = \rho_w g m_2^w \frac{\partial h}{\partial t} \tag{2.8}$$

If the anisotropic soil conditions are integrated by considering where the direction of the hydraulic conductivity is inclined to an arbitrary angle to the x-axis, (2.8) can be expressed as shown below

$$\frac{\partial}{\partial x}\left(k_{xx}\frac{\partial h}{\partial x} + k_{xy}\frac{\partial h}{\partial y}\right) + \frac{\partial}{\partial y}\left(k_{yx}\frac{\partial h}{\partial x} + k_{yy}\frac{\partial h}{\partial y}\right) = \rho_w g m_2^w \frac{\partial h}{\partial t} \tag{2.9}$$

where k_1 = major coefficient of permeability, k_2 = minor coefficient of permeability, α = inclined angle between k_1 and the x-axis, $k_{xx} = k_1 cos^2\alpha + k_2 sin^2\alpha$, $k_{yy} = k_1 sin^2\alpha + k_2 cos^2\alpha$, $k_{xy} = k_{yx} = (k_1 - k_2)\sin\alpha\,\cos\alpha$. m_2^w denotes the rate of absorption or release of water by a soil due to a change in matric suction. Lam et al. (1987) described the variation of m_2^w as the soil changes from saturated to unsaturated conditions as shown in Figure 2.5. The authors stressed that the value of m_2^w was equal to the slope of the water retention curve. Furthermore, they stated that under the assumptions of a constant total stress and an equilibrium condition

between a pore-air pressure and the pore-water pressure, m_2^w becomes equal to m_1^w in the saturated zone.

2.7 Effects of seepage gradient forces on landslide dams and soil slopes

Seepage forces exist wherever there is a difference in total head between two points in a porous medium that allows water movement. The governing conditions for the initiation of seepage and internal erosion depend on seepage gradient forces which must be sufficient for soil particle mobilization and entrainment. Fox and Wilson (2010) expressed the forces exerted by the seepage of groundwater on bank sediment as

$$F_s = \rho g \frac{\partial h}{\partial y} \tag{2.10}$$

where ρ is the fluid density, g is acceleration due to gravity, and $\partial h / \partial y$ is the hydraulic gradient. For a locally uniform seepage, the exit hydraulic gradient (i) can also be obtained through the relationship between seepage direction (λ) and slope angle (β) (Ghiassian and Ghareh 2008):

$$i = \frac{\sin \beta}{\sin \lambda} \tag{2.11}$$

Howard and McLane (1988) classified three forces acting on an interfacial soil particle located at the interface between a porous medium and the surface runoff produced by the emerging seepage. These forces are: (1) the tractive force of the surface runoff F_w, the force of the effluent seepage F_s, and the gravitational force F_g. Howard and McLane assumed that these forces act through the centroid of the soil element, however, F_w acts above and F_s below the centroid. The following balance of

moments, as presented by Howard and McLane (1981), represents the conditions of incipient motion:

$$[F_w d\cos\alpha + F_s d\cos(\theta + \psi - \alpha) - F_g d\sin(\alpha - \theta)]/2 = 0 \qquad (2.12)$$

where d = grain diameter, and the angles α, θ and ψ are defined as shown in Figure 2.6. The three force components are further expressed in terms of material and hydraulic properties as described below.
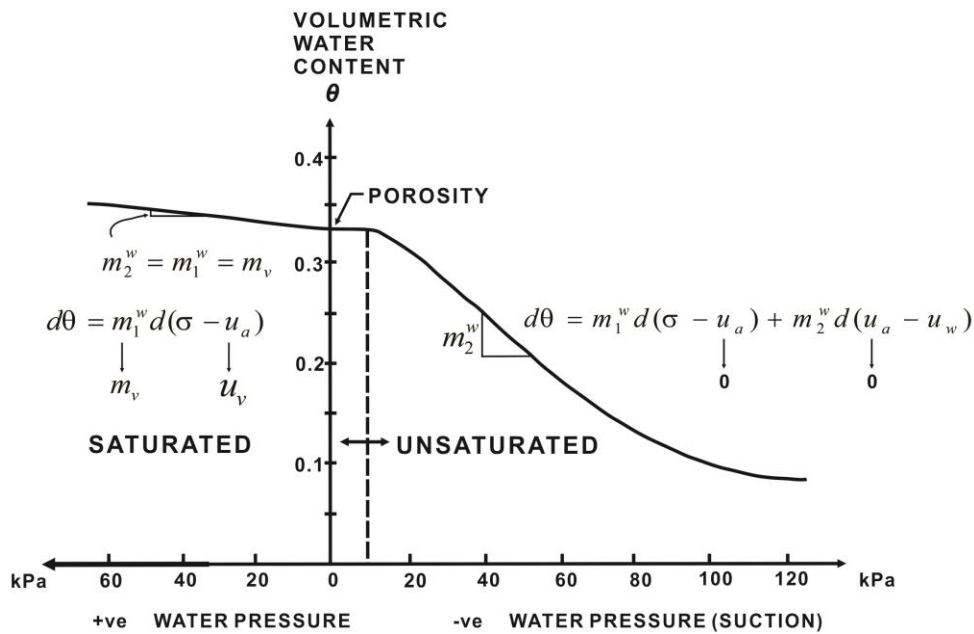
Figure 2.5 Moisture content retention curve and m_2^w for unsaturated-saturated soil (Lam et al. 1987)

Tractive force: According to Howard and McLane (1988), the tractive force acting on an individual soil element can be determined by multiplying the projected area of the particle by the average bed shear stress

$$F_w = C_1 \frac{\pi}{4} d^2 \tau \qquad (2.13)$$

where C_1 = grain shape and exposure factor.
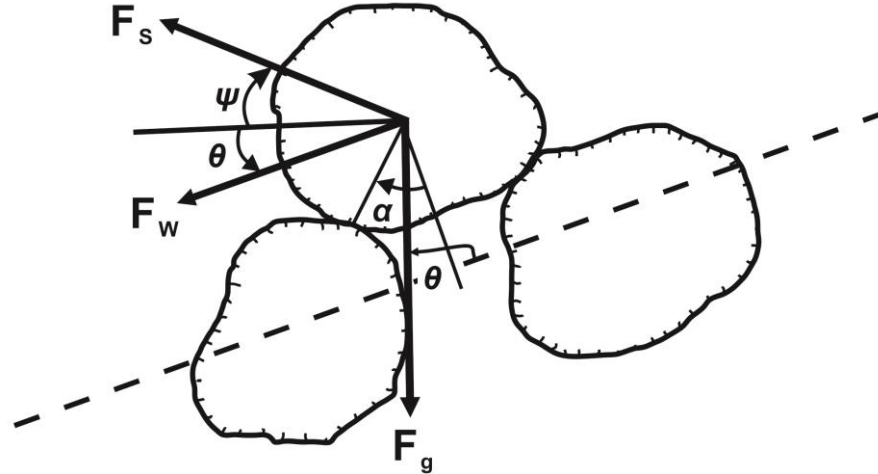
Figure 2.6 Schematic diagram of a soil element subjected to three kinds of seepage forces: F_w = tractive force due to surface runoff, F_s = seepage force, and F_g = gravitational force (Howard and McLane 1988).

Seepage force: The drag force acting on a single grain in a linear laminar seepage flow regime is expressed as

$$F_s = \lambda \mu \, du \qquad (2.14)$$

where λ = coefficient of tortuosity which takes into account the effects of adjacent soil elements, μ = dynamic viscosity of the fluid, and u = local average (seepage) velocity.

Particle weight: The buoyant weight of a soil element is expressed as

$$F_g = C_3 \frac{\pi}{6} (\sigma - \rho) g d^3 \qquad (2.15)$$

where σ = density of the soil element and C_3 = shape coefficient.

The direction of groundwater seepage paths within a saturated soil is not always uniform; this has been found to be influenced by the soil anisotropy and heterogeneity including the spatial distribution of topographic potential. The occurrence of liquefaction in a static, cohesionless soil has been linked to the effect of a one-dimensional uniform seepage force which has an upward vertical component with a magnitude equal to the submerged unit weight of the soil (Iverson and Major 1986; Fox and Wilson 2010). The hydraulic gradient in the direction of seepage flow can be expressed with respect to the slope angle and the exit angle of the seepage. The angular relationship between a seepage flow line and the seepage exit angle is schematically expressed in Figure 2.7. The difference in total head across the unit surface length is equivalent to the elevation drop x. According to Howard and McLane (1988), the flow line experiences the same head difference over the distance L, so that the hydraulic gradient is expressed as

$$i = \frac{x}{L} = \frac{\sin\theta}{\cos(\theta + \psi)} \tag{2.16}$$

2.8 The internal structure of landslide dams: implications for piping

The internal structure of landslide dams is one of the important factors that control the longevity and stability of natural dams (Costa and Schuster 1988). The likelihood of initiation of internal erosion and piping has been linked to the type of mass movement that formed the landslide dam. Landslide dams formed by translational slides have been found to be more stable than those formed by other processes such as rock avalanches, rock falls, debris flows and rotational slides (Ermini and Casagli 2003). This has been related to the ability of some landslide dam materials to preserve their source stratigraphy (Strom 2013). A typical example is the Usoi Dam (Figure 2.8).
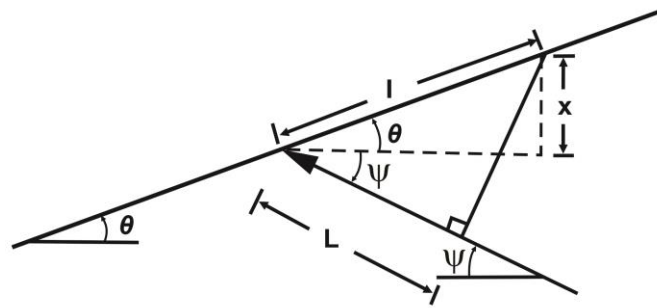
$$L = \cos(\theta + \psi)$$
$$x = \sin\theta$$
$$I = x/L = \sin\theta / \cos(\theta + \psi)$$

Figure 2.7 Schematic representation of the relationship between hydraulic gradient and seepage exit angle (Howard and McLane 1988).

This dam was formed on February 18, 1911, by a strong earthquake which triggered a huge rockslide (with an estimated volume of 2.2 km³) that dammed the Murghab River (Ischuk 2006). The longevity and stability of the Usoi Dam have been related to the type of mass movement that created the impoundment (Hanisch and Söder 2000), coupled with the presence of clast-sized materials, including boulders with an average diameter of 2.5 m (Figure 2.9). The existence of numerous seepage outlets (57 by Ischuk 2006) at the downstream face of the dam, almost at the same topographic level (approximately 3000 m a.s.l), gave further credence on the long-term stability of the dam (Hanisch and Söder 2000; Ischuk 2006; Strom 2013).

Landslide dams formed by block slides have a higher tendency to preserve their original stratigraphy because they are usually comprised of intact bedrock (original source stratigraphy) with a few fractures but generally do not comminute into smaller particles. A better understanding of the fragmentation processes that occur during runout of block slides is important for assessing the potentials for initiation of seepage and piping in the blockage. A conceptual model developed by Davies and

McSaveney (2011) has helped in the understanding of the mechanism of fragmentation in block slides during runout (Figure 2.10).
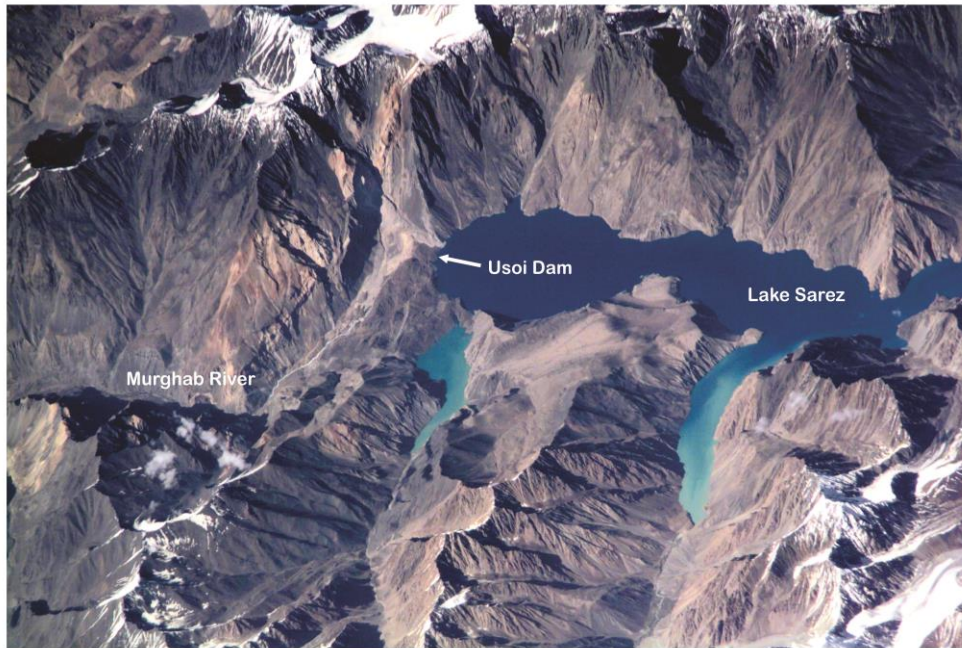
Figure 2.8 The Usoi natural dam was formed in 1911 by a $M_w = 7.7 \pm 0.2$ earthquake that triggered a huge rock slide. The rock slide originated as a wedge-like failure and dammed the Murghab River, creating a lake currently known as the Sarez Lake. Several accounts have been given regarding the existence of numerous active seepage holes at the downstream slope (Image: NASA earth observatory file image).

Numerous cases of seepage and piping occurrence in landslide dams formed by huge block slides have been reported, although these occurrences have not threatened the longevity and stability of these dams. A few examples include the Waikaremoana rockslide dam in New Zealand (Adams 1981), the Klontalersee rockslide dam in Switzerland, and Visocica River rockslide dam in Serbia (Evans et al. 2011).
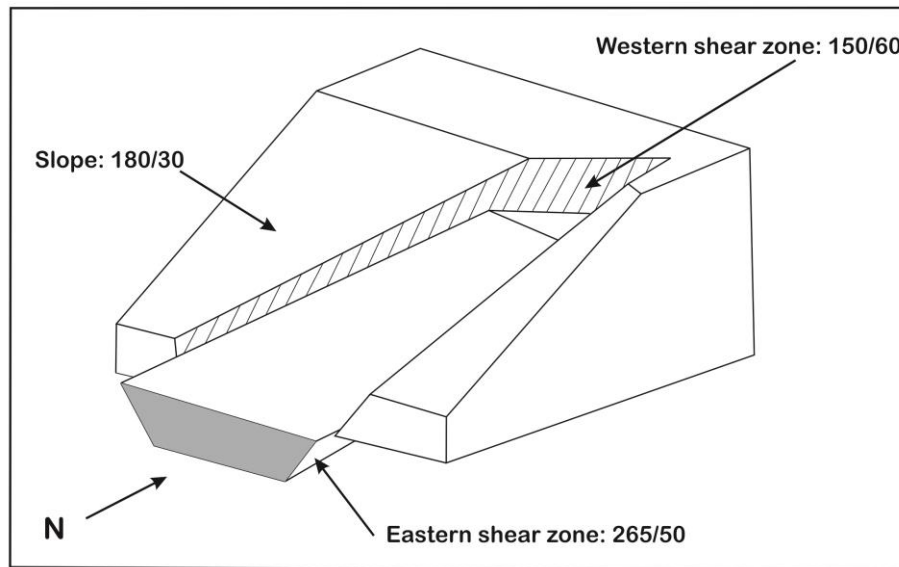
Figure 2.9 A conceptual representation of the type of initial mass movement (*block slide-wedge failure*) that formed the Usoi Dam in the Murghab River (Hanisch and Söder 2000).

The study of the grain size distribution of materials composing landslide dams is not only important for evaluating their evolutionary history, but also for predicting their potential failure mechanisms (Casagli et al. 2003; Wassmer et al. 2004). This is because grain size has a predominant effect on the longevity and overall performance of landslide dams and controls their mechanical resistance to failure by overtopping, piping or seepage (Wassmer et al. 2004). Landslide dams formed by rock avalanche processes are mainly composed of an unstructured fragmented mass of all grains sizes, excluding the uppermost layer which is dominated by larger clasts and boulders (Davies and McSaveney 2011).

Field and laboratory analysis of textural characteristics of several landslide dam materials show that they are mostly poorly to very poorly sorted, matrix- or clast-supported, finely skewed, brecciated, stratified to massive sediments, are usually armored with angular boulders, and are sutured with a matrix of very fine materials

(Weidinger 2006; Capra 2007, 2011). The results of grain size distribution analysis carried out by Casagli et al. (2003) on 42 landslide dams in the Northern Apennines showed that the diameter of the materials ranged from 1×10^{-4} to 1×10^{4} mm.
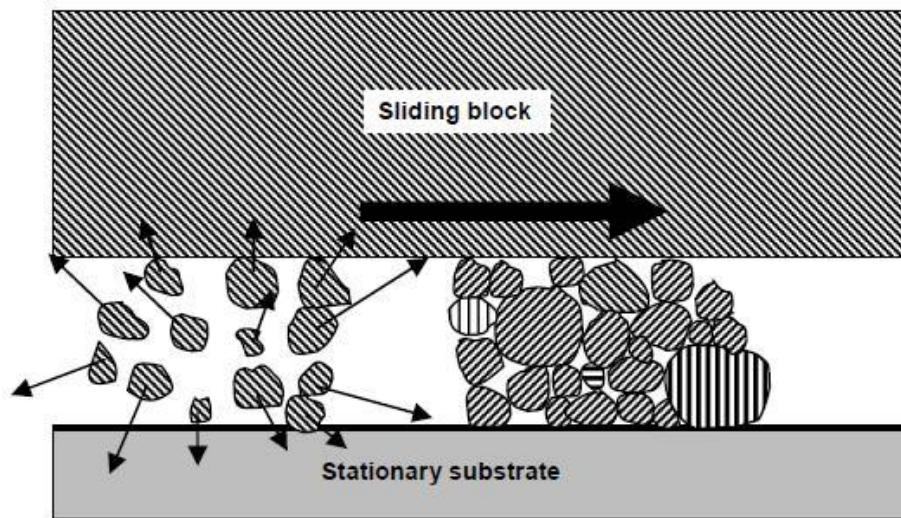
Figure 2.10 Schematic diagram of the fragmentation process that occurs in block slides. The fragmenting particles bear the weight of the blocks, reducing the normal stress between the block and its substrate and increasing the frictional resistance to motion. This phenomenon has been viewed as an important factor contributing to the stability of many landslide dams due to the ability of the block slides to preserve their original stratigraphy, and hence, increases the resistance to fail by piping or overtopping (Davies and McSaveney 2011).

Dunning and Armitage (2011) analyzed the grain size distribution of five representative rock avalanche deposits in New Zealand and the Swiss Alps (Table 2.1). The authors reported that the materials were finely skewed and can be classed as poorly to very poorly sorted.

A vast number of rock avalanche dams display a binary internal structure comprising: (1) a highly pulverized and matrix-supported basal layer which is very

erodible but has low permeability because of its low void ratio, and (2) an upper layer dominated mostly by a coarse blocky carapace of disjointed angular boulders, with large void spaces which support internal erosion and piping (Davies and McSaveney 2011; Strom 2013). This binary internal structure signifies the low likelihood of piping failure than overtopping because the highly pulverized and widely graded materials of the basal layer limit the development of seepage in the dam.

Table 2.1: Sedimentological properties of 5 selected rock avalanche deposits (Dunning and Armitage 2011)

Variable	N	Minimum	Maximum	Mean	Standard Deviation
Mean (Phi)	89	-0.13	-5.69	-2.63	1.31
Median (Phi)	89	-0.82	-6.19	-3.24	1.36
Sorting (Phi)	89	1.46	3.69	2.60	0.48
Gravel (Wt%)	89	46.97	98.65	75.85	12.08
Fractal (d)	89	1.95	3.04	2.44	0.20

2.9 Sedimentological classification of landslide dams (Facies analysis)

Several attempts have been made to classify the sedimentology of rock avalanche deposits using either a facies approach (Schneider et al. 1999; Wassmer et al. 2004) or direct analysis (Hewitt 1998; Casagli et al. 2003). A detailed review of several sedimentological data of landslide dams formed by rock avalanche processes revealed three unique features: crude inverse grading (Cruden and Hungr 1986); preservation of original source stratigraphy (Strom 2006); and presence of highly fragmented but undisaggregated clasts (Davies and McSaveney 2011). A detailed sedimentological classification of some landslide dam is given below.

2.9.1 Flims sturzstrom (Swiss Alps)

According to Wassmer et al. (2004), the Holocene sturzstrom of Flims, Grisons, Switzerland mobilized 12 km³ of Jurassic limestone, which made it one of the largest mass movements on earth. The materials formed a $10km \times 400m$ blockage in the Upper Rhine River Valley. The authors characterized the materials composing the Flims sturzstrom into five sedimentary facies.

The Structured facies comprises thick layers of rock predominated by small-scale oblique fractures that are differentiated by centimeter-thick fine-grained layers. This facies is located mostly in the internal and proximal parts of the deposit. The internal structure of this facies shows a remarkable similarity to the early stage of sturzstrom displacement. This has been attributed to the lithostatic pressure effects caused by the overburden material.

The intermediary facies is a transitional zone marking the boundary between the structured facies and the granular facies. This facies dominates the margins and the uppermost layer of the deposits and hence is mainly composed of clasts embedded in a granular matrix.

The granular facies is mainly composed of destructured breccia with clasts mixed in a sand matrix produced by friction between the rotating clasts. This facies is located mostly in the distal and lateral parts of the deposits. The effect of shear stresses at different scales induced a rotational movement of the smallest clasts.

The brecciated facies dominates the right sight of the Rhine Valley where the avalanche ran into the foot of the slope. The breccia resulting from this collision is characterized by a low amount of matrix and a jigsaw-type deep fragmentation of the clasts.

The washed facies comprises an accumulation of heterometric clasts without any fine matrix which dominates the surficial layer of the deposit. This facies can be attributed to the interaction between the overflowing lake water and the deposit which has resulted in the winnowing of the material downstream from the dam crest.

2.9.2 Volcanic natural dams

Glicken (1991) and Capra (2007, 2011) described the sedimentary architecture of volcanic natural dams formed by volcanic-debris avalanche materials using two end-member facies: *block facies* and *mixed (matrix) facies*. The authors reported that both facies can be present, or one can dominate over the other (Figure 2.11).

The block facies is mainly composed of debris avalanche blocks (unconsolidated or poorly consolidated materials of the source rock), lacking a significant amount of matrix. The size of the debris blocks ranges from tens of centimeters to more than a hundred meters wide (Glicken 1991).

The mixed facies comprises a variety of poorly graded, poorly sorted and unstratified aggregates representing all rock types derived from the original source rock. Evidence of juvenile materials such as magmatic rocks, woody fragments, and clasts of different size ranges are usually embedded in the sand matrix.

2.9.3 Rock avalanche deposits

Dunning and Armitage (2011) analyzed the sedimentological properties and the grain size distribution of five rock avalanche deposits (four from New Zealand and one from the Swiss Alps). The authors characterized the internal structure of these deposits into three distinct facies: *the Carapace facies*, *the Body facies,* and *the Basal facies*. Dunning et al. (2005) asserted that the longevity and stability of rock

avalanche dams are influenced by the thickness of the *Carapace facies*, the valley morphology and the filling rate of the reservoir.
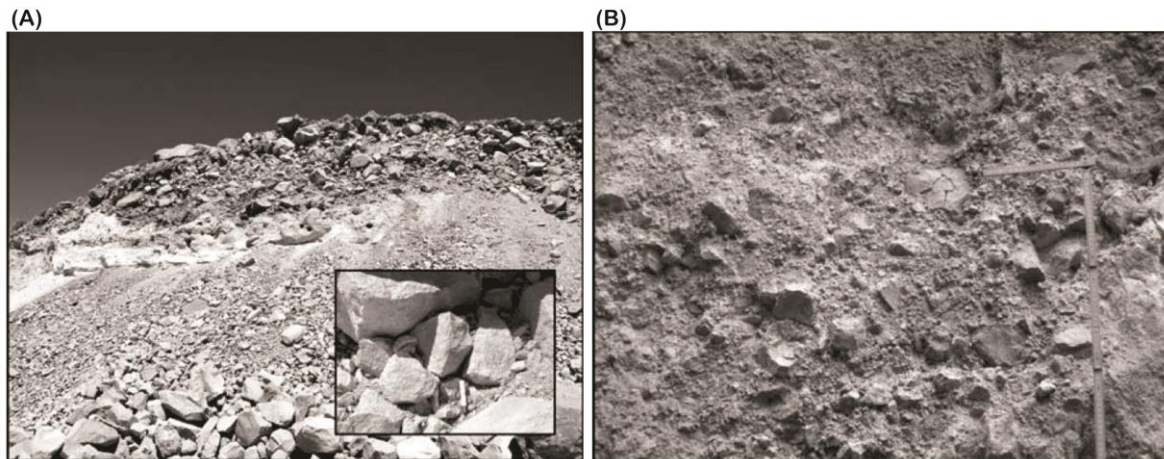
Figure 2.11 Two end-member facies typical of volcanic natural dams. (**A**) Sedimentary architecture of the *block facies* from a debris avalanche deposit near the Parinacota Volcano in Chile. (**B**) Typical textural features of the *mixed* (*matrix*) *facies* of a debris avalanche deposit, in the Nevado de Colima Volcano, Mexico (Capra 2007).

The Carapace facies is the coarsest part of a rock avalanche deposit constituting up to 30% of the total deposit thickness (Dunning and Armitage 2011). The facies is clast-supported and comprises large angular intact bedrock massifs detached from the parent rock during rapid runout. The material within this facies is mostly inversely graded and is separated by the underlying facies by a sharp boundary below which the material is intensely fragmented and matrix-supported. Permeability in this facies is very high, largely due to the clast-supported fabric, and hence the large void spaces that support filtration and restrain failure by overtopping. However, seepage erosion could occur at the boundary between the *carapace facies* and the *body facies* resulting in daylighting, dam-face saturation and

subsequent breaching of the dam (Dunning et al. 2006; Davies and McSaveney 2011; Strom 2013).

The Body facies represents the unit with the greatest thickness within a rock avalanche deposit and is usually the most voluminous in valley-confined deposits. Characteristic features of this facies include impact marks with radial fracture preserved on clasts, altered orientations and thicknesses, matrix-supported, highly fractured but relatively undisaggregated clasts, and preserved source stratigraphy. The grain size distribution and the material properties of this facies vary with respect to the lithology; this has been attributed to its preserved source stratigraphy.

The Basal facies is the smallest unit by volume within a rock avalanche deposit and also constitutes materials altered by passing rock avalanche. The materials forming this facies are derived from the erosion and entrainment of substrate materials (such as soft erodible valley fills and surface vegetation) into the base of the moving debris, and subsequent deposition of the modified mixes of substrate and rock avalanche material (Davies and McSaveney 2011).

CHAPTER 3

GEOPHYSICAL ASSESSMENT OF THE INTERNAL STRUCTURE OF LANDSLIDE DAMS

3.1 Introduction

Landslide dams are common geomorphic features in many mountainous regions of the world. These geomorphic hazards are formed where frequent slope movements and fluvial dissection result in high denudation processes that cause valley floor blockages (Korup et al. 2004). Landslide dams are potentially dangerous natural phenomena which are made up of heterogeneous mass of unconsolidated or poorly consolidated sediments, and thus may fail by overtopping or piping (Schuster et al. 1998). Failure of landslide dams could trigger catastrophic outburst floods and debris flows that could inundate the downstream areas, causing loss of lives and infrastructural damage (King et al. 1989; Becker et al. 2007).

Understanding the predisposing factors and the geomorphic processes that lead to the failure of landslide dams is essential for hazard and risk assessment studies. Empirical and statistical methods have been used to evaluate the stability of many landslide dams (Ermini and Casagli 2003; Korup 2004; Dong et al. 2009), and the potential outflow hydrograph (Evans 1986; Walder and O'Connor 1997; Satofuka 2010). However, these methods are limited by (1) the exclusion of the internal structure and geotechnical properties of landslide dams, and (2) the limited number of analyzed datasets (Ermini and Casagli 2003; Dong et al. 2009).

The leading cause of failure of landslide dams is overtopping caused by an abrupt rise in the upstream lake. Other causes of failure include internal erosion and piping, and the development of progressive seepage erosion that leads to slope instability and failure. The presence of anomalous seepage often leads to the initiation of internal erosion and piping which could potentially trigger the abrupt failure of landslide dams. Therefore, an understanding of the internal structure of landslide dams is essential for the evaluation and prediction of their potential failure mechanisms (Casagli et al. 2003). This is because, the potential for overtopping or piping failure of landslide dams depends on their internal sedimentology, which in turn depends on the source rock and on the alteration processes that occur during its movement (Davies and McSaveney 2011).

Geophysical investigations play a vital role in characterizing the internal structure of landslide dams, and for the detection of anomalous seepage at its early stage which may develop into full scale piping (Moore et al. 2011; Wang et al. 2013). The microtremor (MTM) chain array technique and the self-potential (SP) surveys are two cost-effective geophysical approaches that can be used to perform detailed on-site assessments regarding the stability of landslide dams. These geophysical techniques are non-destructive and portable, and thus are widely preferred over other methods. This is because they can be applied on rugged terrain and other hydraulic structures where boring and drilling may cause secondary damage to the dam. Similarly, these non-invasive geophysical techniques have been used for the determination of anomalous seepage in embankment dams (Corwin 1990; Sjödahl et al. 2005; Moore et al. 2011) and the phase velocity structure of many sedimentary deposits (Apostolidis et al. 2004; Asten et al. 2005; García-Jerez et al. 2008).

In the context of the present study, the microtremor chain array survey and self-potential measurements were performed at several landslide dams within and outside Japan to evaluate their apparent phase velocity structure and obtain

information regarding the presence of active seepage zones in the dams. This integrated geophysical method research was motivated by the need to characterize the internal structure of landslide dams which could aid in reconstructing the evolutionary mechanisms of the impoundments. The results could help in assessing the stability of the dams and in predicting their potential failure mechanisms, time of failure and the flood hydrograph. The frequency of occurrence of landslide dams in Japan has made these geophysical approaches preferable over other methods. Therefore, the main objectives of this study are: (1) to determine the apparent phase velocity structure of the landslide dams and provide detailed information regarding their internal structure which may give indications on their stability and potential failure mechanisms, (2) to identify potential anomalous seepage zones and other water-saturated zones in the dams and evaluate any likely relationships between these seepage zones and the upstream lake, and (3) to provide information regarding the internal structure of the landslide dams that may constrain the development of seepage and internal erosion. These objectives were achieved by using two integrated passive geophysical methods: the microtremor chain array and the self-potential measurements.

3.2 Site description

3.2.1 Akadani and Kuridaira landslide dams, Japan

The Akadani and Kuridaira landslide dams are located in Nara Prefecture, in the Kii Peninsula of Japan (Figure 3.1). The two landslide dams are among the 17 major landslide dams triggered by the devastating effects of Typhoon Talas (Typhoon no. 12 in Japan) on September 13, 2011 (Hayashi et al. 2013). About 207 landslides, landslide dams, debris flows and other sediment-related disasters were triggered in 21 prefectures with Mie, Nara and Wakayama Prefectures recording the highest number of cases. The volume of sediments produced by the effect of the heavy

rainfall was estimated to be about 100 million m³. A summary of the geomorphic characteristics of the two landslide dams is given in Table 3.1. Materials composing the landslide dams were derived from Paleogene-Neogene sedimentary units comprising weathered layers of sandstones, siltstones and mudstones, as well as detached blocks of intrusive rocks. Emergency countermeasure works such as the installation of drainage pumps, subsurface drainage channels and monitoring sensors were carried out on the sites to stabilize the dams and prevent potential occurrence of flood disasters (SABO 2012).
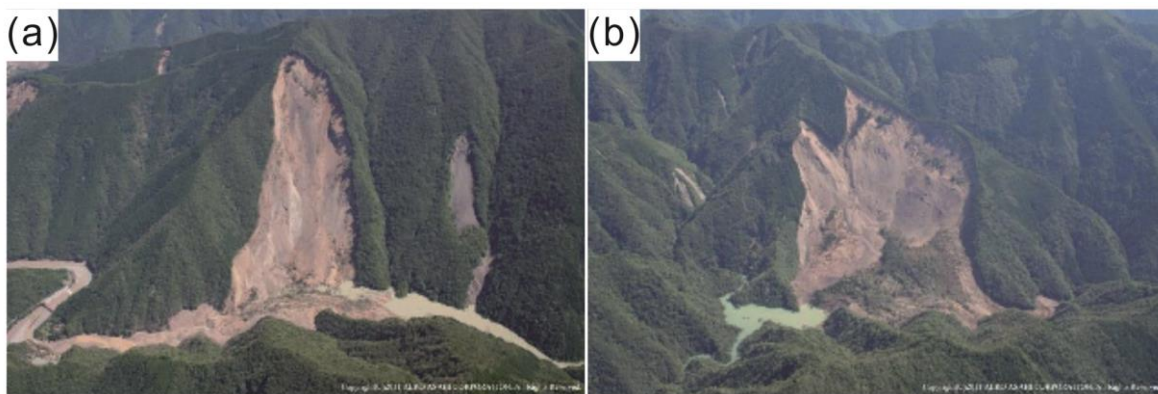
Figure 3.1(a) Akadani landslide and landslide dam **(b)** Kuridaira landslide and landslide dam (Image: Aero Asahi Corp.)

Table 3.1: Geomorphic characteristics of the Akadani and Kuridaira landslide dams

Landslide				Landslide dam			
Area	Length (m)	Width (m)	Volume (m³)	Height (m)	Blockage volume (m³)	Lake volume (m³)	Catchment area (km²)
Akadani	670	300	9,354,000	67	10,154,000	5,500,000	13.2
Kuridaira	600	500	25,133,000	100	24,133,000	7,500,000	8.7

3.2.2 Higashi-Takezawa and Terano landslide dams, Japan

The landslide dams in Higashi-Takezawa and Terano districts, hereinafter referred to as the Higashi-Takezawa and Terano landslide dams are located in the Imogawa River basin, in Niigata Prefecture, Japan (Figure 3.2). The landslide dams were triggered by the October 2004 $M_w = 6.8$ earthquake which struck Niigata Prefecture in northeastern Japan. This earthquake triggered about 1,419 shallow landslides and 75 deep-seated landslides in the vicinity of the epicenter (Nagai 2008). Detailed on-site preliminary surveys indicated that 362 of these landslides had widths greater than 50 m, while 12 landslides had volumes greater than 1×10^6 m³ (Sassa 2005). A large amount of materials displaced by the earthquake formed landslide dams at 55 locations in the Imogawa River. Materials forming these river impoundments were derived from poorly indurated and structurally deformed Neogene-Quaternary sedimentary deposits comprising mudstones, and alternating units of sandstone and mudstone including conglomerates.

The Higashi-Takezawa landslide dam was formed by a landslide which blocked the Imogawa River, depositing some of its materials at the opposite side of the river valley. The length, width and depth of the landslide that formed the Higashi-Takezawa landslide dam were 350 m, 295 m and 30 m, respectively; while the length and volume of the landslide dam were 350 m and 655,940 m³, respectively (Nagai 2008). Extensive countermeasure works were carried out at the dam several days after the occurrence of the event, to stabilize the dam and avert imminent danger posed by the blockage. The countermeasure works included the installation of 12 drainage pumps, construction of temporary spillways, and installation of a temporary drainage conduit (Nagai 2008). The landslide in Terano district formed a landslide dam 4.5 km north of the Higashi-Takezawa landslide. The landslide mass blocked the Imogawa River, forming a landslide dam. Numerous countermeasure

works have been done on the dam to increase its stability and avert potential overflow of the upstream lake.
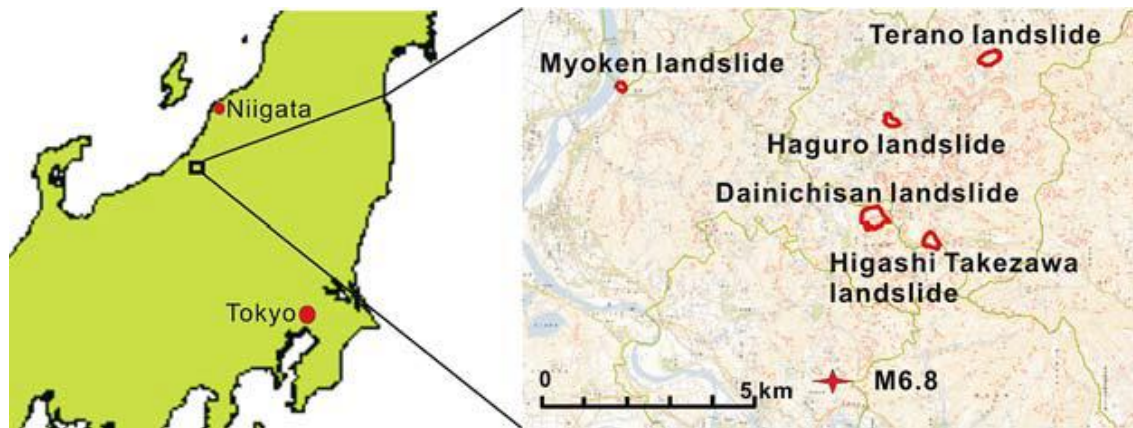
Figure 3.2 Map of the study area indicating the major landslides triggered by the earthquake (Sassa 2005)

3.2.3 Kol-Tor landslide dam, Kyrgyzstan

The landslide dam in Kol-Tor gorge, (hereinafter called the Kol-Tor landslide dam) is located about 90 km southeast of Bishkek, the capital city of Kyrgyzstan. The dam was formed by a rock avalanche that originated from the left side of the valley and blocked the valley floor. According to Janský (2010), the lake impounded by the landslide dam was initially formed by a moraine dam. Subsequent rock avalanche processes caused further blockage of the stream channel and led to an increase in the height and depth of the dam and the upstream lake, respectively. The lower part of the dam is comprised of moderately consolidated glacigenic sediments from the underlying moraine deposits while the upper part comprises poorly sorted clastic sediments including gravel and boulders. The length, width and height of the dam are 1,800, 600, and ~25 m, respectively. The landslide dam and the upstream lake are located at an altitude of 2,400~2,735 m and 2,726 m, respectively, while the lake volume, maximum depth and total surface area are 1.83×10^6 m³, 14.8 m and

2.215×10^5 m², respectively (Figure 3.3a; Janský 2010). The lake is mostly recharged by snowmelt, rainfall, water from glaciers, and subsurface springs. The existence of many subsurface cavities at the downstream end of the dam has been attributed to the effects of the melting glaciers, coupled with incessant precipitations that have led to a steady rise in the upstream lake (Figure 3.3b). Geophysical investigations were carried out on the dam to evaluate the stability of the dam due to the existence of many subsurface cavities at the downstream slope of the landslide dam. Hence, the need to evaluate the internal structure of the impoundment which will aid in flood risk assessment can be performed effectively.
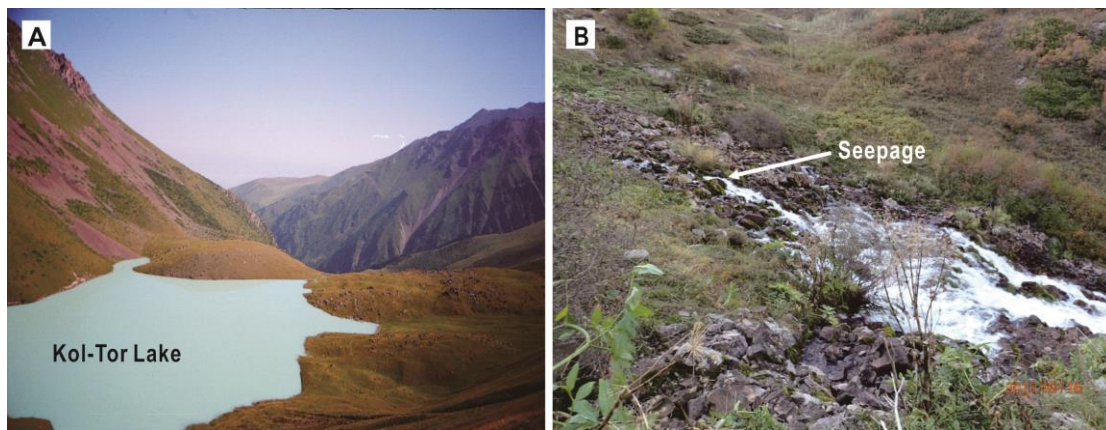
Figure 3.3 A Upstream lake impounded by the Kol-Tor landslide dam **B** Seepage/spring at the downstream area of the dam.

3.3 Geophysical surveys

3.3.1 Microtremor array survey

Microtremors or microseisms are terms used in the field of earthquake engineering to describe the constant vibrations that occur at the Earth's surface. Microtremors comprise body and surface wave motions of low energy with amplitudes in the range of 10^{-4} to 10^{-2} mm (Okada 2003; Roberts and Asten 2004). Microtremors

originating from natural phenomena (climatic variations and ocean waves) have frequencies lower than 1 Hz, while microtremors with frequency greater than 1 Hz are known to originate from anthropogenic activities such as industrial operations, road traffic and machinery (Okada 2003). The microtremor (MTM) method is a passive surface wave technique used for the measurement of natural and artificial surface waves. The technique has been used to obtain shear-wave velocity (V_S) structure and apparent phase velocity depth-profiles of geologic structures to depth range of 100 to 1000 m (Asten 2004).

The MTM method has been applied in the study of the internal structure and the dynamic characteristics of landslide dams (Wang 2013; Wang et al. 2015), and other subsurface structures (Nakamura 1989; Ibs-von Seht and Wohlenberg 1999; Arai and Tokimatsu 2004; Roberts and Asten 2004). Similarly, the method has been used in determining the geometry of geologic structures, evaluation of soil types, and variation of their dynamic properties with depth (Apostolidis et al. 2004), and in the estimation of thickness and shear-wave velocity of sands overlying lower-velocity clays (Asten 2004). Data obtained from passive seismic investigations are processed and interpreted to yield a shear-wave velocity depth-profile of the site. The MTM method has a lot of advantages over other geophysical techniques due to the following reasons: (1) the technique is cost-effective when used to explore deep sedimentary basins in contrast to other commonly used techniques, (2) it can accurately estimate shear-wave velocity structure of deep sedimentary basins because of the high sensitivity of phase velocity relative to the phase velocity of Rayleigh wave, (3) it utilizes artificial and natural noise sources, and hence can be used in heavily populated metropolitan cities, and (4) the technique is environmentally-friendly because artificial seismic sources are not required (Satoh et al. 2001; Apostolidis et al. 2004).

Rayleigh-wave phase velocity varies with frequency or wavelength depending on the shear-wave velocity over a depth of ca. 1 wavelength (Brown et al. 2000). Like shear-wave velocities, Rayleigh-wave phase velocities depend on the dynamic properties of the soil such as density, Poisson's ratio and compression-wave velocity (Brown et al. 2000). The two methods commonly used for processing microtremor data are the frequency (f) − wave-number (k) power spectral density method $(f$-$k)$ and the spatial autocorrelation method (SPAC) (Aki 1957, 1965; Okada 2003). The SPAC method has a significant advantage over the f-k method in that the former can effectively yield wave scalar velocity in multidirectional or omnidirectional wave field (Asten 2004). The most commonly used arrays for SPAC measurements are circular/semi-circular arrays and triangular arrays comprised of multiple triangles. Triangular chain arrays with side lengths up to 300 m have been used to obtain shear-wave velocity structure of a sedimentary basin depth of about 1 km (Asten 2004). In this study, Rayleigh-waves propagating from a wide range of azimuthal angles were obtained using an array of nested triangles comprised of 12 geophones arranged horizontally along a survey line (Figure 3.4).
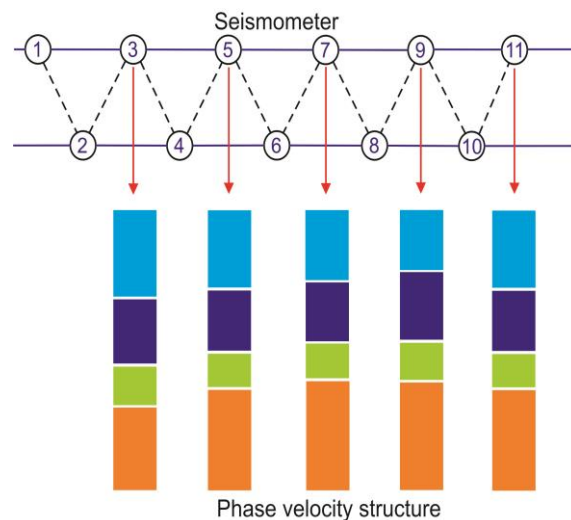
Figure 3.4 Microtremor measurements using an array of nested triangles comprised of 12 geophones (Wang et al. 2015)

Side lengths of the nested triangles were varied from 1.5 to 3 m depending on the depth of investigation and desired range of Rayleigh-wave wavelengths. Also, the time interval for each measurement ranged from 15 to 30 minutes. Repeated measurements were made on each survey line to minimize errors caused by occasional passage of trains and vehicles which affects the result by producing noisy SPAC coherencies. Apparent variation of phase velocity is obtained by interpolation with a kriging technique to obtain a two-dimensional phase velocity profile reflective of the internal geologic structure of the site.

3.3.2 Self-potential survey

The self-potential (SP) method is a passive geophysical technique that responds to naturally-occurring potentials in the earth's surface. The SP method is unique in its ability to detect natural or 'spontaneous' voltages in the ground generated by hydraulic, thermal and chemical processes. SP surveys are useful for the localization and quantification of groundwater flows and pollutant plume spreading, and in the estimation of pertinent hydraulic properties of aquifers (water table, hydraulic conductivity). Quite recently, the SP method has been successfully used in solving various geotechnical and civil engineering problems especially in geothermal exploration. The self-potential method has been employed in embankment dam engineering for the delineation of anomalous zones that correspond to preferential seepage paths (Corwin 1991). Also, the technique has been applied in the monitoring of seepage, internal erosion and piping in landslide dams, natural and artificial levees (Bolève et al. 2009; Moore et al. 2011; Thompson et al. 2012).

There is a dearth of literature on streaming potential produced in subsurface fractures and fluid paths. Laboratory experiments on streaming potential using channel flow models have been studied in detail (Ahmad 1964; Bogoslovsky and

Ogilvy 1973). Results obtained from both studies show that there is a direct relationship between self-potential (SP) and hydraulic head (ΔP- the driving force behind the fluid movement). The authors also observed that SP fields in fissured media differ from those in unconsolidated porous media. Ogilvy et al. (1969) asserted that clay-filled fissures with low permeability are characterized by low SP values. Their report also showed that SP values are affected by salinity content. Laboratory experimental result has shown that the involved coupling coefficients depended on the fluid chemistry, conductivity and pH, and on the soil or rock properties (Jouniaux et al. 2009).

Landslide dams are generally composed of unconsolidated or poorly consolidated materials which have no filter zones or engineered water barrier to prevent seepage, and hence may allow the development of internal erosion and seepage from barrier lakes and reservoirs. An understanding of the relationship between groundwater flow through porous media and self-potential is critical for the successful application of the technique in poorly consolidated materials of landslide dams. Internal erosion and seepage monitoring in natural and artificial dams utilizes the SP method due to its response to subsurface fluid paths through the mechanism of streaming potential. Streaming potential is an electrokinetic process that describes the interaction between subsurface fluid path and electric flow within a porous rock mass or a saturated soil (Glover et al. 2012; Jouniaux and Ishido 2012). In a saturated system, under static conditions, equilibrium exists due to a balance of electric charge across the solid-fluid interface. Streaming potential evolves from hydraulic action which offsets the equilibrium of the system giving rise to charge imbalance that generates electric currents (Ishido et al. 1983). Electrokinetic process takes place within the pore spaces of saturated soils under constant hydraulic flow. This process involves the exchange of charged ions within the pore spaces and thus, initiates an electric current field also referred to as the streaming current (Figure 3.5). In natural

conditions, the occurrence of streaming potentials is as a result of the double layer of ions associated with the interaction between the mineral grains and pore-water (Allegre et al. 2010).

Self-potential measurements were made using the total field method, which measures the potential difference between a fixed base electrode and a roving electrode connected to a long reel of wire (Figure 3.6). This method was chosen because of its flexibility in placing the mobile electrode and usually gives small cumulative error than the gradient method (Lowrie 2007). Non-polarizing copper/copper sulphate electrodes (model no: RE-5; diameter 0.035 m, length 0.15 m), manufactured by M.C. Miller Inc., USA, were used in all the measurements. At each station, a small amount of salted bentonite mud was added to a pre-dug shallow hole to enhance the coupling between the electrode and the ground, especially in dry terrain covered by gravelly deposits. SP measurements were made using Metex m-6000m voltmeter of high sensitivity and high input impedance, which were connected to a laptop computer installed with a real-time data logging software.
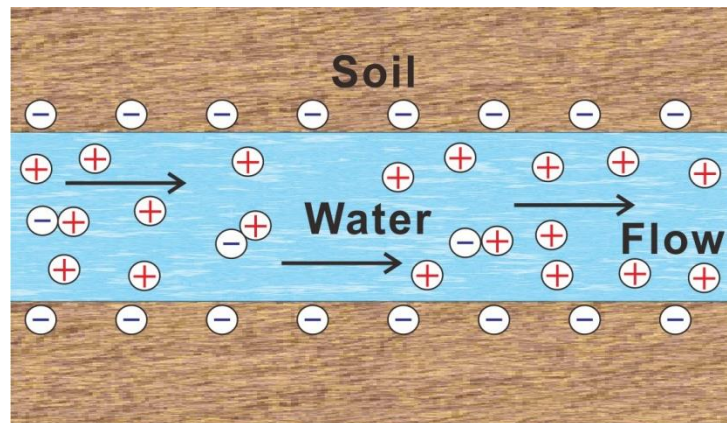
Figure 3.5 Schematic diagram of streaming potential in the pore space of a saturated soil (Wang et al. 2015)
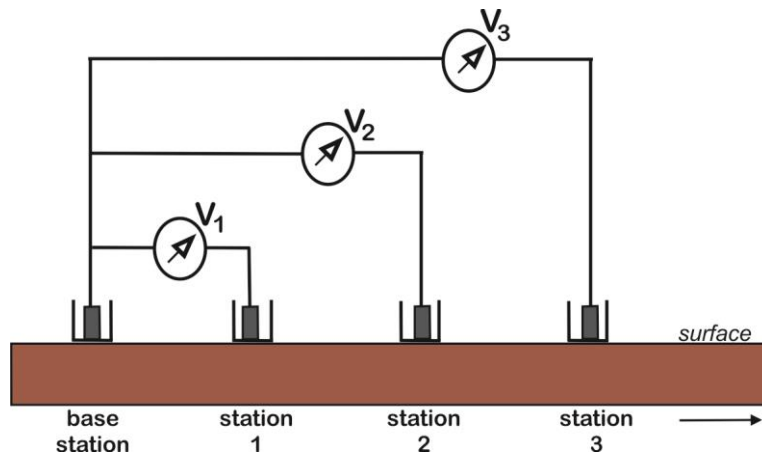
Figure 3.6 Direct measurement of self-potential using the total field method (Lowrie 2007)

3.4 Results and discussion

In the first step of the investigations, a number of preliminary studies were performed at selected sites. Initially, a microtremor array survey was performed at an irrigation dam in Miyoshi city, Hiroshima, Japan, to ascertain the applicability of the technique in evaluating the phase velocity profile of landslide dams. The Miyoshi dam is a small irrigation dam located in Miyoshi City, Hiroshima Prefecture, Japan (Figure 3.7). The dam and the impounded lake are located at an elevation of 246 and 253 m a.s.l. The dam height and dam crest width are about 18 and 1.5 m, respectively while the maximum dam width and angle of the downstream slope are about 100 m and 35~40°. The dam impounds a lake with an estimated volume of 220,000 m^3. The dam was specifically constructed for the supply of water to several agricultural terraces in the downstream area. This was done through a drainage pipe (sluiceway) of approximately 0.3 m in diameter located ~5 m below the dam crest. Similarly, excess water from the upstream lake is released into the downstream area through an uncontrolled spillway channel located at the left bank of the dam. Microtremor chain array survey was conducted on the dam to evaluate the hydraulic behaviour of

the dam and determine the applicability of the technique in evaluating the internal structure of landslide dams.

The microtremor chain array survey was performed along a survey line on the Miyoshi dam crest. The array size was fixed at 1.5 m while the time for each measurement was fixed at 30 minutes. Several measurements were made during the investigation to minimize noisy SPAC coherencies caused by frequent traffic disturbance from the nearby expressway. Figure 3.8 shows the front view of the dam and the phase velocity profile along the dam crest. It is should be noted that the surveyed line on the dam crest started from the right bank of the dam and terminated at the spillway channel, shown in Figure 3.8a. The phase velocities of the dam materials generally vary from 100 to 900 m/s. The uppermost layers of the dam exhibited low phase velocities that ranged from 100 to 140 m/s which may indicate the moderately consolidated nature of the materials. Based on the result, we found that phase velocities in the range of 100 to 120 m/s corresponded to the depth where the drainage pipe was located (i.e. towards the left bank of the dam; Figure 3.8b). This may reflect the loose nature of the surrounding sediments apparently caused by high seepage gradient forces given that the upstream lake is mostly at its maximum level all through the year. Furthermore, the geometry of the dam can be delineated by the high phase velocity values of 540~900 m/s characteristic of the right abutment. Therefore, the result of this preliminary investigation demonstrated the reliability of the MTM chain array method in the evaluation of internal structure of landslide dams.

Figure 3.7 Topographic map of Miyoshi area showing Miyoshi irrigation dam
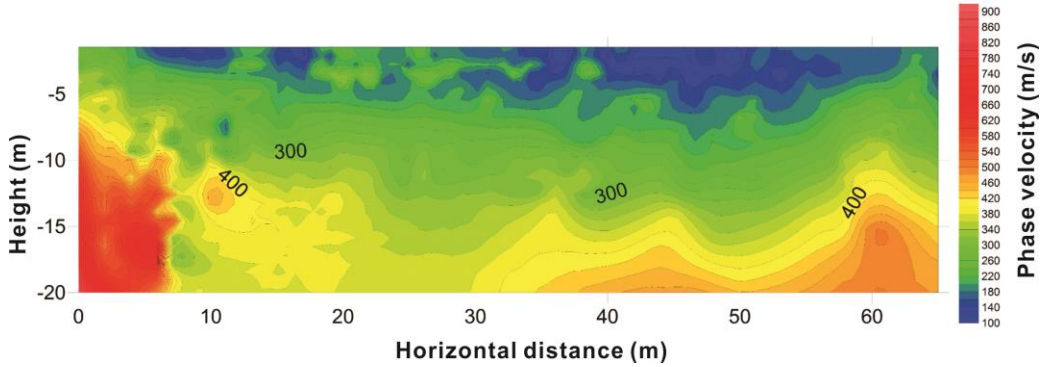
Figure 3.8 Phase velocity depth-profile of Miyoshi irrigation dam

3.4.1 Akadani and Kuridaira landslide dams

Microtremor and SP measurements were carried out at several locations at Akadani and Kuridaira landslide dams. Survey lines were chosen depending on the terrain conditions. In total, four MTM survey lines ($A' - A, B' - B, C' - C,$ and $D' - D$), and three SP survey lines ($a' - a, b' - b,$ and $c' - c$) were traversed at Akadani landslide dam, while one MTM survey line ($A - A'$) and two SP survey lines ($a - a', b - b'$) were covered at Kuridaira landslide dam (Figure 3.9). Figure 3.10 shows the results of microtremor surveys at Akadani landslide dam. Low phase velocity values ranging from 100 to 500 m/s were obtained at survey lines located close to the impounded lake (lines $B' - B, C' - C,$ and $D' - D$). These low phase velocity values can be attributed to: (1) the effect of an artificial drainage pipe (at line $D' - D$) laid inside the dam for lowering of the upstream lake, and (2) the high hydraulic conductivity of the underlying materials which were made up of poorly consolidated sediments from the distal part of the landslide. In contrast, phase velocities in the range of 240 to 780 m/s were obtained near the central part of the dam (line $A' - A$). The observed increase in phase velocity with depth is as a result of an increase in density and a decrease in porosity, from the unconsolidated upper sediments to the highly consolidated bedrock. Most importantly, the nature of the slope movement and its effects on the displaced material were obvious at line $A' - A$. The result indicates that the internal structure of the dam is characterized by highly comminuted upper layer (1 to 20 m) and intensely deformed and folded lower layer (21 to 65 m) typical of deep-seated slope movements.

The variation of self-potential near the upstream side is much strong compared to the central part of the landslide dam, and hence may imply the absence of well developed seepage paths in the dam. This is summarized in Figure 3.11, which shows the self-potential profile along lines $a' - a, b' - b,$ and $c' - c$. The increasing trend of positive SP anomalies observed towards the central part of the dam corroborates

with the phase velocity profile of the area. In contrast, the high hydraulic conductivity of the poorly consolidated sediments dominating the upper layer of the area near the upstream side may have given rise to negative SP anomalies of several tens of millivolts.

Figure 3.12 shows phase velocity depth profile of survey line $A - A'$ at Kuridaira landslide dam. Phase velocity values varied from 300 to 680 m/s. The internal structure of the landslide dam displays similar characteristics to that of Akadani landslide dam. The uppermost layer comprises highly comminuted and fragmented materials of high hydraulic conductive with phase velocities ranging from 300 to 340 m/s. This layer grades into an intensely folded sub-layer of low permeability with phase velocities varying from 350 to 540 m/s, at depth range of 20 to 60 m. Below this sub-layer lies a moderately folded bedrock of extremely high phase velocities ($560\sim680\ m/s$). Figure 3.13 shows the variation of self-potential along two survey lines near the upstream side ($a' - a$) and towards the downstream side ($b' - b$). The trend of the self-potential measurement on line $a' - a$ is indicative of the absence of water-saturated zones while the trend of self-potential on line $b' - b$ shows negative SP anomalies that may indicate the existence of anomalous seepage or zones of high hydraulic conductivity.
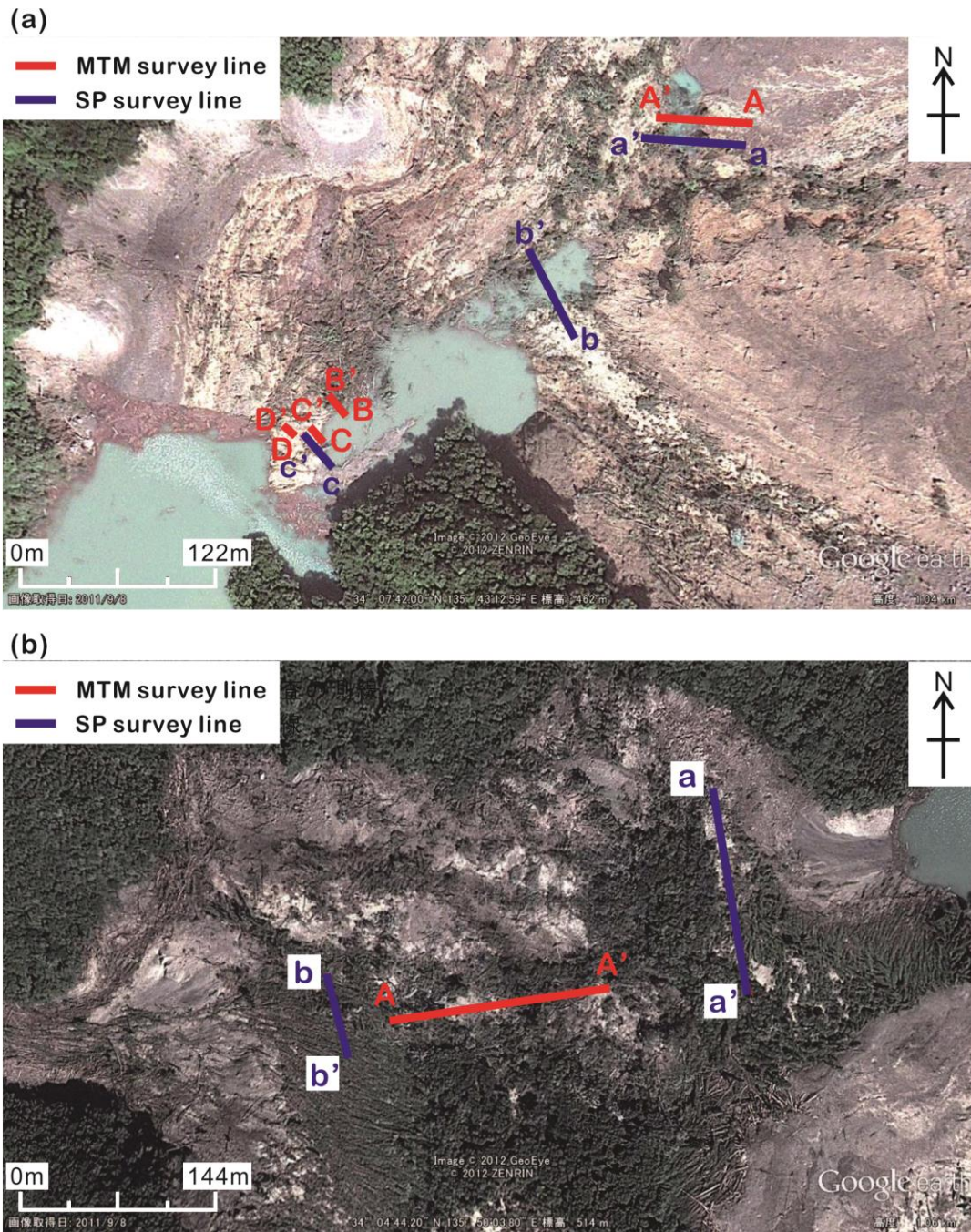
Figure 3.9 Site maps of (**a**) Akadani and (**b**) Kuridaira landslide dams. The survey lines for MTM and SP measurements are marked out.
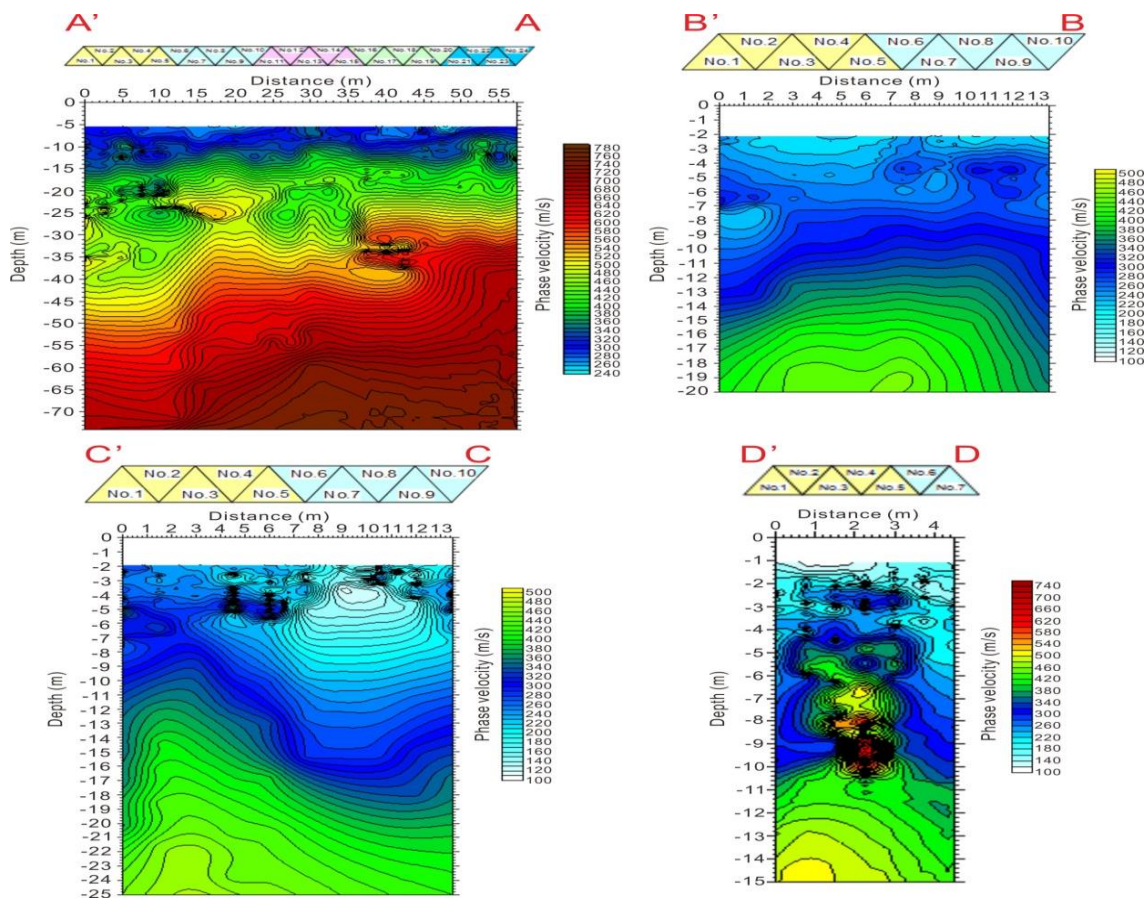
Fig. 3.10 Phase velocity profile along lines $A' - A, B' - B, C' - C$, and $D' - D$ at Akadani landslide dam
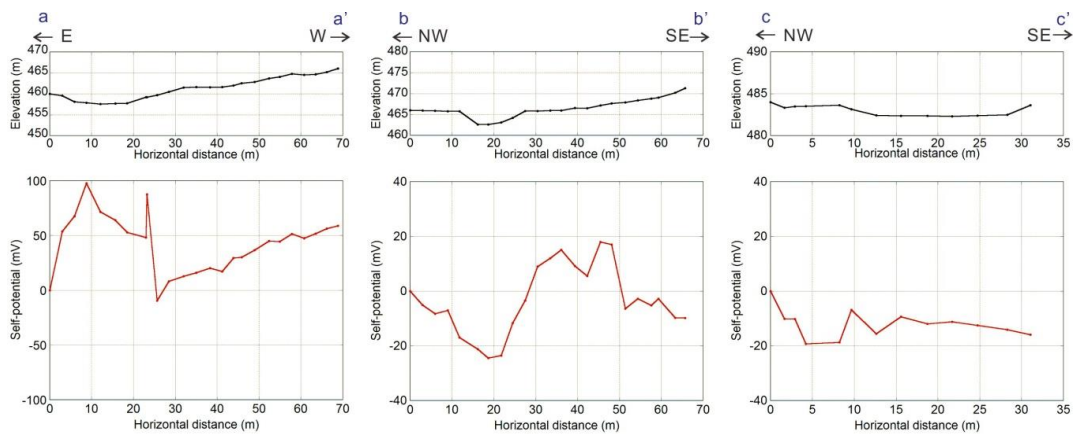
Figure 3.11 Self-potential profile along lines $a' - a, b' - b,$ and $c' - c$ at Akadani landslide dam
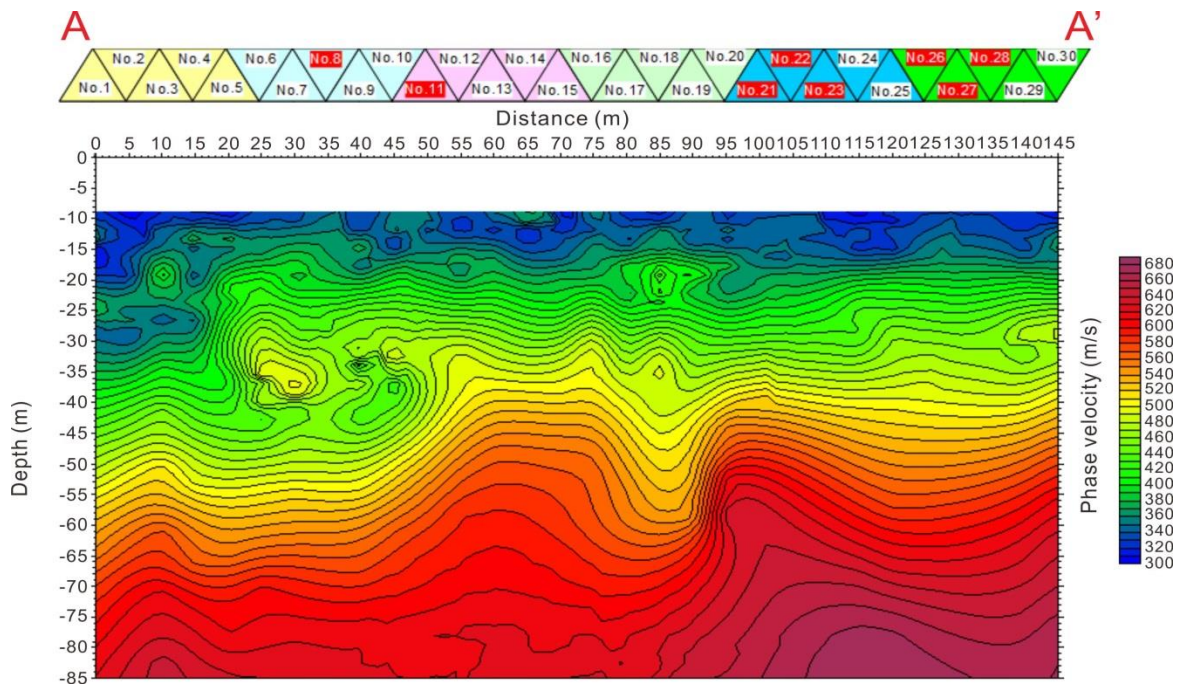
Figure 3.12 Phase velocity profile along line $A - A'$ at Kuridaira landslide dam
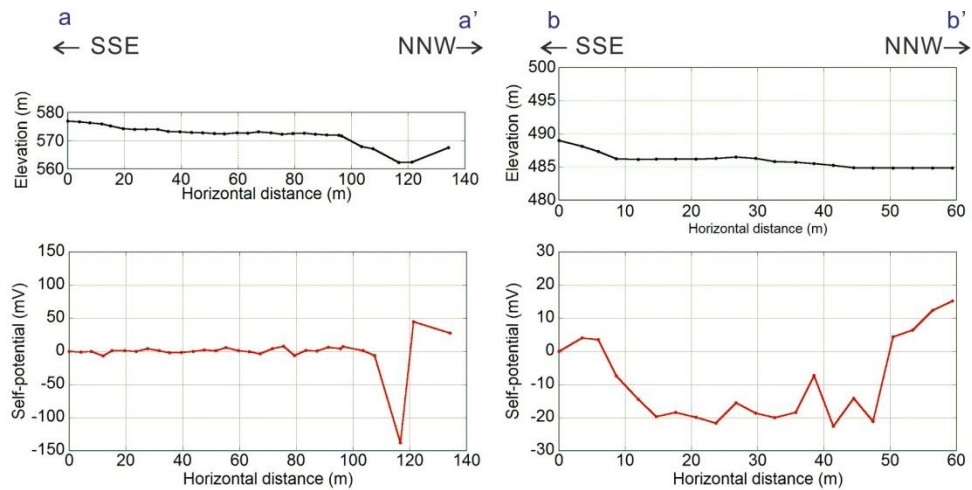
Figure 3.13 Self-potential profile along lines $a - a'$ and $b - b'$ at Kuridaira landslide dam

3.4.2 Higashi-Takezawa and Terano landslide dams

Figure 3.14 shows the survey lines at Higashi-Takezawa landslide dam. A total of 12 geophones were arranged in a triangular chain array with an array size of 3 m. The orientation of the survey lines was made such that one survey line ($CM - CM'$) was perpendicular to the slope of the landslide, while two survey lines ($LM_1 - LM_1'$, and $LM_2 - LM_2'$) were parallel to the slope of the landslide. In all the investigated areas, phase velocity values ranged from 200 m/s to 500 m/s, indicating the general homogeneity of the underlying sediment (Figure 3.15). At survey lines $LM_1 - LM_1'$, and $LM_2 - LM_2'$, which originated from the main body of the landslide towards the center of the landslide dam, phase velocity values decreased from 400 to 200 m/s. This could reflect the degree of deformations and fragmentations suffered by the displaced material during its movement and subsequent deposition into the river.
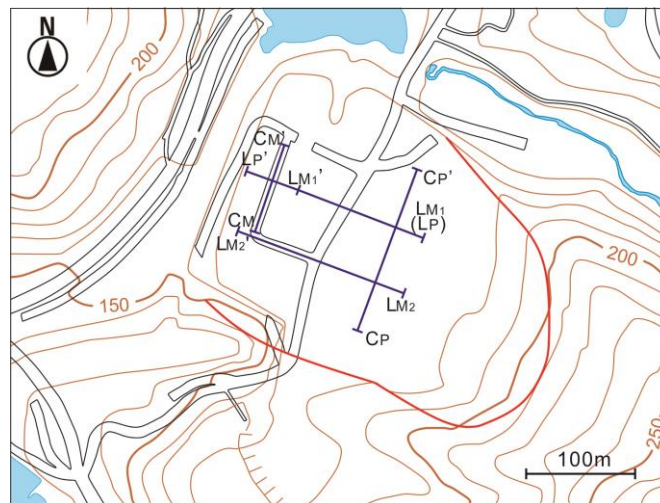
Figure 3.14 Site map of Higashi-Takezawa landslide dam showing the surveyed lines for MTM ($LM_1 - LM_1'$, $LM_2 - LM_2'$, and $CM - CM'$) and SP ($LP' - LP$ and $CP - CP'$) survey lines

From the results, the boundary between the bedrock and the displaced material was found to vary from 330 to 350 m/s. Hence, the underlying materials can be divided

into two distinct zones, *Zone A* and *Zone B*, based on phase velocity depth profile. The upper layer of the landslide dam is dominated by *Zone A*, at depths ranging from 1 to 18 m. Phase velocity values in this zone varies from 80 to 200 m/s. This zone is analogous to layers dominated by poorly consolidated and highly fragmented materials of high hydraulic conductivity characteristic of many landslide dams. We interpret several areas of very low phase velocities as zones of anomalous seepage or water saturated zones, especially at survey line $CM - CM'$, where V_s values varied from 80 to 100 m/s. In contrast, *Zone B* is dominated by structurally deformed and highly folded sediments with phase velocity values in the range of 200 to 350 m/s. The thickness of this zone varies from 15 to 20 m. The high phase velocity values of this zone have been attributed to its high density and rigidity modulus. It is worthy to mention that the interaction between the displaced material and the substrate during the movement resulted in pulverization, and hence the absence of no clear boundary.

Figure 3.16 shows the results of SP surveys on lines $LP' - LP$ and $CP - CP'$. Self-potential anomalies were predominantly positive at survey line $LP' - LP$, except at the center of the landslide dam (i.e., the distal part of the landslide corresponding to line $CM - CM'$), where a very high negative anomaly of about $-36\ mV$ was recorded. The similarities in results obtained with SP and MTM surveys on line $CM - CM'$ confirm the existence of anomalous seepage at the center of the dam. Similarly, more than 85% of the total SP results at survey line $CP - CP'$ showed negative anomalies. These low negative anomalies could be attributed to abrupt variations in hydraulic conductivities between the displaced materials overlying the undeformed bedrock.
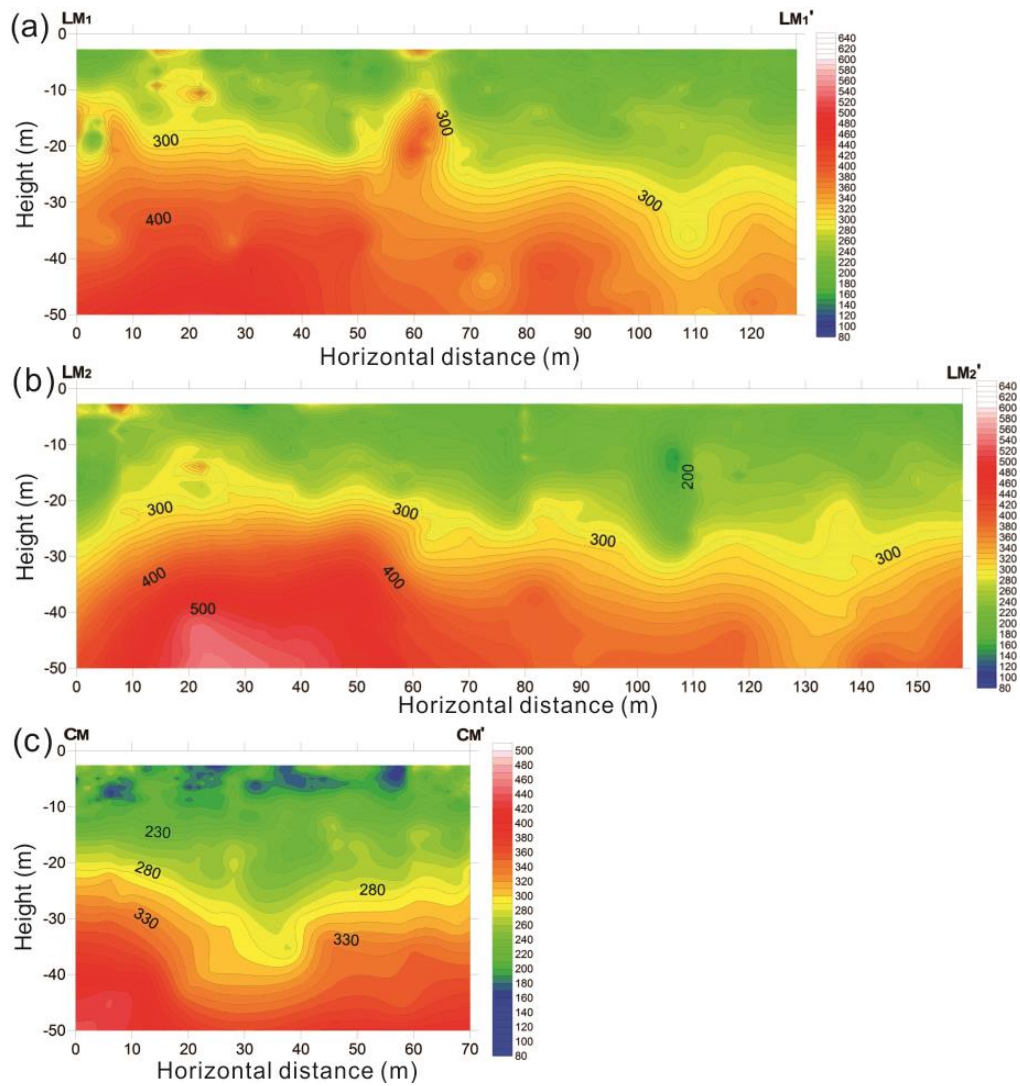
Figure 3.15 Phase velocity profile along survey lines $LM_1 - LM_1{'}$, $LM_2 - LM_2{'}$, and $CM - CM{'}$ at Higashi-Takezawa landslide dam
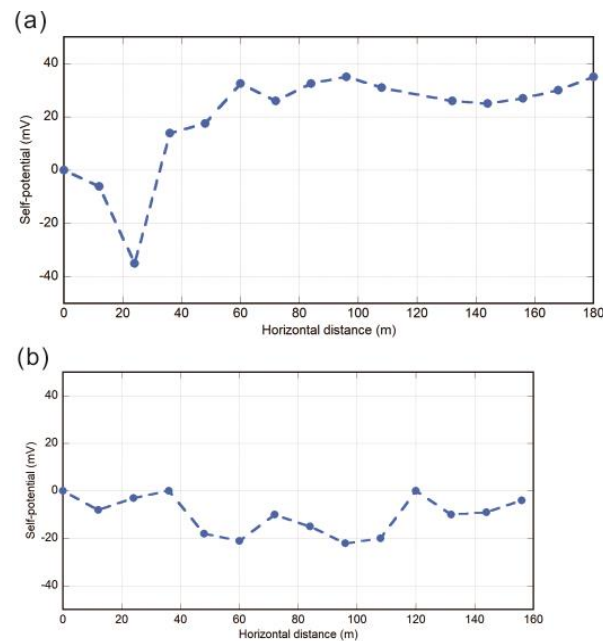
Figure 3.16 Self-potential profiles along lines $LP' - LP$ and $CP - CP'$ at Higashi-Takezawa landslide dam

Figure 3.17 shows the topographic map of the Terano landslide dam in Niigata, Japan. Microtremor surveys were performed in August 2014 on survey lines $CM - CM'$ and $TM - TM'$ while self-potential surveys were carried out on survey lines $CP - CP'$ and $LP - LP'$. The survey lines were chosen such that line $TM - TM'$ was parallel to the landslide while $CP - CP'$ and $LP - LP'$ were parallel and perpendicular (i.e. along the dam crest) to the upstream slope of the dam. Figure 3.18 shows the phase velocity profile along the two surveyed lines. From the survey results, the phase velocity profile can be divided into three distinct layers. The upper layer had phase velocity which ranges from 140 to 280 m/s, the middle layer with phase velocity that ranges from 280 to 360 m/s while the basal layer with phase velocity in the range of 360 to 480 m/s. In Figure 3.18a, the discordant trends of phase velocities within the middle layer may suggest the effect of the impact force of the sliding mass on the valley floor which modified the internal structure of the landslide dam. While previous studies

by Sassa et al. (2005) had approximated the angle of the sliding surface to be ~20°, the middle and basal layers of the landslide materials at line $TM - TM'$ dips toward the impounded lake with an inclination angle that varies from 5~10° (Figure 3.18b). This lower dip angle may be attributed to: (1) the transient internal modifications that occurred as the materials moved along a sliding surface that was originally parallel to the bedding planes, and (2) subsequent deposition into the stream channel that caused changes in the stress states of the displaced materials. Figure 3.19 shows the self-potential profiles along survey lines $CP - CP'$ and $LP - LP'$. The negative self-potential anomalies in the order of 7 to 15 mV obtained at horizontal distance of 4 to 28 m on line $CP - CP'$ could be attributed to the influence of the upstream lake on the poorly consolidated landslide dam materials (Figure 3.19a). Similarly, a large negative SP anomaly of ~46 mV obtained at a horizontal distance of 68 m on the same survey line may suggest the existence of subsurface conduits or cracks created during the landslide damming event. SP anomalies are predominantly positive (14~108 mV) on the left side of survey line $LP - LP'$, while the negative trend of the SP anomaly toward the right side of the survey line could further indicate the presence an anomalous seepage zone in the dam (Figure 3.19b).
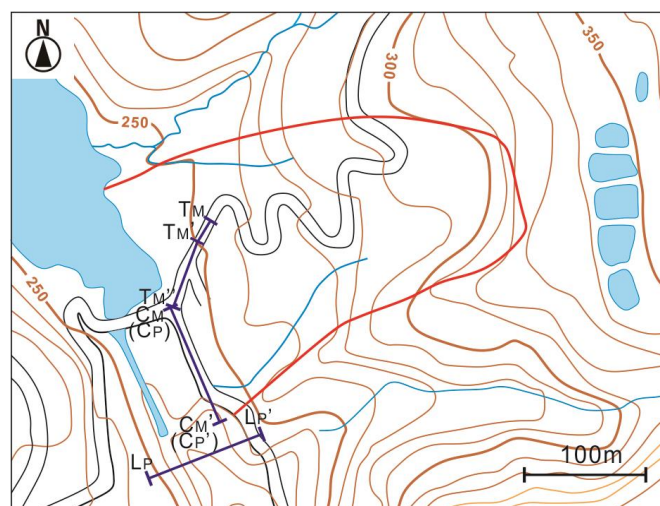
Figure 3.17 Site map of Terano landslide dam.
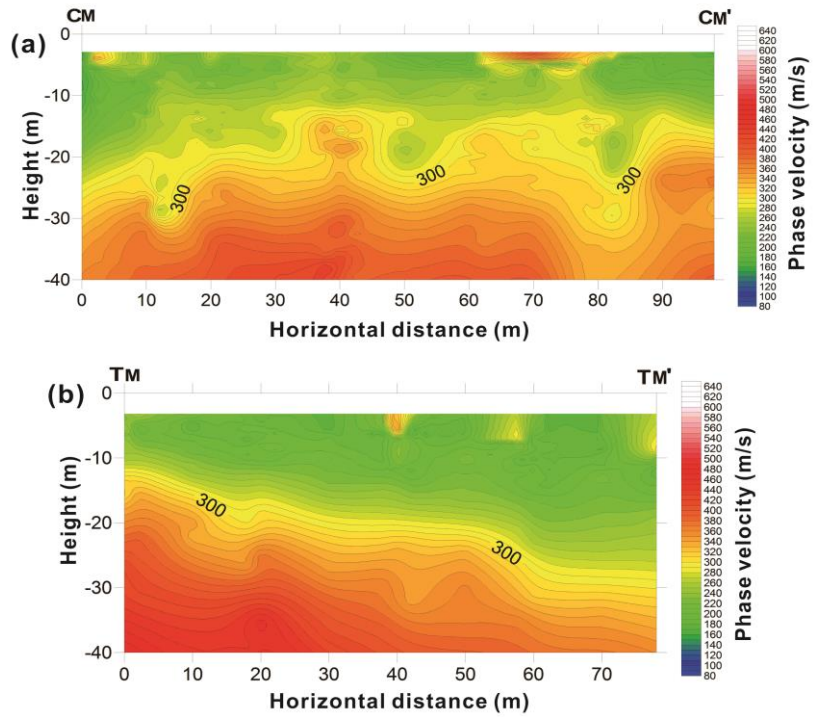
Figure 3.18 Phase velocity profile along the survey lines at Terano landslide dam
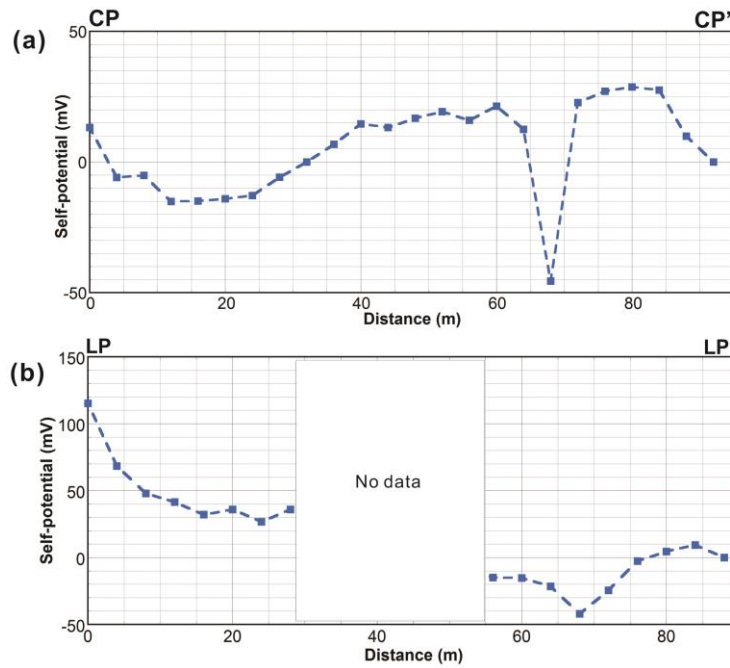
Figure 3.19 Self-potential profiles at Terano landslide dam

3.4.3 Kel-Tor landslide dam

Figure 3.20 shows the results of MTM and SP surveys at Kol-Tor landslide dam. The array size for the MTM survey and electrode spacing for the SP measurements were 10 m, respectively. Apparent phase velocity profiles within the dam varied from 240 to 760 m/s. The result shows marked variations in phase velocities including several concentrated zones of low phase velocities that ranges from 240 to 280 m/s (Figure 3.20a). This could be attributed to the different geomorphic processes that caused the blockage and other weak zones that may correspond to several seepage exit points at the downstream end of the dam. This is consistent with the evolutionary history of the dam which was initially formed by moraine sediments and was subsequently covered by rock avalanche deposits (Jansky et al. 2010). The low phase velocity of 240 to 460 m/s that dominates the upper half of the landslide dam can be ascribed to the moderately consolidated nature of the sediments which are comprised of clast-supported and inversely graded materials of high hydraulic conductivity. Similarly, the marked variations in phase velocity of the upper layer may suggest the prolonged effects of seasonal glacier-ice melt, torrential rainfall and occasional rise in the upstream lake that have led to several overflowing of the lake waters. The underlying layer is characterized by asymmetrical zones of high phase velocities (460 to 760 m/s) that dips rightward (towards the upstream lake) with an inclination of 28~35°, and leftward (towards the downstream slope) with an inclination of 18~55°. The highly consolidated nature of the glacigenic sediments may have contributed to the high phase velocity of this layer. Similarly, the curvilinear trends of phase velocities within the underlying glacigenic sediments may result from changes in stress states of the sediments caused by the deposition of the rock avalanche materials.

Figure 3.20b shows self-potential profile along the survey line. The result indicates that the left side of the survey line (0~180 m) is dominated by negative SP anomalies

that varies from $4\sim22\ mV$ while the right side is dominated by positive SP anomalies that varies from $10\sim46\ mV$. This trend is consistent with the hydrological regime of the surrounding catchment basin. Apart from an active seepage zone that corresponds to a horizontal distance of 150 m, a few other seepage exit points were observed at the downstream slope at horizontal distances of 80 m, 150 m, and 170 m, respectively. The prevalence of these seepage points or springs has been related to the increased melting of glacier ice coupled with incessant rainfall that increased the level of the upstream lake. These zones were mostly characterized by very low phase velocities that vary from 240 m/s to 280 m/s. Based on our field investigations, we estimated that the turbidity of the seepage/spring water varies from 5~10 NTU, and thus may imply that the dam materials are not been eroded downstream. Based on the results of the present study, it was found that the Kel-Tor landslide dam could remain stable, provided the hydrogeological factors are below a critical state. Above this critical state, high pore-water pressures could develop and lead to an uncontrolled seepage that could trigger the abrupt failure of the dam.
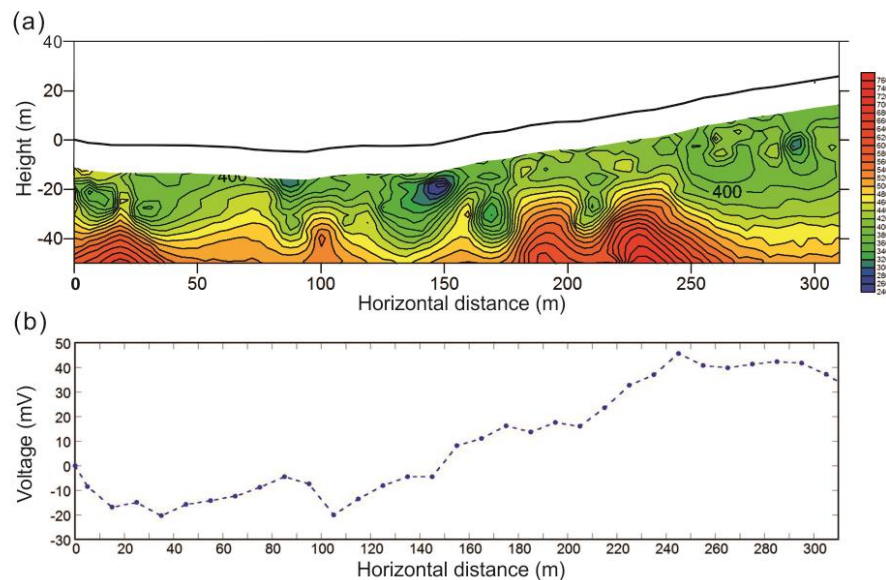
Figure 3.20 Phase velocity and self-potential profiles along the surveyed lines at Kol-Tor landslide dam

3.5 Conclusions

This research demonstrates the significance of geophysics in geotechnical investigation of the internal structure and the hydraulic behaviour of landslide dams. Currently used numerical models and stability indices sometimes present poor prediction accuracy stemming from the lack of information regarding the internal structure and the hydraulic properties of landslide dams. An integrated geophysical approach comprising microtremor array and self-potential measurements were successfully combined to delineate potential seepage zones and determine the phase velocity profile of landslide dams. The two main reasons for using these two geophysical methods are due to the following: (1) they are cost-effective compared to other techniques used in the exploration of deep sedimentary basins; and (2) they are environmentally friendly and portable, and hence can be used in rugged terrain with restricted vehicular access. In this study, a series of geophysical investigations at selected landslide dams have indicated that the degree of comminution and pulverization within a landslide dam is controlled by the type of landslide that formed the dam and its travel distance.

Our geophysical investigations successfully determined the phase velocity structure of three landslide dams in Japan (located at Akadani, Kuridaira and Higashi-Takezawa districts) and one landslide dam in Kyrgyzstan (Kel-Tor gorge) using the SPAC method. Seismic data obtained from the triangular arrangement of 12 seismometers were resolved to reveal information regarding the thickness of the underlying strata, as well as their phase velocity structure. In general, our investigations found that the internal structure of the dams was characterized by two distinct morphologies: (1) an upper layer comprising highly fragmented and poorly consolidated material of high hydraulic conductivity derived during the movement of the landslide; and (2) a lower layer characterized by intensely folded and structurally deformed strata of high density and low permeability, indicating the

structural modifications suffered by the material during its movement. The internal structure of the landslide dams was interpreted as those characteristic of landslides formed by translational slides which originated from movements along weak bedding planes. In such landslides, the degree of comminution and fragmentation are low compared to dams formed by rock avalanche processes.

One important aspect of this investigation is the successful application of self-potential measurements in detecting several SP anomalies associated with zones of anomalous seepage in the landslide dams. Self-potential survey at the sites provided information regarding the hydrogeological factors controlling the development of anomalous seepage within the impoundments. The self-potential data indicated the existence of anomalous seepage at the downstream area of the Kel-Tor landslide dam. The data also revealed the presence of several water saturated zones in the landslide dams at Akadani, Kuridaira and Higashi-Takezawa districts of Japan. However, extensive investigations need to be conducted at these sites to ascertain if these zones of anomalous seepage are directly linked to the upstream lake.

CHAPTER 4

EXPERIMENTAL INVESTIGATION OF THE HYDROMECHANICAL CONSTRAINTS FOR PIPING FAILURE OF LANDSLIDE DAMS

4.1 Introduction

A clear understanding of the processes that lead to seepage and piping–induced failure of landslide dams is important for hazard management studies, and for the mitigation and prevention of disasters caused by the potential outburst floods. The internal structure of landslide dams plays a vital role in understanding the failure mechanisms of valley-confined deposits, and most importantly, for evaluating the mechanical resistance of landslide dams to failure by either piping or overtopping (Wassmer et al. 2004). Acquiring grain size data is critical for accurate assessment of landslide dams, but limited sedimentological data is available, due to crude sampling methods and the challenges posed by rugged terrain and poorly exposed deposits. Nevertheless, the study of sedimentological characteristics of natural river blockages is imperative for natural hazard assessment studies, as they have a major influence on the overall strength of dams, and control the rate of breach development (Fread 1988; Casagli et al. 2003). Grain size distribution analysis has been used to study the internal structure of some landslide dams (Crosta et al. 2006; Dunning 2006; Duman 2009; Dunning and Armitage 2011; Shugar and Clague 2011; Wang et al. 2013). Field and laboratory analysis of textural characteristics of several landslide dam materials

show that they are mostly poorly to very poorly sorted, matrix- or clast-supported, finely skewed, brecciated, stratified to massive sediments, are usually armored with angular boulders, and are sutured with a matrix of very fine materials (Weidinger 2006; Capra 2007, 2011).

Numerous experimental methods have been used to simulate the development of internal erosion and piping in earth dams and landslide dams (Wit et al. 1981; Brauns 1985; Maknoon and Mahdi 2010). Hanson et al. (2010) analyzed variation in erodibility of different soil materials due to internal erosion in dams by conducting large-scale outdoor model tests. They observed that the rate of erosion in differing soil materials varied in orders of magnitude. Marot et al. (2012) used a triaxial cell device coupled with a hydraulic system to study the influence of angularity of coarse fraction grains on the internal erosion process. They concluded that the angularity of coarse fraction grains may increase the erosion resistance of the tested soils by a factor of five. Richards and Reddy (2012) performed laboratory experiments on the initiation of backward erosion in cohesive and non-cohesive soils using a triaxial test device called a true-triaxial test apparatus. They observed that the primary mode of failure of non-cohesive soils was by backward erosion, which required a seepage velocity of 0.8~1.1 cm/s to initiate piping in uniformly graded sands. Ke and Takahashi (2012) studied the mechanical effect of internal erosion on gap-graded non-cohesive soils by conducting one-dimensional seepage tests using a fixed-wall permeameter. These authors concluded that the onset of internal erosion is indicated by loss of fine material, coupled with a significant increase in hydraulic conductivity.

Significant results have been obtained from experimental studies using triaxial cell chambers, constant-head permeameter, and other laboratory methods such as hole erosion tests (HET) and jet erosion tests (JET). However, none of these methods have simulated the potential failure mechanisms of landslide dams triggered by

internal erosion and piping.   This paper presents a series of experiments conducted to investigate the hydromechanical constraints of soils on the development of internal erosion and piping in landslide dams. The experiments were performed in a flume equipped with monitoring sensors and transducers capable of recording transient changes during the process. The two main objectives of this research are: (1) to identify the various failure mechanisms of landslide dams under varying hydromechanical properties of the materials forming the dams; and (2) to evaluate and infer the probable physical properties of dam materials and conditions most appropriate for long term stability of such dams. The research methodology aims at providing new ideas and insights on stability analysis of landslide dams, considering the sparse research to date on the material properties of landslide dams which are relevant in dam breach analysis and flood routing.

4.2 Experimental methods

Trapezoidal-shaped landslide dams were built in the laboratory after a series of field investigations were carried out on two recent landslide dams (Akatani and Kuridaira landslide dams) formed in 2011, in the Kii Peninsula of southwest Japan. The choice of these sites as reference cases for this study was prompted by several factors, including (1) the relatively large volume of the two impoundment materials, of 9.4 million m^3 and 13.9 million m^3, respectively, (2) the characteristic nature of the landslide dam materials, which are dominantly composed of disjointed angular boulders (averaging 1~10 m in diameter), and cobble-sized clasts sutured in a fine-grained matrix (Figure 4.1a), and (3) the significance of drainage pipes buried in the two sites, which function as artificial drainage channels for lowering of the upstream lake, so as to avoid potential overflow (Figure 4.1b). The experimental dams were built to partially reproduce the geometry of landslide dams in real case scenarios,

with efforts made to minimize unavoidable scaling issues resulting from space and time constraints.
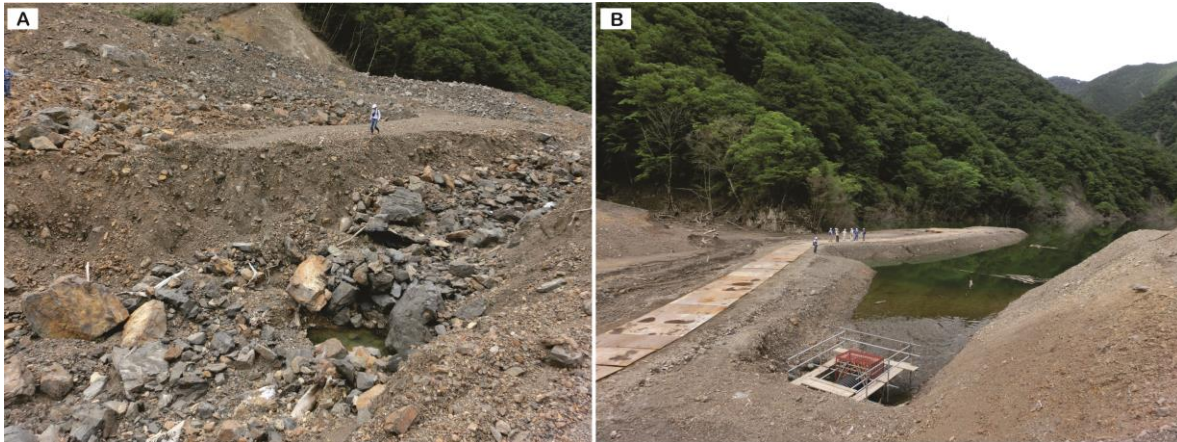
Figure 4.1 a Exposed section of the materials composing the Akatani landslide dam **b** Upstream side of the Akadani landslide dam showing water inflow into the dam through an artificial drainage pipe. Note: People for scale.

4.2.1 Modification of the flume tank

A schematic diagram of the flume tank with the location of sensors and workstation used in the recording of data is shown in Figure 4.2. The experimental setup is generally comprised of a lateral displacement transducer, a water level probe, two laser displacement sensors, a manually-operated flow-meter, four pulleys, and a work station (KYOWA EDX-100A and a high speed computer). All the sensors were connected to a standard real-time monitoring and recording unit comprised of a universal recorder (KYOWA EDX-100A) and a computer. Two digital video cameras were strategically positioned to record the failure sequence of the dams. The experimental setup was designed to simulate: (1) the internal erosion process and piping development in relation to the nature of the material forming the

impoundment; (2) the failure mechanisms of landslide dams made of materials of varying geotechnical properties; and (3) the rate of development of piping.

Prior to the construction of the tank, the size, scale, and position of the dam model were considered to enable timely collection of accurate data. The flume tank was 2 m long, 0.45 m high and 0.45 m wide, and was made entirely of glass, with two 4 cm diameter drainage outlets at the downstream end to allow steady discharge of fluidized sediments (Figure 4.3). The tank was made of 5 mm-thick acrylic sheets (plexiglass) of high transparency which enables visual observation of wetting front propagation, deformation and failure mechanism of the dam models. The flume was gently tilted to make a bed slope of 5°. The construction and modification of the flume tank considered the dimensions of other flume tanks used by previous studies, including the 1 m × 0.6 m × 0.45 m model used by Sidle et al. (1995), 5 m × 0.3 m × 0.5 m (Awal et al. 2009), 1.5 m × 1 m (Wilson 2009), 1.4 m × 1 m (Wilson 2011), and 0.5 m × 0.5 m × 0.5 m (Fox et al. 2014) flumes.
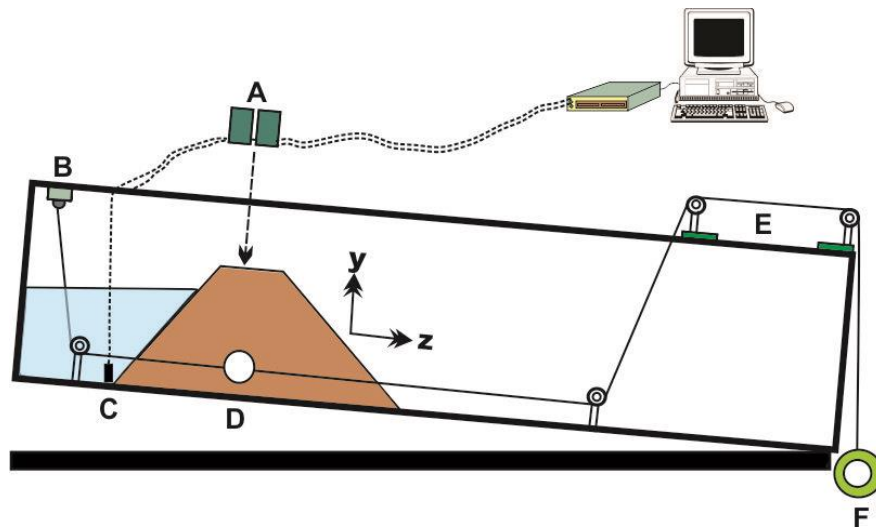
Figure 4.2 Experimental setup with sensor positions. **A** Laser displacement sensors **B** Linear displacement transducer **C** Upstream lake level sensor **D** Ball target **E** Pulleys **F** Suspended weight of 2.21 N.

4.2.2 Laser displacement sensors

Two CMOS multifunction analog displacement sensors (*IL-series 600*) were used to measure transient dynamic changes in the dam height as internal erosion and piping progressed through the dams. These intelligent laser displacement sensors were attached to a wooden overboard such that pre-failure crest settlements and concave-upward depressions associated with the onset of internal erosion and piping can be monitored. One of the sensors, hereafter referred to as H_{d1}, was positioned directly above the center of the dam crest, while the other sensor, hereafter referred to as H_{d2}, was fixed 0.07 m from the dam center. These measurements were made by allowing a maximum vertical distance of 0.25 m between the dam crest and the sensor heads (Figure 4.3). The sensors have a measuring range 0.2~1.0 m and a mounting range of 0.6 m.
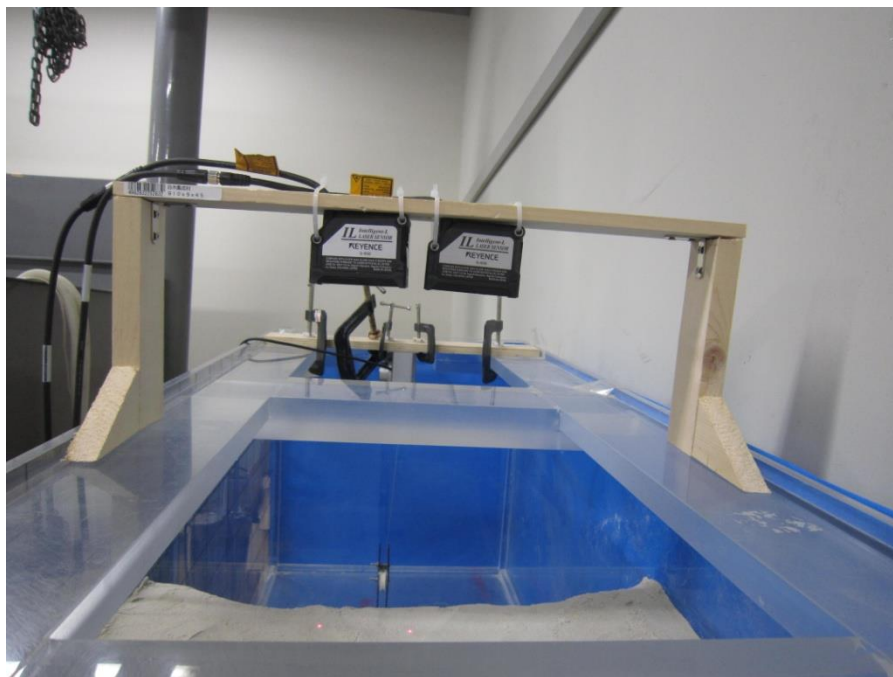
Figure 4.3 Location of laser displacement sensors used in monitoring crest settlement and the dynamic changes in the dam height as a result of internal erosion and piping.

4.2.3 Linear displacement transducer

A linear displacement transducer (*model: DTPS-D-1KS*) was used to monitor the onset of internal erosion through to the development of a continuous piping hole in the dams. The transducer has a measuring range of 1.0 m and maximum response speed of 0.2 m/s. The transducer was fixed at the upper end of the flume tank, and a thin metallic wire attached to the sensor head was connected to a plastic ball of similar weight to the materials used in the experiments. The ball was buried at the center of the dam crest, while the outer end of the metallic wire, suspended by a known weight, passed through four stationary pulleys (Figure 4.4).

Figure 4.4 Location of the linear displacement transducer inside the flume tank.

4.2.4 Upstream water level probe

A pore-water pressure transducer (*model: BPR-A-50KPS*) was used in measuring transient changes in the upstream lake level. The pore-water pressure transducer,

with rated capacity of 50 kPa, was fixed at a stationary position near the upstream dam toe to ensure accurate measurement and recording of data (Figure 4.2). The upstream lake was recharged from a drainage hose fed by a water tap, while the inflow rate was controlled with a flow-meter fixed at the upper part of the flume box (Figure 4.5).
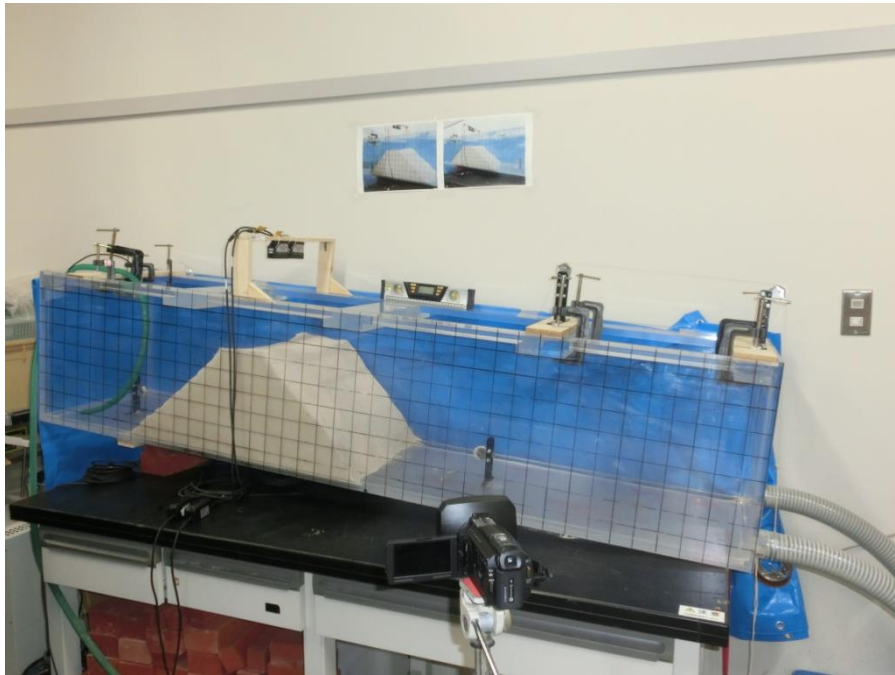
Figure 4.5 Setup of the laboratory experiment showing the location of monitoring sensors and the rubber hose used for filling of the upstream lake.

4.3 Experimental procedure and properties of the soils used

The dam models were built 0.4 m downslope from the upstream water inlet and were uniformly compacted by gently tapping successive five cm thick soils laid on the floor of the flume tank, using a wooden mallet. Friction was increased at the sides of the flume by ensuring maximum compaction of soil near the flume wall. Internal erosion was initiated by laying uniformly sized pebbles encased in a plastic

mesh at the center of the dam (Figure 4.6 a and b). The encased pebbles were laid such that a flume bed slope of 10° was obtained (Figure 4.7). The plastic ball attached to the linear displacement transducer was laid in the dam and held at critical tension by a suspended weight. The dam models were built at constant upstream and downstream slope angles of 35° and 50°, respectively. Prior to the start of each experiment, the pore-water pressure sensor was immersed in a water-filled jar for several minutes to ensure accurate measurement. A manually-operated flow meter with an initial discharge set at 1.2×10^{-4} m³/s was used to control the rate of inflow into the upstream lake. The flow rate was maintained until the upstream water level reached two-thirds of the dam height, at which stage water began to flow into the dam through the artificial channel. This filling strategy was adopted because the overtopping failure of landslide dams was not considered in this study.
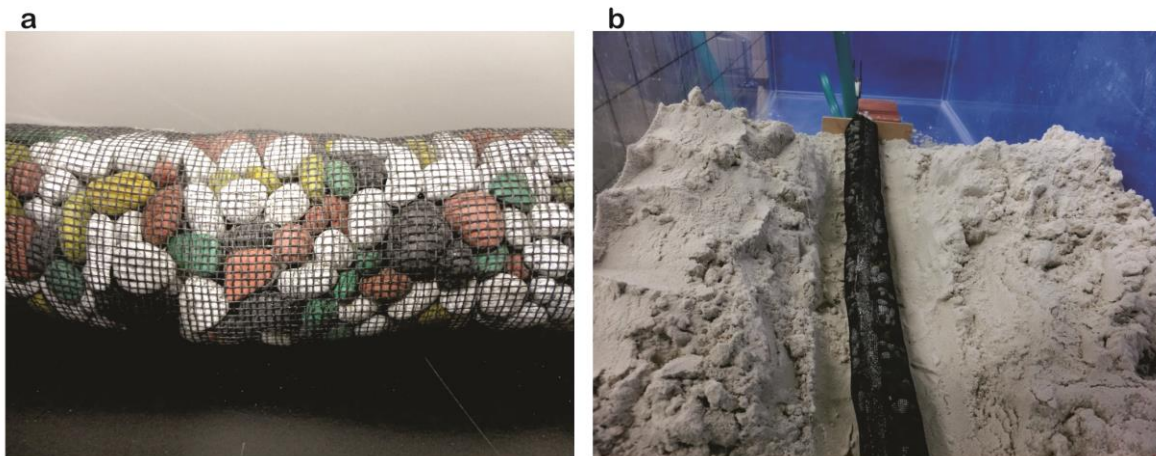
Figure 4.6 a The encased pebbles used to initiate internal erosion. **b** Laying of the encased pebbles during the construction of the dam model

The stability of landslide dams is, to a certain degree, controlled by the nature of the materials composing the dams. Landslide dams are generally composed of fragmented materials which have a wide range of sediment sizes (Costa and Schuster 1988; Schuster 1995; Davies and McSaveney 2011; Dunning and Armitage 2011).

Reproducing field prototypes of landslide dams in a flume is challenging, especially with respect to downsizing the impoundment materials to laboratory-scale experiments.
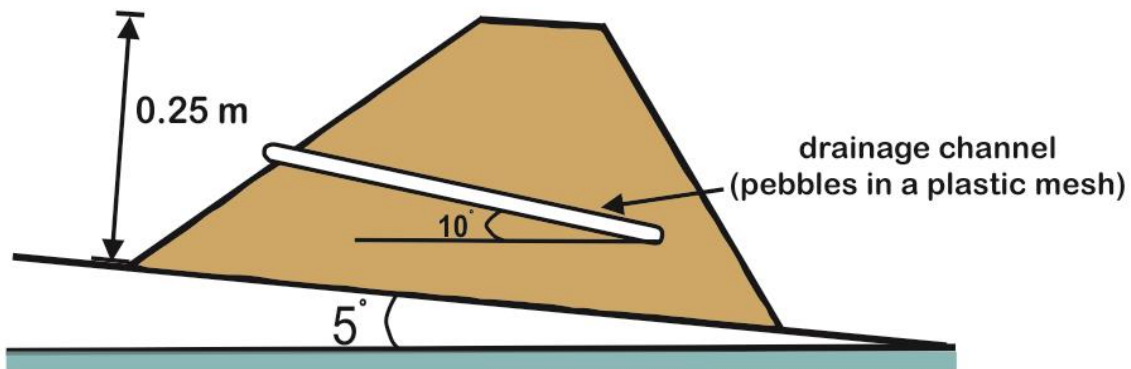
Figure 4.7 Schematic diagram of the landslide dam geometry.

The mechanical and hydraulic properties of the dam materials are given in Table 4.1. In the first step of the experiments, 2000 ml of water and 40 kg of each material were rigorously mixed using a mechanical mixer. The soil samples were used to build dams of a uniform crest and height (H_d) of 0.1 m and 0.25 m, respectively (Figure 4.10). Summaries of the characteristics of the experiments carried out on dams built with mixed and homogeneous materials are given in Tables 4.2 and 4.3, respectively. The initial discharge rate Q_i was constant in all experimental runs, whereas T_e and T_b represent the time of onset of internal erosion and time of dam crest collapse, respectively. Consequently, the materials used in this study comprised mixed and homogeneous samples of industrial silica sands (numbers 4, 5, 6, 7, and 8) in varying proportions (Figure 4.8 and 4.9).
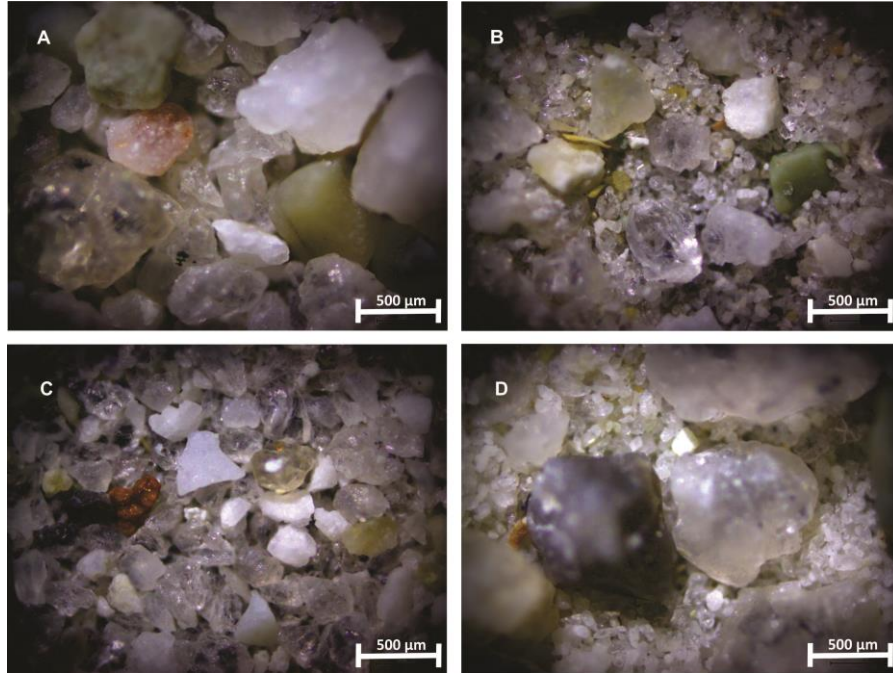
Figure 4.8 Photomicrographs of reconstituted materials of dam mixes *A*, *B*, *C* and *D*.
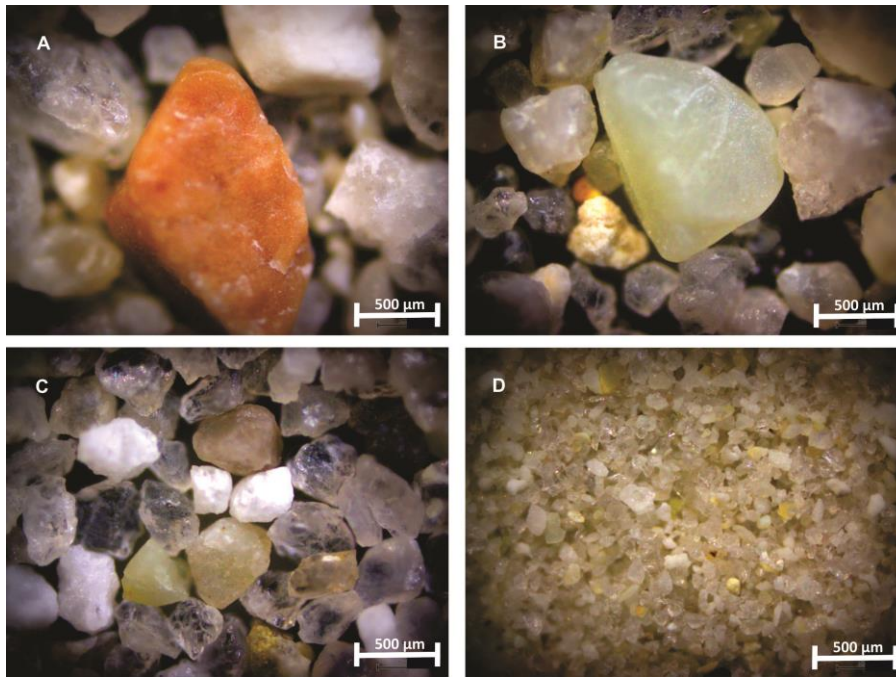
Figure 4.9 Photomicrographs of homogeneous materials of dam mixes *E*, *F*, *G* and *H*.

Table 4.1 Mechanical and hydraulic properties of the dam materials

Sample name	D_{50} (mm)	C_u	C_c	ρ_{dry} (Mg/m³)	e_o	n (%)	k (m/s)
Dam mix A	0.236	4.051	0.993	1.33	0.99	49.7	3.9×10^{-6}
Dam mix B	0.358	5.887	2.407	1.30	1.04	51.0	3.1×10^{-4}
Dam mix C	0.186	3.393	0.883	1.19	1.23	55.2	4.8×10^{-5}
Dam mix D	0.118	1.990	0.852	1.22	1.17	53.9	1.1×10^{-5}
Dam mix E	0.799	2.474	1.385	1.21	1.19	54.3	3.2×10^{-4}
Dam mix F	0.235	1.310	0.990	1.18	1.25	55.6	6.1×10^{-4}
Dam mix G	0.264	2.315	0.947	1.15	1.30	56.5	8.2×10^{-4}
Dam mix H	0.124	1.726	1.195	1.02	1.59	61.4	5.8×10^{-5}

Table 4.2 Summary of experiments carried out for dams composed of mixed materials

Run series	Material	Composition (%)	T_e (s)	T_b (s)	Characteristic features
1	Dam mix A	Equal amounts of SS 4, 5, 6, 7 and 8	90	160	Piping and hydraulic fracturing
2	Dam mix B	SS-5 and SS-8 (70:30)	98	145	Piping followed by pipe roof collapse
3	Dam mix C	SS-6 and SS-8 (30:70)	82	158	Piping followed by pipe roof collapse
4	Dam mix D	SS-4 and SS-8 (30:70)	86	184	Well-defined piping hole which supported the pipe roof

Table 4.3 Summary of experiments carried out for dams composed of homogeneous materials

Run series	Material	Composition (%)	T_e (s)	T_b (s)	Characteristic features
1A	Dam mix E	SS-4 (100)	80	240	Seepage; Downstream slope saturation; Toe bulging followed by slope unraveling
2A	Dam mix F	SS-5 (100)	85	195	Seepage; Downstream slope saturation; Toe bulging; Progressive sloughing
3A	Dam mix G	SS-6 (100)	75	230	Poorly developed piping hole; Downstream slope unraveling
4A	Dam mix H	SS-8 (100)	60	260	Formed well-defined piping hole; Supported the pipe roof

Figure 4.10 a Side view of the flume tank. **b** Front view of a dam showing the downstream slope prior to commencement of an experiment.

4.4 Results and Discussion

4.4.1 Observed phases of the breach evolution process

Several phases of the breach evolution process were observed during repeated experiments. Qualitative assessments and observations, coupled with data obtained from precision sensors, helped to distinguish the various stages. The breach development processes observed included: (1) pipe development; (2) pipe enlargement; (3) crest settlement; (4) hydraulic fracturing; and (5) progressive sloughing. While the breach development process followed the sequence listed above in some dams, others failed retrogressively, resulting in late-stage overtopping of the dams. Therefore, before describing the results, it is pertinent to define and describe the various failure phases observed in this study.

4.4.2 Pipe development

This process is related to the formation of a continuous piping hole, as a result of increased action of seepage forces through the soil micropores. The initial stage of this process starts with the initiation of internal erosion, which in this case, was enhanced by concentrated seepage through the artificial drainage channel. An abrupt drop in velocity of the seeping water at the opposite end of the drainage channel, about 5 cm before the downstream slope face, reduces the pressure of the seeping water through the soil micropores. However, the erosive cycle continues as a result of high pore-water pressure, leading to a partial reduction of the shear strength of the soil, as observed at the downstream slope face in the form of a '*wet spot*'. Summarily, the numerous complex mechanisms leading to the initiation of internal erosion and subsequent development of a piping hole include (1) generation of high pore-water pressure due to the incessant action of the seepage flux, which reduces the apparent cohesion of the soil, (2) increase in seepage forces through the soil micropores, which reduces the effective stress of the soil and produces drag

forces sufficient for soil particles to be detached and entrained downstream; and (3) gradual evolution of the existing micropores, essentially caused by the hydraulic shear stress exerted by the seeping water. A continuous pipe is formed through the dam once appreciable aggregates of soil particles are removed and transported downstream by the flowing water. From observation during the experiments, it was noted that at the onset of the pipe development process, the initial diameters of the developing pipes were mostly smaller than or equal to the diameter of the artificial drainage channel.

4.4.3 Pipe enlargement

The mechanism of pipe enlargement can be related to the effect of the hydrodynamic forces produced by the flowing water on the hydromechanical properties of the soil under varying physicochemical conditions. The evolution of the pipe through the dam changes the dynamics of the seeping water from low-pressure flow through the soil micropores to high-pressure flow through the enlarging pipe. At this stage, the enlargement of the pipe and subsequent progression of the breaching process is usually rapid, and thus depends on several properties of the soil, including the interlocking effect, the shear strength, and density of the soil, as well as the energy of the flowing water. The tractive force theory based on the bed load formula suggests that the amount of sediment transported per second per unit width of a conduit q_s is a function of shear stress τ (Singh, 1996):

$$q_s = f(\tau) \tag{4.1}$$

Thus, the erodibility of the soil at the periphery of the flow path and the hydraulic shear stress are two key factors which determine the rate of erosion and the time of progression through to completion of the breaching process. The complexity of the

pipe enlargement process with respect to sediment transport mechanics has been described by the excess shear stress equation:

$$\varepsilon = k_d(\tau_a - \tau_c)^a \qquad\qquad (4.2)$$

where ε is the sediment transport rate (m/s), k_d is the erodibility coefficient (m³/N-s), τ_a is the hydraulic shear stress on the soil boundary (Pa), τ_c is the critical shear stress (Pa), and a is an exponent, usually assumed to be 1 (Hanson and Cook 1997; Fell et al. 2003). Enlargement of the pipe depends on the ability of the material to support the pipe roof. Hence, observations from the series of experiments showed that most of the homogeneous dams failed by progressive saturation of the downstream slope. In contrast, well-defined piping holes were formed in dams composed of mixed materials with a higher piping tendency, as evident in dam mixes *D* and *H,* where the pipe roofs survived for a relatively longer time.

4.4.4 Crest settlement

This process was observed in all the experiments, but the evolution process varied with the material forming the dam. In this case, crest settlement is related to the formation of a concave-upward depression at the center of the dam crest, as a result of internal erosion and piping within the material underlying the dam crest. This phenomenon is usually initiated by seepage forces through the dam, and can be associated with several other processes, such as soil arching, cracking, and hydraulic fracturing. The effect is more pronounced in low-density fine-grained soils and cohesionless soils of high void ratios, in which the development of very high pore-water pressure conditions leads to the reduction of the effective stress of the soil. Crest settlement was more evident in dams built with homogeneous materials than in those built with reconstituted materials, excluding dams containing a significant amount of fines, such as dam mixes *D* and *H.*

4.4.5 Hydraulic fracturing

This failure mechanism is common in dams built with reconstituted materials. The hydraulic fracturing process is initiated by differential settlement, arising from the different compressibilities of the soils, coupled with uneven compaction. This leads to the development of tensile stresses in weak or soft zones as pore-water pressure increases through the dam. Observations during the experiments found that as soon as the upstream lake level reached the tip of the encased pebbles, seepage forces converged into the pebbles and any other hydraulically weak zone, leading to erosion of soil particles along the developing conduit. The crack formation can be related to increased pore-water pressure, which reduces the minor effective principal stress across the plane of the crack ($\sigma_3 < 0$). This further implies that hydraulic fractures occur once the pore-water pressure in the dam is greater than or equal to the total stress σ_3, or equal to the tensile strength of the soil, σ_t (Mattson et al. 2008).

4.4.6 Progressive sloughing

This type of failure was observed in dams built with very loose cohesionless materials (dam mixes *E, F,* and *G*), and to a lesser extent in dams built with dam mixes *A* and *B*, but was rarely seen in dams built with very fine sand and silt. The process is often triggered when the seepage forces are less than or equal to the shear strength of the soil. Thus, the inability of the seeping water to produce sufficient drag forces needed to dislodge and entrain the soil particles and form a continuous piping channel leads to gradual seepage flow towards the downstream slope. The saturation of the downstream slope due to seepage leads to the reduction of the effective stress of the soil and subsequently causes very small slumps and slides in the form of cantilever failures to occur at the toe of the slope. This, in turn, leaves very steep faces which fail under increased pore-water pressure. This cycle of failure

continues until the exposed section of the dam yields to the effect of increased pore-water pressure, and slides downstream, leading to the partial breaching of the dam.

4.5 General description of the experiments

The initial condition set for the experiments assumed that either the dammed lake is of low discharge or the location where the landslide blocked the valley is relatively 'dry' (Korup 2004). Hence, no tailwater was present at the downstream area, since the slope of the flume tank was 5°. After building the dam model, the upstream lake level was gradually increased until the water reached the tip of the encased pebbles. The hydrological trend and failure mechanisms of the dams were largely controlled by the hydromechanical properties of the soil materials. The two major failure modes observed were seepage and piping. While piping failure was dominant in dams composed of very fine materials or mixed soils with an appreciable amount of fines, seepage, and downstream slope saturation were dominant in dams built with homogeneous cohesionless soils.

The first physical defects observed during the experiments were the formation of longitudinal cracks at the upper part of the upstream slope, as the level of the upstream lake rose with time. This was usually followed by the settlement of the entire dam, and subsequent formation of concave-upward depressions at the center of the dam crest. The increase in seepage gradient along the encased pebbles enhanced initiation of internal erosion at the boundary between the dam material and the encased pebbles. Progression of internal erosion through the dam was manifested by the appearance of a *wet spot* on the downstream slope (Figure 4.11a). Generally, two primary transverse cracks are formed near the left and right banks of the dam. With time, these transverse cracks were crosscut by miniature cracks from which small slumps and slides may occur. Evolution of the piping hole at the downstream slope could be rapid or may collapse instantaneously, depending on the

shear strength of the dam material (Figure 4.11b). The breaching process continued with enlargement of the piping hole due to steady saturation, and subsequent collapse of the pipe wall through existing cracks and weak zones on the slope (Figure 4.11c). The piping hole diameter increased with corresponding increase in the discharge through the dam, causing a rapid drawdown of the upstream lake. The pipe roof collapsed once pore-water pressure was greater than or equal to the effective stress of the dam material (Figure 4.11d). The collapse of the pipe roof led to a gradual rise in the upstream lake until the energy of the eroding medium was able to dislodge and transport the collapsed sediments downstream. The experiments ended by the formation of a wide breach channel, with base width ranging from 0.1 m to 0.35 m (Figure 4.11e).
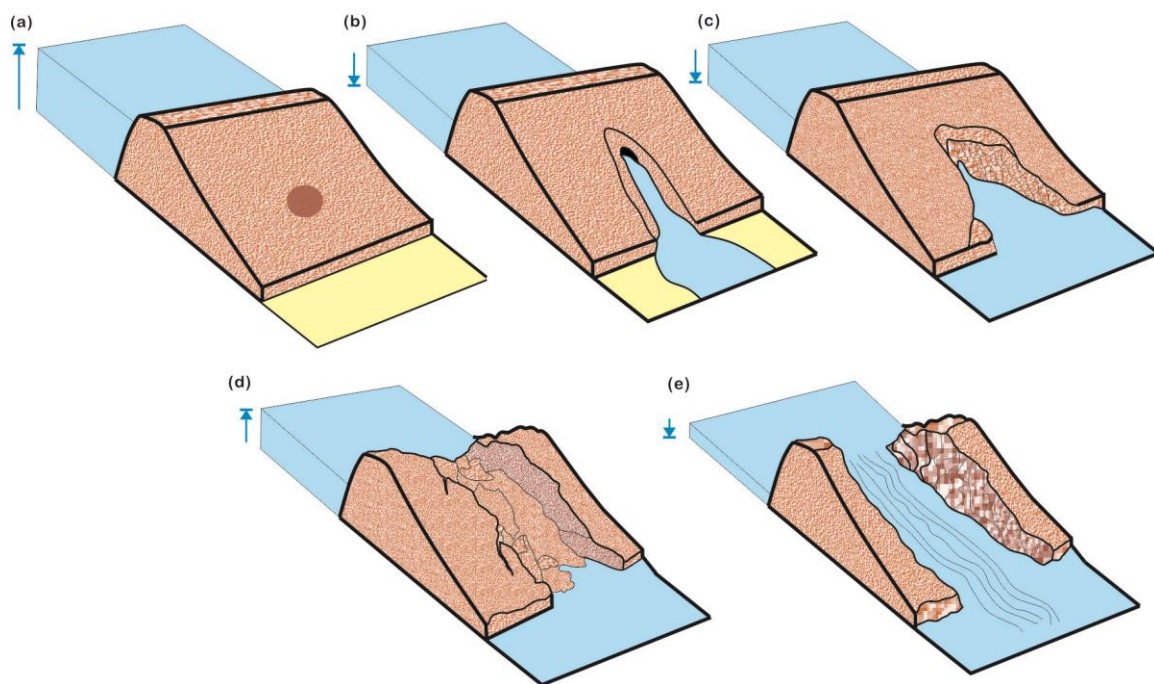
Figure 4.11 Evolution of the breaching process (**a**) Wet spot at the downstream slope (**b**) Formation and growth of a piping hole (**c**) Pipe progression and enlargement (**d**) Pipe roof collapse (**e**) Final breach profile of the dam (Okeke et al. 2013).

4.5.1 Failure mechanisms of dams built with mixed materials

Four representative experiments were carried out to assess the potential for piping and failure of dams composed of mixed materials of varying physical properties (Table 4.2). The characteristic physical properties of the reconstituted materials influenced the stage hydrographs and the deformation behaviour of the dams. The potential for formation of a continuous piping hole through the dams increased with an increase in percentage fines content. The mechanism of failure of the dams was primarily initiated by piping, although the likelihood of the developing pipe to form a uniform cylindrical hole varied with the density and magnitude of shear stress exerted by the seeping water. Similarly, the ability of the dam material to support the roof of the piping hole varied with the amount of fines in the soil. It is observed that the dam mix *D* material (Run series 4) manifested higher tendency of sustaining the roof of the piping hole in comparison with other materials, where the roof of the poorly developed piping holes collapsed instantaneously under steady propagation of the wetting front. Hydraulic fractures caused by internal stress redistribution increased with an increase in heterogeneity of the materials. Figure 4.12 shows the hydrological trends and mechanisms of breach evolution in dams composed of mixed materials. A steady rise in upstream lake level initiated a hydraulic head gradient that produced seepage forces through the dams. This consequently led to the formation of concave-upward depressions, mostly at the center of the dam crest. The formation of these depressions on the dams may be attributed to internal instability caused by suffusion which triggered the development of extensive cracks and soft zones (Figure 4.13). The rate of change of volume (settlement) of the unsaturated dam materials and the decrease in shear strength may be attributed to the relationship between wetting front propagation and the hydromechanical properties of the materials. The onset of internal erosion is marked by buckling of the ball target due to loss of tension induced by the shear stress of the seeping water.
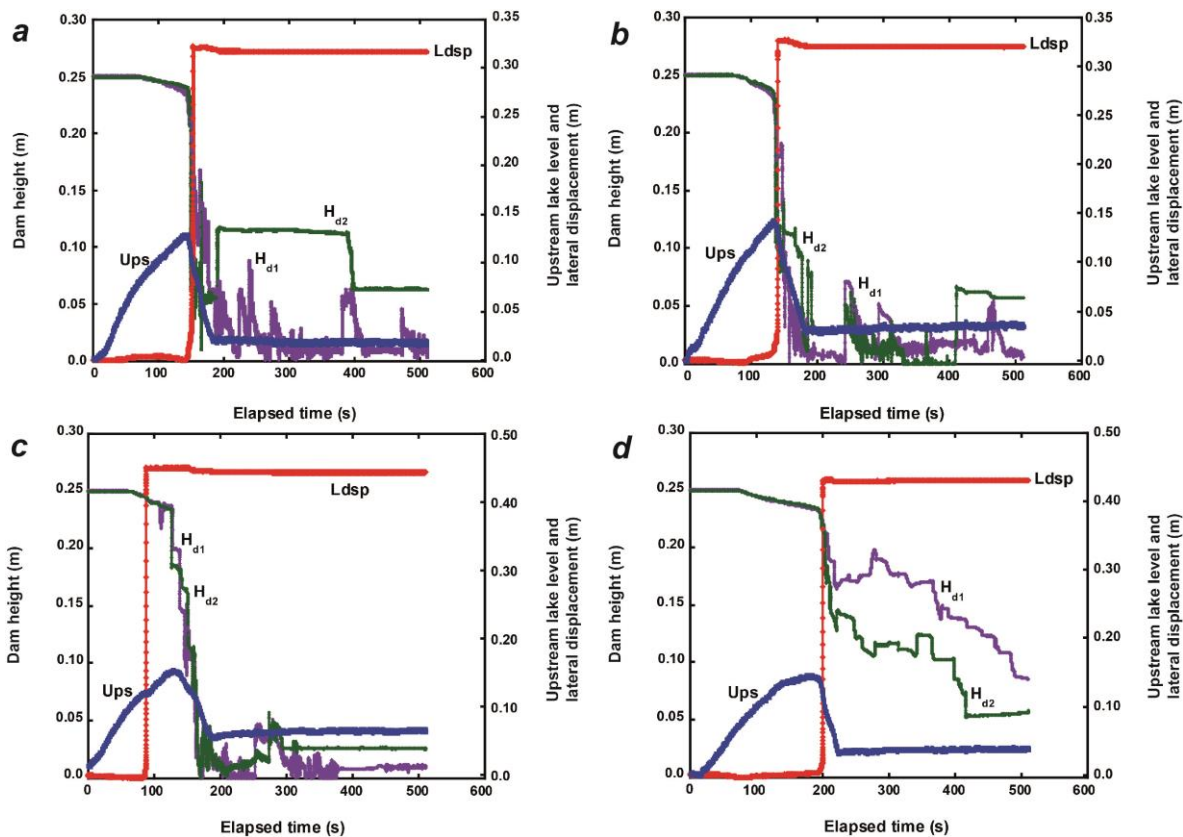
Figure 4.12 Hydrological trends and mechanisms of breach evolution in dams composed of dam mixes: (**a**) *A* (**b**) *B* (**c**) *C* (**d**) *D*.

It is interesting to note that the progression of seepage and formation of a piping hole coincided with lowering of the upstream lake level (as a result of steady discharge through the piping hole), and retraction of the ball target attached to the linear displacement transducer. The results indicate that the progression and enlargement of the piping hole were controlled by cohesion, grain size distribution, particle density and energy of the eroding medium. The general deformation behaviour of the dams composed of heterogeneous and anisotropic cohesionless materials was characterized by the formation of cracks (longitudinal and transverse) aligned perpendicular and parallel to the dam axis. The final stage of the breach

evolution process was marked by the formation of a wide breach channel with base width ranging from 0.1 m to 0.25 m.
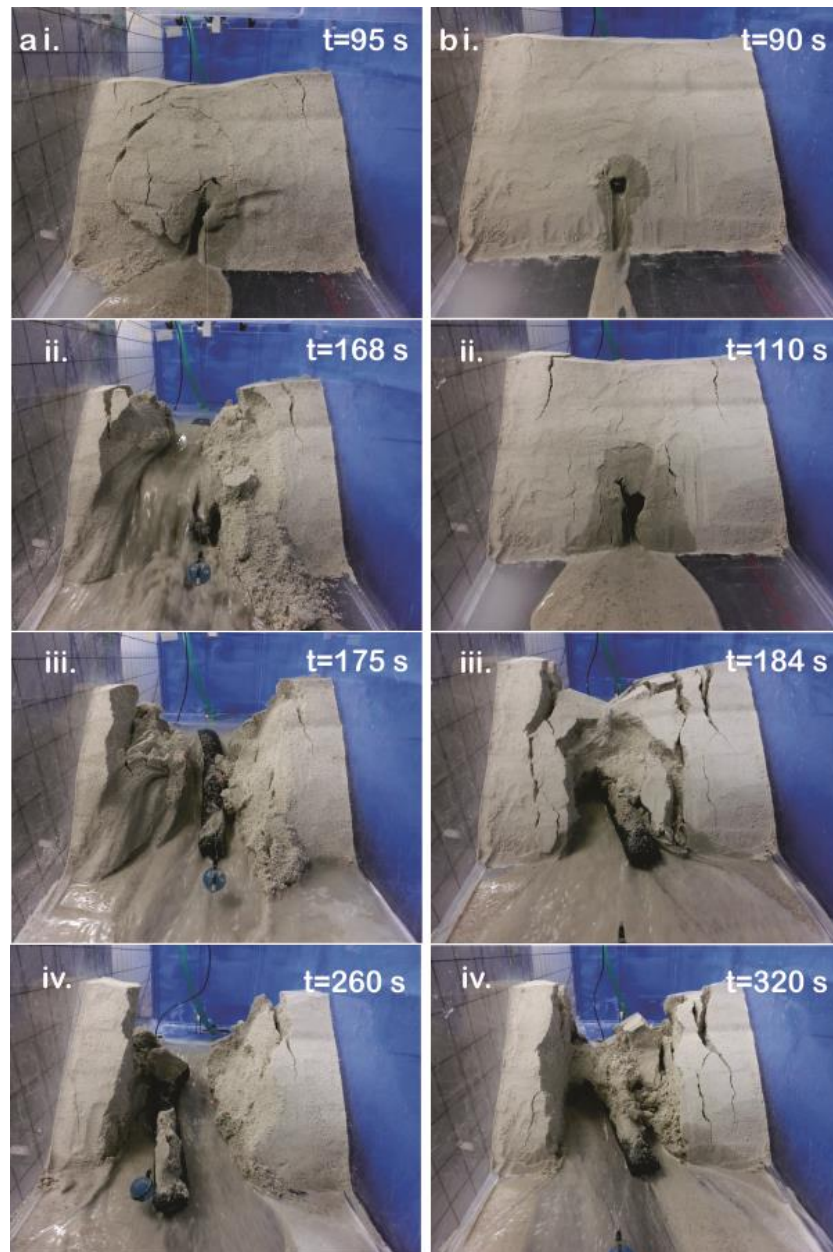
Figure 4.13 Failure mechanisms of dams built with (**a**) dam mix *A* and (**b**) dam mix *D* showing piping and subsequent collapse of the dam crest.

4.5.2 Failure mechanisms of dams built with homogeneous materials

The failure mechanisms of dams composed of homogeneous and isotropic cohesionless materials were assessed with four different soils (Table 4.3). A steady rise in the upstream lake initiated a hydraulic head which enhanced concentrated seepage through the artificial drainage channel. Propagation of wetting front was observed to occur at rates higher than those observed in dams built with mixed materials. Steady propagation of wetting front within the unsaturated cohesionless dam materials resulted in a decrease in matric suction (negative pore-water pressure) which caused a reduction in interstitial voids, as evidenced by the formation of concave upward depressions at the central part of the dam crest. Figure 4.14 shows the hydrological trends and failure mechanisms of dams built with homogeneous and isotropic cohesionless materials. The onset of internal erosion and mobilization of the soil particles adjacent to the drainage channel coincided with buckling of the ball target and formation of cracks, thereby triggering initial deformation of the dam crest. Internal redistribution of stresses initiated by intense seepage led to several processes including hydraulic cracking, dam crest settlement, downstream face saturation and toe bulging, and downstream slope unraveling. The majority of these processes were apparent in experiments conducted with dam mixes *E*, *F,* and *G*, where steady seepage through the dams resulted in exfiltration, sapping erosion, undercutting and sloughing of the partially liquefied soil. In contrast, the experiment conducted with dam mix *H* revealed a well-formed piping hole that lasted for a relatively longer time (Figure 4.15). The rapid drawdown of the upstream lake level could be related to the rate of enlargement of the piping hole due to the erosive forces of the seeping water, which continued until the material supporting the pipe roof collapsed into the channel. The results indicate that the potential to form a piping hole through the dams decreased with an increase in density and hydraulic conductivity.
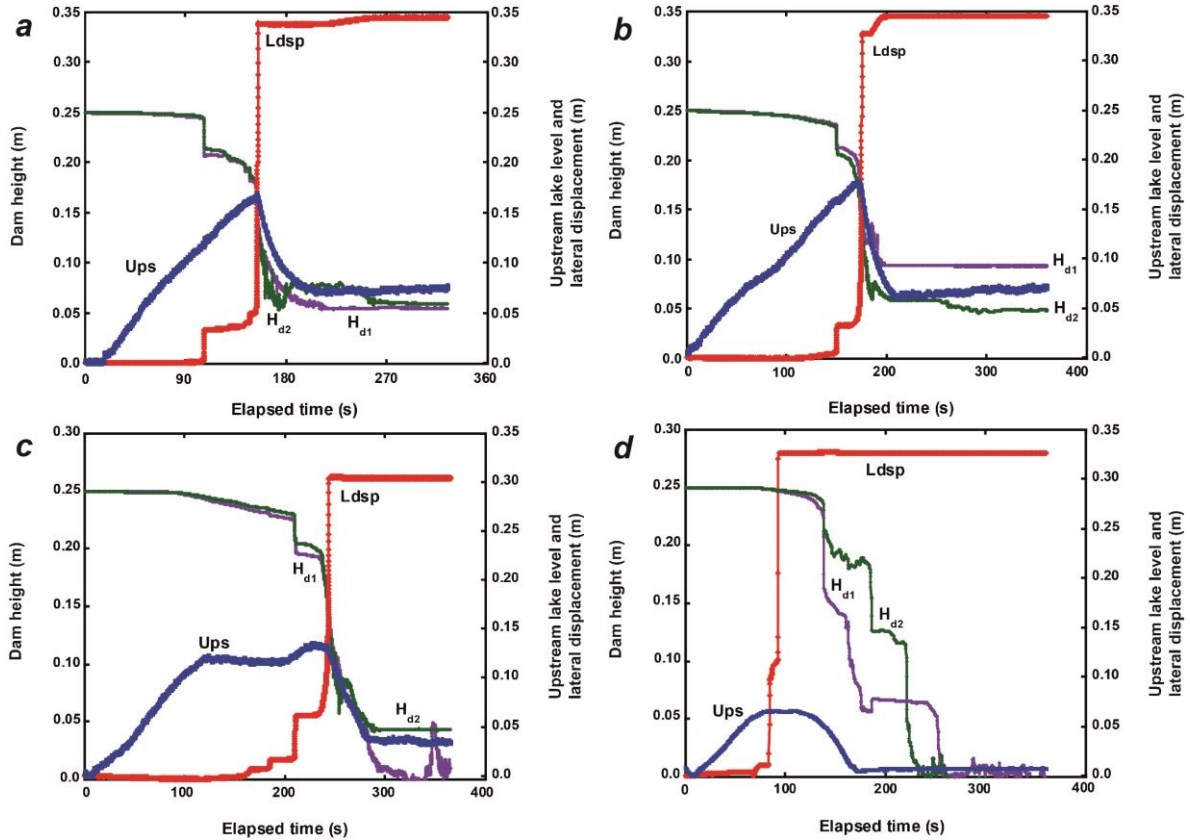
Figure 4.14 Hydrological trends and mechanisms of breach evolution in dams composed of dam mixes: (**a**) *E* (**b**) *F* (**c**) *G* (**d**) *H*.

4.5.3 Effects of grading and density on the erodibility of the dam materials

Figure 4.16 shows the relationship between the time of collapse of the dam crest, T_b and dry bulk density of the various soils composing the dams. Variations in hydromechanical behaviour were more evident in dams composed of soils of lower density than in those built with soils of higher density. An exception to this case was dam mix *D* (T_b, 184 s), where the interlocking bonds between very fine particles of silica sand 8 and coarser particles of silica sand 4 at optimum water content seemed to be stronger than in other soil samples. Previous studies of internal erosion and soil erodibility observed that progression of the piping hole and erodibility of material at the periphery of the piping hole depended on the compaction density

and water content (Hanson and Robinson 1993; Fell et al. 2003). Field erodibility tests conducted by Chang et al. (2011) on two landslide dams triggered by the 12 May 2008 M_s 8.0 Wenchuan earthquake in Sichuan Province of China showed that increase in bulk density was inversely proportional to the coefficient of erodibility with depth. Furthermore, large-scale physical tests carried out by Hanson et al. (2010) in their investigation of the impact of erosion resistance on internal erosion in embankment dams identified that erosion resistance for the same embankment material increased with an increase in compactive effort and water content. Observations made during the experiments in our present study yield similar results. Similarly, a comparison between the failure process of run series 4 (dam mix D) and run series 2A (dam mix F) shows that even at a higher erosion rate q_s, the breach evolution process of the two dams varied greatly. Figure 4.17 shows the relationship between the initial void ratio of the dam materials and the time of collapse of the dam crest (T_e and T_b). The time of onset of internal erosion, T_e, and the time of dam crest collapse, T_b, reveals the effect of internal instability caused by suffusion. This led to early initiation of internal erosion in dams composed of mixed materials, even at lower void ratios, due to selective removal of fines from the soil matrix and subsequent destabilization of the soil structure. This result indicates that void ratio and other physical properties such as permeability, percentage fines content, and density affect the initiation and progression of internal erosion in dams.

Figure 4.18 shows the variation of T_e and T_b versus coefficient of uniformity C_u in all the experimental runs. The result indicates that the higher the C_u the longer the time of onset of internal erosion T_e and the shorter the time of collapse of the dam crest T_b. In general, short T_e and long T_b were recorded in experiments carried out with the homogeneous materials with C_u that ranges from 1.310~2.474, in comparison with the mixed materials where T_e increases with an increase in C_u. The relative short T_b characteristic of the mixed materials can be attributed to selective

transportation and washing out of fines from the coarser soil matrix and thus, reflects the decreasing trend of T_b with respect to C_u. Figure 4.19 shows the relationship between coefficient of curvature and T_e and T_b for the mixed and homogeneous materials. For the homogeneous materials, it can be seen that T_e is directly proportional to C_c, while T_b is inversely proportional to C_c. Similar trend is observed in the mixed materials except for dam mix B that has a C_c of 2.407. Furthermore, a plot of D_{10} versus T_e and T_b clearly shows that D_{10} is inversely proportional to T_e, and thus, increases with an increase in T_b (Figure 4.20). This phenomenon can be related to the significance of fines content and gradation on the initiation and progression of internal erosion in cohesionless materials.

Furthermore, the relationship between initial void ratio and the dimensionless settlement index S_I (Figure 4.21) clearly shows the behaviour of the dam materials as pore-water pressure and seepage gradient increased through the dams:

$$S_I = \frac{s}{1000 \times H \log\left[\frac{t_2}{t_1}\right]} \tag{4.3}$$

where s is crest settlement in mm between times t_1 and t_2, and H is the dam height in meters (Charles 1986). The general deformation behaviour of the dams shows that settlement increased with an increase in void ratio. Low density cohesionless soils with high void ratios, such as silts, are generally brittle, and thus are prone to cracking during differential settlement. This process is usually associated with the formation of tension cracks and other weak zones of low stress condition. A typical example is the Red Willow Dam in southwest Nebraska, USA. The dam is a 38.4-m high homogeneous embankment made up of low plasticity silts. Emergency investigations conducted by the US Bureau of Reclamation discovered sinkholes at the downstream face, whereas cracks appeared above the outlet works conduit and other locations near the right abutment. The brittle nature of the embankment material coupled with the low density and plasticity index of the soil led to the

settlement of the crest to about 1.2 m below the original height, which caused the reservoir level to be lowered.
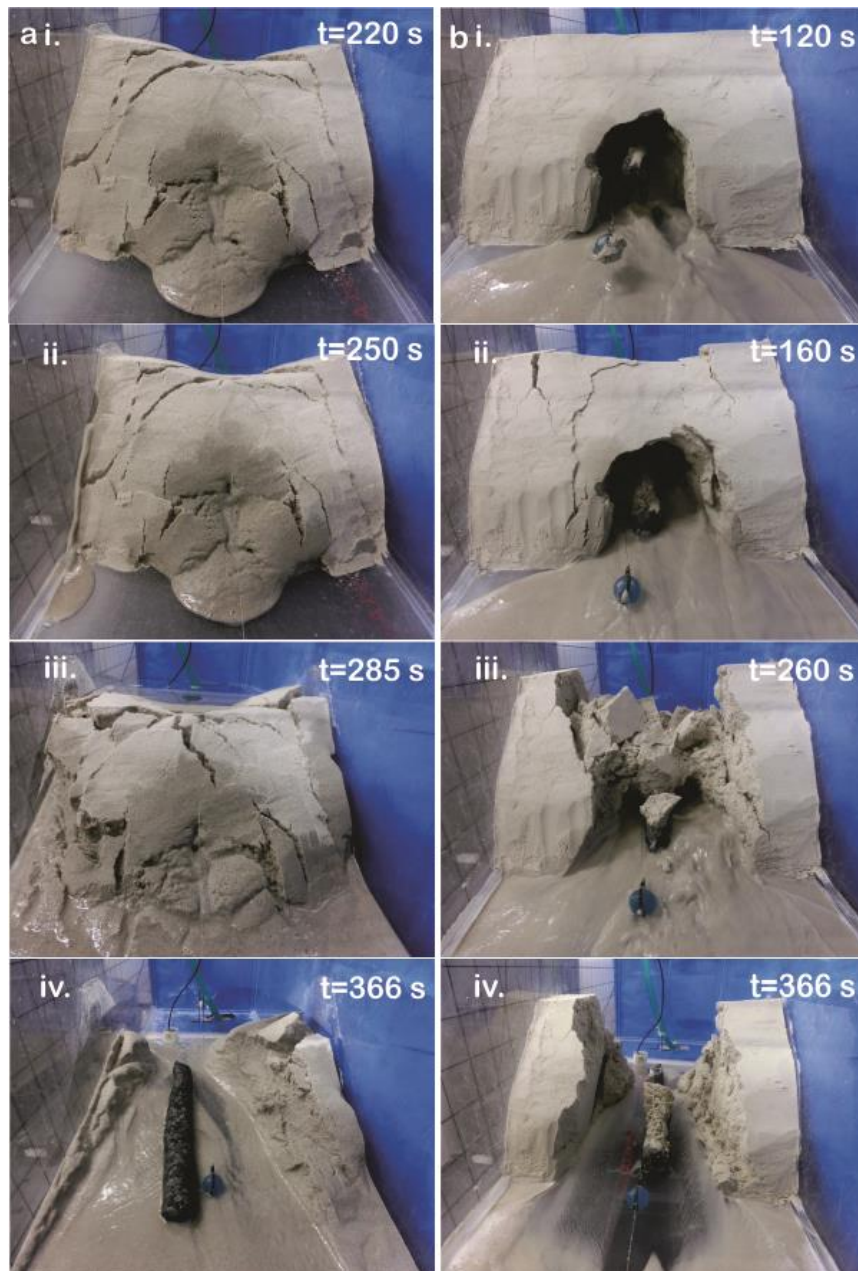
Figure 4.15 Failure mechanisms of dams built with (**a**) dam mix *G* and (**b**) dam mix *H* showing hydraulic cracking, downstream face saturation and piping
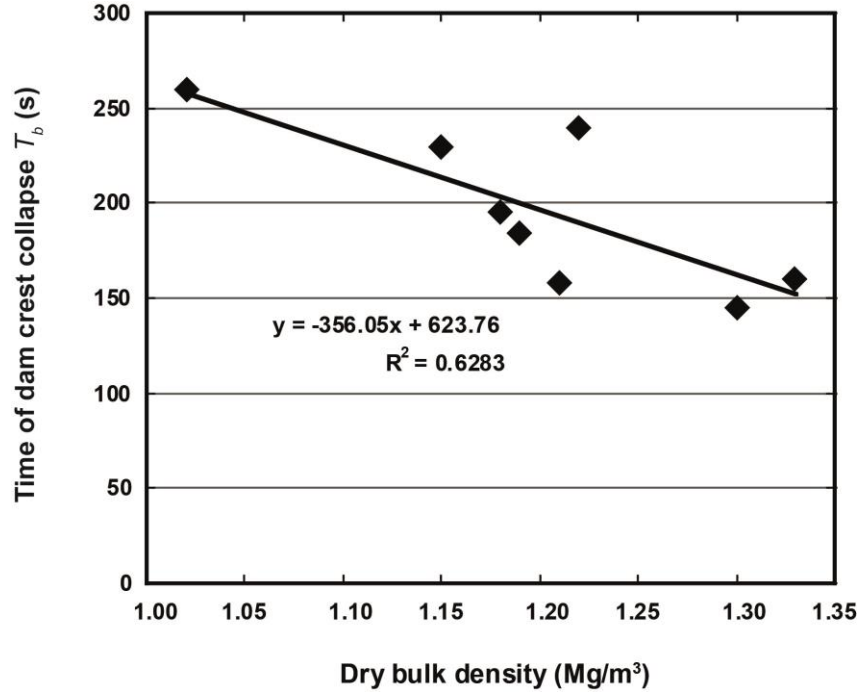
Figure 4.16 Relationship between time of dam crest collapse T_b and dry bulk density.

Figure 4.22 shows the relationship between S_I and C_u for the mixed and homogeneous materials. The result shows that S_I decreases with an increase in C_u. The high S_I observed in the homogeneous materials could be attributed to the internally unstable nature of the materials including other factors such as density and hydraulic conductivity. In contrast, the mixed materials show an S_I value that decreases with an increase in fines content and gradation. Furthermore, the relationships between S_I and C_c, and S_I and D_{10} are scattered and hence may not be useful in making correlations on the hydraulic behaviour of the dams (Figure 4.23 and 4.24). The plots, however, may show further insights into the relationships between the deformation behaviour of the dams and the physical properties of materials.

4.6 Natural analogues of seepage and piping in landslide dams

As mentioned before, the potential for seepage and piping failure of landslide dams can be attributed to the textural and sedimentological properties of the impoundment material, as well as the hydrological characteristics of the upstream lake. From a sedimentological perspective, the likelihood of piping and seepage failure of rock avalanche dams is high in comparison with landslide dams that preserved the original stratigraphy of their source rock.
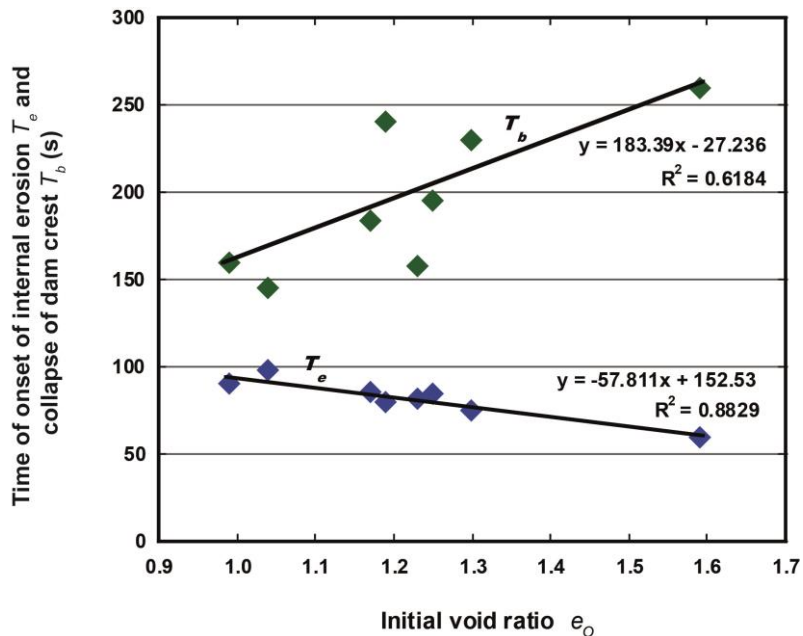
Figure 4.17 Relationships between time of onset of internal erosion T_e, time of collapse of dam crest T_b and initial void ratio e_o.

A vast number of rock avalanche dams are comprised of fragmented materials and are mostly characterized by a binary internal structure consisting of: (1) a highly pulverized and matrix-supported basal layer which is very erodible but has low permeability because of its low void ratio; and (2) an upper layer dominated mostly by a coarse blocky carapace of disjointed angular boulders, with large void spaces

that support internal erosion (Davies and McSaveney 2011; Strom 2013). Similarly, Dunning et al. (2006) identified three distinct sedimentological facies in rock avalanche dams: the *Carapace, Body* and *Basal facies*. The high hydraulic conductivity of the *Carapace facies* and the relative nature of its unstructured comminuted mass serves as a channel for seepage erosion and piping. This phenomenon is analogous to the 1992 failure of the Rio Toro landslide dam in Alajuela Province of Costa Rica. The dam failed by seepage and piping when the upstream lake level reached an elevation of 934~936 m and seeped into the upper pervious and blocky carapace layer, resulting in progressive failure and undermining of the downstream slope (Mora et al. 1993). Another similar event is the 2004 failure of the Tsatichhu landslide dam in Bhutan, which failed by a combination of dam face saturation and progressive seepage through the upper *Carapace facies* (Dunning et al. 2006). The failure mechanisms of these two natural analogues displayed similar characteristics with the results of our present study.
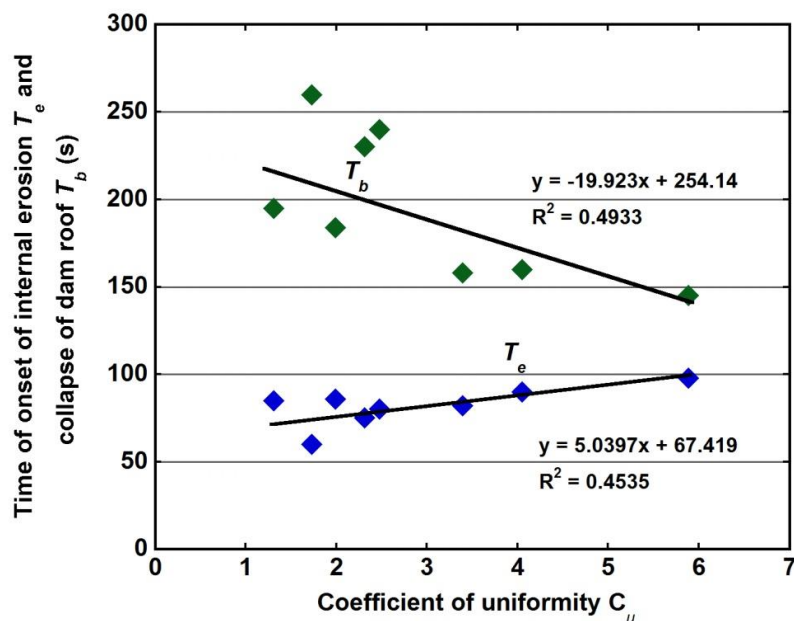
Figure 4.18 Relationship time of onset of internal erosion T_e, time of collapse of dam crest T_b and coefficient of uniformity.
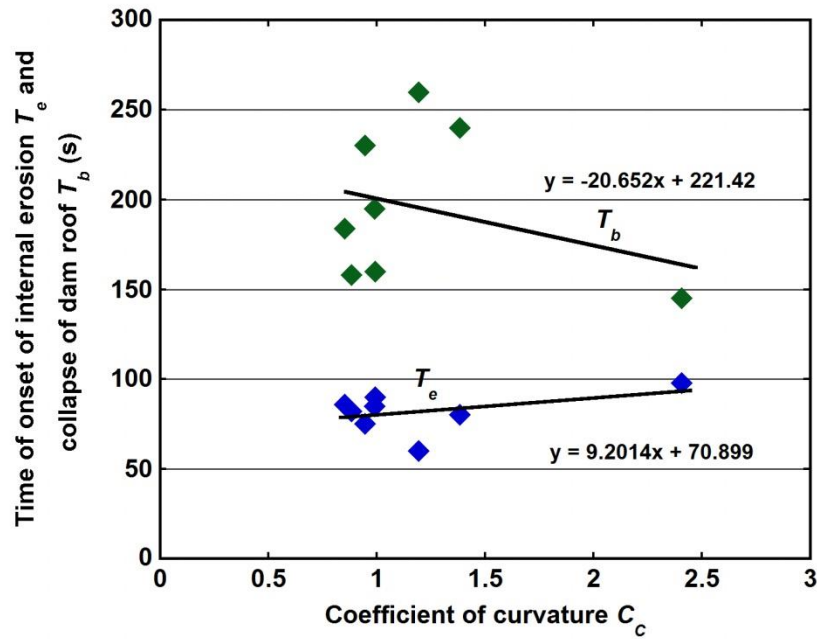
Figure 4.19 Relationship between time of onset of internal erosion T_e, time of collapse of dam crest T_b and coefficient of curvature.
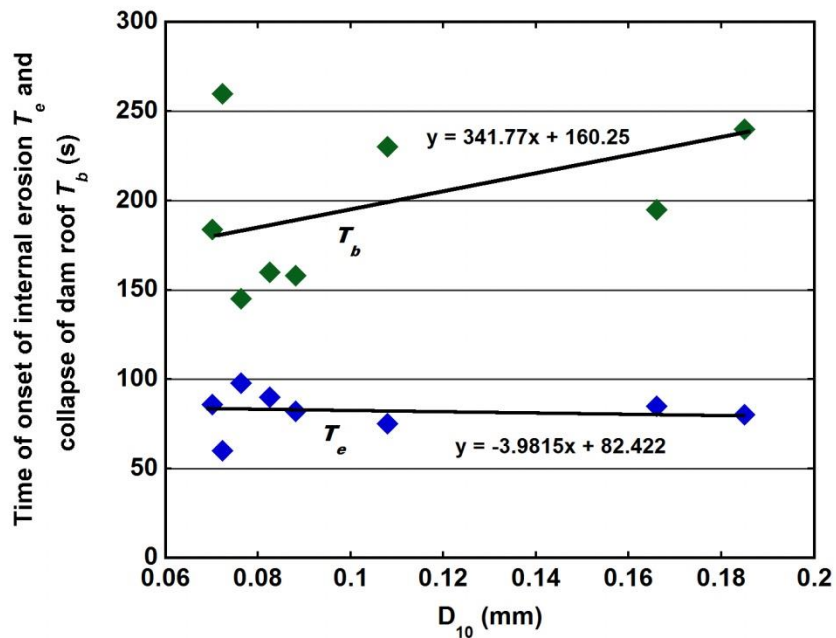
Figure 4.20 Relationship between time of onset of internal erosion T_e, time of collapse of dam crest T_b and D_{10}.
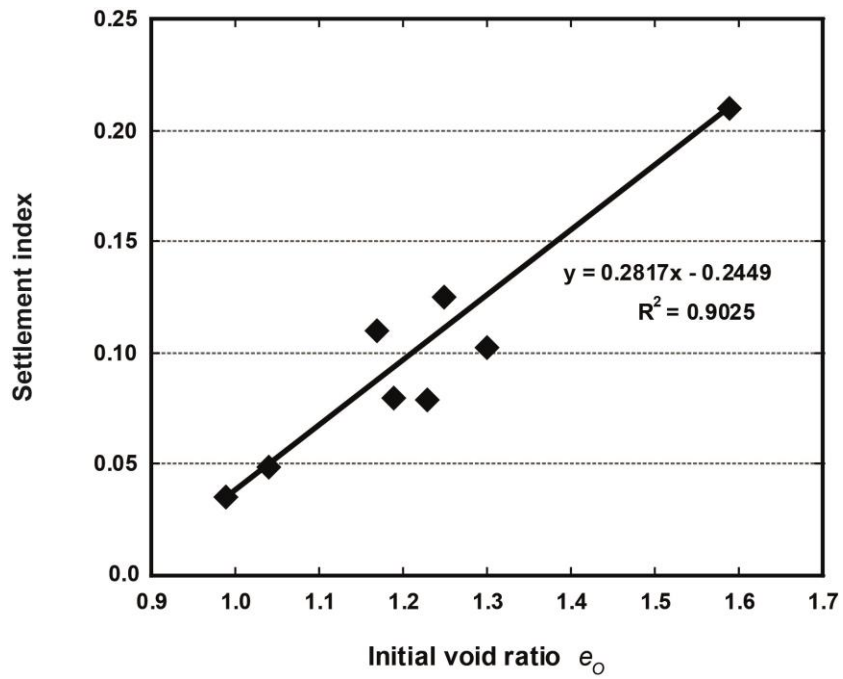
Figure 4.21 Relationship between settlement index and initial void ratio e_o.
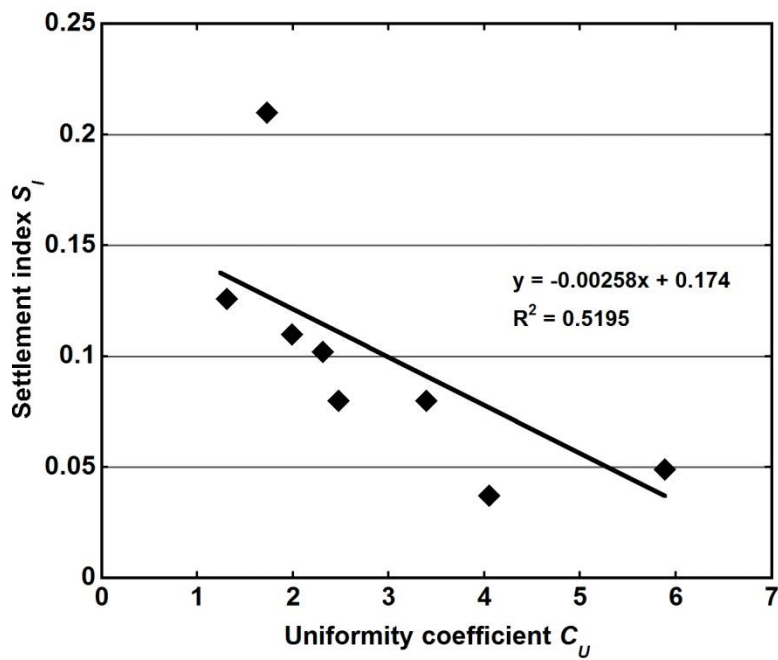
Figure 4.22 Relationship between settlement index and coefficient of uniformity.
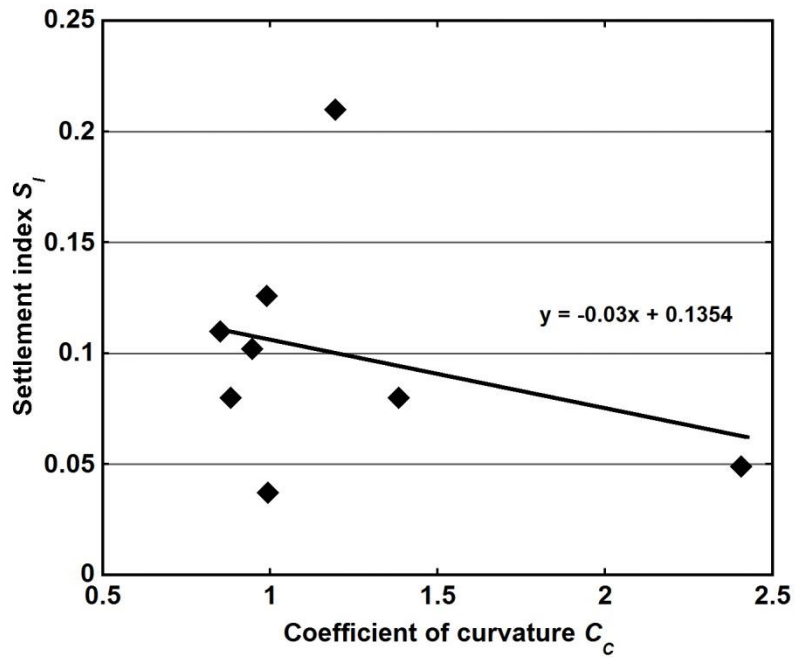
Figure 4.23 Relationship between settlement index and coefficient of curvature.
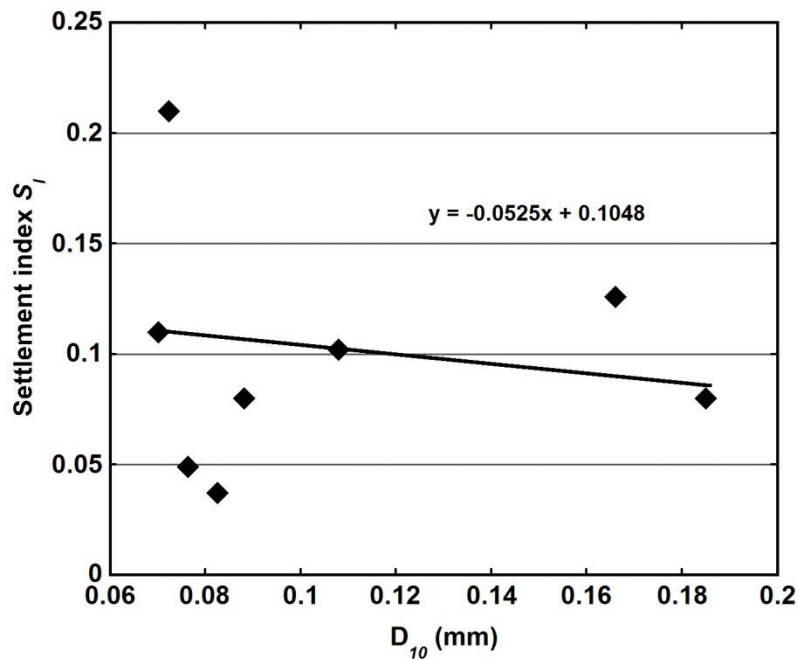
Figure 4.24 Relationship between settlement index and D_{10}.

4.7 Conclusions

A comprehensive experimental investigation was conducted to study the hydromechanical constraints of soils in the initiation and development of piping in landslide dams, with emphasis on the potential failure mechanisms of dams composed of various soil materials. Landslide dams were built in a flume tank, and internal erosion within the dams was initiated using an artificial drainage channel composed of uniform pebbles encased in a plastic mesh. Initial condition assumed that the upstream lake was 'dry'. Thus, the upstream lake was recharged at a steady state flow rate of 1.2×10^{-4} m³/s.

The various phases of the breach evolution process observed in this research included: pipe development, pipe enlargement, crest settlement, hydraulic fracturing and unraveling of the downstream slope. The potential for formation of a continuous piping hole in dams composed of homogeneous soils decreases with an increase in bulk density and hydraulic conductivity. Dams composed of homogeneous soils failed mostly by seepage and downstream slope saturation (Dunning et al. 2006), whereas piping holes were formed in dams built with mixed soils, depending on the percentage fines content and the interlocking bonds between the soil particles.

This study did not measure erodibility coefficients of the dam materials, as it can be obtained from the hole erosion tests (HET) (Wan and Fell 2004). However, it is evident from the results obtained here that the time of failure and the potential breach evolution mechanisms of the dams were controlled by soil density, including other factors such as void ratio, permeability and degree of compaction, except in a few cases such as dam mix D (run series 4), where the interparticle bonds between the soil particles and low permeability of the material affected soil erodibility. Early onset of internal erosion was observed in dams built with mixed materials, especially

in the case of dam mix *A*. This condition may be attributed to suffusion, which caused adverse changes in permeability, porosity, void ratio and pore-water pressure distribution in the soil. Conversely, the time of onset of internal erosion in the homogeneous dams increased with an increase in permeability.

Crest settlement and associated features such as cracking and hydraulic fracturing occurred in all the experiments, but were characteristically pronounced in the homogeneous dams, mostly in dams built with dam mixes *F* and *G*. The mechanism of dam crest collapse in dams built with mixed materials originated from two primary transverse cracks running parallel to the downstream slope, whereas the collapse mechanism of the homogeneous dams began from a longitudinal crack perpendicular to the downstream slope.

Although the breach evolution process observed in this study and the hydromechanical behaviour of the dams were constrained by space and time scales adapted in the flume experiments, the results provide valuable insights into the factors controlling the potential for seepage and piping failure of landslide dams. However, hole erosion tests (HET) need to be conducted on the finer materials used in these experiments to further evaluate the relationship between soil erodibility and hydraulic shear stress.

CHAPTER 5

EXPERIMENTAL INVESTIGATION OF THE CRITICAL HYDRAULIC GRADIENTS FOR SEEPAGE-INDUCED FAILURE OF LANDSLIDE DAMS

5.1 Introduction

Landslide dams and other natural river blockages such as moraine dams and glacier-ice dams are formed in narrow valleys bordered by oversteepened slopes. Active geological processes in these settings such as erosion and weathering often lead to the availability of highly fractured and hydrothermally altered bedrock which constitute source materials for hillslope processes and landslide dam formation (Costa and Schuster 1988; Clague and Evans 1994; Korup et al. 2010). These potentially dangerous natural phenomena occur mostly in seismically-active regions where high orographic precipitations on rugged mountain terrain associated with frequent earthquakes and snowmelt contribute to several geological processes that lead to mass wasting and river-damming landslides (Korup and Tweed 2007; Allen et al. 2011; Evans et al. 2011; Crosta et al. 2013). Failure of landslide dams could trigger the sudden release of stored water masses from lakes created by these damming events. This consequently produces catastrophic outburst floods and debris flows that inundate the downstream areas, causing loss of lives and infrastructural damage (O'Connor and Costa 2004; Bonnard 2011; Plaza et al. 2011). For example, the worst

recorded case of landslide dam disaster occurred during the 1786 Kangding-Luding earthquake in Sichuan Province, southwest China (Dai et al. 2005). The earthquake triggered a huge landslide which dammed the Dadu River but failed ten days later and generated a catastrophic outburst flood that drowned more than 100,000 people. Similarly, Chai et al. (2000) presented a comprehensive account of the catastrophic failure of three landslide dams (Dahaizi, Xiaohaizi, and Deixi), triggered by the August 1933, Ms 7.5 earthquake in Diexi town, Sichuan Province, China. These landslide dams failed two months later, triggering catastrophic outburst floods that traveled more than 250 km downstream, and claimed about 2,423 lives. Therefore, timely evaluation of landslide dams is important for prevention of catastrophic dam failures and mitigation of disasters caused by downstream flooding of the released water masses.

Seepage erosion is one of the undermining factors affecting the stability and long-term performance of landslide dams and embankment dams. Many civil engineering and geoenvironmental studies have defined subsurface erosion processes by several terms such as piping, heave or blowout, seepage erosion, tunneling or jugging, internal erosion and sapping or spring sapping (Zaslavsky and Kassiff 1965; Jones 1981; Higgins 1982, 1984; Hutchinson 1982; Hagerty 1991; Wörman 1993; Terzaghi et al. 1996). However, a few researchers have made clear distinctions between the different processes involved in soil destabilization caused by seepage and piping (Jones 1981; Bryan and Yair 1982; Dunne 1990). The role of seepage in increasing positive pore-water pressure and causing apparent reduction of matric suction $(u_a - u_w)$ in unsaturated soils has been documented in the literature (Fredlund et al. 1978; Lam et al. 1987; Fredlund et al. 2012). Generally, landslide dams, stream banks and soil slopes are composed of unconsolidated materials which exist in unsaturated conditions. The stability of landslide dams in unsaturated conditions depends on the

presence of matric suction which increases the shear strength of the soil τ, as described in the equation proposed by Fredlund et al. (1978):

$$\tau = c' + (\sigma_n - u_a)\tan\phi' + (u_a - u_w)\tan\phi^b$$

(5.1)

where c' = effective cohesion of the soil, $(\sigma_n - u_a)$ = net normal stress on the failure plane, ϕ' = effective friction angle with respect to the net normal stress, $(u_a - u_w)$ = matric suction, ϕ^b = angle indicating increase in shear strength relative to matric suction. Transient changes from unsaturated to saturated conditions under steady-state seepage initiate high hydraulic gradients that accentuate subsequent reduction of apparent cohesion of the soil. This, in turn, increases seepage forces that accelerate soil mobilization, exfiltration and downstream entrainment of the eroded soil particles, as described by the equation:

$$F_s = \gamma_w i$$

(5.2)

where F_s = seepage force per unit volume, i = hydraulic gradient, γ_w = unit weight of water. Detailed research on seepage erosion processes in unsaturated soils and the effects of pore-water pressure on the stability of soil slopes have been carried out by Hutchinson (1982), Iverson and Major (1986), Howard and McLane (1988), Fredlund (1995), Skempton and Brogan (1994), Crosta and Prisco (1999), Rinaldi and Casagli (1999), Dapporto et al. (2001), Lobkovsky et al. (2004), Wilson et al. (2007), Fox et al. (2007), Cancienne et al. (2008), Pagano et al. (2010).

The concept of hydraulic criteria for assessing the likelihood of initiation of internal erosion in soils is based on the hydraulic load acting on a soil particle which must exceed the drag forces of the seeping water. This is related to the critical hydraulic gradient i_c, defined as the hydraulic gradient at which the effective stress of the soil

becomes negligible. Apparently, a large number of theoretical and experimental approaches have been used to obtain critical hydraulic gradients in embankment dams, levees, dykes and other water-retaining structures. For example, Terzaghi (1943) obtained i_c value of 1 for upward directed seepage flow as described by the following equation:

$$i_c = \frac{\gamma'}{\gamma_w}$$

(5.3)

where γ' = submerged unit weight of soil, and γ_w = unit weight of water. However, Skempton and Brogan (1994) observed selective erosion of fines in internally unstable cohesionless soils for upward flow conditions at critical hydraulic gradients ($i_c = 0.2\sim0.34$) lower than that obtained from Terzaghi's classical approach. Similarly, Den Adel et al. (1988) carried out tests for horizontal seepage flow and obtained critical hydraulic gradient values of 0.16 to 0.17 and 0.7 for unstable and stable soils, respectively. Ahlinhan and Achmus (2010) performed experiments with unstable soils for upward and horizontal seepage flows and obtained critical hydraulic gradient values of 0.18 to 0.23. Ke and Takahashi (2012) obtained critical hydraulic gradients of 0.21 to 0.25 for internal erosion with binary mixtures of silica sands under one-dimensional upward seepage flow.

Whilst a lot of research has been done on critical hydraulic gradients for internal erosion, problems still exist in defining and ascribing limit values of hydraulic gradients for seepage erosion. For instance, Samani and Willardson (1981) proposed the hydraulic failure gradient i_f, defined as the hydraulic gradient at which the shear strength of a confined soil is reduced by the drag forces of the seeping water. Wan and Fell (2004) introduced i_{start} and i_{boil} to represent critical hydraulic gradients for the onset of internal erosion and boiling, respectively. However, the conventional

one-dimensional upward seepage tests can only be used to determine the hydraulic criteria for seepage erosion in granular materials with the exclusion of other factors such as dam geometry (dam height, dam crest width, upstream and downstream slope angles), and rate of inflow into the upstream reservoir. Hence, elaborate evaluation of the influence of these geometrical and hydraulic factors on seepage processes in landslide dams would require carrying out flume experiments where the characteristic deformation behaviour of the dam models would allow for accurate determination of the limit values of these hydraulic parameters.

5.2 Brief review of seepage erosion in soils

Comprehensive research on seepage erosion mechanisms in landslide dams (Meyer et al. 1994; Davies and McSaveney 2006), levees and earth embankments (Richards and Reddy 2007), hillslopes (Ghiassian and Ghareh 2008), and stream banks (Fox and Wilson 2010), have all been completed. Variations in experimental results and opinions are strictly based on the design and method of experiment adopted, coupled with size and scale effects arising from the nature of material tested.

Seepage erosion involves the detachment and entrainment of finer soil particles through a porous medium under a hydraulic gradient caused by the seeping water. The various processes involved in seepage erosion mechanisms in hillslopes and landslide dams have been identified. For example, sapping, as defined by Hagerty (1991) involves exfiltration over a broad area on a sloping surface such that large lenticular cavities appear as a result of concentrated seepage which removes soil particles at the exit point and increases the diameter of the evolving channel over time. Iverson and Major (1986) derived a generalized analytical method for the evaluation of seepage forces considering static liquefaction and Coulomb failure under steady uniform seepage in any direction within a hillslope. They observed that slope destabilization occurred as a result of seepage force vector, which represents a

body force that corresponds to the hydraulic gradient potential. They concluded that slope stability will invariably occur when the direction of the seepage flow is such that $\lambda = 90° - \phi$, whereas the existence of a vertically upward seepage component results in Coulomb failure at similar conditions required for static liquefaction. Howard (1988) used flume experiments and numerical simulations to evaluate sapping processes and sapping zone morphology in homogeneous, isotropic sand mixtures. His experiments identified three distinct zones at the sapping face: mass wasting zone, sapping zone and fluvial transport zone, whereas numerical simulations performed by Howard and McLane (1988) revealed that the rate of mass wasting at the sapping face is dependent on the rate of sediment transport through the fluvial transport zone.

Perzlmaier et al. (2007) presented an overview of empirically-derived critical hydraulic gradients for initiation of backward erosion in a range of soil types based on field experience in several dams and levees (Table 5.1). Richards and Reddy (2010) evaluated piping potential in earth structures using a modified triaxial system, referred to as the true triaxial piping test apparatus (TTPTA). This apparatus was designed for controlling confining stresses and determining critical hydraulic gradients and critical velocities required for initiation of internal erosion. Their tests found that the critical hydraulic gradient and the critical seepage velocity for internal erosion in uniform fine-grained quartz sand varied from 1.8×10^{-3} to 2.4×10^{-3} and 8.1×10^{-3} to 1.1×10^{-2} m/s, respectively. They concluded that the critical seepage velocity is an essential parameter for evaluation of piping potentials in non-cohesive soils. Moffat et al. (2011) used a rigid wall permeameter to study internal erosion susceptibility in widely graded cohesionless soils by imposing a unidirectional flow in either upward or downward directions such that a constant average hydraulic gradient was maintained across the specimen. They found that suffusion occurred by 'episodic migration' of the finer fraction when the imposed

average hydraulic gradient was increased. Chang and Zhang ([2012]) determined the critical hydraulic gradients for internal erosion under complex stress states using a computer-controlled triaxial testing apparatus which allowed for independent control of hydraulic gradient and stress states. They found that under isotropic stress states, the initiation hydraulic gradient i_{start} increased with an increase in effective mean stress. They further observed that under the same confining stress, the initiation gradients obtained under compression stress states were higher than those obtained under extension stress states. These findings may have cleared up some of the ambiguities associated with critical hydraulic gradients determined under one-dimensional seepage tests as noted by Fell and Fry ([2013]), due to the inability of the conventional method to monitor stress states of soils.

However, despite the wealth of research done so far, not much has been reported on the influence of geometrical and hydraulic conditions for seepage erosion development in landslide dams. This paper presents a comprehensive experimental programme conducted to investigate transient pore-water pressure variations and the critical hydraulic gradients for seepage-induced failure of landslide dams. A series of experiments were conducted in a flume tank modified to accurately determine the limit values of hydraulic gradients at the various stages of the dam failure process. This is in contrast to the conventional one-dimensional upward directed seepage tests performed in a modified triaxial chamber. The main objectives of this research are summarized as follows: (1) to determine the critical hydraulic gradients required for initiation i_{ini} and failure i_f of landslide dams under different geometrical and hydraulic conditions, as well as the critical seepage velocities for erosion and debris flow mobilization; (2) to investigate the effects of pore-water pressure during seepage processes and its role in initiating seepage erosion and dam failure; and (3) to identify the various failure mechanisms of landslide dams under steady-state seepage.

Table 5.1: Comparison of empirically-derived critical average gradients i_c for initiation of backward erosion and piping in different soil types (Perzlmaier et al. 2007)

	Soil type				
	Gravel	Coarse sand	Medium sand	Fine sand	Source
Chugaev	0.25	0.25	0.15	0.12	Chugaev (1962)
Chugaev reduced	0.25	0.25	0.11	0.10	Chugaev (1962)
Bligh	0.11	0.083	-	0.067	Bligh (1910)
Lane	0.095	0.067	0.056	0.048	Lane (1935)
Muller-Kirchenbauer, lower limit	-	0.12	0.08	0.06	Müller-Kirchenbauer et al. (1993)
Muller-Kirchenbauer, upper limit	-	0.17	0.10	0.08	Müller-Kirchenbauer et al. (1993)
Weijers & Sellmeijer, C_u = 1.5	0.28	0.18	0.16	0.09	Weijers & Sellmeijer (1993)
Weijers & Sellmeijer, C_u = 3	0.34	0.28	0.24	0.14	Weijers & Sellmeijer (1993)

5.3 Experimental methods

5.3.1 Testing facility

The experiments were conducted in a rectangular flume tank 2 m long, 0.45 m wide and 0.45 m high. The flume tank was made of 5 mm-thick acrylic sheets (plexiglass) of high transparency which enables visual observation of wetting front propagation, deformation and failure mechanism of the dam models. The flume was tilted to make a bed slope of $\psi = 5°$. The downstream end of the flume was equipped with two 4 cm-diameter holes for outflow of fluidized sediments. The water entering the upstream reservoir was provided by a rubber hose attached to a water tap while discharge into the upstream reservoir was controlled by a flowmeter connected to the drainage hose. The generation and dissipation of pore-water pressures during the experiments were monitored with three pore-water pressure sensors, hereafter referred to as *p1, p2,* and *p3,* with rated capacity of 50 kPa each (Figure 5.1a). The sensors were fixed underneath the center of the flume bed through three 10 mm-diameter holes drilled on a horizontal line at the center of the flume bed. The sensors were separated by horizontal distances of 0.1 m and 0.103 m, respectively. Each of the pore-water pressure sensors was equipped with an L-shaped manometer attached to the outer wall of the flume to ensure an equal balance between the fluid pressure and atmospheric pressure. Transient variation in upstream reservoir level was monitored with a water level probe positioned near the toe of the upstream slope. Deformations and settlements caused by seepage and pore-water pressure buildup were monitored with two 0.1 m-range CMOS multi-function analog laser displacement sensors attached to a wooden overboard (Figure 5.1b). The two sensors, hereafter referred to as H_{d1} and H_{d2}, were separated by a distance of 0.04 m.

5.3.2 Soil characteristics

A series of experiments were conducted using different soils and testing conditions. Table 5.2 shows a summary of all the experiments conducted under different testing conditions while the results of the critical pore-water pressures and critical seepage velocities obtained from the tests are summarized in Table 5.3. Uniform commercial silica sand no. 8 was used to build the dam models, except in *Exp 1* to *3* where the dam models were composed of different proportions of silica sand nos. 5 and 8, including industrial pebbles and gravel, hereafter referred to as sandfill dam (*SD*), gravelly dam I (*GV-I*), and gravelly dam II (*GV-II*), respectively. The grain size distribution curves of all the materials used are shown in Figure 5.2. The mechanical and hydraulic characteristics of the materials used in the experiments are summarized in Table 5.4. Silica sand nos. 5 and 8 are generally composed of subangular to angular grains with dry repose angles of 32° and 35°, respectively. Constant-head permeability tests and other soil property tests were carried out on the soils based on the physical conditions (bulk density and antecedent moisture content) used in building the dam models in accordance with standards of the Japanese Geotechnical Society (JGS).
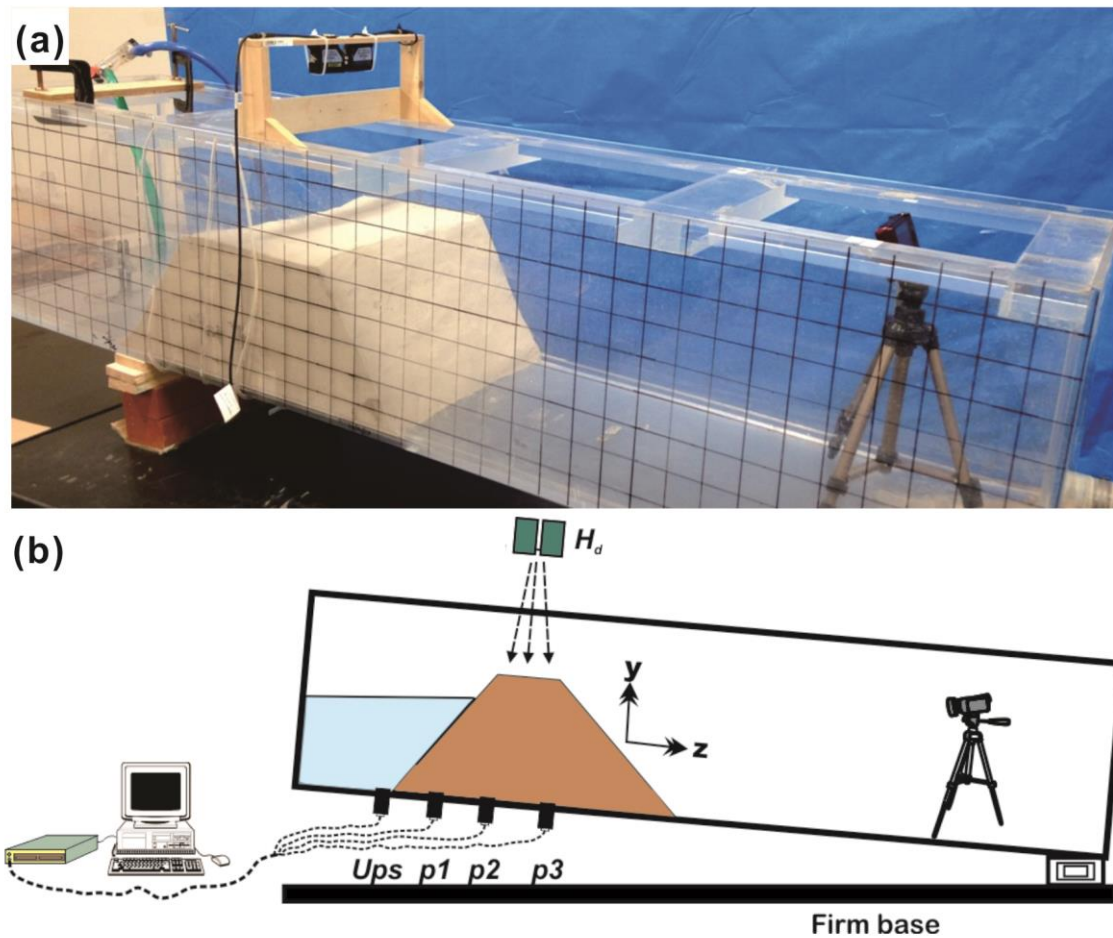
Figure 5.1 (**a**) Side view of the flume tank before the commencement of an experiment (**b**) Experimental setup. *Hd* Laser displacement sensors *Ups* Upstream water level probe *p1*, *p2*, and *p3* Pore-water pressure sensors.

5.3.3 Landslide dam model Ccnstruction and eperimental pocedure

Landslide dam models of different geometries were built approximately 0.4 m downslope from the upstream water inlet (Figure 5.3a). Effort was made in building the dam models so as to simulate naturally existing landslide dam prototypes.

Table 5.2: Summary of all the experiments at different testing conditions

Test specification	Test no.	H_d (m)	D_{crw} (m)	α (deg)	β (deg)	Q_{in} (m³/s)	ρ_{dry} (Mg/m³)	e_o	i_{ini-1}	i_{ini-2}	i_{f1}	i_{f2}	T_b (s)
				Dam geometry									
Dam composition	Exp 1	0.25	0.1	40	55	2×10^{-4}	1.10	1.41	0.119	0.101	0.77	0.61	340
	Exp 2	0.25	0.1	40	55	2×10^{-4}	1.56	0.71	0.092	0.123	1.82	0.87	920
	Exp 3	0.25	0.1	40	55	2×10^{-4}	1.44	0.84	0.053	0.101	1.48	1.20	1360
Rate of inflow into the upstream reservoir (filling rate)	Exp 4	0.25	0.1	35	50	1.67×10^{-5}	1.07	1.48	0.097	0.099	1.38	0.90	1750
	Exp 5	0.25	0.1	35	50	5×10^{-5}	1.07	1.48	0.122	0.089	1.50	0.94	1300
	Exp 6	0.25	0.1	35	50	1×10^{-4}	1.07	1.48	0.115	0.067	1.48	0.99	1100
	Exp 7	0.25	0.1	35	50	1.67×10^{-4}	1.07	1.48	0.103	0.08	1.36	1.32	890
Antecedent moisture content at low compactive effort ($e_o = 1.76$)	Exp 8	0.25	0.1	35	55	1.5×10^{-4}	0.96	1.76	0.118	0.08	1.70	0.92	800
	Exp 9	0.25	0.1	35	55	1.5×10^{-4}	0.96	1.76	0.094	0.084	1.59	0.94	720
	Exp 10	0.25	0.1	35	55	1.5×10^{-4}	0.96	1.76	0.104	0.085	1.57	1.00	680
	Exp 11	0.25	0.1	35	55	1.5×10^{-4}	0.96	1.76	0.103	0.053	1.40	1.07	620
Antecedent moisture content at high compactive effort ($e_o = 1.21$)	Exp 12	0.25	0.1	35	55	1.3×10^{-4}	1.20	1.21	0.087	0.133	1.17	0.64	980
	Exp 13	0.25	0.1	35	55	1.3×10^{-4}	1.20	1.21	0.147	0.123	1.22	0.70	840
	Exp 14	0.25	0.1	35	55	1.3×10^{-4}	1.20	1.21	0.093	0.125	1.28	0.95	760
	Exp 15	0.25	0.1	35	55	1.3×10^{-4}	1.20	1.21	0.042	0.103	1.30	1.00	740
Downstream slope angle	Exp 16	0.25	0.15	35	30	1×10^{-4}	1.01	1.62	0.123	0.091	1.01	0.73	2300
	Exp 17	0.25	0.15	35	40	1×10^{-4}	1.01	1.58	0.091	0.099	1.03	0.74	1500
	Exp 18	0.25	0.15	35	50	1×10^{-4}	1.01	1.52	0.128	0.053	1.39	0.61	1150
	Exp 19	0.25	0.15	35	60	1×10^{-4}	1.01	1.48	0.099	0.092	1.37	0.58	900
Dam height	Exp 20	0.15	0.15	40	50	1.2×10^{-4}	1.10	1.41	0.111	0.063	1.17	0.55	890
	Exp 21	0.20	0.15	40	50	1.2×10^{-4}	1.10	1.41	0.045	0.133	1.30	0.79	1020
	Exp 22	0.25	0.15	40	50	1.2×10^{-4}	1.10	1.41	0.103	0.043	1.33	0.82	1080

Dam crest width	Exp 23	0.30	0.15	40	50	1.2×10^{-4}	1.10	1.41	0.116	0.071	1.35	0.85	1280
	Exp 24	0.25	0.20	35	55	1.67×10^{-4}	1.14	1.32	0.086	0.083	1.60	0.86	1380
	Exp 25	0.25	0.25	35	55	1.67×10^{-4}	1.14	1.32	0.118	0.081	1.78	0.89	2600

H_d = dam height; D_{crw} = dam crest width; α = upstream slope angle; β = downstream slope angle; Q_{in} = inflow rate into the upstream reservoir; ρ_{dry} = dry bulk density; e_o = initial void ratio; i_{ini-1} = critical hydraulic gradient for seepage erosion initiation (between sensors p_1 and p_2); i_{ini-2} = critical hydraulic gradient for seepage erosion initiation (between sensors p_2 and p_3); i_{f1} = critical hydraulic gradient for collapse of the dam crest (between sensors p_1 and p_2); i_{f2} = critical hydraulic gradient for collapse of the dam crest (between sensors p_2 and p_3); T_b = time of collapse of the dam crest

Table 5.3: Summary of results of critical pore-water pressures and critical seepage velocities obtained from the tests

Test specification	Test no.	Q_{in} (m³/s)	p_{crit-1} (kPa)	p_{crit-2} (kPa)	p_{crit-3} (kPa)	V_{crit-1} (m/s)	V_{crit-2} (m/s)	Characteristic failure mechanism
Dam composition	Exp 1	2×10^{-4}	1.30	1.24	1.08	7.10×10^{-6}	5.68×10^{-6}	Type I
	Exp 2	2×10^{-4}	1.64	1.49	1.38	1.14×10^{-6}	5.39×10^{-7}	Type II
	Exp 3	2×10^{-4}	1.45	1.35	1.34	1.49×10^{-6}	1.21×10^{-6}	Transitional: Type II to Type I
Rate of inflow into the upstream reservoir (filling rate)	Exp 4	1.67×10^{-5}	1.47	1.35	0.98	1.05×10^{-6}	7.39×10^{-7}	Type I
	Exp 5	5×10^{-5}	1.65	1.18	0.96	1.14×10^{-6}	7.15×10^{-7}	Type I
	Exp 6	1×10^{-4}	1.68	1.20	1.01	1.18×10^{-6}	7.85×10^{-7}	Type II
	Exp 7	1.67×10^{-4}	1.52	1.50	1.19	1.07×10^{-6}	1.01×10^{-6}	Type II
Antecedent moisture content at low compactive effort ($e_o = 1.76$)	Exp 8	1.5×10^{-4}	1.50	1.06	1.03	1.37×10^{-6}	7.60×10^{-7}	Type II
	Exp 9	1.5×10^{-4}	1.39	1.11	1.01	1.44×10^{-6}	8.49×10^{-7}	Type I
	Exp 10	1.5×10^{-4}	1.49	1.10	0.87	1.59×10^{-6}	1.02×10^{-6}	Type I
	Exp 11	1.5×10^{-4}	1.43	1.12	0.83	1.30×10^{-6}	9.52×10^{-7}	Type I
Antecedent moisture	Exp 12	1.3×10^{-4}	1.41	1.20	1.15	1.29×10^{-6}	7.60×10^{-7}	Type II

		Q_{in}	p_{crit-1}	p_{crit-2}	p_{crit-3}	V_{crit-1}	V_{crit-2}	Type
content at high compactive effort ($e_o = 1.21$)	Exp 13	1.3×10^{-4}	1.40	1.19	1.02	1.28×10^{-6}	7.50×10^{-7}	Type II
	Exp 14	1.3×10^{-4}	1.38	1.22	0.99	1.08×10^{-6}	8.50×10^{-7}	Type II
	Exp 15	1.3×10^{-4}	1.40	1.20	0.96	1.03×10^{-6}	7.98×10^{-7}	Type II
Downstream slope angle	Exp 16	1×10^{-4}	1.52	1.32	1.29	9.50×10^{-7}	6.75×10^{-7}	Type II
	Exp 17	1×10^{-4}	1.40	1.20	1.08	9.35×10^{-7}	6.64×10^{-7}	Type II
	Exp 18	1×10^{-4}	1.44	1.06	0.83	1.30×10^{-6}	4.60×10^{-7}	Type I
	Exp 19	1×10^{-4}	1.50	1.03	0.99	1.28×10^{-6}	5.30×10^{-7}	Type I
Dam height	Exp 20	1.2×10^{-4}	1.13	0.78	0.98	1.24×10^{-6}	5.99×10^{-7}	Type I
	Exp 21	1.2×10^{-4}	1.48	1.21	1.22	1.38×10^{-6}	8.40×10^{-7}	Type II
	Exp 22	1.2×10^{-4}	1.60	1.40	1.29	1.40×10^{-6}	8.90×10^{-7}	Type II
	Exp 23	1.2×10^{-4}	1.72	1.37	1.01	1.43×10^{-6}	9.10×10^{-7}	Type II
Dam crest width	Exp 24	1.67×10^{-4}	1.70	1.40	1.10	1.53×10^{-6}	8.20×10^{-7}	Type I
	Exp 25	1.67×10^{-4}	2.01	1.68	1.48	1.69×10^{-6}	8.55×10^{-7}	Type I

Q_{in} = inflow rate into the upstream reservoir; p_{crit-1} = critical pore-water pressure for collapse of the dam crest at $p1$; p_{crit-2} = critical pore-water pressure for collapse of the dam crest at $p2$; p_{crit-3} = critical pore-water pressure for collapse of the dam crest at $p3$; V_{crit-1} = critical seepage velocity (between sensors $p1$ and $p2$); V_{crit-2} = critical seepage velocity (between sensors $p2$ and $p3$)

Table 5.4: Mechanical and hydraulic characteristics of the materials used in the experiments

Sample name	Test no.	Sediment mixture (%)	D_{50} (mm)	C_u	C_c	Gravel (%)	Sand (%)	Fines (%)	K (m/s)
Sandfill dam (SD)	Exp 1	Silica sand 5 (100)	0.799	2.474	1.385	-	99.5	0.5	5.5×10^{-4}
Gravelly dam I (GV-I)	Exp 2	Silica sand 8-gravel mix (40:60)	0.284	79.870	0.069	34	49.6	16.4	3.8×10^{-5}
Gravelly dam II (GV-II)	Exp 3	Silica sand 8-pebbles-gravel mix (30:30:40)	0.201	3.520	1.047	22.6	62.9	14.5	6.0×10^{-5}
Silica sand no. 8	Exp 4~25	Silica sand 8 (100)	0.124	1.726	1.195	-	67.1	32.9	5.8×10^{-5}

D_{50} = median grain size; C_u = coefficient of uniformity; C_c = coefficient of curvature; K = coefficient of permeability
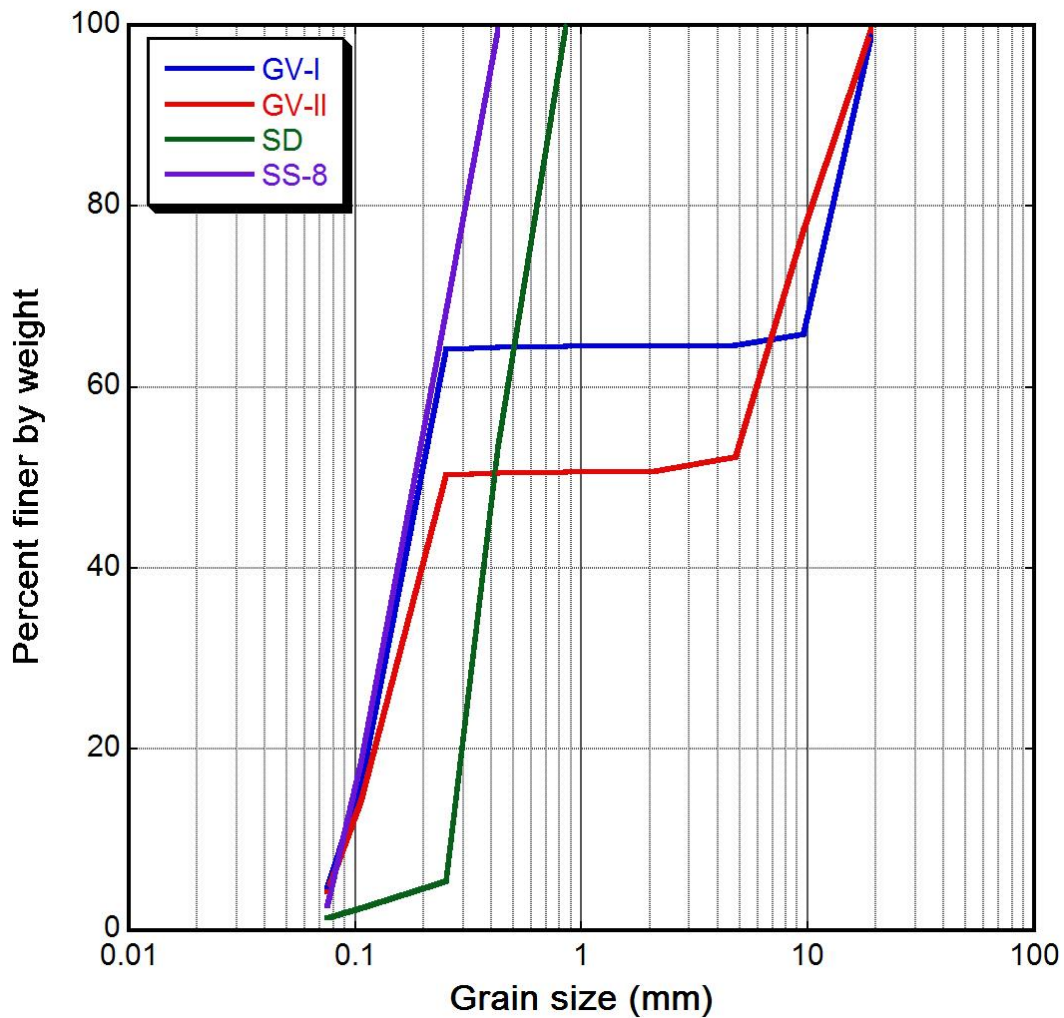
Figure 5.2 Grain size distribution curves of the dam materials. *GV-I* Gravelly dam I, *GV-II* Gravelly dam II, *SD* Sandfill dam, *SS-8* Silica sand no. 8.

Mechanically mixed soils were placed in the flume tank in equal lifts using the moist tamping method. Initially, oven-dried soils were mixed with a known volume of water and then compacted to obtain the desired moisture content and bulk density. All the experiments were conducted with an antecedent moisture content of 5%, except in *Exp 8* to *15* where the antecedent moisture content was varied from 5% to 20%. The geometrical characteristics of the dam models are shown in Figure 5.3b.

The dam height H_d and the dam crest width D_{crw} were varied from 0.15 m to 0.3 m and 0.1 m to 0.25 m, respectively. The angles α and β representing the upstream and downstream slope angles were varied from 35° to 40° and 30° to 60°, respectively.

Seven different series of experiments, all summing up to 27 runs of tests, were carried out, each with intent to assess transient pore-water pressure variations and the critical hydraulic gradients for seepage erosion initiation and dam failure under steady-state seepage. The main experiments were conducted after carrying out a series of initial tests which were mostly done to check sensor reliability, result validation, test repeatability and selection of appropriate mixtures of materials. However, the results of experiments conducted on dams built with dam crest width D_{crw} of 0.1 m and 0.15 m are excluded in this paper due to some challenges posed by the monitoring sensors. The initial conditions set for all the tests assumed that the upstream reservoir was empty. Filling of the upstream reservoir was carried out with a rubber hose attached to a water tap, and connected to a manually-operated flowmeter. A steady-state seepage through the dam models was achieved by ensuring that the upstream reservoir level remained constant at approximately two-thirds of the dam height. Real-time data was acquired by connecting all the sensors to a standard high-speed monitoring and recording workstation comprised of two synchronized universal recorders (*PCD-330B-F*) and a computer. Sampling frequency was set at 50 Hz for all the tests.

At the beginning of each experiment, discharge into the upstream reservoir was set at the desired value using a manually-operated flowmeter. The discharge was maintained until the upstream reservoir level equaled two-thirds of the dam height. Afterward, an equilibrium hydraulic head was established by ensuring that the upstream reservoir level remained constant prior to the collapse of the dam crest. The change from unsaturated to saturated state began during the filling of the upstream reservoir. Consequently, loss of matric suction due to positive pore-water

pressure buildup under steady-state seepage, as observed from sensor *p3* (Figure 5.4), marked the onset of static liquefaction and exfiltration of water from the downstream toe, which further led to debris flow mobilization and dam failure.
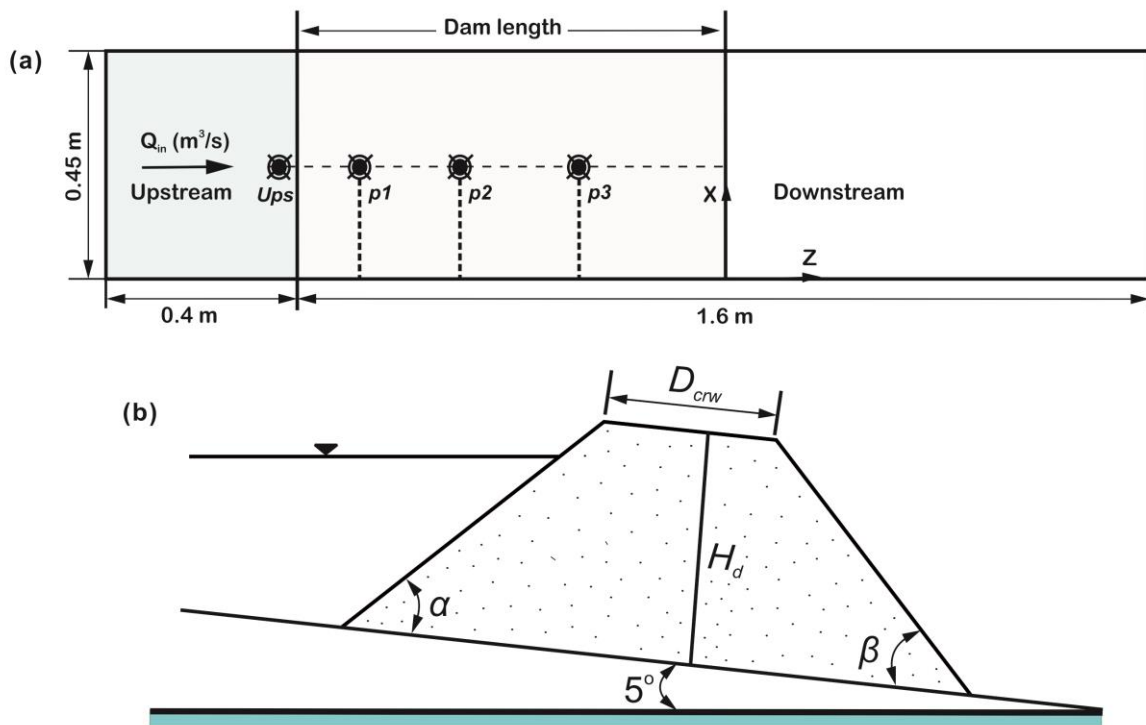
Figure 5.3 (**a**) Plan view of the flume tank indicating the position of the dam model and monitoring sensors (**b**) Schematic diagram of the dam geometry (not to scale).

5.4 Determination of critical hydraulic gradients

Variations in hydraulic gradients (i_1 and i_2) through the dam models were determined from pore-water pressure values obtained from the experiments. Darcy (1856) in Fredlund et al. (2012) postulated that the rate of water flow through a soil mass was equal to the hydraulic gradient, as described by the equation:

$$v_w = -k_w \frac{\partial h_w}{\partial z} \tag{5.4}$$

where v_w = flow rate of water (m³/s), k_w = coefficient of permeability with respect to the water phase (m/s), $\partial h_w/\partial z$ = hydraulic gradient in the z-direction. Hydraulic heads, h_1, h_2, and h_3 at three different locations within the dam models were computed from pore-water pressure values using the following equation (Figure 5.4):

$$h = \frac{u_w}{\gamma_w \cos^2 \psi} \tag{5.5}$$

where u_w = pore-water pressure (kPa), γ_w = unit weight of water (kN/m³), ψ = flume bed slope angle (degree). Therefore, hydraulic gradient i_1 between sensors $p1$ and $p2$ was determined as described by the equation below:

$$i_1 \approx \frac{-[(h_2 + h_{02}) - (h_1 + h_{01})]}{L_1 / \cos \psi} \tag{5.6}$$

Similarly, the hydraulic gradient, i_2 between sensors $p2$ and $p3$ was determined as follows:

$$i_2 \approx \frac{-[(h_3 + h_{03}) - (h_2 + h_{02})]}{L_2 / \cos \psi} \tag{5.7}$$

where h_{01}, h_{02} and h_{03} represent corresponding vertical distances between the flat firm base and the slope bed, whereas L_1 and L_2 are horizontal distances between $p1$ and $p2$, and $p2$ and $p3$, respectively. Two limit values of hydraulic gradients, corresponding to the onset of initiation of seepage erosion i_{ini} and collapse of the dam crest i_f, were determined based on results obtained from the initial tests.
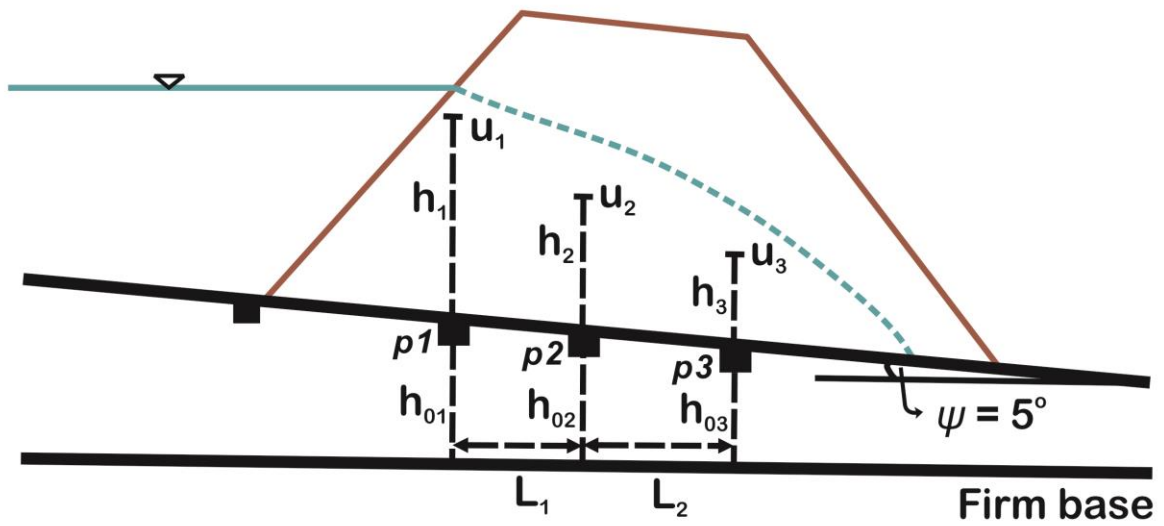
Figure 5.4 Schematic diagram for the determination of hydraulic gradients.

CHAPTER 6

RESULTS OF CRITICAL HYDRAULIC GRADIENTS FOR SEEPAGE-INDUCED FAILURE OF LANDSLIDE DAMS

6.1 General Description of the Experiments

Two characteristic types of dam failure (*Type I* and *Type II*) were observed during the experiments and were found to depend on the geometry and hydromechanical characteristics of the dam materials. These were further subdivided into several interrelated failure processes which included wetting front propagation, downstream slope saturation, exfiltration, sapping/seepage-face erosion, toe bifurcation, undermining and progressive sloughing of the downstream face, and late-stage overtopping.

Type I involves failures which could be related to static liquefaction of the soil mass under steady-state seepage that reduced the apparent cohesion of the soil and led to debris flow mobilization. This type of failure was primarily initiated by sapping erosion which occurred as a result of steady exfiltration of water at the downstream toe; which by extension, triggered gradual undercutting and debuttressing of the downstream slope as the mobilized mass 'flowed' downstream, thus lowering the dam height (Figure 6.1a). Dam failure occurred by overtopping as the upstream reservoir level reached the tip of the partially saturated dam material, eroding the entire crest to form a wide breach channel. This type of failure was characteristic of experiments conducted with low upstream inflow rates, low compactive effort

$(e_o = 1.76)$, high downstream slope angle $(\beta \geq 40°)$, and dam crest width greater than 0.15 m.

Type II involves failures triggered by downslope propagation of the wetting front and subsequent mobilization of the fluidized material at the upper part of the downstream face. This failure mechanism was characterized by downstream toe bifurcation and abrupt collapse of a large flank of the slope due to intense saturation which originated from the dam crest and progressed towards the downstream toe (Figure 6.1b). Dam failure occurred by the formation of a hydraulic crack aligned perpendicular to the downstream face due to the reduction of the effective stress of the soil. This type of failure occurred mostly in dams of low downstream slope angle $(\beta \leq 40°)$, high shear strength of the soil relative to the shear stress of the seeping water, and high compactive effort $(e_o = 1.21)$.

6.2 Influence of Dam Composition

Three types of materials (*SD, GV-I,* and *GV-II*) were used to investigate transient changes in pore-water pressures and variations in hydraulic gradients under steady-state seepage through the dam models (*Exp 1~3*; Table 5.2 and 5.3). The dam models were built to obtain initial void ratios of 1.41, 0.71 and 0.84 for *SD, GV-I,* and *GV-II* materials, respectively. The resulting trends of pore-water pressures within the dam models indicate gross anisotropy and heterogeneity in dams composed of *GV-I* and *GV-II*, whereas the low critical pore-water pressures obtained in the dam built with homogeneous *SD* material demonstrates the liquefaction potential of cohesionless and isotropic sands (Figure 6.2). The failure mechanism of the *SD* dam was basically characteristic of the *Type I* failure pattern. Enlargement of the sapping zone was characterized by occasional mass failures which were enhanced by a decrease in the effective stress of the soil as the energy of the exfiltrating water increased. In contrast, *GV-I* material showed *Type II* failure mechanism, whereas the failure

mechanism of *GV-II* material evolved from *Type II* to *Type I* (Figure 6.3). Critical pore-water pressure values (p_{crit-1}) determined at *p1*, which correspond to the onset of failure of the dams were 1.30 kPa, 1.64 kPa and 1.45 kPa for *SD, GV-I,* and *GV-II,* respectively. The observed trends of pore-water pressures within the dams were found to be inversely proportional to the initial void ratio e_o (Table 5.3), and directly proportional to the coefficient of uniformity C_u of the dam materials (Table 5.4). This could be potentially caused by capillary rise within the materials which depends on the grain size distribution and bulk density of the constituent soil mass that, in itself, affected the porosity of the soil. Thus, the stability and deformation characteristics of the dams increased as the grain size distribution changed from poorly to well graded. Similarly, the critical hydraulic gradients for seepage erosion initiation i_{ini}, increased with a decrease in pore size, while the critical hydraulic gradient for collapse of the dam crest i_f, was influenced by the grain size distribution. The effect of grain size distribution on the development of seepage in the dams was evidenced by the variations in seepage velocity as the dynamics of the seeping water changed from laminar flow to turbulent flow (Table 5.3). The fact that the longevity of the dam built with *GV-II* material (v_{crit-2}, 1.21×10^{-6} m/s) was higher than those built with *SD* and *GV-I* materials (v_{crit-2}, 5.68×10^{-6} m/s and 5.39×10^{-6} m/s, respectively) demonstrates that other physical parameters such as particle density, hydraulic conductivity and gravel content affect seepage development in landslide dams and soil slopes (Kokusho and Fujikura 2008).
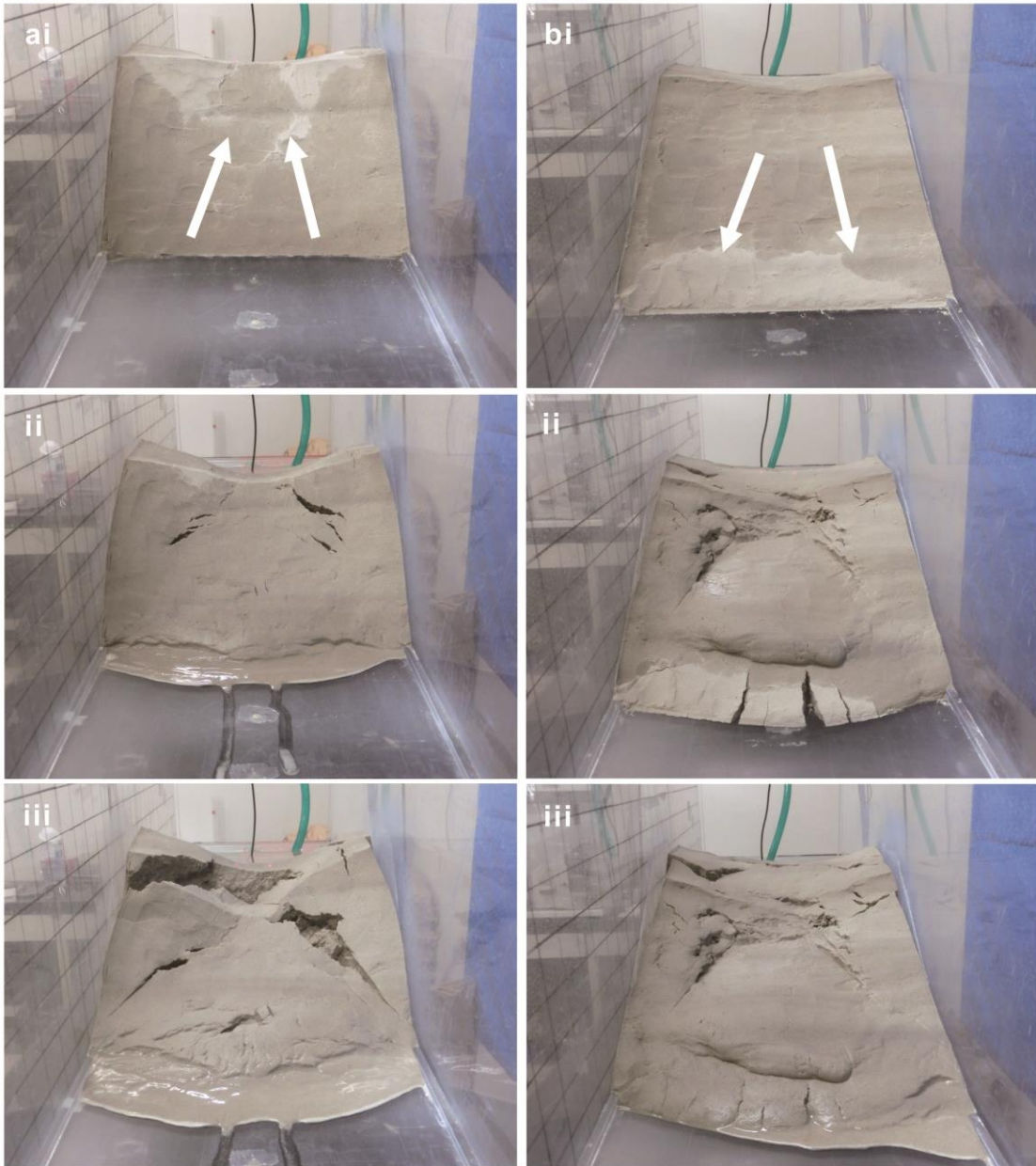
Figure 6.1 Typical failure mechanisms of the dams showing **(a)** *Type I* - Upslope propagation of wetting front, exfiltration, sapping and sloughing of the fluidized soil mass **(b)** *Type II* - Downslope propagation of wetting front, bifurcation, and undermining of the slope toe.
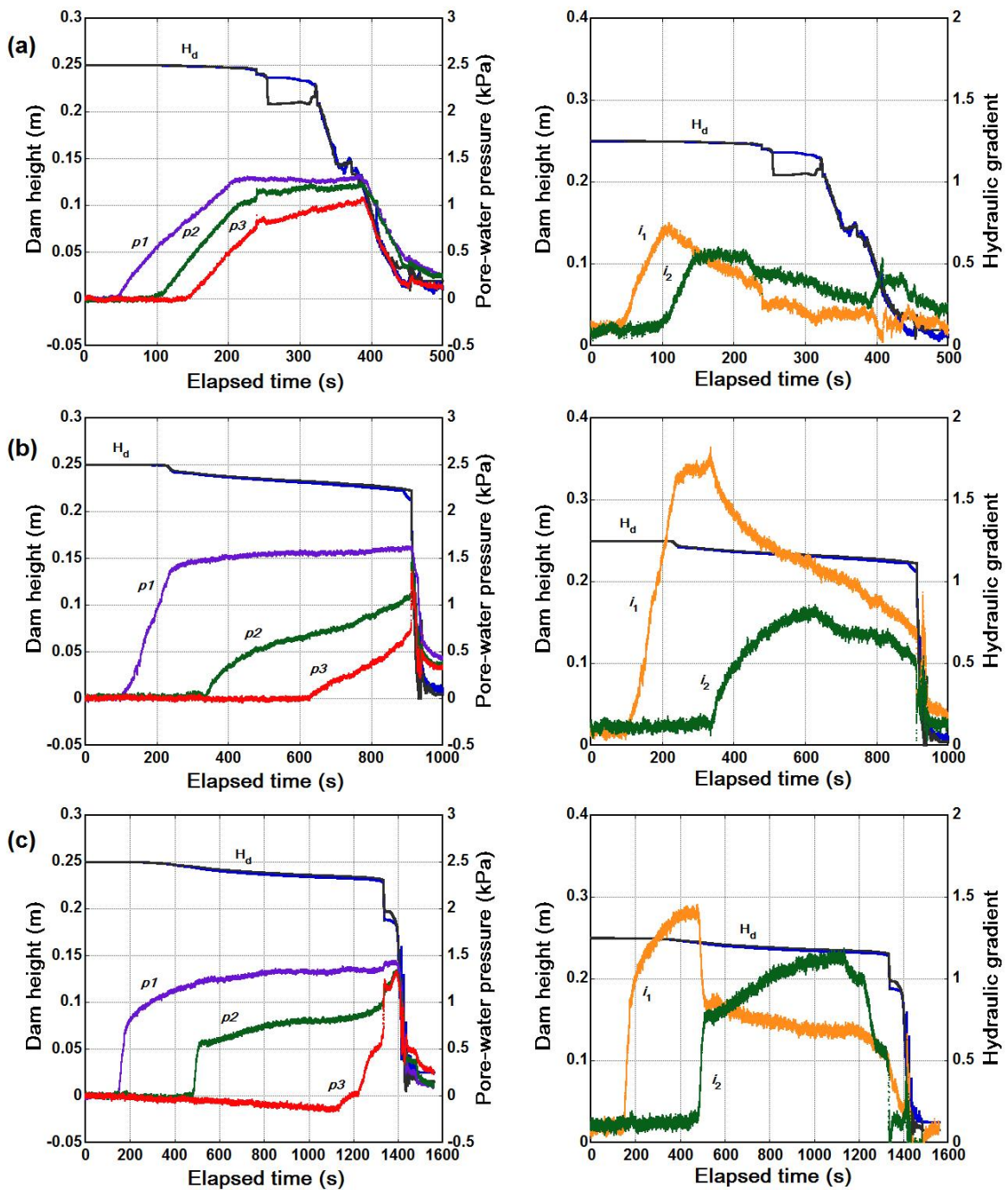
Figure 6.2 Time-dependent transient changes in pore-water pressures and trends of hydraulic gradients in dams built with (**a**) *Sandfill dam* (**b**) *Gravelly dam I* and (**c**) *Gravelly dam II*.

Figure 6.3 Photographic sequence of seepage-induced failure of dams built with **(a)** *Gravelly dam I* and **(b)** *Gravelly dam II.*

6.3 Rate of Inflow into the Upstream Reservoir

Exp 4-7 were conducted to evaluate the influence of inflow rate Q_{in} into the upstream reservoir. The dam models were built with uniform geometrical and physical characteristics (Table 5.2). Figure 6.4 shows the variations in pore-water pressures through the dams at steady-state inflow rates of 1.67×10^{-5} m³/s, 5×10^{-5} m³/s, 1×10^{-4} m³/s, and 1.67×10^{-4} m³/s. The filling rate of the upstream reservoir initiated seepage processes that changed the dynamics of the pore-water pressures. The critical hydraulic gradients for initiation of seepage erosion (i_{ini-1} and i_{ini-2}) varied from 0.067 to 0.122. A low p_{crit-1} value of 1.52 kPa was determined in the experiment conducted with Q_{in} of 1.67×10^{-4} m³/s, relative to Q_{in} of 5×10^{-5} m³/s ($p_{crit-1} = 1.65$ kPa) and 1×10^{-4} m³/s ($p_{crit-1} = 1.68$ kPa) (Table 5.3). This was caused by a rapid increase in the hydraulic head which initiated high seepage gradients that reduced the effective stress of the soil, leading to differential settlement, hydraulic cracking, and lowering of the dam crest. Thus, the rate of reduction of the shear strength of the soil due to a decrease in matric suction depends on the rate of inflow into the upstream reservoir Q_{in} and the rate of propagation of the wetting front. Trends of hydraulic gradients through the dams indicate that i_{f1} decreased with an increase in Q_{in}, whereas i_{f2} increased with an increase in Q_{in}, suggesting a corresponding increase in seepage velocity between sensors *p1* and *p2* (Table 5.2; Figure 6.5). Critical seepage velocities determined from the tests show that v_{crit-2} increased from 7.39×10^{-7} m/s for Q_{in} of 1.67×10^{-5} m³/s to 1.01×10^{-6} m/s for Q_{in} of 1.67×10^{-4} m³/s. Exfiltration, sapping and undercutting of the downstream toe, characteristic of *Type I* failure mechanism, occurred at low inflow rates as a result of low seepage processes that led to liquefaction and collapse of the dam crest (*Exp 4* and 5). In contrast, hydraulic cracking, downstream face saturation, and toe bifurcation characteristic of *Type II* failure mechanism, occurred in experiments conducted with high inflow rates (*Exp 6*

and 7; Figure 6.6). The experimental results demonstrate that the stability and time of collapse of the dam crest T_b decreased with an increase in inflow rate into the upstream reservoir. This was evidenced by the characteristic failure mechanism of the dam models which evolved from *Type I* to *Type II* with a corresponding increase in Q_{in} (Table 5.3).
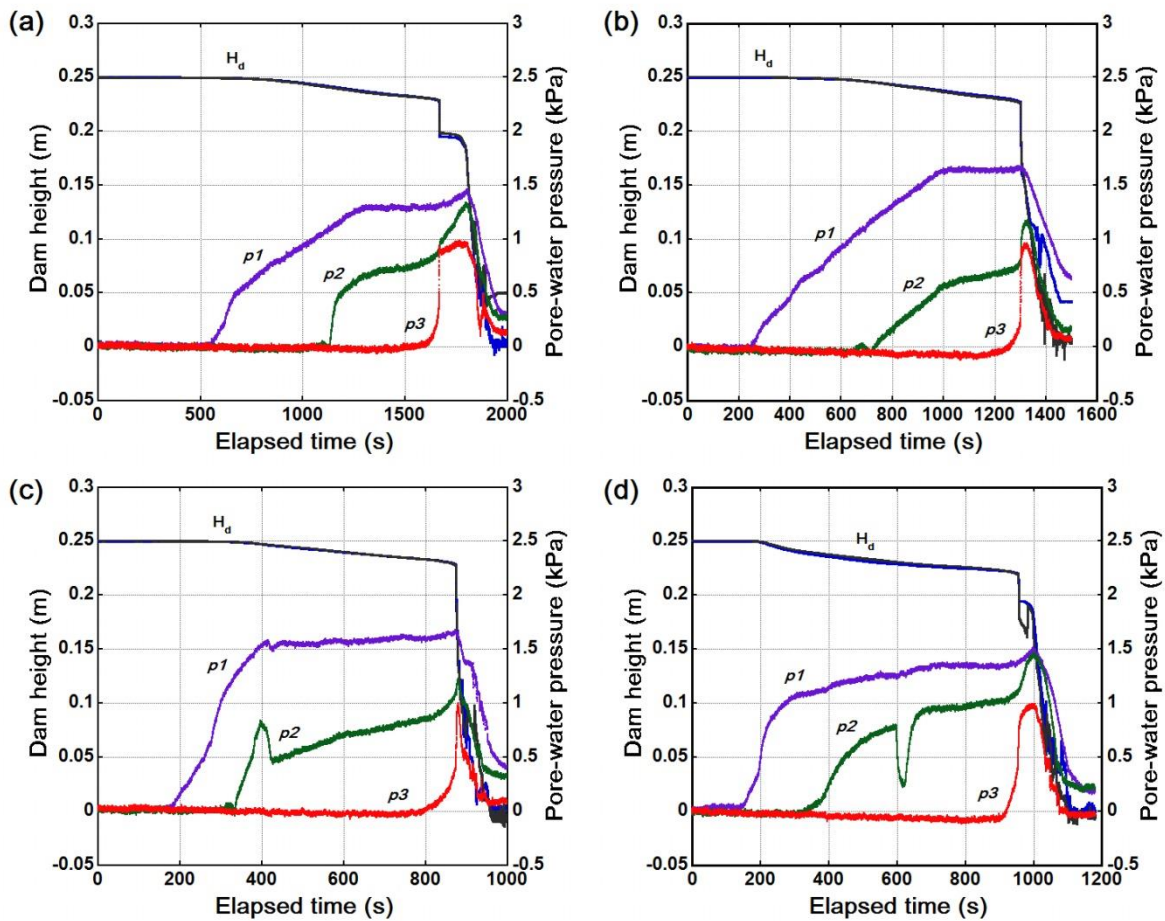
Figure 6.4 Transient variations in pore-water pressures in experiments conducted with upstream inflow rates of (**a**) 1.67×10^{-5} m³/s (**b**) 5×10^{-5} m³/s (**c**) 1×10^{-4} m³/s (**d**) 1.67×10^{-4} m³/s.
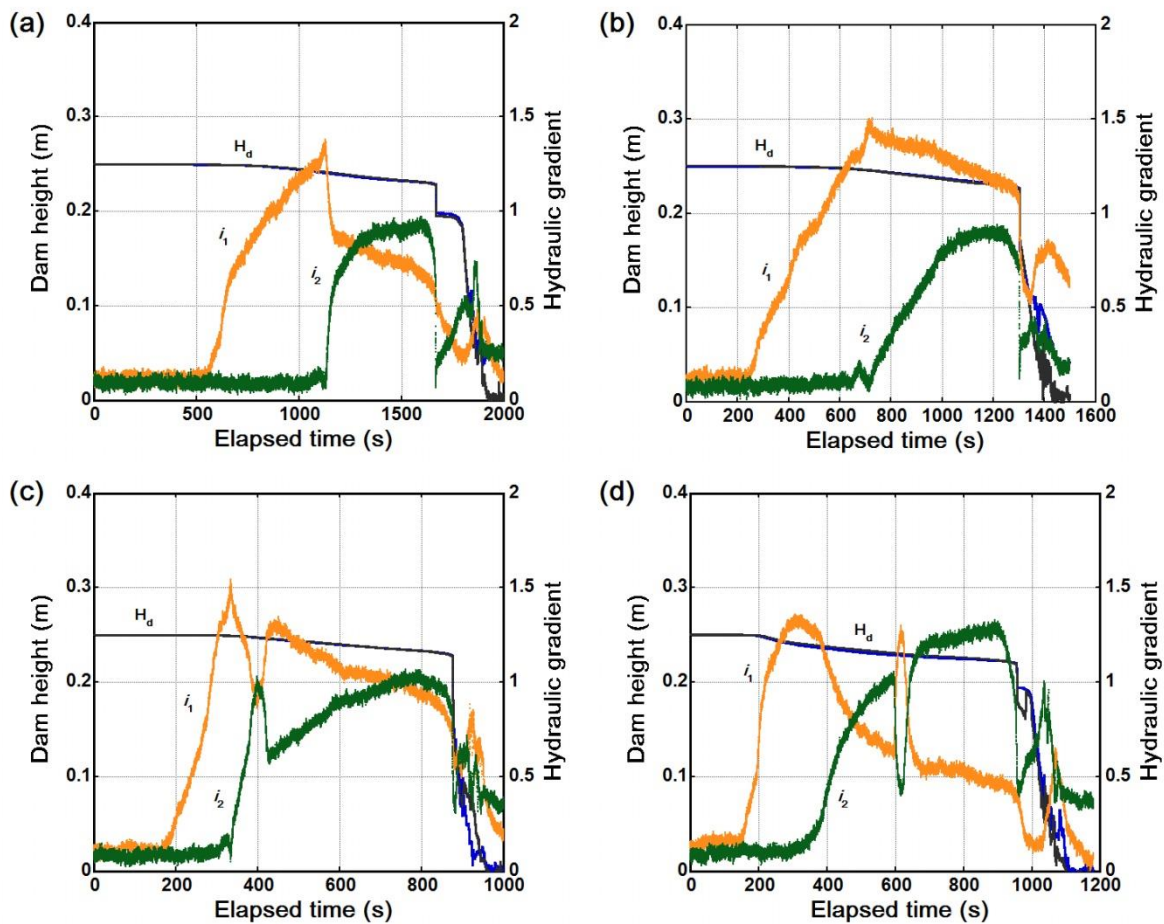
Figure 6.5 Transient changes in hydraulic gradients in experiments conducted with upstream inflow rates of **(a)** 1.67×10^{-5} m³/s **(b)** 5×10^{-5} m³/s **(c)** 1×10^{-4} m³/s **(d)** 1.67×10^{-4} m³/s.

6.4 Influence of material condition

Soil wetting is a major cause of shear strength reduction and volume change in unsaturated soils and also a common occurring factor in collapsible soils and expansive soils. *Exp 8-11* were conducted to assess the influence of antecedent moisture content *w* on the deformation behaviour of landslide dams under steady-state seepage. Antecedent moisture contents of the soils were increased by 5% during soil preparation and dam model construction.
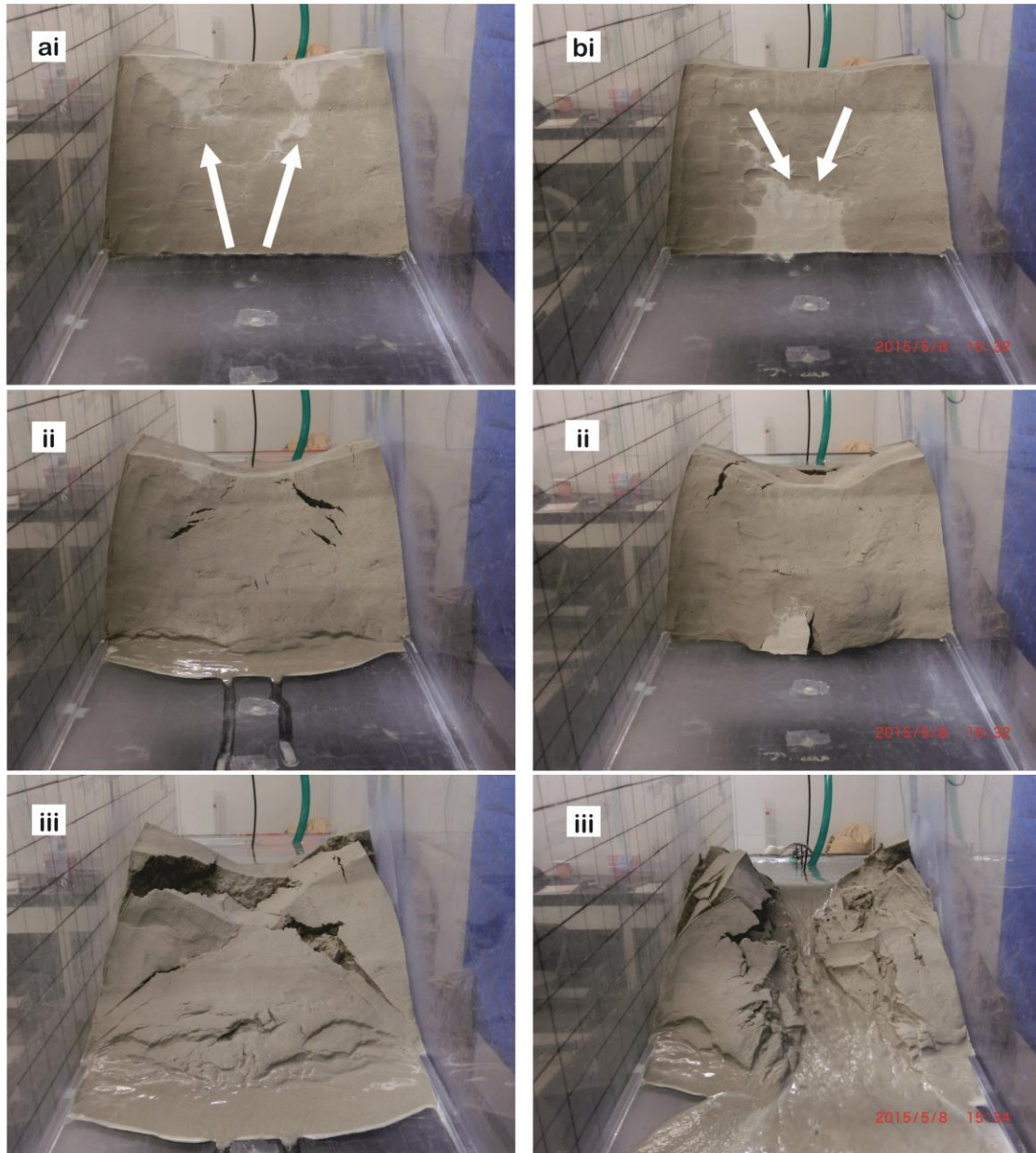
Figure 6.6 Photographic sequence of the typical failure mechanism of experiments conducted with upstream inflow rates of **(a)** 1.67×10^{-5} m³/s and **(b)** 1.67×10^{-4} m³/s.

Figure 6.7 shows the resulting trends of hydraulic gradients through the dams. A linear relationship was observed between the antecedent moisture content and the rate of deformation and collapse of the dam models (Fredlund 1999). It is noteworthy to mention that the critical hydraulic gradients (i_{f1} and i_{f2}) coincided with the onset of dam deformation and crest settlement. Measured critical hydraulic gradients for seepage erosion initiation varied from 0.053 to 0.118, while the critical hydraulic gradient for failure of the dams increased with an increase in antecedent moisture content. Similarly, the reduction of capillary forces due to an increase in soil moisture content caused the critical seepage velocity to decrease from 1.31×10^{-6} m/s for $w = 5\%$ to 9.52×10^{-7} m/s for $w = 20\%$. The failure mechanism of the dams evolved from *Type II* to *Type I* as antecedent moisture content increased through the dams. The rate of exfiltration and sapping erosion at the downstream toe increased from low saturated soils to high saturated soils. This was attributed to the reduction of matric suction caused by wetting resulting in high void ratios that accentuated the abrupt collapse of the dams.

Figure 6.8 shows trends of hydraulic gradients and the failure mechanism of dam models built with the same antecedent moisture contents (5%, 10%, 15% and 20%), but packed at a higher compactive effort, $e_o = 1.21$ (*Exp 12-15*). The characteristic trends displayed by the hydraulic gradients, as well as the low critical seepage velocities determined from the experiments indicate, that the initial void ratio e_o of the soil affected the failure mechanism of the dams. It may be important to note that i_{f1} and i_{f2} increased with an increase in antecedent moisture content, thus suggesting that the dynamics of the seeping water were mainly characteristic of a laminar flow. The stability of the dam models increased as antecedent moisture content decreased from 20% to 5%, as observed from T_b and p_{crit-3}, and thus indicates the effect of pore-water pressures in reducing the effective stress of the soil (Table 5.2 and 5.3). This effect can be related to the influence of matric suction on

the liquefaction potential and shear strength reduction in partially saturated soils (Simon and Collison 2001; Okamura and Soga 2006).
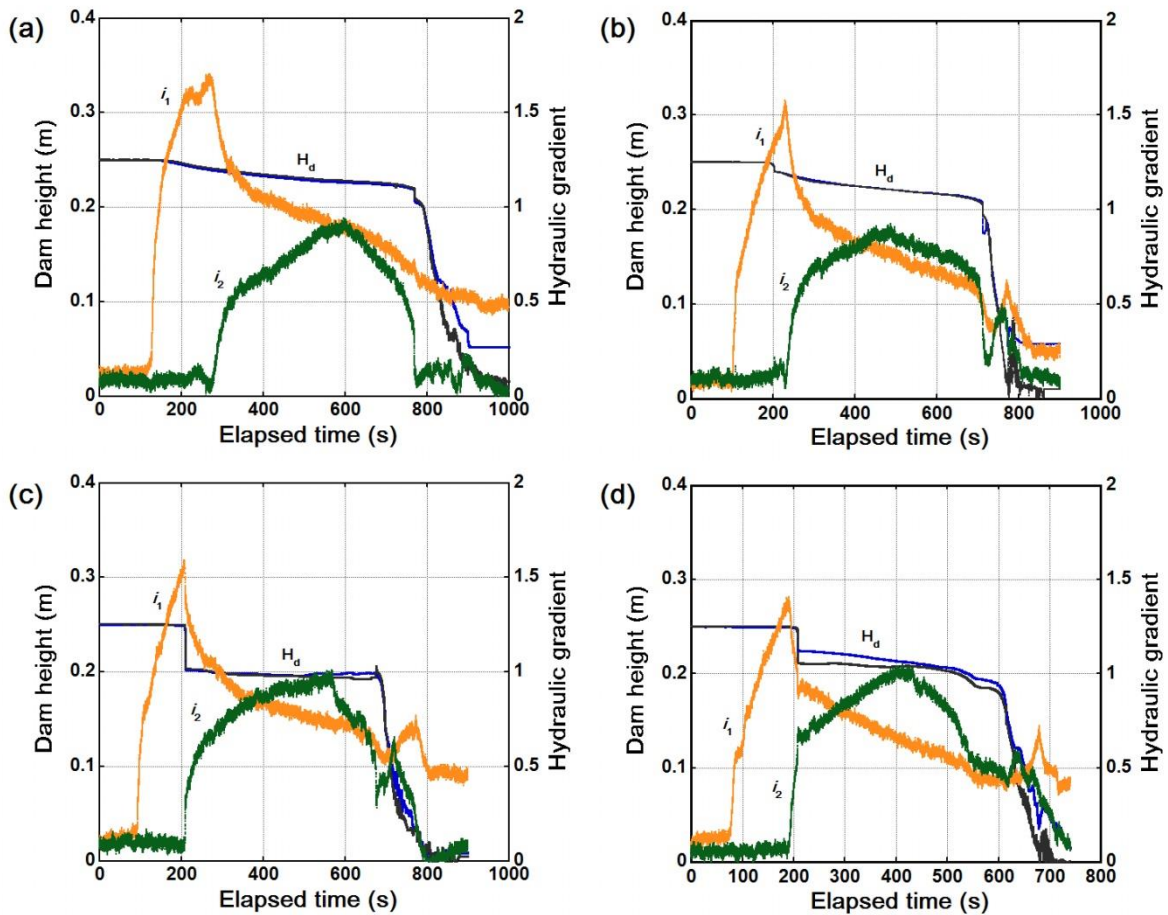
Figure 6.7 Trends of hydraulic gradients in dams built with an e_o of 1.76 and antecedent moisture contents of **(a)** 5% **(b)** 10% **(c)** 15% **(d)** 20%.

Comparison between *Exp 8~11* and *Exp 12~15* shows that the deformation and collapse mechanism of the dam models were more pronounced in dams with an e_o of 1.76 (*Exp 8~11*) than in those with an e_o of 1.21 (*Exp 12~15*) (Figures 6.9 and 6.10). Similarly, a comparison between the critical hydraulic gradients measurements in *Exp 8~11* and *Exp 12~15* shows that the critical hydraulic gradients decreased with a

decrease in initial void ratio. The observed trends of wetting front propagation and the transient changes in pore-water pressures suggest that seepage flow through the dam materials were not essentially controlled by matric suction but by a hydraulic head gradient (Fredlund and Rahardjo 1993).
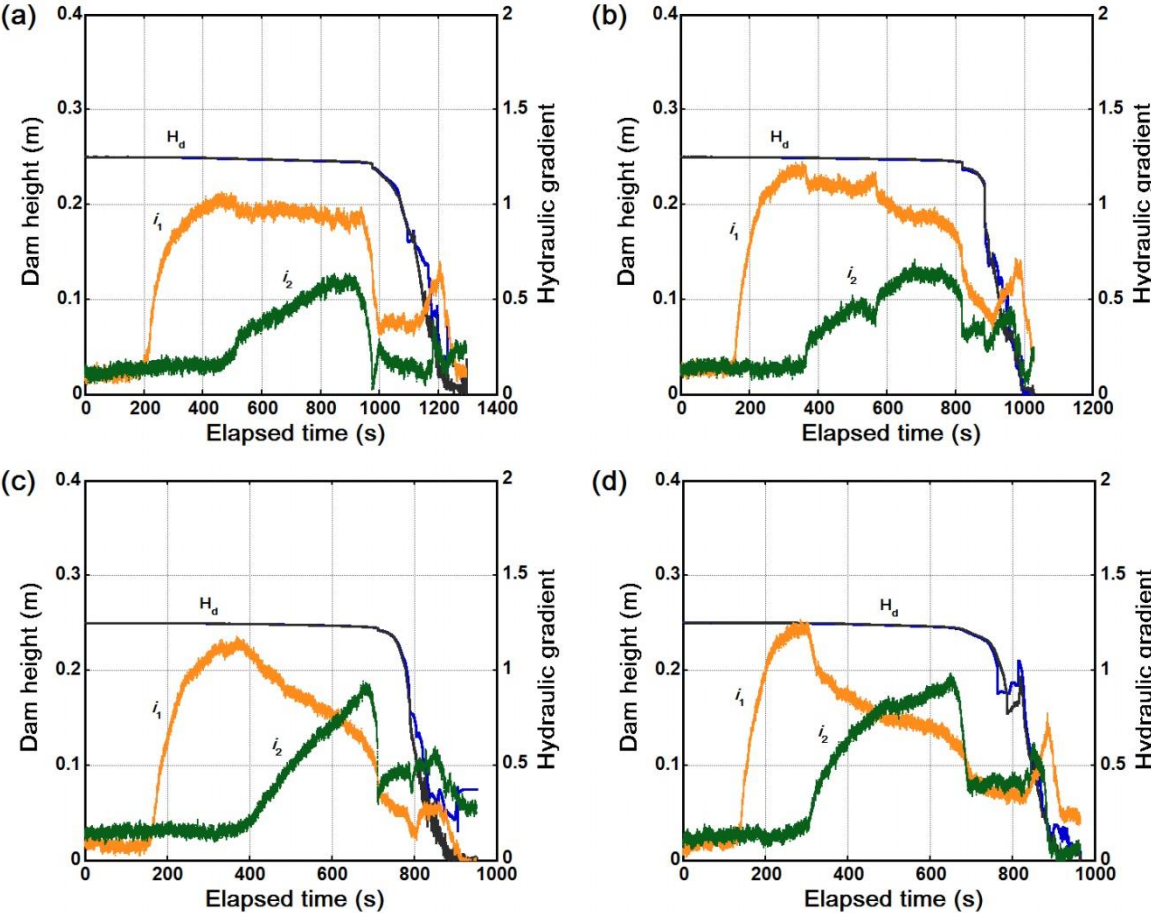
Figure 6.8 Trends of hydraulic gradients in dams built with an e_o of 1.21 and antecedent moisture contents of **(a)** 5% **(b)** 10% **(c)** 15% **(d)** 20%.
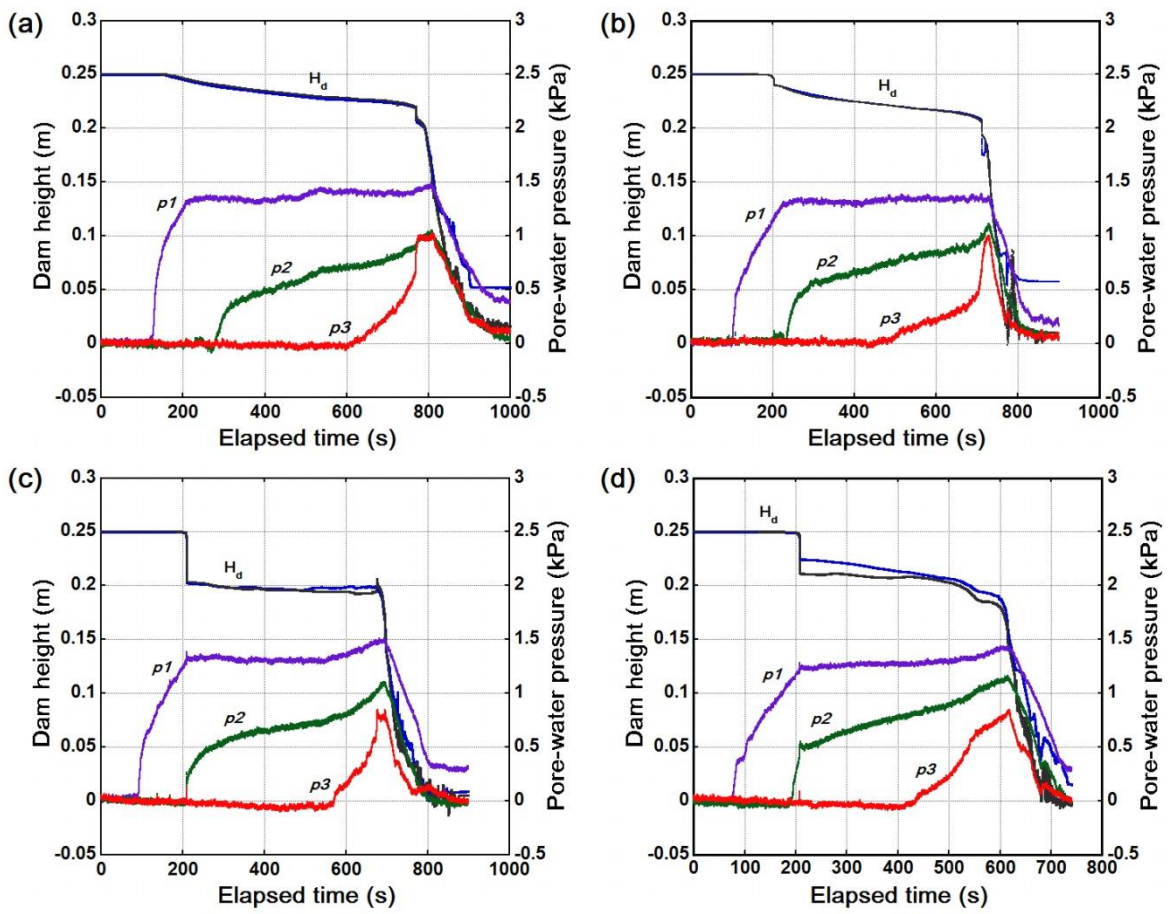
Figure 6.9 Evolution of pore-water pressures in dams built with an e_o of 1.76 and antecedent moisture contents of **(a)** 5% **(b)** 10% **(c)** 15% **(d)** 20%.
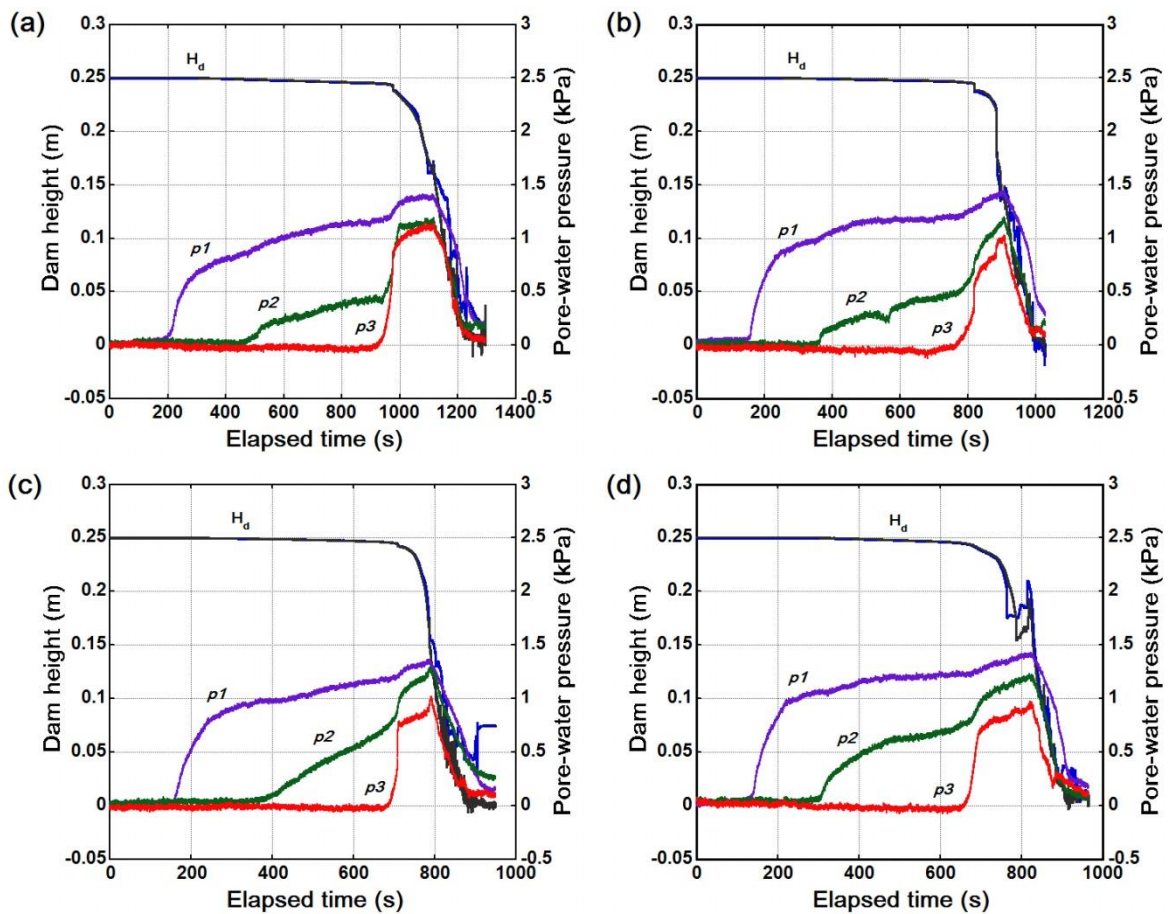
Figure 6.10 Evolution of pore-water pressures in dams built with an e_o of 1.21 and antecedent moisture contents of **(a)** 5% **(b)** 10% **(c)** 15% **(d)** 20%.

6.5 Influence of dam geometry

The geometry of landslide dams is one of the major factors contributing to seepage erosion and slope instability. The two major factors that control the critical hydraulic gradient for instability in soil slopes are the downstream slope angle β and the gradient of the soil layer ψ (Iverson and Major 1986; Budhu and Gobin 1996). Basically, the internal friction angle of a dry cohesionless soil, at zero external pressure, is equal to the maximum stable slope angle of the soil. However, the soil mass collapses to a lower slope angle if steady-state seepage occurs.

A series of experiments were conducted to evaluate the effects of downstream slope angle β on the critical hydraulic gradients for failure of landslide dams (*Exp 16-19*). The downstream slope angles were varied from 30° to 60°. A close examination of the results indicates that the stability of the dams increased as the downstream slope angle decreased from 60° to 30° (Table 5.2). The time of collapse of the dam crest increased from $\beta = 60°$ (T_b, 900 s) to $\beta = 30°$ (T_b, 2300 s). Similarly, i_{f1} increased with an increase in β, whereas i_{f2} decreased with an increase in β (Figure 6.11). Also, the critical seepage velocity decreased with an increase in β, indicating high failure potentials in dams of high downstream slope angles (Table 5.3). The variations in pore-water pressures and the failure mechanism of the dams are shown in Figure 6.12. The failure mechanism of the dams built with β in the range of 30° to 40° was initiated by bifurcation of the downstream toe (*Type II*), whereas exfiltration, sapping and undermining of the downstream toe were characteristic of dams built with β in the range of 41° to 60° (*Type I*). Budhu and Gobin (1996) remarked that for a soil which has ϕ of 30°, the exit hydraulic gradient at the slope face increases from 1 (when $\lambda = \beta$) to a limit value of $\sin \beta$ (when $\lambda = 90°$).

The influence of dam height on the stability and longevity of landslide dams under steady-state seepage was evaluated in dams built with different dam heights H_d, ranging from 0.15 m to 0.3 m (Table 5.2 and 5.3). The experiments were conducted at a constant upstream inflow rate of 1.2×10^{-4} m³/s (*Exp 20-23*). A positive correlation was observed between the critical hydraulic gradients for dam failure (i_{f1} and i_{f2}) and the dam height. The values of i_{f1} and i_{f2} increased from 1.17 and 0.55 for $H_d = 0.15$ m, to 1.35 and 0.85 for $H_d = 0.30$ m (Table 5.2; Figure 6.13). Critical pore-water pressure values correlating with the onset of failure of the dams increased from 1.13 kPa ($H_d = 0.15$ m) to 1.72 kPa ($H_d = 0.30$ m) (Figure 6.14). The results show that at constant α and β, the stability of the dams increased with a decrease in dam height H_d. This was further evidenced by the failure mechanism of the dams which evolved

from *Type I* for $H_d = 0.15$ m to *Type II* for $H_d = 0.30$ m. The results indicate that the height of landslide dams is an important parameter for assessing the stability of natural river blockages.

Exp 24-25 were conducted to evaluate the influence of dam crest width D_{crw} on the failure mechanism of landslide dams. A steady-state seepage was maintained at a constant upstream inflow of 1.67×10^{-4} m³/s. The results of transient variations in pore-water pressures and the corresponding trends of hydraulic gradients in the dams built with D_{crw} of 0.20 m and 0.25 m (*Exp 24* and *25*) are shown in Figure 6.15. The critical hydraulic gradients for seepage erosion initiation (i_{ini-1} and i_{ini-2}), varied from 0.081 to 0.118. Exfiltration, sapping and debuttressing of the downstream toe, characteristic of *Type I* failure pattern, were the major failure mechanisms of the dams (Figure 6.16). The rate of propagation of the wetting front through the dams was strongly influenced by D_{crw}/H_d. High D_{crw}/H_d resulted in high values of i_{f1}, i_{f2}, and v_{crit}. The continual propagation of wetting front through the dams resulted in a gradual reduction of the effective stress of the soil, and subsequent mobilization of the liquefied mass which travelled downstream with an initial speed of 1.2×10^{-5} m/s. The episodic occurrence of hydraulic cracks and undermining and sloughing of the fluidized slope mass continued until the dam breached by overtopping. The results demonstrate that at constant hydraulic and geometrical conditions (H_d, α and β), i_{f1} and i_{f2}, as well as $v_{crit,}$ increased with an increase in D_{crw}, indicating that the critical seepage velocity and the critical hydraulic gradient for seepage erosion in landslide dams are influenced by dam crest width D_{crw} and D_{crw}/H_d.

6.6 Discussion

Figure 6.17 shows the critical hydraulic gradients for collapse of the dam crest (i_{f1} and i_{f2}) measured between *p1* and *p2*, and *p2* and *p3* in the vertical axis plotted

against the inflow rate into the upstream lake in the horizontal axis for *Exp 4~7*. The result shows that i_{f1} decreases with an increase in Q_{in}, while i_{f2} increases with steady increase in Q_{in}. This seems to be largely attributable to the rate of propagation of wetting front through the dam that ultimately effects the generation of pore-water pressures and subsequent destabilization of the soil. Similarly, the relationships between i_{f1} and i_{f2} versus antecedent moisture content (w) for $e_o = 1.76$ clearly show the same hydraulic behaviour (Figure 6.18). This inadvertently indicates that the critical hydraulic gradients for failure of unsaturated or partially saturated cohesionless soils are by far higher than the critical hydraulic gradients for failure of saturated cohesionless soils. This condition has been related to the influence of matric suction (negative pore-water pressure) that tends to increase the stability of unsaturated or partially saturated soils. Figure 6.19 shows the relationships between i_{f1} and i_{f2} versus antecedent moisture content for $e_o = 1.21$. The trends of the plots show that both i_{f1} and i_{f2} increases with an increase in antecendent moisture content. This suggests that high hydraulic gradients are required to trigger instability in unsaturated or partially saturated landslide dams. Figures 6.20 and 6.21 shows the relationships between i_{f1} and i_{f2} in the vertical axis plotted against the downstream slope angle and the dam height in the horizontal axis. For the upstream slope angle, i_{f1} increases with an increase in β while i_{f2} decreases with steady increase in β. For the dam height, both i_{f1} and i_{f2} increases for a steady increase in H_d which indicates the effects of dam height on the stability of landslide dams.

6.7 Summary

An extensive experimental programme was carried out to investigate the effects of transient variations in pore-water pressures and the critical hydraulic gradients for seepage-induced failure of landslide dams using a flume tank specifically designed

for accurate determination of these hydraulic parameters. A steady-state seepage was maintained by ensuring that the upstream reservoir level remained constant prior to the collapse of the dam crest. Limit values of hydraulic gradients and seepage velocities were determined for different hydromechanical and geometrical conditions. Based on the experimental results, the following conclusions can be drawn:

1. Sapping was the most dominant mechanism of slope destabilization observed in all the experiments. Other significant interrelated failure processes of the dam models included wetting front propagation, downstream face saturation, exfiltration, hydraulic cracking, toe bifurcation, downstream slope undercutting, sloughing and late-stage overtopping.

2. Two characteristic types of failure, which depend on the geometrical and hydromechanical properties of the dams were observed: *Type I* and *Type II*. *Type I* commonly occurred in dams built with low compactive effort (e_o = 1.76), high downstream slope angle ($\beta \geq 40°$), crest width greater than 0.15 m, and moisture content lower than 15%. This type of failure was initiated by exfiltration, sapping, and upslope propagation of the wetting front towards the dry upper region of the dam crest. *Type I* failure mechanism shares similar characteristics to the three distinct zones of slope deformation triggered by sapping, which are: fluvial, sapping and undermining zones, as reported by Howard and McLane (1988). In contrast, *Type II* was found in dams of low downstream slope angle ($\beta \leq 40°$), dam height greater than 0.25 m, high upstream inflow rates and high compactive effort (e_o = 1.21). Failure in these dams was triggered by downslope propagation of the wetting front, bifurcation of the damp lowermost part of the downstream toe, sapping erosion and sloughing of the fluidized slope material.

3. The build-up of positive pore-water pressure under steady-state seepage and its effects on the apparent cohesion of the soil were evaluated for different upstream inflow rates and antecedent moisture contents. The results indicated that the stability and longevity of the dam models increased with a decrease in upstream inflow rate and antecedent moisture content. Thus, demonstrating the significance of pore geometry, particle density, gradation, and hydraulic conductivity of materials forming landslide dams in the development of seepage processes.

4. In all the experiments, the critical hydraulic gradients for seepage erosion initiation (i_{ini-1} and i_{ini-2}) ranged from 0.042 to 0.147. The critical hydraulic gradient for collapse of the dam crest i_f was strongly influenced by several factors, such as the initial void ratio (compactive effort), antecedent moisture content, particle density, grain size distribution, inflow rate into the upstream reservoir and the geometrical characteristics of the dams.

5. In the dams built with mixed materials, i_{f1} and i_{f2} increased with an increase in uniformity coefficient. The critical hydraulic gradient for collapse of the dam crest i_f increased with an increase in inflow rate into the upstream reservoir (filling rate). Similarly, i_{f1} and i_{f2} were controlled by the combined effects of antecedent moisture content and porosity of the soil. At low void ratios, i_{f1} decreased with an increase in antecedent moisture content, whereas i_{f2} increased as antecedent moisture content increased through the dams. However, at high void ratios, under the same antecedent moisture contents, i_{f1} and i_{f2} increased with an increase in antecedent moisture content, suggesting seepage flow dynamics typical of laminar flows.

6. Furthermore, both i_{f1} and i_{f2} increased with an increase in H_d and D_{crw}, whereas i_{f1} increased with an increase in β, and i_{f2} decreased as β increased.

This indicates that the critical hydraulic gradient for dam failure for near-horizontal flow ($\psi = 5°$), depends on β.

7. These experiments demonstrate that seepage mechanisms in landslide dams comprised of unsaturated homogeneous and isotropic cohesionless materials are influenced by the hydraulic properties of the materials, as well as the geometrical characteristics of the dams.

8. The textural characteristics of the materials used in these experiments are typical of landslide dams formed by rock avalanche processes where fragmentation and pulverization of the rock materials cause seepage processes to develop in the upper blocky carapace layer.

9. However, further research should be done considering a wide range of sediment sizes and the addition of commercially available kaolinite clay to evaluate the mechanism of shear strength reduction under steady-state seepage. It is believed that performing unsaturated seepage analysis and limit equilibrium analysis, with regards to the results and conditions set for these experiments, could give further insights on the critical conditions for stability of landslide dams under steady-state seepage.
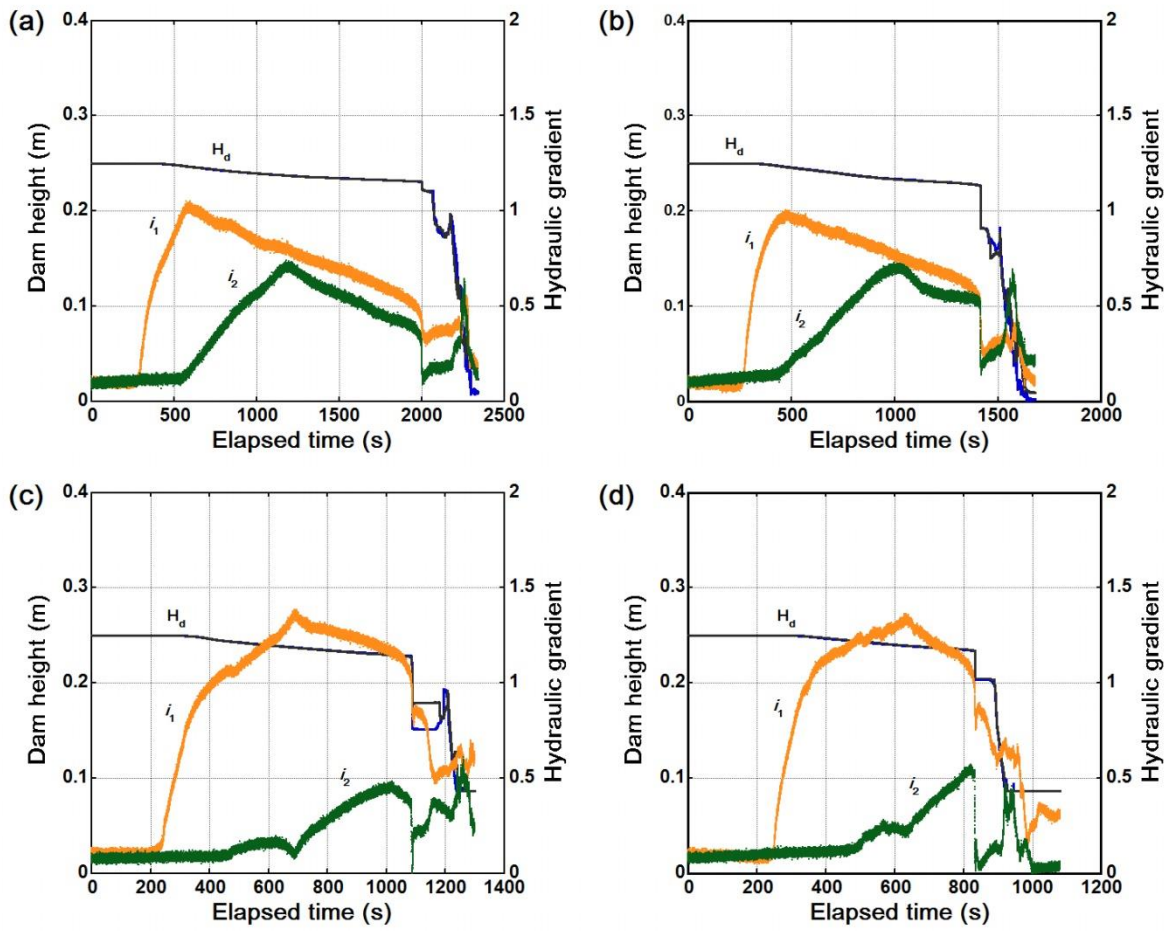
Figure 6.11 Trends of hydraulic gradients in dams built with downstream slope angles of **(a)** 30° **(b)** 40° **(c)** 50° **(d)** 60°.
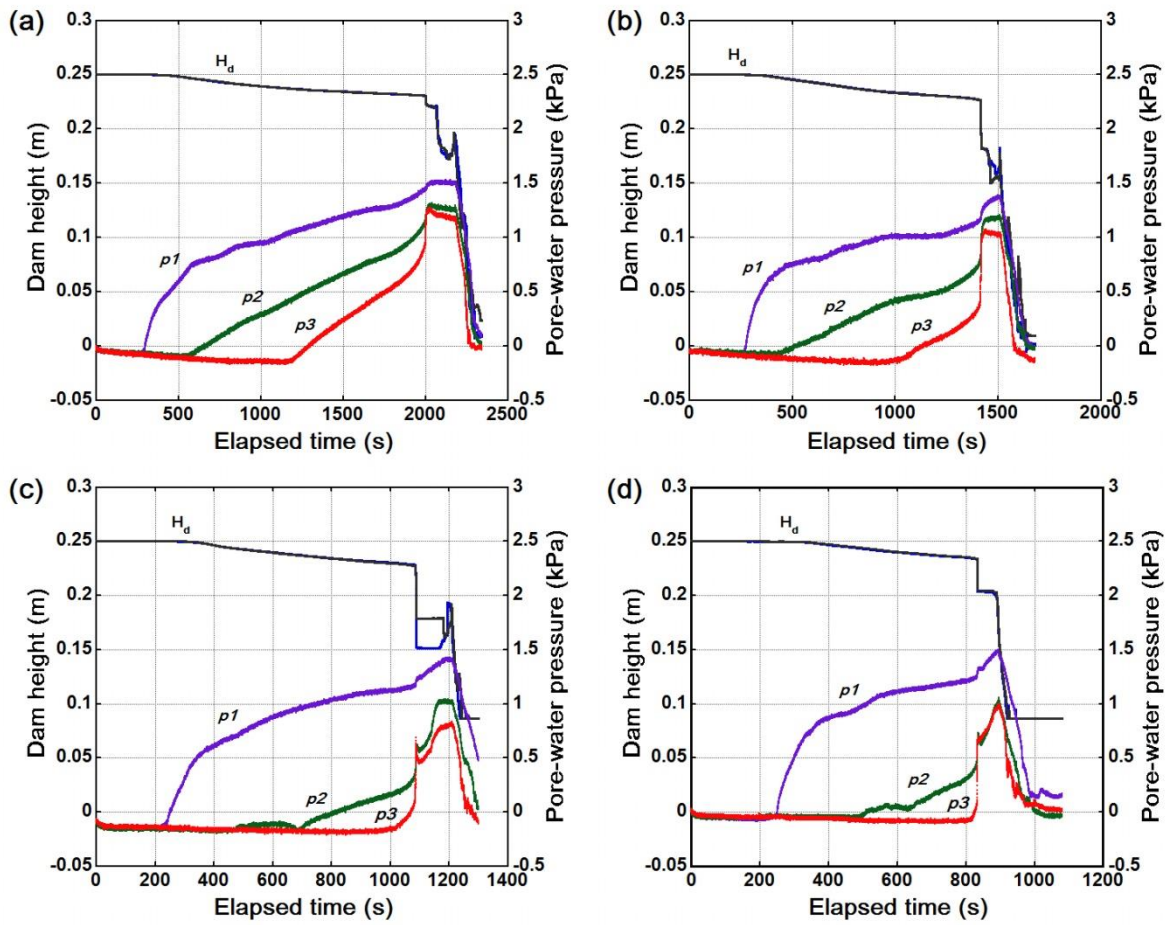
Figure 6.12 Variations in pore-water pressures in dams built with downstream slope angles of **(a)** 30° **(b)** 40° **(c)** 50° **(d)** 60°.
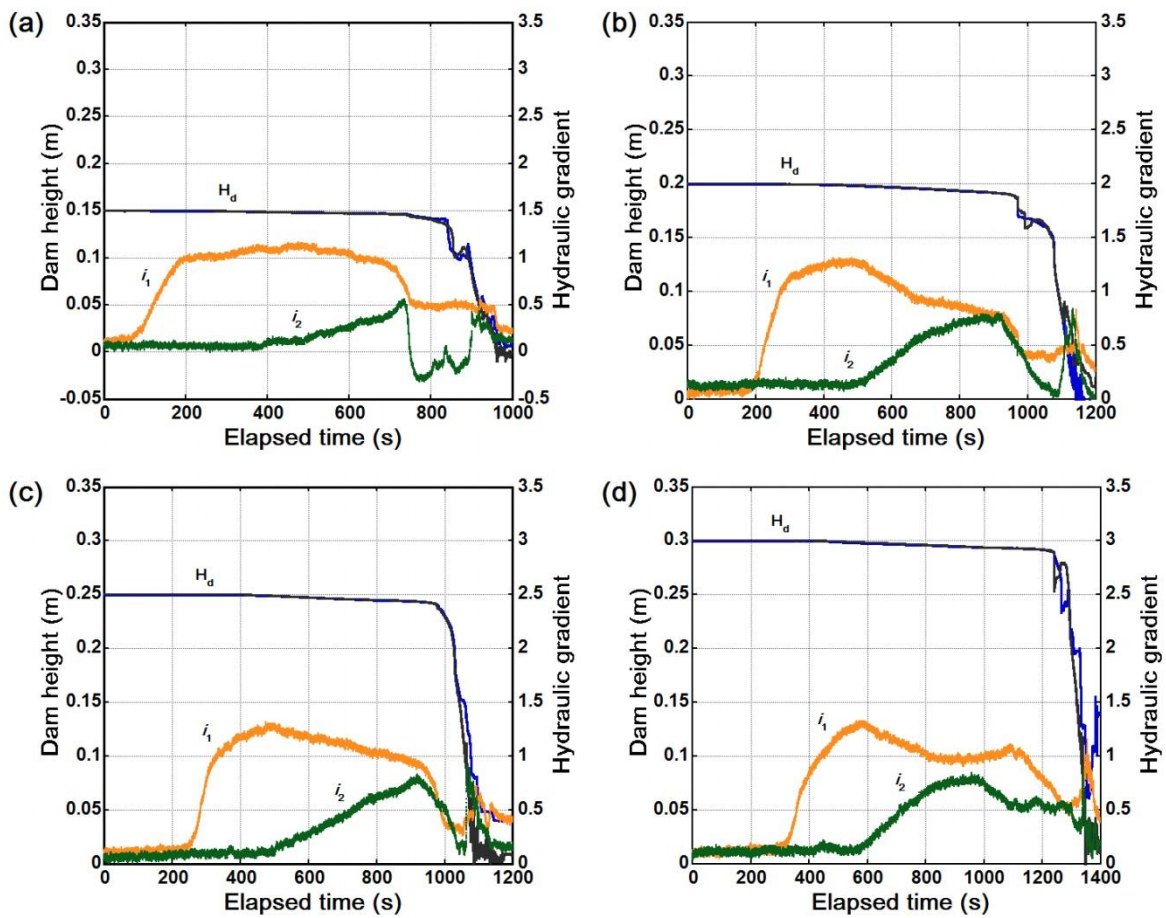
Figure 6.13 Trends of hydraulic gradients in dams built with dam heights of **(a)** 0.15 m **(b)** 0.20 m **(c)** 0.25 m **(d)** 0.30 m.
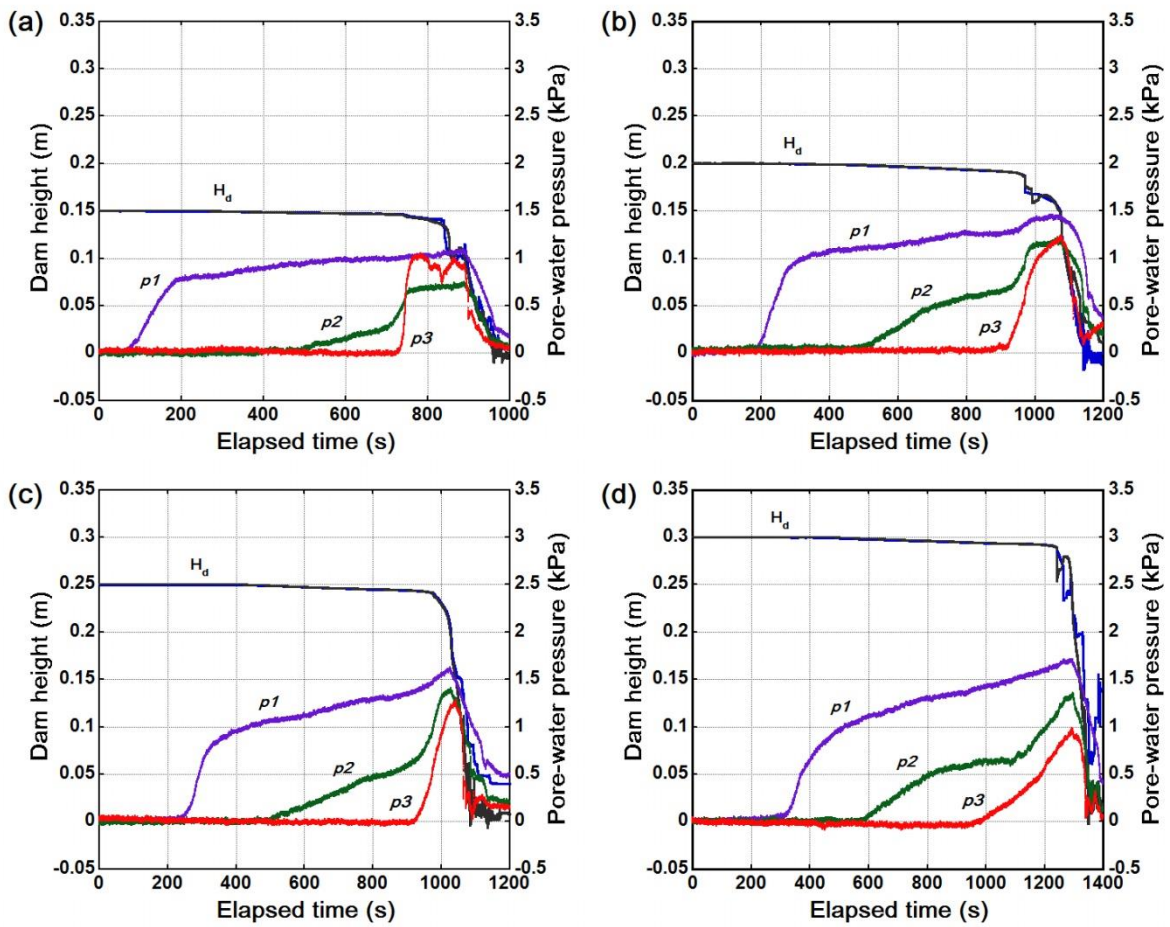
Figure 6.14 Transient changes in pore-water pressures in dams built with dam heights of **(a)** 0.15 m **(b)** 0.20 m **(c)** 0.25 m **(d)** 0.30 m.
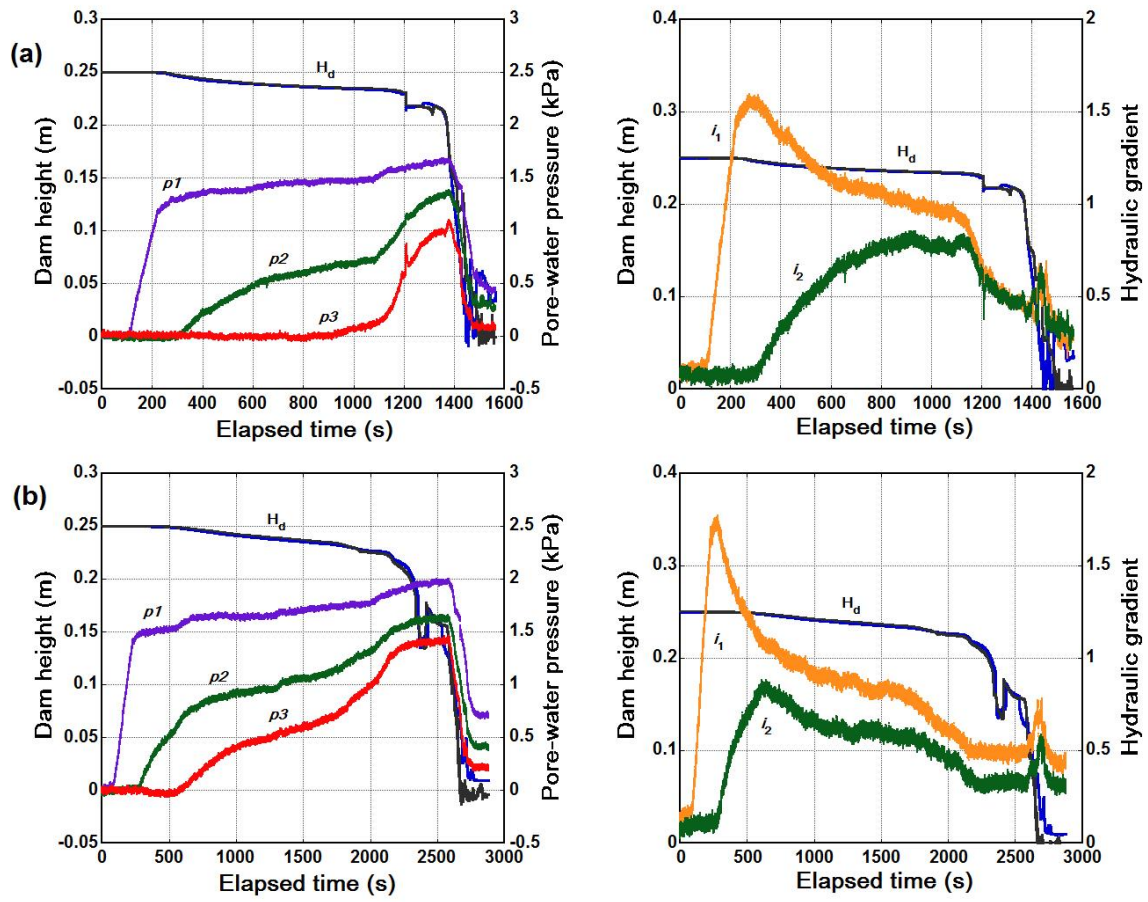
Figure 6.15 Evolution of pore-water pressures and hydraulic gradients in dams built with dam crest widths of **(a)** 0.20 m **(b)** 0.25 m.
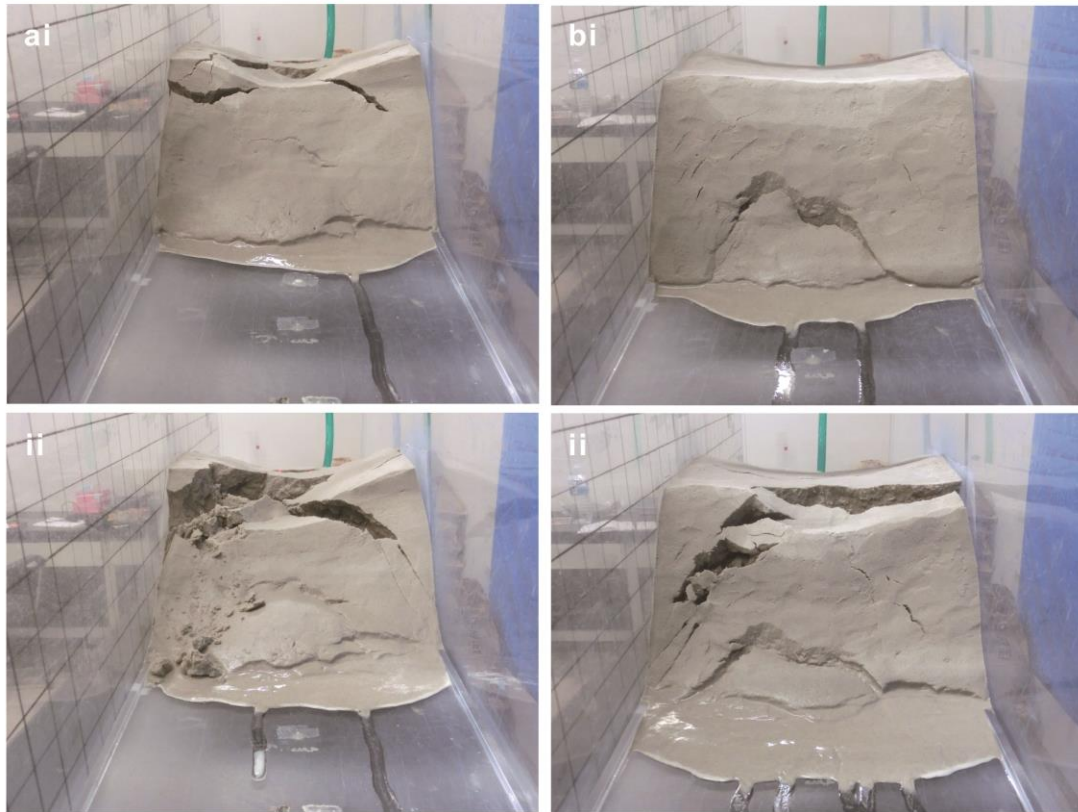
Figure 6.16 Exfiltration, sapping and downstream toe debuttressing under steady-state seepage in dams built with dam crest widths of **(a)** 0.20 m **(b)** 0.25 m.
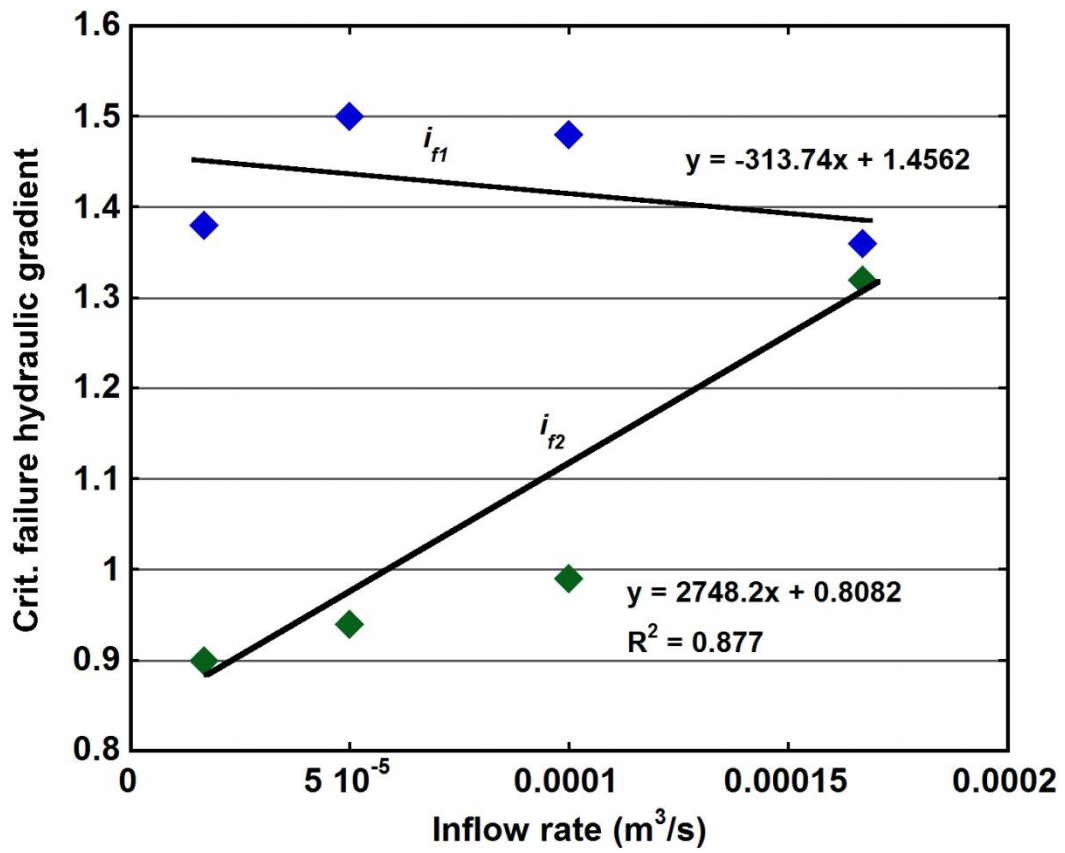
Figure 6.17 Relationship between critical hydraulic gradients for collapse of the dam crest and inflow rate into the upstream lake
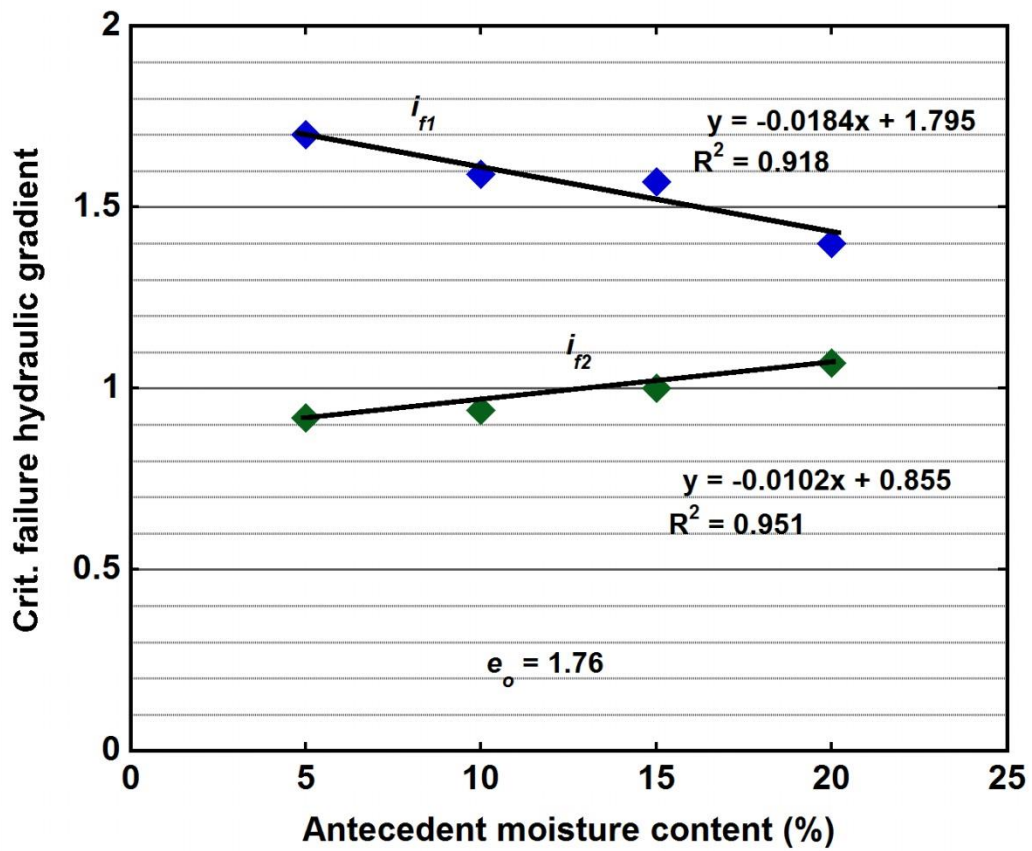
Figure 6.18 Relationship between critical hydraulic gradients for collapse of the dam crest and antecedent moisture content for $e_o = 1.76$
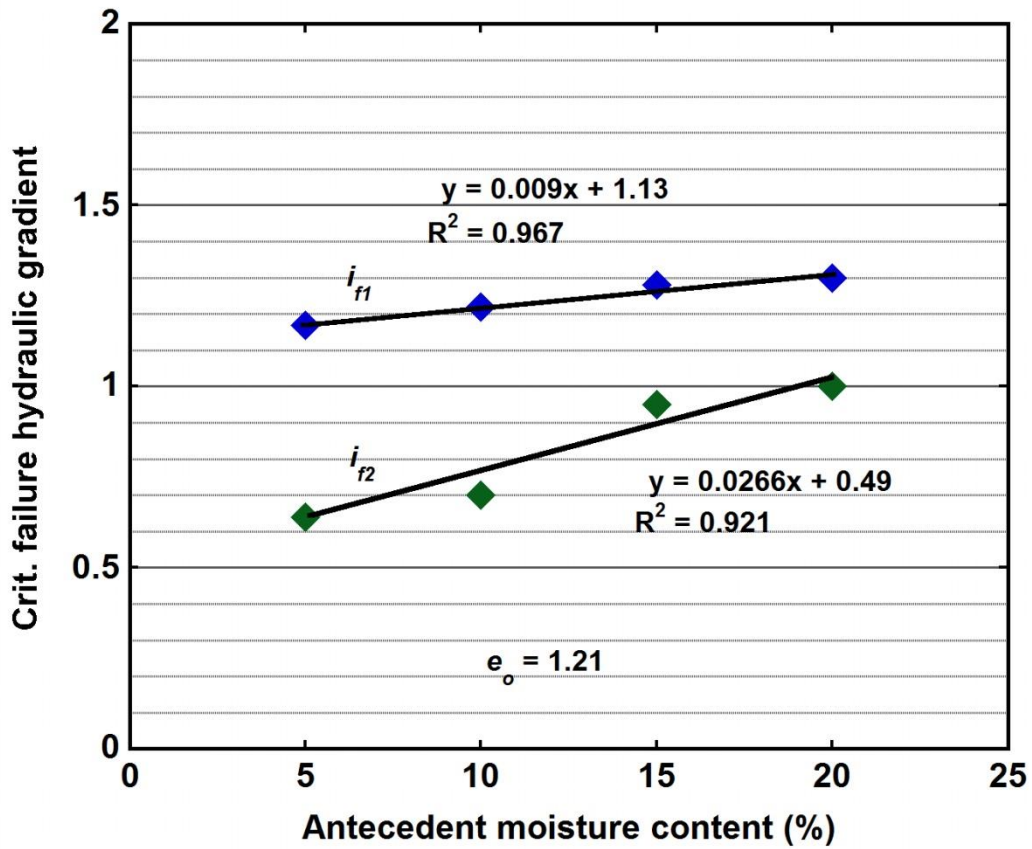
Figure 6.19 Relationship between critical hydraulic gradients for collapse of the dam crest and antecedent moisture content for $e_o = 1.21$
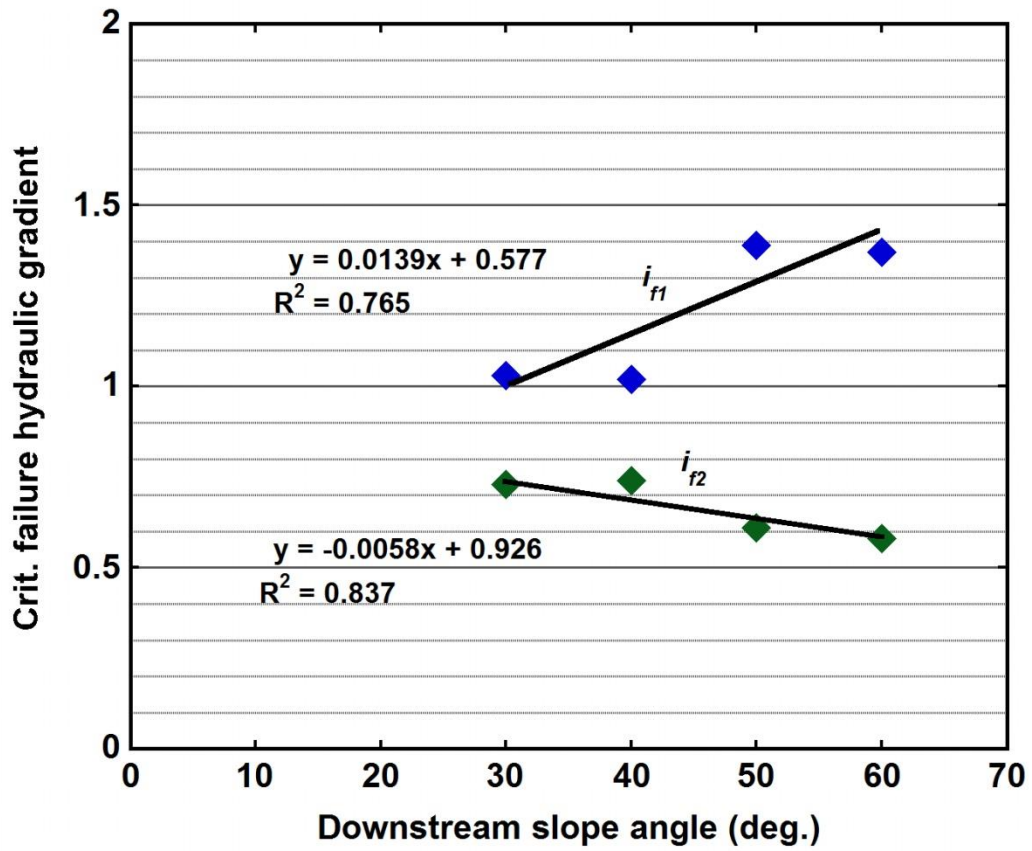
Figure 6.20 Relationship between critical hydraulic gradients for collapse of the dam crest and the downstream slope angle
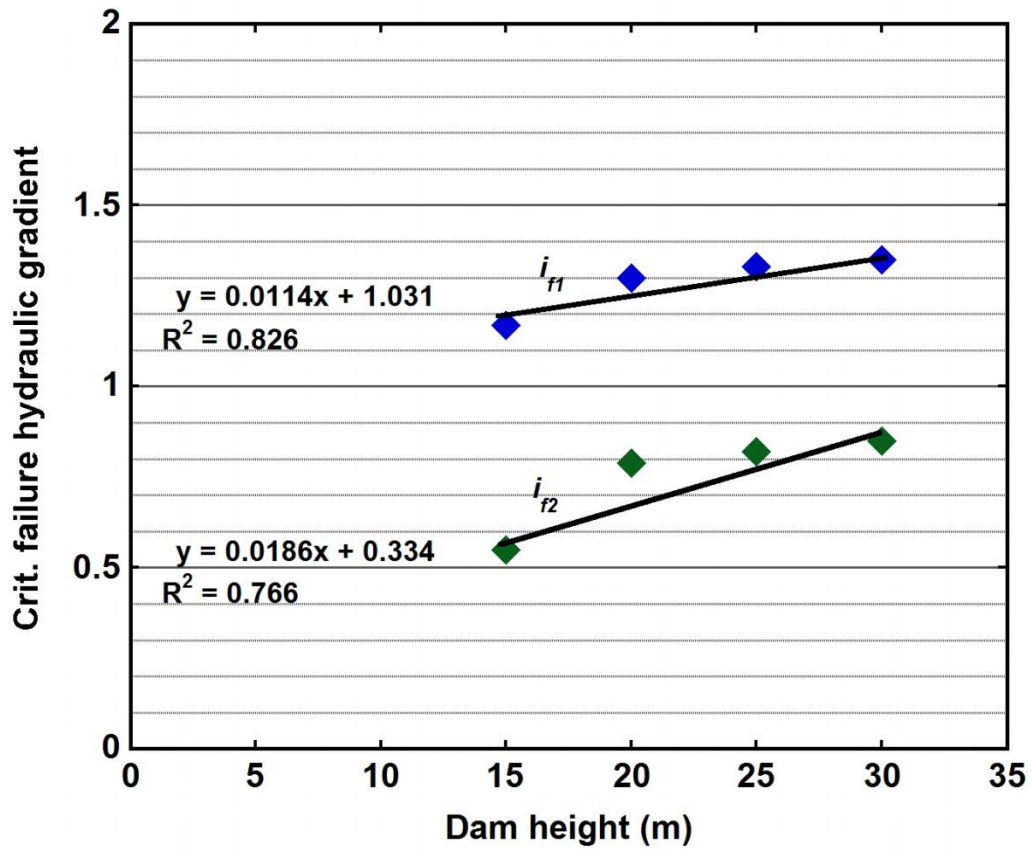
Figure 6.21 Relationship between critical hydraulic gradients for collapse of the dam crest and the dam height

CHAPTER 7

EXPERIMENTAL INVESTIGATION OF THE PREMONITORY CONDITIONS FOR PIPING FAILURE OF LANDSLIDE DAMS

7.1 Background

The occurrence of landslides and rock avalanche processes can result in the natural damming of stream channels and gorges. Such events are common in many mountainous regions where several geomorphological and hydro-climatic factors favour the occurrence of many geomorphic processes including landslide dams (Hewitt 1982; Hermanns et al. 2004). Once a landslide dam is formed, breaching could occur and result in the release of the impounded lake water upstream of the dam. This oftentimes triggers catastrophic outburst floods that could potentially cause a lot of disasters in the downstream areas (Evans 1986; O'Connor and Beebee 2009). The probability of failure of landslide dams remains an integral part of flood risk modeling and hazard assessment studies. Costa and Schuster (1988) reported that the longevity of landslide dams depends on several factors including the rate of seepage through the dam; the internal structure and material properties of the dam; the size, shape, and volume of the blockage; and the rates of sediment and water flow into the upstream lake. Therefore, a better understanding of the premonitory conditions for internal instability and failure of landslide dams is essential for flood risk assessment and disaster prevention.

Internal erosion and piping are among the major failure modes of landslide dams. The vulnerability of landslide dams to seepage and internal erosion has been related to the internal structure and the material properties of the dams (Strom 2006, 2013; Okeke and Wang 2016). The formation of a lake upstream of a landslide dam can lead to the development of high seepage pressures that may initiate internal erosion which could progress to form a piping hole. Seepage triggers instability in landslide dams by: (1) causing a reduction in the resisting forces of the dam materials by increasing the pore-water pressure, (2) the evolution of seepage gradient forces that tend to pull the soil particles apart, and (3) mobilization and downstream entrainment of soil particles towards an unprotected exit. Landslide dams are predominantly unsaturated or partially saturated, and hence the presence of matric suction (negative pore-water pressure) induces an apparent cohesion that increases the stability of landslide dams. However, an increase in pore-water pressure results in the reduction of matric suction which in turn results in internal instability and failure.

Predicting the premonitory conditions for the initiation of internal erosion and piping has been a major concern to geomorphologists and hydraulic engineers. Numerous attempts have been made to evaluate the complex mechanisms of internal erosion and piping in landslide dams and other hydraulic structures (Ojha et al. 2008; Amaya et al. 2009; Vorogushyn et al. 2009). For instance, Bonelli and Benahmed (2010) proposed a simplified mechanically based approach for the prediction of time of piping failure of cohesive dams which can be expressed in a general form as

$$\Delta t_u \approx t_{er} ln \left[\frac{R_u}{R_d} \right] \qquad (7.1)$$

where Δt_u is the time of collapse of the piping hole (breaching time), R_u denotes the maximum radius of the piping hole before roof collapse, R_d represents the initial radius of the piping hole at the time of detection, and t_{er} represents the time of piping erosion, generally expressed as

$$t_{er} = \frac{2\rho_{dry}L}{C_e\Delta p} \qquad (7.2)$$

where ρ_{dry} is the dry density of the material, L is the length of the piping hole, C_e is Fell's coefficient of soil erosion, and Δp is pressure drop in the piping hole. Furthermore, the peak outflow through the orifice which can be expressed as

$$Q_{peak} = \pi R_u^{5/2} \sqrt{\frac{2g(\Delta H_w - R_u)}{kR_u + 4f_b c_L(H_{dam} - R_u)}} \qquad (7.3)$$

where Q_{peak} is the peak outflow, ΔH_w represents change in reservoir water level, H_{dam} denotes dam height, and f_b is turbulent friction factor in the pipe. However, this mechanically based approach is only applicable in dams made of cohesive materials of high plasticity which can support the roof of the piping hole. Therefore, more research needs to be done in view of the differing physical properties of dam materials.

According to ICOLD (2013), the four most important premonitory indices for the assessment of the hydraulic behaviour of dams are: (1) magnitude and variation of pore-water pressures, (2) the rate, magnitude and location of internal and external deformations, (3) the amount, location, turbidity and origin of seepage in the dam, and (4) the magnitude and rate of settlement. Similarly, Fell at al. (2005) described some primary features observed in embankment dams in the early stages of piping, including the presence of muddy leakages, sand boils, settlements, cracking,

whirlpool in the reservoir, sinkholes and the development of high pore-water pressures.

Therefore, the main objectives of this research are to evaluate the premonitory factors for internal erosion and piping failure of landslide dams and to obtain a better understanding of the failure mechanisms of landslide dams as triggered by piping. These objectives were achieved by performing large-scale (outdoor) physical experiments using different kinds of precision sensors and geophysical methods to obtain real time data representative of the deformation behaviour of the dams.

7.2 Experimental methods

7.2.1 Experimental setup and site description

The experiments were performed in a research facility located on Eshima Island, about 20 km northeast of Matsue city, Shimane Prefecture, Japan (Figure 7.1). The experimental facility comprises a horseshoe-shaped trapezoidal barrier of length 8 m and height 2 m, with an open end for the construction of the dam models (Figure 7.2). The trapezoidal barrier was constructed of a homogeneous material of low hydraulic conductivity to minimize the development of anomalous seepage. Furthermore, several layers of tarpaulin sheets were used to cover the internal (reservoir area) and external parts of the barrier to minimize seepage and rainfall infiltration. The barrier was constructed such that the internal and external slope ratios were fixed at $1H:1V$ and $1.5H:1V$, respectively. The upstream lake was recharged from a drainage hose connected to a local water main. The deformation behaviour of the dam models was monitored with two multi-function analog laser displacement sensors suspended by a cylindrical metallic rod. The two sensors were separated by a horizontal distance that ranged from 1 to 1.5 m. The rate of internal erosion and piping was measured with a turbidity sensor (model: VisoTurb$^{(R)}$ 700 IQ

SW) installed near the potential exit point of the seepage water to record transient changes in turbidity of the fluidized sediments. Transient variation in the upstream reservoir was monitored with a 50 kPa capacity pore-pressure transducer, while the hydrodynamic changes that occurred during the onset of internal erosion and piping were monitored with three pore-pressure transducers. The three transducers hereinafter referred to as *PWP-1*, *PWP-2*, and *PWP-3* were inserted into a PVC pipe of diameter, 0.075 m, and laid above the artificial drainage channel. Internal deformations associated with the onset of internal erosion were monitored with four strain gauges inserted into a PVC pipe and laid about 0.5 m above the artificial drainage channel. The strain gauges are hereinafter referred to as *ID-1*, *ID-2*, *ID-3* and *ID-4*. Two high-speed recording cameras were strategically positioned at different places to capture the deformation mechanisms of the dam models. The internal structure of the dam models before and after the experiments was evaluated by conducting microtremor chain array surveys along the dam crest. Self-potential measurements were also carried out along the dam crest to monitor the onset of internal erosion and piping. All the sensors were connected to a standard real-time monitoring and recording unit comprised of a universal recorder (KYOWA EDX-100A) and a laptop computer.

Figure 7.1 Map of Eshima Island indicating the location of the experimental site.

7.2.2 Soil characteristics and dam model construction

The materials used in building the dam models were sourced from a landslide (hereinafter referred to as the Mihata landslide) which occurred on 6 August 2012, in Mihata district, near Izumo city, Shimane Prefecture, Japan (Figure 7.3). The materials consist of highly weathered igneous and sedimentary rocks including andesite, rhyolite, ferruginized sandstone, and mudstone. Table 7.1 shows the physical properties of the materials. The soil consists of 35.5% gravel, 37.5% sand, 20.9% silt and 6.1% clay size particles. The grain size distribution curves of the materials are shown in Figure 7.4. The average coefficient of curvature, coefficient of uniformity and effective grain size of the soil were 0.686, 93.33 and 0.015 mm, respectively.
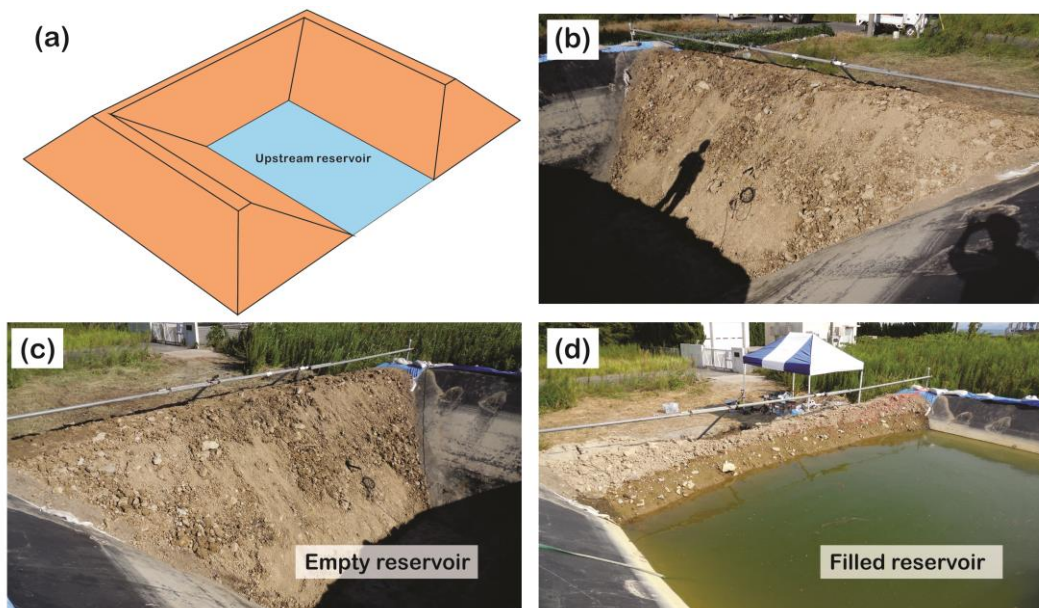
Figure 7.2 The experimental facility. (**a**) A schematic diagram of the reservoir (**b~c**) Upstream side of the dam before the commencement of an experiment (**d**) The reservoir level at full capacity.

A series of large-scale (outdoor) landslide dam models were constructed using a mini-excavator and other heavy-duty equipment. In the early stages, a hand-propelled vibratory plate compactor was used to compact the ground to ensure homogeneity of the underlying foundation material. Internal erosion and piping were initiated by laying uniform gravel and cobbles in a 0.2-m wide rectangular channel (Figure 7.5). Subsequently, the material used in building the dam models was placed in equal lifts and then compacted with a hand-propelled vibratory plate compactor. The geometrical characteristics of the dam models are shown in Figure 7.6. The dam height and the dam crest width ranged from 1.7 to 2 m and 0.8 to 0.95 m, respectively, while α and β which represents the upstream and downstream slope angles were varied from 38 to 41° and 37 to 38°, respectively.

The experiment started with the filling of the upstream reservoir. The discharge into the reservoir was maintained until the reservoir level reached a maximum level considered safe for the operation of the dam. Subsequently, an equilibrium hydraulic head was maintained by establishing a static water level. In all the experimental runs, a large channel was excavated at the toe of the downstream slope to minimize backwater flooding and to ensure accurate readings from the turbidity sensor.

Table 7.1: Summary of the physical properties of the materials used in the experiments

Sample number	Bulk density (Mg/m³)	Dry density (Mg/m³)	Specific gravity (Mg/ m³)	Water content (%)	Void ratio	Degree of saturation (%)
1	1.646	1.358	2.688	21.1	0.978	58.0
2	1.398	1.150	2.725	21.6	1.370	43.0
3	1.179	0.979	2.639	20.4	1.695	31.8
4	1.355	1.124	2.682	20.5	1.385	39.7

| 5 | 1.66 | 1.359 | 2.773 | 22.8 | 1.041 | 60.7 |
| 6 | 1.510 | 1.288 | 2.674 | 17.2 | 1.075 | 42.8 |

Figure 7.3 Early stages of construction of the dam models showing: (**a**) The landslide at Mihata district, near Izumo, Japan (**b**) Toe part of landslide from where the landslide materials were sourced (**c~f**) Offloading of the landslide materials at the experimental site in Eshima Island.
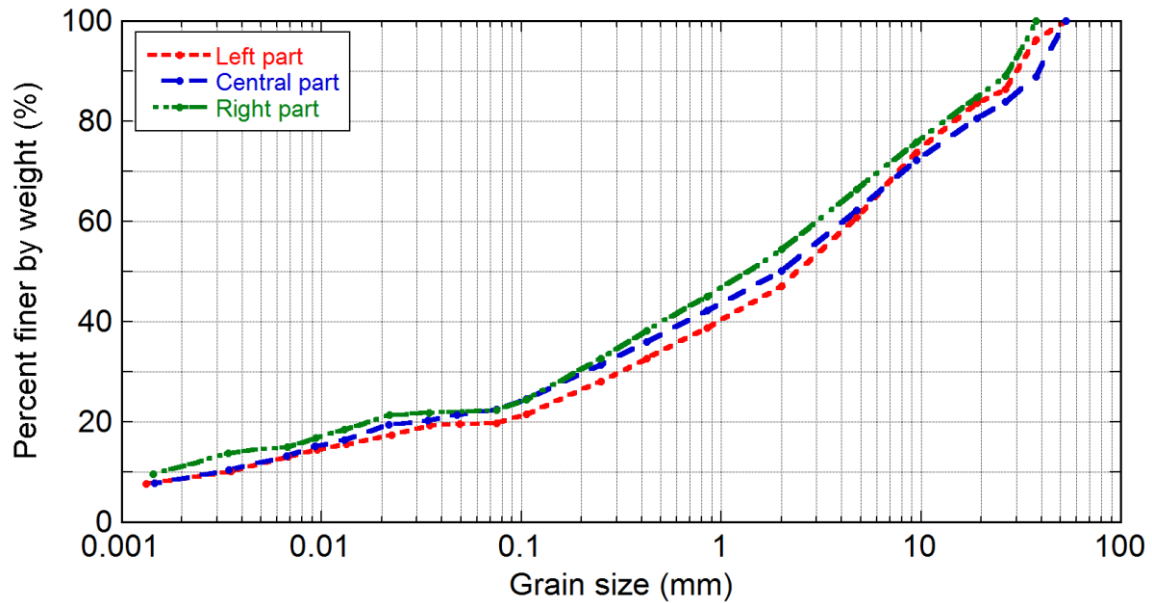
Figure 7.4 Grain size distribution curves of the landslide materials used in the experiments.
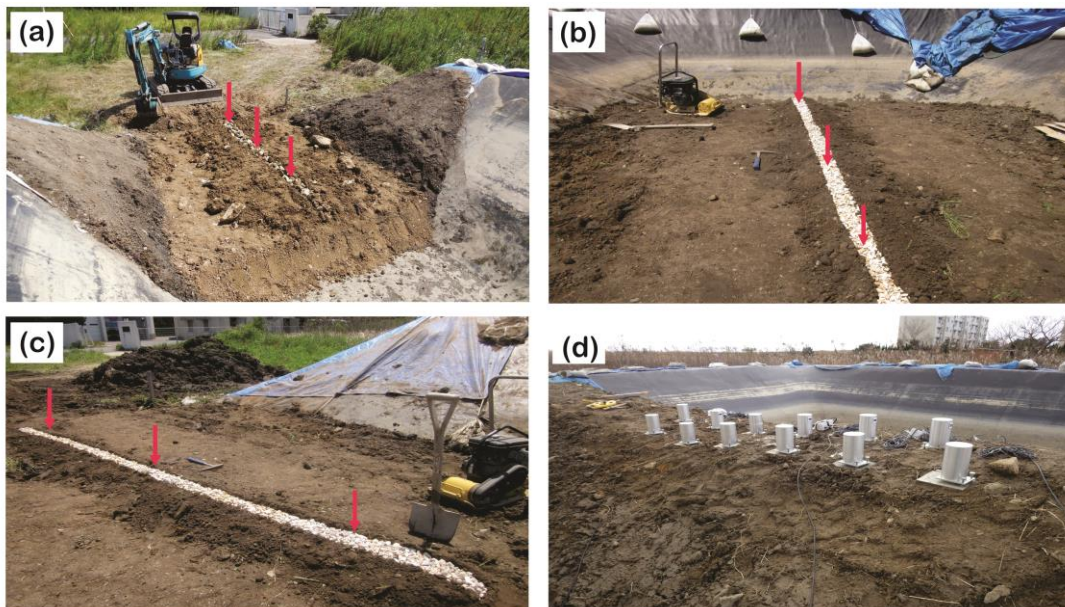
Figure 7.5 Early stages of construction of the dam models showing: (**a~c**) Laying of an artificial drainage channel at the center of the dam (**d**) Setup of geophones on the dam crest for microtremor array survey.
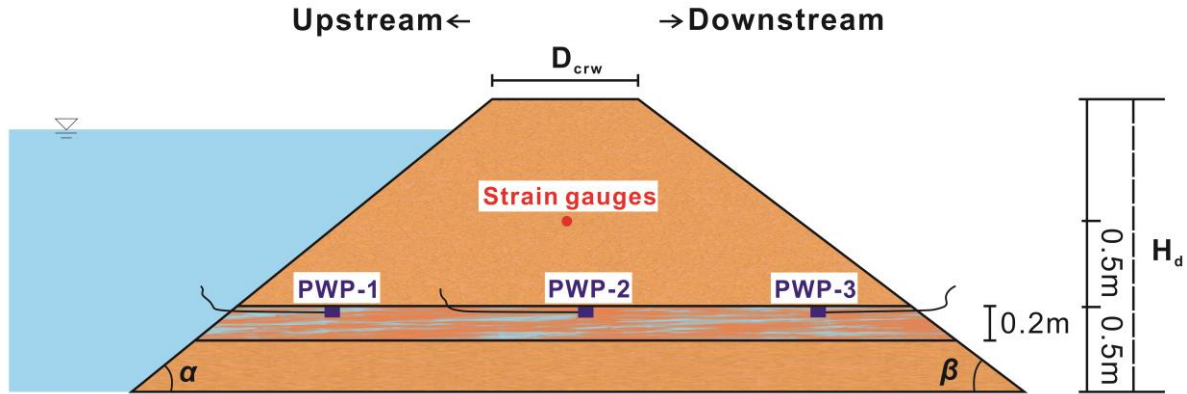
Figure 7.6 Geometric characteristics of the dam models.

7.3 Results and discussion

7.3.1 Experiment 1

Figure 7.7 shows the evolution of a piping hole and the deformation behaviour of the dam model used in *Experiment 1*. The dam material was partially saturated prior to the filling of the upstream reservoir, and hence the stability of the dam was controlled by the presence of negative pore-water pressures. The filling of the upstream reservoir induced the development of transient seepage through the dam due to a steady rise in the upstream lake. The early stages of initiation of internal erosion in the dam involved an abrupt drop in pressure of the seeping water through the upstream side of the artificial drainage channel.

The buildup of significantly high positive pore-water pressures and the subsequent reduction of the effective stress of the soil in the periphery of the drainage channel initiated minor internal deformations. Consequently, the reduction of the shear strength of the soil due to an increase in seepage gradient forces along the drainage channel resulted in soil particle mobilization and entrainment towards the downstream face. The internal erosion process progressed into piping as evidenced by the gradual outwash of hyperconcentrated flows from a poorly developed hole at

the toe of the downstream face ("*A*" in Figure 7.7). This was followed by a steady propagation of the wetting front and a gradual decrease in the dam height ("*B*" in Figure 7.7).

The erosion processes that led to the evolution of the piping hole caused further (internal) deformations that resulted in the gradual unraveling of the downstream toe under steady-state saturation (Figures 7.7C and 7.8). It is interesting to note that the outwash of the fluidized sediments from the evolving pipe coincided with the internal deformations recorded by the strain gauges. This indicates the effects of the erosive forces of the flowing water in the gradual reduction of the shear strength of the dam material.
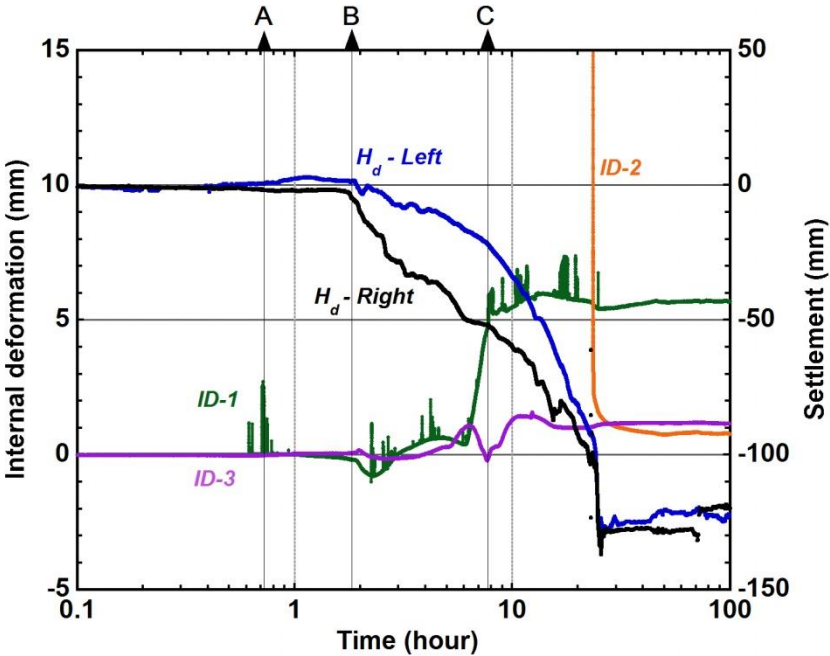
Figure 7.7 Evolution of a poorly developed piping hole and the deformation mechanism of the dam during experiment 1.

Figure 7.8 Gradual unraveling of the downstream toe under steady-state saturation.

Figure 7.9 shows the transient changes in turbidity of the hyperconcentrated flow and the deformation behaviour of the dam model. At the initial stages, the turbidity of the effluent seepage was lower than 55 NTU. However, the evolution of the piping hole at the downstream face caused the turbidity value to increase from 55 NTU to about 70 NTU ("*A*" in Figure 7.9). This phenomenon marked the early onset of piping in the dam. This was followed by a rapid increase in turbidity of the hyperconcentrated flow, indicating the progression of internal erosion and piping through the dam ("*B*" in Figure 7.9). The rate of enlargement of the piping hole under intense erosion can be directly related to the gradual decrease in height of the dam due to the removal of the underlying material. The pipe enlargement process peaked with a sharp decrease in dam height which corresponded with high values of turbidity that ranged from 350 to 400 NTU ("*C*" in Figure 7.9). Pore-water pressure data obtained from the last stages of the test revealed that PWP-1 and PWP-3 were as high as 11.8 kPa and 8.7 kPa, respectively, while the corresponding critical

hydraulic gradients for collapse of the dam (i_{f1} and i_{f2}) were 4.3 and 3.2, respectively (Figure 7.10).

Figure 7.11 summarizes the time-dependent failure sequence of the dam model. The emergence of the seepage water at the downstream face triggered further saturation and undercutting of the downstream toe that resulted in the evolution of several cracks on the dam crest. The inability of the piping hole to evolve into a larger hole can be attributed to the low plasticity nature of the dam material. Hence, failure was mostly triggered by dam face saturation, hydraulic cracking, settlement, downstream toe undercutting and progressive unraveling.
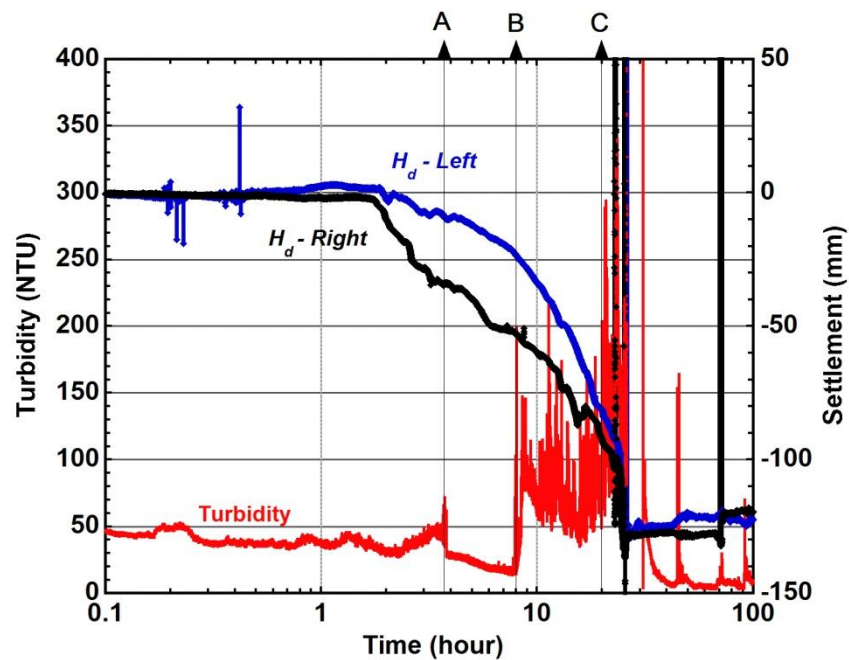
Figure 7.9 Stage hydrograph and variation of turbidity of the hyperconcentrated flow in *Experiment 1*
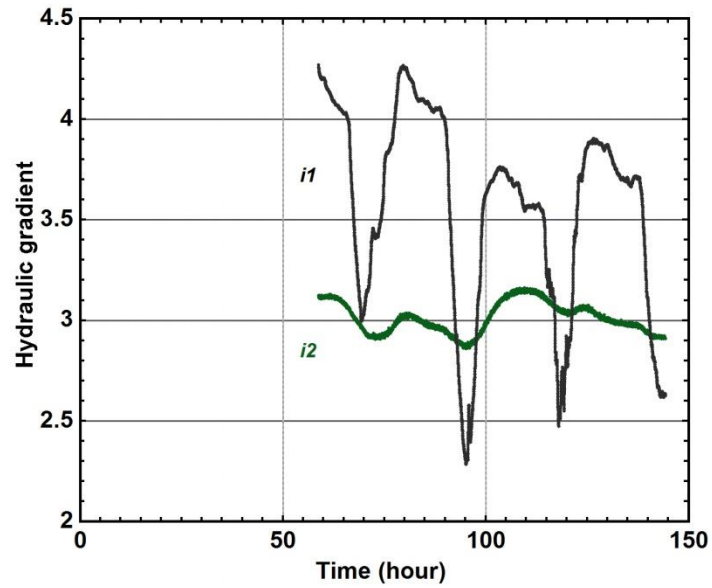
Figure 7.10 Trends of critical hydraulic gradients obtained during the experiment.
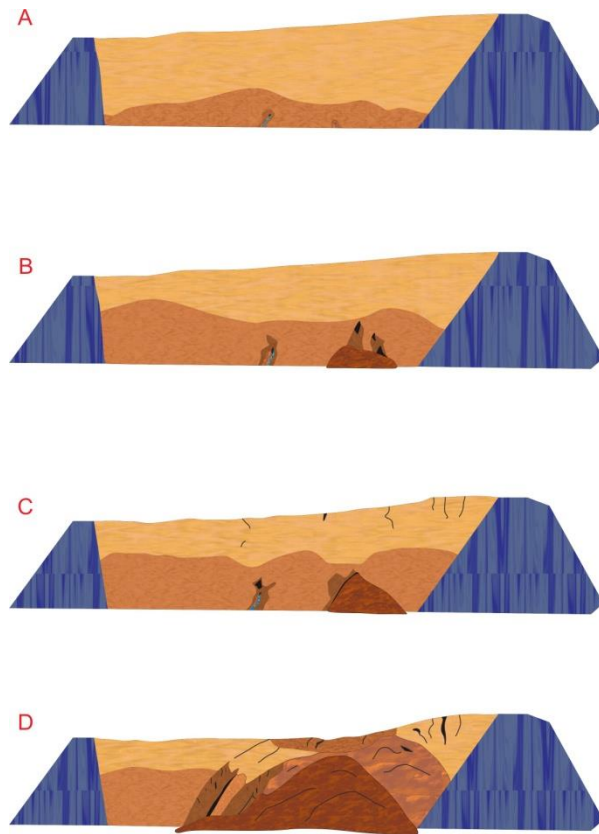
Figure 7.11 Schematic diagram of the failure sequence of the dam in *Experiment 1*.

7.3.2 Experiment 2

Figure 7.12 shows the time-dependent deformation mechanism of the dam model under steady-state seepage conditions. The gradual rise in the reservoir level and the subsequent increase in pore-water pressures caused internal stress redistribution that resulted in the formation of concave upward depressions (settlements) on the dam crest ("*A*" in Figure 7.12). The low compactive effort of the dam material relative to the material used in *Experiment 1* may have contributed to the high susceptibility of the dam to internal erosion. Early onset of internal erosion was detected by the strain in the pipe attached with four strain gauges. The increase in seepage gradient forces within the artificial drainage channel triggered particle mobilization and entrainment that resulted in further redistribution of internal stresses as recorded by the strain gauges ("*B*" in Figure 7.12). The onset of piping was marked by the emergence of very turbid seepage water from the downstream toe, which caused the turbidity of the seepage water to sharply increase from 40 NTU to 270 NTU ("*A*" in Figure 7.13). The variation of the turbidity reading is an indication of the episodic erosive action of the seepage water. It is worthy to mention that the characteristic physical properties of the dam materials could not support the formation of a continuous piping hole through the dams. Hence, seepage was the primary failure mechanism. The inability of the dam materials to support the roof of the piping hole hindered further enlargement of the pipe. Consequently, the saturation of the downstream face under steady-state seepage resulted in the gradual undercutting of the downstream toe, leading to slope instability and progressive failure (lateral spread). This phenomenon is linked with very high turbidity values ("*B*" in Figure 7.13) caused by the erosion and downstream transport of the mobilized materials.
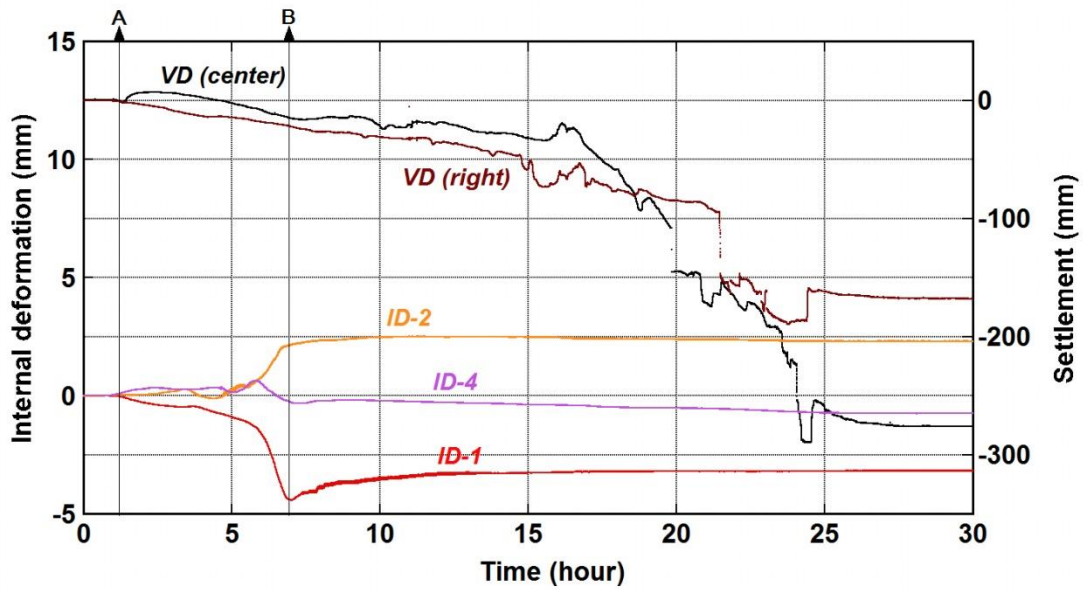
Figure 7.12 Deformation behaviour of the dam under steady-state seepage conditions
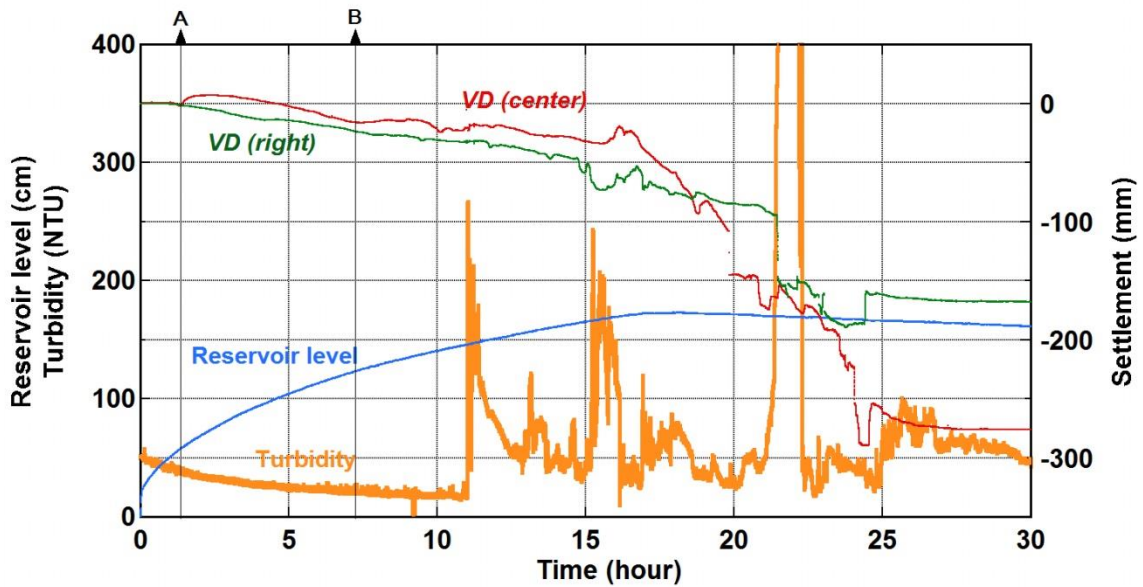
Figure 7.13 Stage hydrograph and variation in turbidity of the seepage water during *Experiment 2*

7.3.3 Experiment 3

Figure 7.14 shows the trends of pore-water pressures and turbidity in the dam model used in *Experiment 3*. The dam was built to a height and dam crest with of 1.98 and 0.89 m, respectively, while the upstream and downstream slope angles were 41 and 38°, respectively. The rapid rise in pore-water pressures through the dam resulted in the development of high seepage gradient forces that caused abrupt erosion and outwash of the dam materials to an exit point on the downstream face. This is evidenced by the rapid increase in turbidity of the effluent seepage to about 2500 NTU. The evolution of seepage at the exit face of the downstream slope resulted in the upslope propagation of the wetting front, leading to progressive sloughing and settlement of the dam crest. The gradual undercutting and sloughing of the downstream slope under steady-state seepage further triggered several cycles of turbidity flows with peaks which varied from 1100 to 2200 NTU.
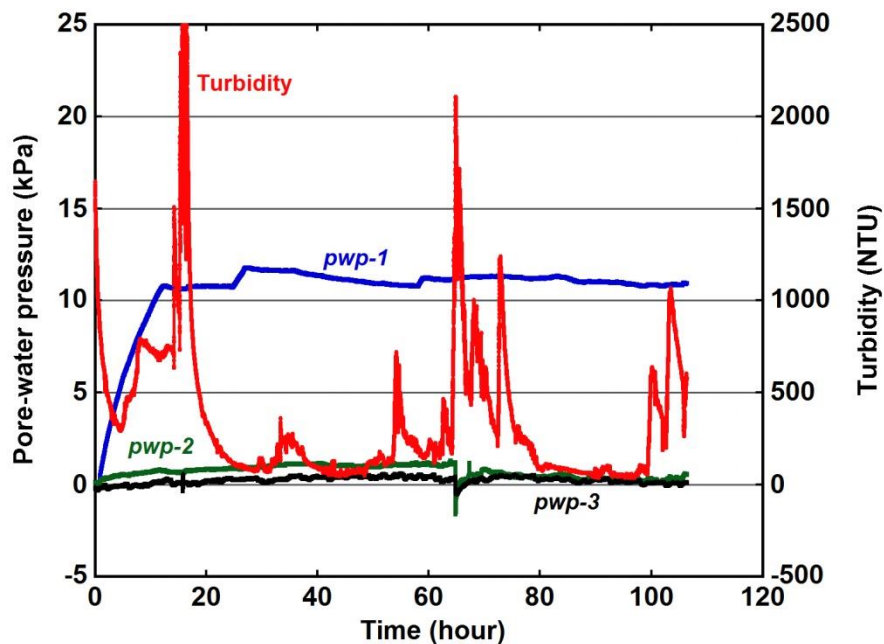
Figure 7.14 Trends of pore-water pressures and variation in turbidity of the seepage water in *Experiment 3*.

Figure 7.15 shows the trends of hydraulic gradients and the deformation mechanism of the dam model under steady-state seepage conditions. The measured critical hydraulic gradient for the collapse of the dam crest (i_{f2}) was found to coincide with the high turbidity of the seepage water, and thus indicates the early onset of internal instability of the dam (Figure 7.15b). Further increase in i_{f2} was associated with gradual deformation of the dam crest. Consequently, failure was generally triggered by downstream slope saturation, undercutting and sloughing of the fluidized materials as shown in Figure 7.16.

Turbidity of the seepage water has been ascribed as one of the direct evidences of internal erosion in engineered dams and landslide dams. Hyperconcentrated flows or seepage waters that contain a significant amount of suspended soil particles (sediments) are indicative of the evolution of internal erosion and piping. According to Brown and Gosden (2008), the significant premonitory factors for early warning on internal erosion and piping in dams are turbidity and seepage flows. For instance, the U.S Army Corps of Engineers investigated the occurrence of high turbidity seepage at the right abutment of the Howard Hanson Dam in Washington State, USA. In situ measurements revealed that the turbidity of the seepage flow was higher than 1,000 NTU (Figure 7.17). The formation of a large depression at the upstream slope of the right abutment, coupled with the rapid transmission of dye through the right abutment and the abnormally high turbidity value caused the U.S Army Corps of Engineers to revise the performance rating of the dam from class II (potentially unsafe) to class I (unsafe).

The movement of water through the interstitial voids of soil materials is controlled by several factors including the hydraulic conductivity of the soil, density, gradation, soil type, and the amount of fines. Two important parameters that have been used in the evaluation of internal erosion and piping in embankment dams and landslide

dams are the plasticity index and erodibility. The likelihood of initiation of internal erosion is much higher in materials of high erodibility than in those of lower erodibility (Table 7.2). Fell et al. (2008) classified the erodibility of soils based on plasticity index and the amount of fines (Table 7.3). Therefore, the high erodibility of the materials used in these experiments, coupled with the small amount of fines could be attributed to the inability of the materials to form a continuous piping hole.
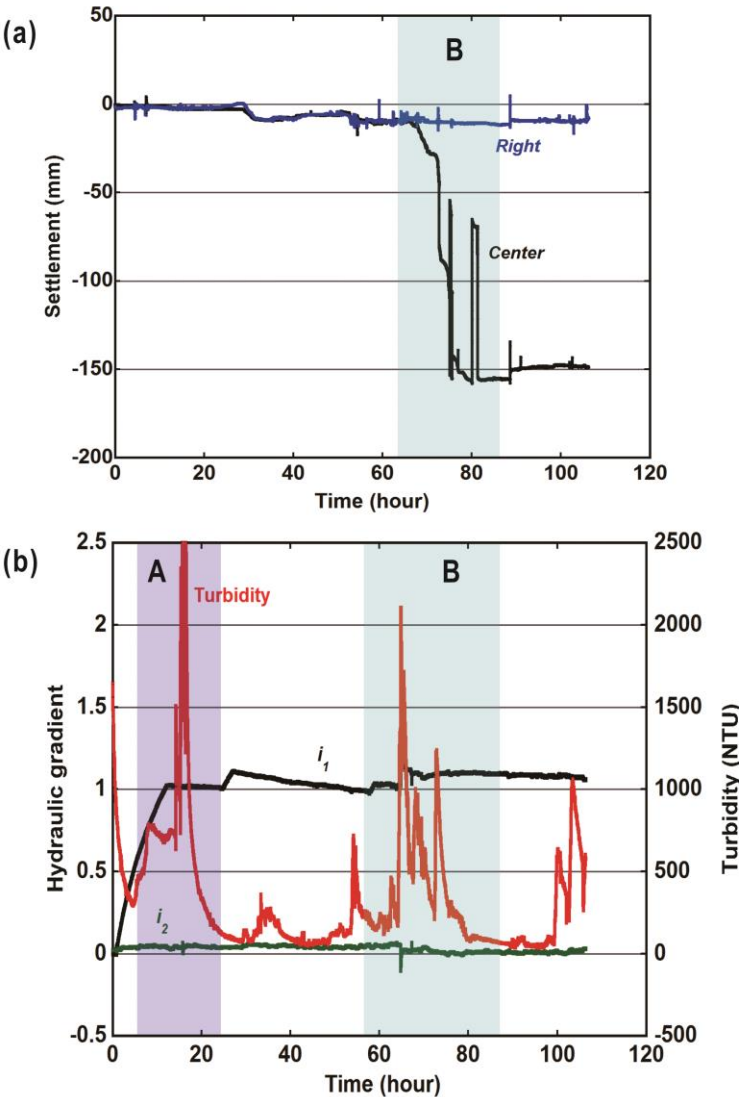
Figure 7.15 Stage hydrograph and deformation mechanism of the dam model used in *Experiment 3* under steady-state flow conditions.
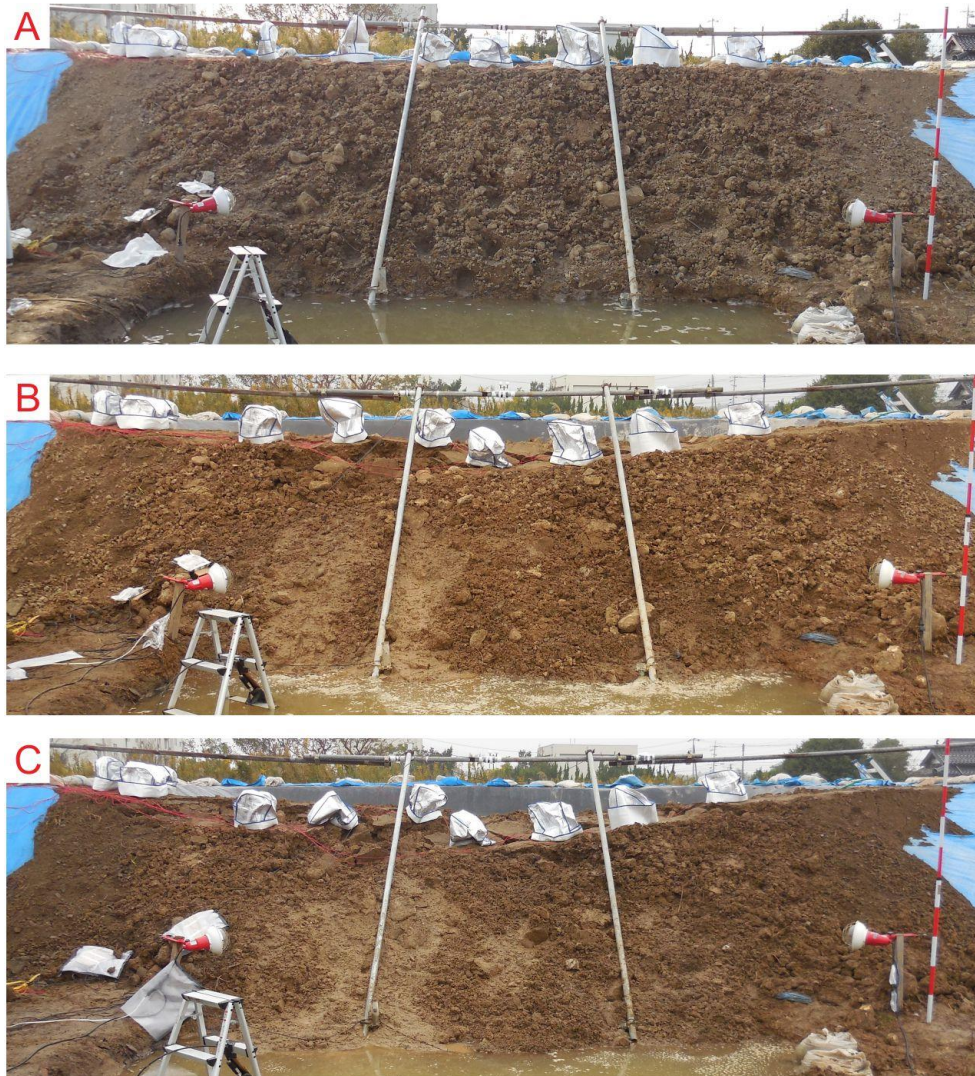
Figure 7.16 Time-dependent deformation behaviour of the dam model used in *Experiment 3* under steady-state flow conditions.

Figure 7.17 Investigation of seepage in Howard Hanson Dam, USA. (**a**) Turbid water collected from a vertical drain at the right abutment, (**b**) Occurrence of a large depression at the upstream slope of the right abutment.

Table 7.2: Classification of erosion resistance of different soils (Sherard 1953)

Category 1	Plastic clay, $PI > 15$, well compacted.
Greatest Piping Resistance	Plastic clay, $PI > 15$, poorly compacted.
Category 2	Well-graded material with clay binder, $6 < PI < 15$, well compacted.
Intermediate Piping Resistance	Well-graded material with clay binder, $6 < PI < 15$, poorly compacted.
	Well-graded, cohesionless material, $PI < 6$, well compacted.
Category 3	Well-graded, cohesionless material, $PI < 6$, poorly compacted.
Least Piping Resistance	Very uniform, fine, cohesionless sand, $PI < 6$, well compacted.
	Very uniform, fine, cohesionless sand, $PI < 6$, poorly compacted.

Table 7.3: Erosion resistant of soils from concentrated leaks (ICOLD 2013)

Degree of erosion	Soil classification
1. Extremely erodible	All dispersive soils, Sherard's pinhole classes D1 and D2; or Emerson Crumb Class 1 and 2. AND SM with <30% fines
2. Highly erodible	SM with >30% fines; SC with <30% fines; ML; SC with >30% fines; CL-ML
3. Moderately erodible	CL; CL-CH; MH; CH with liquid limit <65
4. Erosion resistant	CH with liquid limit >65

7.4 Conclusions

Large-scale (outdoor) experiments were conducted with the sole purpose of investigating the premonitory conditions for internal erosion and piping in landslide dams. The experimental scheme and the results obtained indicated the significance of using precision sensors (pore-water pressure transducers, strain gauges, laser displacement sensors, turbidity sensors, and reservoir water level probe) in combination with non-invasive geophysical techniques (self-potential and microtremor array surveys) in monitoring the performance of landslide dams. This study showed that the turbidity of the seepage water can be effectively used in the prediction of the rate of internal erosion and the breaching time of landslide dams.

Reasonable agreement between the negative self-potential anomalies which ranged from -18 to -20 mV and the emergence of very turbid hyperconcentrated flows from the downstream face, gives credence to the notion that turbidity can be used as an important parameter for monitoring the performance of landslide dams (Figure 7.18).

The onset of internal erosion under steady-state seepage conditions was found to correlate with the initial internal deformations recorded by the strain gauges. A relationship was found between the rate of erosion of the dam material and the formation of concave upward depressions on the dam crests. The relative difference in the hydraulic behaviour and evolutionary trend of the dam highlighted the difference in plasticity index, erodibility and other physical properties of the materials composing the dams.
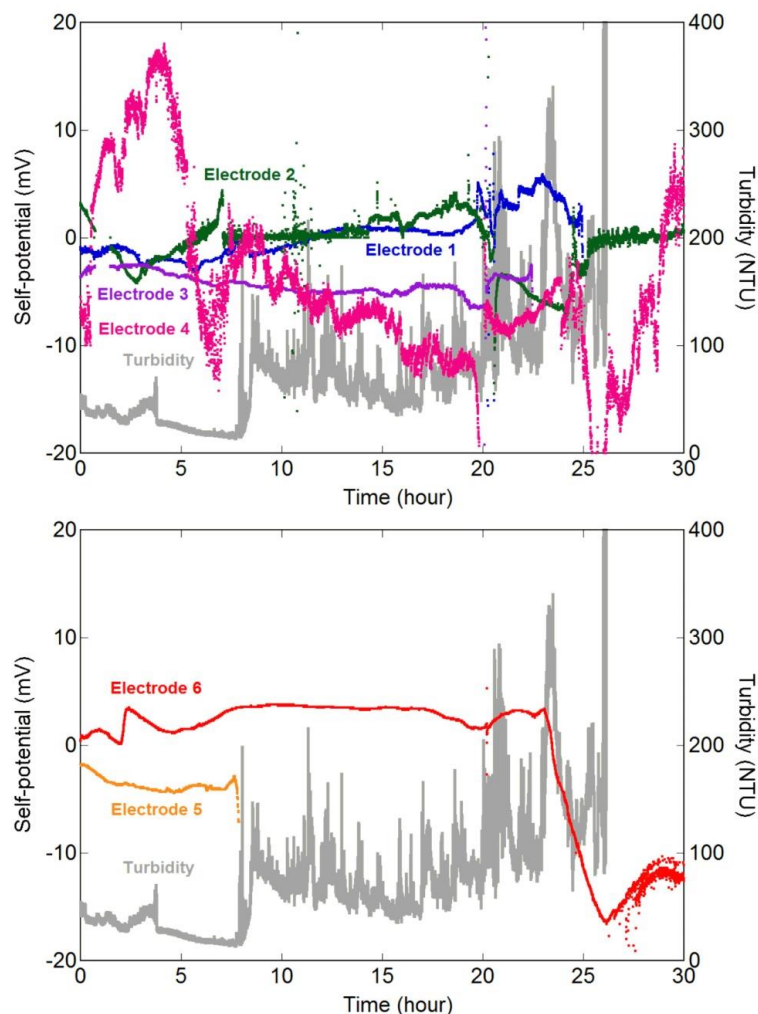
Figure 7.18 Variations in turbidity and self-potential during internal erosion and piping in *Experiment 1.*

CHAPTER 8

CONCLUSIONS AND FUTURE WORK

Landslide dams are common in tectonically active regions where the influence of several predisposing factors such as earthquakes, volcanic eruptions, rainfall, snowmelt and glacially over-steepened slopes trigger landslides that block stream channels. These regions are characterized by the abundance of landslide source materials like volcanic deposits, hydrothermally altered materials, and fractured and disjointed bedrock. Internal erosion and piping are among the most common failure modes of landslide dams and embankment dams. Indeed, a lot of attention has been given to overtopping failure of landslide dams, including several flood routing models that have been developed for flood risk assessments. However, historical statistics of natural dam failures reveals the need for an improved understanding of the complex mechanisms of internal erosion and piping which could aid in the development of piping-based breach models. In the present study, an attempt was made to evaluate the complex relationship that exists between the internal structure and material characteristics of landslide dams and the hydrodynamics of the upstream lake. This was done through a series of field (geophysical) investigations, flume experiments and large-scale (outdoor) physical experiments. The main conclusions obtained from this study are summarized in this chapter. Recommendations for further work are also presented.

8.1 Major conclusions

8.1.1 Geophysical assessment of the internal structure of landslide dams

An integrated geophysical approach which comprises the microtremor chain array and self-potential surveys was used to evaluate the internal structure and material properties of landslide dams in relation to the probability of failure by piping. The microtremor chain array method was successfully used to determine the apparent phase velocity depth profile of the investigated landslide dams in Japan and Kyrgyzstan using the SPAC method. Based on the results of the microtremor chain array surveys, the internal structure of the dams can be divided into two distinct morphologies: an upper layer of low phase velocities that comprises poorly consolidated and highly fragmented materials of high hydraulic conductivity, and a lower layer of high phase velocity which is mostly characterized by intensely folded and structurally deformed strata of high density and low permeability. Similarly, the self-potential survey results provided valuable information regarding the hydrogeological conditions of the dams. A good agreement between zones of high negative SP anomalies and very low phase velocity values indicated the existence of anomalous seepage zones or water-saturated areas. However, our interpretation is limited by the distance traversed on a single line. Hence, more investigations need to be done to evaluate any possible link between the upstream lake and the zones of anomalous seepage. This non-invasive integrated geophysical approach has demonstrated its reliability for assessing the likelihood of piping failure in landslide dams.

8.1.2 Hydromechanical constraints on piping failure of landslide dams

A series of experiments were conducted to evaluate the hydromechanical constraints on the piping failure of landslide dams. The experimental facility comprised a flume tank equipped with precision sensors. The entire breach evolution process can be

divided into five phases: pipe development, pipe enlargement, crest settlement, hydraulic fracturing and downstream slope unraveling. The failure mechanisms of the dams were influenced by several parameters including the hydraulic conductivity, pore geometry, gradation, fines percentage and density of the soil. Seepage was the dominant failure mechanism of dams comprised of homogeneous materials while piping was evident in the dams composed of mixed materials. In general, the ability of the material to support the roof of the piping hole increased with an increase in the amount of fines and the interlocking bonds binding the materials. The time of onset of internal erosion was found to decrease with an increase in void ratio, while the breaching time of the dams increased with an increase in void ratio.

8.1.3 Critical hydraulic gradients for landslide dam failure by seepage

An investigation of the critical hydraulic gradients for seepage-induced failure of landslide dams was performed under different hydraulic and geometrical conditions. The experiments were conducted in a flume tank modified to record transient changes in pore-water pressures and trends of hydraulic gradients during under steady-state seepage conditions. The deformation behaviour of the dams can be divided into two types: *Type I* and *Type II*. Two limit values of hydraulic gradients that correspond to the onset of internal erosion and collapse of the dam crest were determined. In general, the initiation hydraulic gradients varied from 0.042 to 0.147. The critical hydraulic gradient for collapse of the dam crest was influenced by the uniformity coefficient of the materials. Similarly, the hydraulic gradient for dam failure increased with an increase in inflow rate into the upstream lake. Other physical parameters that influenced the failure hydraulic gradient are the initial void ratio, dam geometry, and antecedent moisture conditions.

8.1.4 Premonitory factors for internal erosion and piping in landslide dams

The premonitory factors for onset of internal erosion and piping in landslide dams were investigated through a series of large-scale (outdoor) physical experiments. Landslide dam models were constructed in a horseshoe-shaped barrier constructed of low permeability material to minimize seepage. The dam models were comprised of materials sourced from a recent landslide. The deformation behaviour of the dam models under steady-state flow conditions was monitored with several precision sensors (pore-water pressure transducers, strain gauges, laser displacement sensors, reservoir water level probe and a turbidity sensor) and other geophysical techniques. The turbidity of the seepage water that emerged from the downstream face was ascribed as an important parameter for the assessment of the hydraulic performance of landslide dams. Transient variation in turbidity of the effluent seepage coincided with the deformation behaviour of the dams under steady-state flow conditions. Early onset of internal erosion was determined through the deformations experienced by the strain gauges.

8.2 Recommendations for future work

The main factors controlling the stability and longevity of landslide dams are: (1) the type of landslide that formed the dam; and (2) the triggering factor(s) that caused the mass movement. A number of studies have found that landslide dams formed by translational slides are more stable than those formed by other processes such as rock avalanches, rock falls, debris flows and rotational slides. This has been related to the ability of landslides to preserve their source stratigraphy. Landslide dams formed by block slides have a higher tendency to preserve their original stratigraphy because they are usually comprised of intact bedrock with a few fractures but generally do not comminute into smaller particles. A conceptual model developed by Davies and McSaveney (2011) has helped in the understanding of the mechanism of

fragmentation in block slides during long runout. Numerous cases of seepage and piping occurrence in landslide dams formed by huge block slides have been reported, although these occurrences have not threatened the longevity and stability of these dams. A few examples include the Waikaremoana rockslide dam in New Zealand, the Klontalersee rockslide dam in Switzerland, and Visocica River rockslide dam in Serbia. These huge landslide dams were formed by deep-seated block slides of high intact bedrock which made them stable against failure by piping or overtopping. A detailed analysis of case histories has revealed that landslide dams formed by earthquake and rainfall are the most unstable form of river blockages. Similarly, high cases of slope instabilities (failures) were reported in landslide dams formed by translational landslides than in those formed by rock avalanche processes.

In the last 5 years, field and laboratory experiments on the piping failure of landslide dams formed by rock avalanche processes have been carried out. Important insights have been gained into the mechanisms of piping in rock avalanche dams. The present research aims at evaluating the stability and longevity of landslide dams triggered by translational slope movements, where about 70% of the original stratigraphy of their source rock is usually preserved. Whilst many detailed studies have been concluded on the sedimentology (Wassmer et al. 2004; Capra 2007, 2011; Dunning et al. 2005; Dunning 2006; Dunning and Armitage 2011), and seepage and piping failure of rock avalanche dams (Mora et al. 1993; Dunning et al. 2006), little or none has been done on landslide dams formed by translational movements. Shear-wave velocity profile of several landslide dams in Japan suggests that the internal structure of these deposits is strongly deformed and intensely folded, reflecting the modifications the materials suffered during movement. Therefore, further research needs to be conducted on the mechanisms of seepage and internal erosion in stratified landslide dams.

REFERENCES

Adams J (1981) Earthquake-dammed lakes in New Zealand. Geology, 9(5):215-219

Adushkin VV (2000) Explosive initiation of creative processes in nature, Combustion, Explosion, and Shock Waves 36:695–703

Adushkin VV, Pernik LM, Zykov YN (1993) Modeling of explosion-triggered rockslides for construction of the Kambarata 1 hydroelectric power dam, Republic of Kyrgyzstan, Landslide News 7: 7–9

Ahlinhan MF, Achmus M (2010) Experimental investigation of critical hydraulic gradients for unstable soils. In: Burns SE, Bhatia SK, Avila CMC, Hunt BE (eds) Proceedings of the Fifth International Conference on Scour and Erosion, San Francisco, California, doi: 10.1061/41147(392)58, pp 599-608

Ahmad MU (1964) A laboratory study of streaming potentials. Geophysical Prospecting, 12(1):49-64

Aki K (1957) Space and time spectra of stationary stochastic waves, with special reference to microtremors. Bulletin of Earthquake Research Institute, Vol 35, pp. 415-456

Aki K (1965) A note on the use of microseisms in determining the shallow structures of the earth's crust. Geophysics, 30(4):665-666

Allegre V, Jouniaux L, Lehmann F, Sailhac P (2010) Streaming potential dependence on water-content in Fontainebleau sand. Geophysical Journal International, 182(3):1248-1266

Allen SK, Cox SC, Owens IF (2011) Rock avalanches and other landslides in the central Southern Alps of New Zealand: a regional study considering possible climate change impacts. Landslides, 8(1):33-48

Allen SK, Schneider D, Owens IF (2009) First approaches towards modelling glacial hazards in the Mount Cook region of New Zealand's Southern Alps. Natural Hazards and Earth System Sciences, 9(2):481-499

Amaya PJ, Massey-Norton JT, Stark TD (2009) Evaluation of seepage from an embankment dam retaining fly ash. Journal of Performance of Constructed Facilities, 23(6):406-414

Apostolidis P, Raptakis D, Roumelioti Z, Pitilakis K (2004) Determination of S-wave velocity structure using microtremors and SPAC method applied in Thessaloniki (Greece). Soil dynamics and earthquake engineering, 24(1):49-67

Arai H, Tokimatsu K (2004) S-wave velocity profiling by inversion of microtremor H/V spectrum. Bulletin of the Seismological Society of America, 94(1):53-63

Asten MW (2004) Passive seismic methods using the microtremor wave field for engineering and earthquake site zonation. In Proceedings of the SEG 74th Annual Meeting

Asten MW, Stephenson WR, Davenport PN (2005) Shear-wave velocity profile for Holocene sediments measured from microtremor array studies, SCPT, and seismic refraction. Journal of Environmental & Engineering Geophysics, 10(3):235-242

Auer I, Böhm R, Jurković A, Orlik A, Potzmann R, Schöner W, Ungersböck M, Brunetti M, Nanni T, Maugeri M, Briffa K (2005) A new instrumental precipitation dataset for the greater alpine region for the period 1800–2002. International Journal of Climatology, 25(2):139-166

Awal R, Nakagawa H, Fujita M, Kawaike K, Baba Y, Zhang H (2011) Study on piping failure of natural dam. Annuals of Disaster Prevention Research Institute Kyoto University 54:539-547

Baker DM, Lillie RJ, Yeats RS, Johnson GD, Yousuf M, Zamin ASH (1988) Development of the Himalayan frontal thrust zone: Salt Range, Pakistan. Geology, 16(1):3-7

Becker JS, Johnston DM, Paton D, Hancox GT, Davies TR, McSaveney MJ, Manville VR (2007) Response to landslide dam failure emergencies: Issues resulting from the October 1999 Mount Adams landslide and dam-break flood in the Poerua River, Westland, New Zealand. Natural Hazards Review, 8(2):35-42

Bernet M, Zattin M, Garver JI, Brandon MT, Vance JA (2001) Steady-state exhumation of the European Alps. Geology, 29(1):35-38

Blanckenburg F, Davies JH (1995) Slab breakoff: a model for syncollisional magmatism and tectonics in the Alps. Tectonics, 14(1):120-131

Bligh WG (1910) Dams, barrages and weirs on porous foundations. Engineering News 64(26):708–710

Bo MW, Fabius M, Fabius K (2008) Impact of global warming on stability of natural slopes. In Proceedings of the 4th Canadian Conference on Geohazards: From Causes to Management, Presse de Univ. Laval, Quebec

Bogoslovsky VV, Ogilvy AA (1973) Deformations of natural electric fields near drainage structures. Geophysical Prospecting, 21(4):716-723

Bolève A, Revil A, Janod F, Mattiuzzo JL, Fry JJ (2009) Preferential fluid flow pathways in embankment dams imaged by self-potential tomography. Near Surface Geophysics, 7(5-6):447-462

Bonnard C (2011) Technical and human aspects of historic rockslide-dammed lakes and landslide dam breaches. In: Evans SG, Hermanns RL, Strom A, Scarascia-Mugnozza G (eds) Natural and artificial rockslide dams. Springer Berlin Heidelberg, pp. 101-122

Bonelli S, Benahmed N (2010) Piping flow erosion in water retaining structures: inferring erosion rates from hole erosion tests and quantifying the failure time. In

IECS 2010, 8th ICOLD European Club Symposium Dam Safety-Sustainability in a Changing Environment, ATCOLD Austrian National Committee on Large Dams, 6 p

Bonelli S, Marot D, Ternat F, Benahmed N (2007) Assessment of the risk of internal erosion of water retaining structures: dams, dykes and levees. Intermediate Report of the European Working Group of ICOLD. Technische Universitât Munchen, Berichte des Lehrstuhls und der Versuchsanstalt fûr Wasserbau und Wasser wirtschaft, 114

Bookhagen B, Thiede RC, Strecker MR (2005) Late Quaternary intensified monsoon phases control landscape evolution in the northwest Himalaya. Geology, 33(2):149-152

Bromhead EN, Coppola L, Rendell HM (1996) Valley-blocking landslide dams in the eastern Italian Alps. In Proc. 7th Int. Symp. on Landslides, Vol. 2, pp 655-660

Brown LT, Diehl JG, Nigbor RL (2000) A simplified procedure to measure average shear-wave velocity to a depth of 30 meters (VS30). In: Proceedings of 12th world conference on earthquake engineering

Brown AJ, Gosden JD (2008) Defra research into internal erosion. In: 15th British Dams Society Conference, Warwick

Brauns J (1985) Stability of layered granular soil under horizontal groundwater flow. Proceedings of the 15th International Congress on Large Dams, vol 1, Lausanne

Bryan RB, Jones JAA (1997) The significance of soil piping processes: inventory and prospect. Geomorphology, 20(3):209-218

Bryan R, Yair A (1982) Badland geomorphology and piping. Geobooks Norwich, pp 1-22

Budhu M, Gobin R (1995) Seepage-induced slope failures on sandbars in Grand Canyon. Journal of geotechnical engineering, 121(8):601-609

Budhu M, Gobin R (1996) Slope instability from ground-water seepage. Journal of hydraulic Engineering, 122(7):415-417

Cancienne RM, Fox GA, Simon A (2008) Influence of seepage undercutting on the stability of root-reinforced streambanks. Earth surface processes and landforms, 33(11):1769-1786

Capra L (2007) Volcanic natural dams: identification, stability, and secondary effects. Natural Hazards 43(1):45-61

Capra L (2011) Volcanic Natural Dams Associated with Sector Collapses: Textural and Sedimentological Constraints on Their Stability. In: Evans SG, Hermanns RL, Strom A, Scarascia-Mugnozza G (eds) Natural and Artificial Rockslide Dams. Springer Berlin Heidelberg, pp 279-294

Casagli N, Ermini L, Rosati G (2003) Determining grain size distribution of the material composing landslide dams in the Northern Apennines: sampling and processing methods. Engineering geology, 69(1):83-97

Castelltort S, Goren L, Willett SD, Champagnac JD, Herman F, Braun J (2012) River drainage patterns in the New Zealand Alps primarily controlled by plate tectonic strain. Nature Geoscience, 5(10):744-748

Cedergren HR (1977) Seepage, drainage, and flow nets, 2nd edn. Wiley, New York, pp 1–534

Cenderelli DA, Kite JS (1998) Geomorphic effects of large debris flows on channel morphology at North Fork Mountain, eastern West Virginia, USA. Earth Surface Processes and Landforms, 23(1): 1-19

Chai HJ, Liu HC, Zhang ZY, Xu ZW (2000) The distribution, causes and effects of damming landslides in China. Journal of Chengdu University of Technology 27:302–307

Chang DS, Zhang LM (2012) Critical hydraulic gradients of internal erosion under complex stress states. Journal of geotechnical and geoenvironmental engineering, 139(9):1454-1467

Chang DS, Zhang LM, Xu Y, Huang RQ (2011) Field testing of erodibility of two landslide dams triggered by the 12 May Wenchuan earthquake. Landslides 8(3):321-332

Charles JA (1986) The significance of problems and remedial works at British earth dams. In: Proceedings of BNCOLD/IWES Conference on Reservoirs, Edinburgh, pp 123-141

Chigira M, Yagi H (2006) Geological and geomorphological characteristics of landslides triggered by the 2004 Mid Niigta prefecture earthquake in Japan. Engineering Geology, 82(4):202-221

Chugaev RR (1962) Gründungsumriss von Wasserbauwerken (in Russian) Moskau – Leningrad.

Clague JJ, Evans SG (1994) Formation and failure of natural dams in the Canadian Cordillera. Geological Survey of Canada, Bulletin 464

Coppola L, Bromhead EN (2008) Fossil landslide dams and their exploitation for hydropower in the Italian Dolomites, Bollettino della Societa Geologica Italiana 127:163–171

Corwin RF (1990) The self-potential method for environmental and engineering applications. Geotechnical and environmental geophysics, 1:127-145

Corwin RF (1991) Evaluation of effects of cutoff wall construction on seepage flow using self-potential data, east embankment Wells dam. Report for Douglas County Public Utility District No. 1, Washington

Costa JE, Schuster RL, (1988) The formation and failure of natural dams. Geological Society of America Bulletin 100:1054-1068

Crosta GB, Frattini P, Agliardi F (2013) Deep seated gravitational slope deformations in the European Alps. Tectonophysics, 605:13-33

Crosta GB, Frattini P, Fusi N, Sosio R (2006) Formation, characterization and modelling of the 1987 Val Pola rock-avalanche dam (Italy). Italian J Eng Geol Envir, Special Issue 1:145-150

Crosta G, Prisco CD (1999) On slope instability induced by seepage erosion. Canadian Geotechnical Journal, 36(6):1056-1073

Crozier MJ (2010) Deciphering the effect of climate change on landslide activity: A review. Geomorphology, 124(3):260-267

Cruden DM, Hungr O (1986) The debris of the Frank Slide and theories of rockslide-avalanche mobility. Canadian Journal of Earth Sciences, 23(3):425-432

Cruden DM, Varnes DJ (1996) Landslides: investigation and mitigation. Chapter 3-Landslide types and processes. Transportation research board special report, (247)

Dai FC, Lee CF, Deng JH, Tham LG (2005) The 1786 earthquake-triggered landslide dam and subsequent dam-break flood on the Dadu River, southwestern China. Geomorphology, 65(3):205-221

Dai FC, Xu C, Yao X, Xu L, Tu XB, Gong QM (2011) Spatial distribution of landslides triggered by the 2008 Ms 8.0 Wenchuan earthquake, China. Journal of Asian Earth Sciences, 40(4):883-895

Dapporto S, Rinaldi M, Casagli N (2001) Failure mechanisms and pore water pressure conditions: analysis of a riverbank along the Arno River (Central Italy). Engineering Geology, 61(4):221-242

Darcy H (1856) Histoire des Foundataines Publique de Dijon, Dalmont, Paris, pp 590–594

Davies TR, McSaveney MJ, Beetham RD (2006) Rapid block glides: slide-surface fragmentation in New Zealand's Waikaremoana landslide. Quarterly Journal of Engineering Geology and Hydrogeology, 39(2):115-129

Davies TR, McSaveney MJ (2011) Rock-avalanche size and runout–implications for landslide dams. In: Evans SG, Hermanns RL, Strom A, Scarascia-Mugnozza G (eds) Natural and artificial rockslide dams. Springer Berlin Heidelberg, pp. 441-462

Den Adel H, Bakker KJ, Klein Breteler M (1988) Internal Stability of Minestone. In: Kolkman PA, Lindenberg J, Pilarczyk KW (eds) Proceedings of the International Symposium on Modelling Soil–Water–Structure Interaction, International Association for Hydraulic Research (IAHR), Netherlands, Balkema, Rotterdam, pp 225–231

DeCelles PG, Robinson DM, Quade J, Ojha TP, Garzione CN, Copeland P, Upreti BN (2001) Stratigraphy, structure, and tectonic evolution of the Himalayan fold-thrust belt in western Nepal. Tectonics, 20(4):487-509

Delaney KB, Evans SG (2011) Rockslide dams in the northwest Himalayas (Pakistan, India) and the adjacent Pamir Mountains (Afghanistan, Tajikistan), central Asia. In: Evans SG, Hermanns RL, Strom A, Scarascia-Mugnozza G (eds) Natural and artificial rockslide dams. Springer Berlin Heidelberg, pp. 205-242

Disaster Prevention and Relief Division of the River Bureau and Technology and Safety Division of the Policy Bureau, the Ministry of Land, Infrastructure, Transport and Tourism (2008) "Press release dated April 25, 2008, on decision on establishment of the Technical Emergency Control Force (TEC-FORCE)". *http://www.mlit.go.jp/report/press/river06_hh_000001.html* (in Japanese)

Dong JJ, Tung YH, Chen CC, Liao JJ, Pan YW (2009) Discriminant analysis of the geomorphic characteristics and stability of landslide dams. Geomorphology, 110(3):162-171

Duman TY (2009) The largest landslide dam in Turkey: Tortum landslide. Engineering Geology 104(1):66-79

Dunne T (1990) Hydrology, mechanics, and geomorphic implications of erosion by subsurface flow. Geol Soc Amer, Spec Pap 252:1–28

Dunning SA (2006) The grain-size distribution of rock avalanche deposits in valley-confined settings. Italian J Eng Geol Environ 1:117-121

Dunning SA, Armitage PJ (2011) The grain-size distribution of rock-avalanche deposits: implications for natural dam stability. In: Evans SG, Hermanns RL, Strom A, Scarascia-Mugnozza G (eds) Natural and Artificial Rockslide Dams. Springer Berlin Heidelberg, pp 479-498

Dunning SA, Rosser NJ, Petley DN, Massey CR (2006) Formation and failure of the Tsatichhu landslide dam, Bhutan. Landslides 3(2):107-113

Dunning SA, Petley DN, Strom AL (2005) The morphologies and sedimentology of valley confined rock-avalanche deposits and their effect on potential dam hazard. Landslide Risk Management. AT Balkema, Amsterdam, 691-704

Ermini L, Casagli N (2003) Prediction of the behaviour of landslide dams using a geomorphological dimensionless index. Earth Surface Processes and Landforms, 28(1):31-47

Evans SG (1986) Landslide damming in the Cordillera of western Canada. In: Landslide Dams@ sProcesses, Risk, and Mitigation, ASCE, pp. 111-130

Evans SG, Delaney KB, Hermanns RL, Strom A, Scarascia-Mugnozza G (2011) The formation and behaviour of natural and artificial rockslide dams; implications for engineering performance and hazard management. In: Evans SG, Hermanns RL, Strom A, Scarascia-Mugnozza G (eds) Natural and artificial rockslide dams. Springer Berlin Heidelberg, pp. 1-75

Fan X, van Westen CJ, Korup O, Gorum T, Xu Q, Dai F, Huang R, Wang G (2012) Transient water and sediment storage of the decaying landslide dams induced by the 2008 Wenchuan earthquake, China. Geomorphology, 171:58-68

Fell R, Foster MA, Cyganiewicz J, Sills GL, Vroman ND, Davidson RR (2008) Risk Analysis for Dam Safety: A Unified Method for Estimating Probabilities of Failure of Embankment Dams by Internal Erosion and Piping, URS Australia, New South Wales, Sydney, Australia

Fell R, Fry JJ (2013) State of the art on the likelihood of internal erosion of dams and levees by means of testing. In: Bonelli S (ed) Erosion in Geomechanics Applied to Dams and Levees, Chapter 1ISTE-Wiley, London, UK pp 1–99

Fell R, MacGregor P, Stapledon D, Bell G (2005) Geotechnical engineering of dams. CRC Press, 905 p

Fell R, Wan CF (2005) Methods for estimating the probability of failure of embankment dams by internal erosion and piping in the foundation and from embankment to foundation. University of New South Wales, School of Civil and Environmental Engineering

Fell R, Wan CF, Cyganiewicz J, Foster M (2003) Time for development of internal erosion and piping in embankment dams. Journal of Geotechnical and Geoenvironmental Engineering 129(4):307-314

Finnegan NJ, Hallet B, Montgomery DR, Zeitler PK, Stone JO, Anders AM, Yuping L (2008) Coupling of rock uplift and river incision in the Namche Barwa–Gyala Peri massif, Tibet. Geological Society of America Bulletin, 120(1-2):142-155

Fitzsimons SJ, Veit H (2001) Geology and geomorphology of the European Alps and the Southern Alps of New Zealand: A comparison. Mountain Research and Development, 21(4):340-349

Foster M, Fell R, Spannagle M (2000) The statistics of embankment dam failures and accidents. Canadian Geotechnical Journal, 37(5):1000-1024

Foster M, Fell R, Spannagle M (2000) A method for assessing the relative likelihood of failure of embankment dams by piping. Canadian Geotechnical Journal, 37(5):1025-1061

Fox GA, Felice RG, Midgley TL, Wilson GV, Al-Madhhachi AS (2014) Laboratory soil piping and internal erosion experiments: evaluation of a soil piping model for low-compacted soils. Earth Surface Processes and Landforms 39(9):1137-1145

Fox GA, Wilson GV (2010) The role of subsurface flow in hillslope and stream bank erosion: a review. Soil Science Society of America Journal, 74(3):717-733

Fox GA, Wilson GV, Simon A, Langendoen EJ, Akay O, Fuchs JW (2007) Measuring streambank erosion due to groundwater seepage: correlation to bank pore water pressure, precipitation and stream stage. Earth Surface Processes and Landforms, 32(10):1558-1573

Fread DL (1988) The NWS DAMBRK model: Theoretical background/user documentation. Hydrologic Research Laboratory, National Weather Service, NOAA

Fredlund DG (1995) The stability of slopes with negative pore-water pressures. In: Haberfield CM (ed) The Ian Boyd Donald Symposium on Modern Developments in Geomechanics, Monash University, Department of Civil Engineering, Clayton, Victoria, Vol. 3168, pp 99-116

Fredlund DG (1999) The scope of unsaturated soil mechanics: an overview. In: Clifton AW, Wilson GW, Barbour SL (eds) The Emergence of Unsaturated Soil Mechanics: Fredlund Volume. NRC Research Press, Ottawa, Ontario, Canada, pp 140-156

Fredlund DG, Rahardjo H (1993) Soil mechanics for unsaturated soils. John Wiley & Sons

Fredlund DG, Morgenstern NR, Widger RA (1978) The shear strength of unsaturated soils. Canadian geotechnical journal, 15(3):313-321

Fredlund DG, Rahardjo H, Fredlund MD (2012) Unsaturated soil mechanics in engineering practice. John Wiley & Sons, New York, 926 p

Fredlund DG, Xing A, Huang S (1994) Predicting the permeability function for unsaturated soils using the soil-water characteristic curve. Canadian Geotechnical Journal, 31(4):533-546

Frei C, Schär C (1998) A precipitation climatology of the Alps from high-resolution rain-gauge observations. International Journal of Climatology, 18(8):873-900

Fujita M (2012) Huge sediment disasters due to Typhoon Talas. The 3rd International Workshop on Multimodal Sediment Disasters

García-Jerez A, Luzón F, Navarro M, Pérez-Ruiz JA (2008) Determination of elastic properties of shallow sedimentary deposits applying a spatial autocorrelation method. Geomorphology, 93(1):74-88

Gattinoni P, Francani V (2009) A tool for modeling slope instability triggered by piping. World Academy of Science, Engineering and Technology, 56:471-477

Geertsema M, Clague JJ, Schwab JW, Evans SG (2006) An overview of recent large catastrophic landslides in northern British Columbia, Canada. Engineering Geology, 83(1):120-143

Gehrels GE, DeCelles PG, Martin A, Ojha TP, Pinhassi G, Upreti BN (2003). Initiation of the Himalayan orogen as an early Paleozoic thin-skinned thrust belt. GSA today, 13(9):4-9

Ghiassian H, Ghareh S (2008) Stability of sandy slopes under seepage conditions. Landslides, 5(4):397-406

Glicken H (1991) Sedimentary architecture of large volcanic-debris avalanches. In: Smith GA, Fisher RV (eds.) Sedimentation in Volcanic Settings, SEPM, Tulsa, Special Publication 45:99-106

Glover PW, Walker E, Jackson MD (2012) Streaming-potential coefficient of reservoir rock: A theoretical model. Geophysics, 77(2):D17-D43

Gutiérrez M (2005) Climatic geomorphology, Elsevier, Amsterdam

Hagerty DJ (1991) Piping/sapping erosion: 1. Basic considerations. Journal of Hydraulic Engineering, 117:991–1008

Hammack L, Wohl E (1996) Debris-fan formation and rapid modification at Warm Springs rapid, Yampa River, Colorado. The Journal of Geology, 729-740

Hanisch J, Söder CO (2000) Geotechnical assessment of the Usoi landslide dam and the right bank of Lake Sarez. Usoi Landslide dam and lake Sarez. An assessment of hazard and risk in the Pamir mountains, Tajikistan. ISDR Prevention Series, (1):23-42

Hanson GJ, Cook KR (1997) Development of excess shear stress parameters for circular jet testing. ASAE Paper No. 972227, American Society of Agricultural Engineering, St Joseph, Michigan

Hanson, GJ, Robinson, KM (1993) The influence of soil moisture and compaction on spillway erosion. Transactions of the ASAE 36(5):1349-1352

Hanson GJ, Tejral RD, Hunt SL, Temple DM (2010) Internal erosion and impact of erosion resistance. Proceedings of the 30th US Society on Dams Annual Meeting and Conference, Sacramento, California, pp 773-784

Hayashi SI, Uchida T, Okamoto A, Ishizuka T, Yamakoshi T, Morita K (2013) Countermeasures against landslide dams caused by Typhoon talas 2011. Tech Monitor, 20-26

Heede BH (1971) Characteristics and processes of soil piping in gullies. US Department of Agriculture, Forest Service Research Paper, RM-68

Heim A (1932) Bergsturz und Menschenleben. Fretz and Wasmuth Verlag, Zurich, 218 p

Henderson RD, Thompson SM (1999) Extreme rainfalls in the Southern Alps of New Zealand. Journal of Hydrology (NZ), 38(2):309-330

Herman F, Braun J, Dunlap WJ (2007) Tectonomorphic scenarios in the Southern alps of New Zealand. Journal of Geophysical Research: Solid Earth, 112(B4)

Hermanns RL, Niedermann S, Gonzalez Diaz FE, Fauque L, Folguera A, Ivy-Ochs S, Kubik P (2004) Landslide dams in the Argentine Andes. In NATO Advanced Research Workshop Security of natural and artificial rockslide dams, pp. 79-85

Hewitt K (1982) Natural dams and outburst floods of the Karakoram Himalaya. IAHS, 138:259-269

Hewitt K (1998) Catastrophic landslides and their effects on the Upper Indus streams, Karakoram Himalaya, northern Pakistan. Geomorphology, 26(1):47-80

Hewitt K (2009) Catastrophic rock slope failures and late Quaternary developments in the Nanga Parbat–Haramosh Massif, Upper Indus basin, northern Pakistan. Quaternary Science Reviews, 28(11):1055-1069

Hewitt K (2011) Rock avalanche dams on the Trans Himalayan upper Indus streams: a survey of late Quaternary events and hazard-related characteristics. In: Evans SG, Hermanns RL, Strom A, Scarascia-Mugnozza G (eds) Natural and artificial rockslide dams. Springer Berlin Heidelberg, pp. 177-204

Hewitt K, Clague JJ, Orwin JF (2008) Legacies of catastrophic rock slope failures in mountain landscapes. Earth-Science Reviews, 87(1):1-38

Higgins CG (1982) Drainage systems developed by sapping on Earth and Mars. Geology, 10(3):147-152

Higgins CG (1984) Piping and sapping; development of landforms by groundwater outflow. Allen & Unwin, Boston, pp 18–58

Hovius N, Stark CP, Allen PA (1997) Sediment flux from a mountain belt derived by landslide mapping. Geology, 25(3):231-234

Hovius N, Stark CP, Tutton MA, Abbott LD (1998) Landslide-driven drainage network evolution in a pre-steady-state mountain belt: Finisterre Mountains, Papua New Guinea. Geology, 26(12):1071-1074

Howard AD (1988) Groundwater sapping experiments and modeling. Sapping Features of the Colorado Plateau: A Comparative Planetary Geology Field Guide, 491:71-83

Howard AD, McLane CF (1988) Erosion of cohesionless sediment by groundwater seepage. Water Resources Research, 24(10):1659-1674

Howard AD, McLane CF (1981) Groundwater sapping in sediments: theory and experiments. Reports of Planetary Geology Program, 1:283-285

Huggel C, Clague JJ, Korup O (2012) Is climate change responsible for changing landslide activity in high mountains? Earth Surface Processes and Landforms, 37(1):77-91

Huggel C, Kääb A, Haeberli W, Teysseire P, Paul F (2002) Remote sensing based assessment of hazards from glacier lake outbursts: a case study in the Swiss Alps. Canadian Geotechnical Journal, 39(2):316-330

Hutchinson JN (1982) Damage to slopes produced by seepage erosion in sands. In: Landslides and mudflows, Centre of International Projects, GKNT, Moscow, pp 250–265

Ibs-von Seht M, Wohlenberg J (1999) Microtremor measurements used to map thickness of soft sediments. Bulletin of the Seismological Society of America, 89(1):250-259

ICOLD (2013) Internal Erosion of Existing Dams, Levees, and Dikes, and Their Foundations, Bulletin 164 Preprint, International Commission on Large Dams, Paris, France

Inoue K, Mori T, Mizuyama T (2013) Three large historical landslide dams and outburst disasters in the north fossa magna area, central Japan. International Journal of Erosion Control Engineering, 5(2):145-154

Ischuk AR (2006) Usoy natural dam: problem of security (Lake Sarez, Pamir Mountains, Tadjikistan). Italian Journal of Engineering Geology and the Environment, (special issue 1):189-192

Ishido T, Mizutani H, Baba K (1983) Streaming potential observations, using geothermal wells and in situ electrokinetic coupling coefficients under high temperature. Tectonophysics, 91(1):89-104

Iverson RM, Major JJ (1986) Groundwater seepage vectors and the potential for hillslope failure and debris flow mobilization. Water Resources Research, 22(11):1543-1548

Jakob M, Lambert S (2009) Climate change effects on landslides along the southwest coast of British Columbia. Geomorphology, 107(3):275-284

Janský B, Šobr M, Engel Z (2010) Outburst flood hazard: case studies from the Tien-Shan Mountains, Kyrgyzstan. Limnologica-Ecology and Management of Inland Waters, 40(4):358-364

Japan Ministry of Land, Infrastructure, Transport and Tourism (2008) Press release dated April 25, 2008, on decision for establishment of Technical Emergency Control Force (TEC-FORCE). Disaster Prevention and Relief Division of the River Bureau and Technology and Safety Division of the Policy Bureau, http://www.mlit.go.jp/report/press/river06_hh_000001.html (in Japanese)

Jones, JAA (1981) The nature of soil piping: A review of research. Brit. Geomorphol. Res. Group Res. Monogr. Serie 3. Geobooks, Norwich, UK

Jouniaux L, Maineult, A, Naudet V, Pessel M, Sailhac P (2009) Review of self-potential methods in hydrogeophysics. Comptes Rendus Geoscience, 341(10):928-936

Jouniaux L, Ishido T (2012) Electrokinetics in earth sciences: a tutorial. International Journal of Geophysics, 2012. doi:10.1155/2012/286107

Kamp PJ, Tippett JM (1993) Dynamics of Pacific plate crust in the South Island (New Zealand) zone of oblique continent-continent convergence. Journal of Geophysical Research: Solid Earth, 98(B9):16105-16118

Katsube K, Oguchi T (1999) Altitudinal changes in slope angle and profile curvature in the Japan Alps: A hypothesis regarding a characteristic slope angle. Geographical review of Japan, Series B., 72(1):63-72

Kattelmann R (2003) Glacial lake outburst floods in the Nepal Himalaya: a manageable hazard? Natural Hazards, 28(1):145-154

Ke L, Takahashi A (2012) Influence of internal erosion on deformation and strength of gap-graded non-cohesive soil. Proceedings of the Sixth International Conference on Scour and Erosion, Paris, pp 847-854

King J, Loveday I, Schuster RL (1989) The 1985 Bairaman landslide dam and resulting debris flow, Papua New Guinea. Quarterly Journal of Engineering Geology and Hydrogeology, 22(4):257-270

Kokusho T, Fujikura Y (2008) Effect of particle gradation on seepage failure in granular soils. 4th Int'l Conf. on Scour and Erosion, Tokyo, Japan, pp 497-504

Korchevskiy VF, Kolichko AV, Strom AL, Pernik LM, Abdrakhmatov KE (2011) Utilization of data derived from large-scale experiments and study of natural blockages for blast-fill dam design. In: Evans SG, Hermanns RL, Strom A, Scarascia-Mugnozza G (eds) Natural and artificial rockslide dams. Springer Berlin Heidelberg, pp. 617-637

Korup O (2004) Geomorphometric characteristics of New Zealand landslide dams. Engineering Geology, 73(1):13-35

Korup O (2005) Distribution of landslides in southwest New Zealand. Landslides, 2(1):43-51

Korup O (2011) Rockslide and rock avalanche dams in the Southern Alps, New Zealand. In Natural and Artificial Rockslide Dams. Springer Berlin Heidelberg, pp. 123-145

Korup O, McSaveney MJ, Davies TR (2004) Sediment generation and delivery from large historic landslides in the Southern Alps, New Zealand. Geomorphology, 61(1):189-207

Korup O, Montgomery DR (2008) Tibetan plateau river incision inhibited by glacial stabilization of the Tsangpo gorge. Nature, 455(7214):786-789

Korup O, Montgomery DR, Hewitt K (2010) Glacier and landslide feedbacks to topographic relief in the Himalayan syntaxes. Proceedings of the National Academy of Sciences, 107(12):5317-5322

Korup O, Strom AL, Weidinger JT (2006) Fluvial response to large rock-slope failures: Examples from the Himalayas, the Tien Shan, and the Southern Alps in New Zealand. Geomorphology, 78(1):3-21

Korup O, Tweed F (2007) Ice, moraine, and landslide dams in mountainous terrain. Quaternary Science Reviews, 26(25):3406-3422

Kühni A, Pfiffner OA (2001) The relief of the Swiss Alps and adjacent areas and its relation to lithology and structure: topographic analysis from a 250-m DEM. Geomorphology, 41(4):285-307

Lam L, Fredlund DG, Barbour SL (1987) Transient seepage model for saturated-unsaturated soil systems: a geotechnical engineering approach. Canadian Geotechnical Journal, 24(4):565-580

Lane, E.W. 1935. Security from under-seepage masonry dams on earth foundations. Transactions of the American Society of Agricultural Engineers 60(4):929–966

Leland J, Reid MR, Burbank DW, Finkel R, Caffee M (1998) Incision and differential bedrock uplift along the Indus River near Nanga Parbat, Pakistan Himalaya, from

10 Be and 26 Al exposure age dating of bedrock straths. Earth and Planetary Science Letters, 154(1):93-107

Li T (1990) Landslide Management in the Mountain Areas of China. ICIMOD Occasional Paper no.15, International Centre for Integrated Mountain Development, Kathmandu, Nepal

Li T, Schuster RL, Wu J (1986) Landslide dams in south-central China. In: Schuster, RL (ed) Landslide Dams Processes, Risk and Mitigation, ASCE Special Publication vol. 3:146– 162

Lobkovsky AE, Jensen B, Kudrolli A, Rothman DH (2004) Threshold phenomena in erosion driven by subsurface flow. Journal of Geophysical Research, 109:F04010, doi: 10.1029/2004JF000172

Lowrie W (2007) Fundamentals of geophysics. Cambridge University Press, 354 p

Maknoon M, Mahdi, TF (2010) Experimental investigation into embankment external suffusion. Natural Hazards 54(3):749-763

Marot D, Bendahmane F, Nguyen HH (2012) Influence of angularity of coarse fraction grains on internal erosion process. Proceedings of the Sixth International Conference on Scour and Erosion, Paris, pp 887-894

Mattsson H, Hellström JGI, Lundström TS (2008) On internal erosion in embankment dams. Research Report, Luleå University of Technology. Retrieved from http://epubl.ltu.se/1402-1528/2008/14/LTU-FR-0814-SE.pdf

McCook DK (2004) A comprehensive discussion of piping and internal erosion failure mechanisms. In Proceedings, annual dam safety conference, ASDSO Phoenix, Arizona

Meigs AJ, Burbank DW, Beck RA (1995) Middle-late Miocene (> 10 Ma) formation of the Main Boundary thrust in the western Himalaya. Geology, 23(5):423-426

Meyer W, Schuster RL, Sabol MA (1994) Potential for seepage erosion of landslide dam. Journal of geotechnical engineering, 120(7):1211-1229

Mizuyama T, Mori T, Sakaguchi T, Inoue K (2011) Landslide dams and countermeasure method in Japan. Kokon Shoin, 205 (in Japanese)

Moffat R, Fannin RJ, Garner SJ (2011) Spatial and temporal progression of internal erosion in cohesionless soil. Canadian Geotechnical Journal, 48(3):399-412

Mool PK, Bajracharya SR, Joshi SP (2001) Inventory of glaciers, glacial lakes and glacial lake outburst floods. Monitoring and early warning systems in the Hindu Kush-Himalayan Region: Nepal. International Centre for Integrated Mountain Development, 365 pp

Moore JR, Boleve A, Sanders JW, Glaser SD (2011) Self-potential investigation of moraine dam seepage. Journal of Applied Geophysics, 74(4):277-286

Mora S, Madrigal C, Estrada J, Schuster RL (1993) The 1992 Rio Toro landslide dam, Costa Rica. Landslide News 7:19-22

Müller-Kirchenbauer H, Rankl M, Schlötzer C (1993) Mechanism for regressive erosion beneath dams and barrages. In Proceedings of the First International Conference on Filters in Geotechnical and Hydraulic Engineering, ed. J. Brauns, M. Heibaum, and U. Schuler, 369–376. Rotterdam: Balkema.

Nagai Y, Maruyama J, Yoshida K, Yamakoshi T (2008) Emergency response and permanent measures for large landslide dams triggered by the 2004 Mid-Niigata Prefecture Earthquake in Japan. International Journal of Erosion Control Engineering, 1(1):20-29

Nakamura Y (1989) A method for dynamic characteristics estimation of subsurface using microtremor on the ground surface. Railway Technical Research Institute, Quarterly Reports, 30(1)

O'Connor JIME, Beebee RA (2009) 8 Floods from natural rock-material dams. Megaflooding on Earth and Mars, 128

O'Connor JE, Costa JE (2004) The world's largest floods, past and present: their causes and magnitudes (Vol. 1254). US Geological Survey circular, 1254, 13pp

Ogilvy AA, Ayed MA, Bogoslovsky VA (1969) Geophysical Studies of water leakages from reservoirs. Geophysical Prospecting, 17(1):36-62

Oguchi T, Saito K, Kadomura H, Grossman M (2001) Fluvial geomorphology and paleohydrology in Japan. Geomorphology, 39(1):3-19

Ojha CSP, Singh VP, Adrian DD (2008) Assessment of the role of slit as a safety valve in failure of levees. International Journal of Sediment Research, 23(4):361-375

Okada H (2003) The microseismic survey method: Society of exploration geophysicists of Japan. Translated by Koya Suto. Geophysical Monograph Series, 12

Okamura M, Soga Y (2006) Effects of pore fluid compressibility on liquefaction resistance of partially saturated sand. Soils and Foundations, 46(5):695-700

Okeke ACU, Wang F (2016) Hydromechanical constraints on piping failure of landslide dams: an experimental investigation. Geoenvironmental Disasters, 3(1):1-17

Okeke AC, Wang F, Sonoyama T, Mitani Y (2013) Laboratory experiments on landslide dam failure due to piping: An evaluation of 2011 typhooninduced landslide and landslide dam in Western Japan. In Progress of Geo-Disaster Mitigation Technology in Asia, ed. F.W. Wang, M. Miyajima, T. Li, S. Wei, and T.F. Fathani, 525–545. Berlin Heidelberg: Springer

Ouimet WB, Whipple KX, Royden LH, Sun Z, Chen Z (2007) The influence of large landslides on river incision in a transient landscape: Eastern margin of the Tibetan Plateau (Sichuan, China). Geological Society of America Bulletin, 119(11-12):1462-1476

Pagano L, Fontanella E, Sica S, Desideri A (2010) Pore water pressure measurements in the interpretation of the hydraulic behaviour of two earth dams. Soils and foundations, 50(2):295-307

Parker GG (1964) Piping: A Geomorphic Agent in Landform Development of the Drylands. International Association of Scientific Hydrology, 65:103-113

Parker GG, Jenne EA (1967) Structural failure of western highways caused by piping. US Geological Survey, Water Resource Division, Report No. 27

Peng M, Zhang LM (2012) Breaching parameters of landslide dams. Landslides, 9(1):13-31

Perzlmaier S, Muckenthaler P, Koelewijn AR (2007) Hydraulic criteria for internal erosion in cohesionless soil. Assessment of risk of internal erosion of water retaining structures: dams, dykes and levees. Intermediate Report of the European Working Group of ICOLD. Technical University of Munich, Munich, Germany, pp 30-44

Plaza G, Zevallos O, Cadier É (2011) La Josefina Landslide Dam and Its Catastrophic Breaching in the Andean Region of Ecuador. In: Evans SG, Hermanns RL, Strom A, Scarascia-Mugnozza G (eds) Natural and artificial rockslide dams. Springer Berlin Heidelberg, pp. 389-406

Pollet N, Schneider JL (2004) Dynamic disintegration processes accompanying transport of the Holocene Flims sturzstrom (Swiss Alps). Earth and Planetary Science Letters, 221(1):433-448

Porter M, Savigny KW (2002) Natural hazard and risk management for South American pipelines. In: 4th International Pipeline Conference. American Society of Mechanical Engineers, pp. 861-869

Powledge GR, Ralston DC, Miller P, Chen YH, Clopper PE, Temple DM (1989) Mechanics of overflow erosion on embankments. I: Research activities. Journal of Hydraulic Engineering, 115(8):1040-1055

Powledge GR, Ralston DC, Miller P, Chen YH, Clopper PE, Temple DM (1989) Mechanics of overflow erosion on embankments. II: Hydraulic and design considerations. Journal of Hydraulic Engineering, 115(8):1056-1075

Read SAL, Beetham RD, Riley PB (1992) Lake Waikaremoana barrier–a large landslide dam in New Zealand. In Proc. 6th Intern. Symposium on Landslides, pp. 1481-1487

Richards KS, Reddy KR (2007) Critical appraisal of piping phenomena in earth dams. Bulletin of Engineering Geology and the Environment, 66(4):381-402

Richards KS, Reddy KR (2010) True triaxial piping test apparatus for evaluation of piping potential in earth structures. J. ASTM Geotech Test, 33(1):83-95

Richards KS, Reddy KR (2012) Experimental investigation of initiation of backward erosion piping in soils. Geotechnique 62(10):933-942

Richardson SD, Reynolds JM (2000) An overview of glacial hazards in the Himalayas. Quaternary International, 65:31-47

Rinaldi M, Casagli N (1999) Stability of streambanks formed in partially saturated soils and effects of negative pore water pressures: the Sieve River (Italy). Geomorphology, 26(4):253-277

Rinaldi M, Casagli N, Dapporto S, Gargini A (2004) Monitoring and modelling of pore water pressure changes and riverbank stability during flow events. Earth Surface Processes and Landforms, 29(2):237-254

Roberts JC, Asten MW (2004) Resolving a velocity inversion at the geotechnical scale using the microtremor (passive seismic) survey method. Exploration geophysics, 35(1):14-18

Robinson DM, DeCelles PG, Copeland P (2006) Tectonic evolution of the Himalayan thrust belt in western Nepal: Implications for channel flow models. Geological Society of America Bulletin, 118(7-8):865-885

SABO (Erosion and sediment control) Division of the River Bureau, the Ministry of Land, Infrastructure, Transport and Tourism, and the Public Works Research Institute (2010) "Press release dated August 11, 2010, on Assessed Map of the

Relative Susceptibility to Deep Catastrophic Landslides". *http://www.mlit.go.jp/report/press/river03_hh_000252.html* (in Japanese)

SABO (Erosion and sediment control) Division of the Water and Disaster Management Bureau, the Ministry of Land, Infrastructure, Transport and Tourism, and the Public Works Research Institute (2012). "Press release dated September 10, 2012, on Surveys on Deep Catastrophic Landslides at the Stream (small watershed) Level". *http://www.mlit.go.jp/report/press/mizukokudo03_hh_000552.html* (in Japanese).

Samani ZA, Willardson LS (1981) Soil hydraulic stability in a subsurface drainage system. Trans. Am. Soc. Agric. Engrs. 24(3):666-669

Sassa K (1998) Recent urban landslide disasters in Japan and their mechanisms. In Proceedings of 2nd International Conference on Environmental Management, Australia, pp 10-13

Sassa K (2005) Landslide disasters triggered by the 2004 Mid-Niigata Prefecture earthquake in Japan. Landslides, 2(2):135-142

Satofuka Y, Mori T, Mizuyama T, Ogawa K, Yoshino K (2010) Prediction of floods caused by landslide dam collapse. Journal of Disaster Research, 5(3):288-295

Satoh T, Kawase H, Matsushima SI (2001) Estimation of S-wave velocity structures in and around the Sendai Basin, Japan, using array records of microtremors. Bulletin of the seismological society of America, 91(2):206-218

Schmid SM, Kissling E (2000) The arc of the western Alps in the light of geophysical data on deep crustal structure. Tectonics, 19(1):62-85

Schmid SM, Fügenschuh B, Kissling E, Schuster R (2004) Tectonic map and overall architecture of the Alpine orogen. Eclogae Geologicae Helvetiae, 97(1):93-117

Schneider JL, Wassmer P, Ledésert B (1999) The fabric of the sturzstrom of Flims (Swiss Alps): Characteristics and implications on the transport mechanisms.

Comptes Rendus de l'Academie des Sciences Series IIA Earth and Planetary Science, 328(9):607-613

Schuster RL (1995) Landslide dams-a worldwide phenomenon. In: Proceedings of the Annual Symposium of the Japanese Landslide Society, Kansai Branch, Osaka, pp 1-23

Schuster RL (2006) Interaction of dams and landslides-case studies and mitigation. United States Geological Survey Professional Paper 1723, 107 p

Schuster RL, Alford D (2004) Usoi Landslide Dam and Lake Sarez, Pamir Mountains, Tajikistan. Environmental & Engineering Geoscience, 10(2):151-168

Schuster RL, Salcedo DA, Valenzuela L (2002) Overview of catastrophic landslides of South America in the twentieth century. Reviews in Engineering Geology, 15:1-34

Schuster RL, Salcedo DA, Valenzuela L (2002) Overview of catastrophic landslides of South America in the twentieth century. Reviews in Engineering Geology, 15:1-34

Schuster RL, Wieczorek GF, Hope DG (1998) Landslide dams in Santa Cruz County, California, resulting from the earthquake. US Geological Survey professional paper, 1551C

Selby MJ (1982) Hillslope materials and processes. Oxford University Press, 110p

Seward D, Burg JP (2008) Growth of the Namche Barwa Syntaxis and associated evolution of the Tsangpo Gorge: Constraints from structural and thermochronological data. Tectonophysics, 451(1):282-289

Shang Y, Yang Z, Li L, Liu DA, Liao Q, Wang Y (2003) A super-large landslide in Tibet in 2000: background, occurrence, disaster, and origin. Geomorphology, 54(3):225-243

Sherard JL (1953) Influence of soil properties and construction methods on the performance of homogeneous earth dams

Sherard JL, Woodward RJ, Gizienski SF, Clevenger WA (1963) Earth and earth-rock dams: New York, John Wiley and Sons, 722 p

Shugar DH, Clague JJ (2011) The sedimentology and geomorphology of rock avalanche deposits on glaciers. Sedimentology 58(7):1762-1783

Sidle RC, Kitahara H, Terajima T, Nakai Y (1995) Experimental studies on the effects of pipeflow on throughflow partitioning. Journal of Hydrology 165(1):207-219

Simon A, Collison AJ (2001) Pore-water pressure effects on the detachment of cohesive streambeds: seepage forces and matric suction. Earth Surface Processes and Landforms, 26(13):1421-1442

Singh V (1996) Dam breach modeling technology (Vol. 17). Springer Science & Business Media

Singh VP, Scarlatos PD, Collins JG, Jourdan MR (1988) Breach erosion of earthfill dams (BEED) model. Natural Hazards, 1(2):161-180

Sjödahl P, Dahlin T, Johansson S (2005) Using resistivity measurements for dam safety evaluation at Enemossen tailings dam in southern Sweden. Environmental geology, 49(2):267-273

Skempton AW, Brogan JM (1994) Experiments on piping in sandy gravels. Geotechnique, 44(3):449-460

Stewart RJ, Hallet B, Zeitler PK, Malloy MA, Allen CM, Trippett D (2008) Brahmaputra sediment flux dominated by highly localized rapid erosion from the easternmost Himalaya. Geology, 36(9):711-714

Stoffel M, Huggel C (2012) Effects of climate change on mass movements in mountain environments. Progress in Physical Geography, 36(3):421-439

Strom A (2006) Morphology and internal structure of rockslides and rock avalanches: grounds and constraints for their modelling. In: Landslides from Massive Rock Slope Failure, Springer Netherlands, pp. 305-326

Strom A (2010) Landslide dams in Central Asia region. 日本地すべり学会誌, 47(6):309-324

Strom A (2013) Geological prerequisites for landslide dams' disaster assessment and mitigation in Central Asia. In: Wang FW, Miyajima M, Li T, Wei S, Fathani TF (eds) Progress of Geo-Disaster Mitigation Technology in Asia. Springer Berlin Heidelberg, pp 17-53

Sutherland R (1995) The Australia-Pacific boundary and Cenozoic plate motions in the SW Pacific: Some constraints from Geosat data. Tectonics, 14(4):819-831

Swanson FJ, Ouyagi N, Tominaga M (1986) Landslide dams in Japan In: Schuster RL (ed.) Landslide Dams: Process, Risk and Mitigation: ASCE Geotechnical Special Publication, No.3, pp 131-145

Tabata S, Mizuyama T, Inoue K (2002) Landslide Dams and Disasters. Kokon Shoin, p 205 (in Japanese)

Talwani P, Acree S (1984) Pore pressure diffusion and the mechanism of reservoir-induced seismicity. Pure and Applied Geophysics, 122(6):947-965

Tapponnier P, Zhiqin X, Roger F, Meyer B, Arnaud N, Wittlinger G, Jingsui Y (2001) Oblique stepwise rise and growth of the Tibet Plateau. science, 294(5547):1671-1677

Terzaghi K (1960) Storage dam founded on landslide debris, Journal of the Boston Society of Civil Engineers 47: 64–94

Terzaghi K (1943) Theoretical soil mechanics: New York, John Wiley and Sons

Terzaghi K, Peck RB, Mesri G (1996) Soil Mechanics in Engineering Practice, Third Edition: John Wiley & Sons, New York

Thompson S, Kulessa B, Luckman A (2012) Integrated electrical resistivity tomography (ERT) and self-potential (SP) techniques for assessing hydrological processes within glacial lake moraine dams. Journal of Glaciology, 58(211):849-858

Vorogushyn S, Merz B, Apel H (2009) Development of dike fragility curves for piping and micro-instability breach mechanisms. Natural Hazards and Earth System Sciences, 9(4):1383-1401

Walder JS, O'Connor JE (1997) Methods for predicting peak discharge of floods caused by failure of natural and constructed earthen dams. Water Resources Research, 33(10):2337-2348

Wan CF, Fell R (2004) Experimental investigation of internal instability of soils in embankment dams and their foundations, NICIV Report No. R429, University of South Wales, Sydney, Australia

Wang F, Kuwada Y, Okeke AC, Mitani Y, Yang H, Faris F, Hayashi H, Baba S (2015) Detecting Premonitory Phenomena of Landslide Dam Failure by Piping. In Engineering Geology for Society and Territory-Volume 2 (pp. 1171-1175). Springer International Publishing

Wang G, Huang R, Kamai T, Zhang F (2013) The internal structure of a rockslide dam induced by the 2008 Wenchuan (M_w 7.9) earthquake, China. Engineering Geology 156: 28-36

Wang HB, Sassa K, Xu WY (2007) Analysis of a spatial distribution of landslides triggered by the 2004 Chuetsu earthquakes of Niigata Prefecture, Japan. Natural Hazards, 41(1):43-60

Wang JM, Zhang JJ, Wang XX (2013) Structural kinematics, metamorphic P–T profiles and zircon geochronology across the Greater Himalayan Crystalline Complex in south-central Tibet: implication for a revised channel flow. Journal of Metamorphic Geology, 31(6):607-628

Wassmer P, Schneider JL, Pollet N, Schmitter-Voirin C (2004) Effects of the internal structure of a rock–avalanche dam on the drainage mechanism of its impoundment, Flims sturzstrom and Ilanz paleo-lake, Swiss Alps. Geomorphology, 61(1):3-17

Webb AAG, Yin A, Harrison TM, Célérier J, Burgess WP (2007) The leading edge of the Greater Himalayan Crystalline complex revealed in the NW Indian Himalaya: Implications for the evolution of the Himalayan orogen. Geology, 35(10):955-958

Weidinger JT (2006) Landslide dams in the high mountains of India, Nepal and China-stability and life span of their dammed lakes. Italian Journal of Engineering Geology and Environment, 1:67-80

Weidinger JT (2011) Stability and life span of landslide dams in the Himalayas (India, Nepal) and the Qin Ling Mountains (China). In: Evans SG, Hermanns RL, Strom A, Scarascia-Mugnozza G (eds) Natural and artificial rockslide dams. Springer Berlin Heidelberg, pp. 243-277

Weijers JBA, Sellmeijer JB (1993) A new model to deal with the piping mechanism. In Proceedings of the First International Conference on Filters in Geotechnical and Hydraulic Engineering, ed. J. Brauns, M. Heibaum, and U. Schuler, 345–355. Rotterdam: Balkema

Wesnousky SG, Kumar S, Mohindra R, Thakur VC (1999) Uplift and convergence along the Himalayan Frontal Thrust of India. Tectonics, 18(6):967-976

Whitehouse IE (1988) Geomorphology of the central Southern Alps, New Zealand: the interaction of plate collision and atmospheric circulation. The geomorphology of plate boundaries and active continental margins. Zeitschrift für Geomorphologie Supplementbände, 69:105-116

Whitehouse IE, Griffiths GA (1983) Frequency and hazard of large rock avalanches in the central Southern Alps, New Zealand. Geology, 11(6):331-334

Wieczorek GF (1996) Landslide triggering mechanisms. In: Turner AK, Schuster RL (eds.) Landslides: Investigation and mitigation, Transportation research board special report, vol. 247:76-90

Wilson GV (2009) Mechanisms of ephemeral gully erosion caused by constant flow through a continuous soil-pipe. Earth Surface Processes and Landforms 34(14):1858-1866

Wilson G (2011) Understanding soil-pipe flow and its role in ephemeral gully erosion Hydrological Processes 25(15):2354-2364

Wilson GV, Periketi RK, Fox GA, Dabney SM, Shields FD, Cullum RF (2007) Soil properties controlling seepage erosion contributions to streambank failure. Earth Surface Processes and Landforms, 32(3):447-459

Wit JD, Sellmeijer JB, Penning A (1981) Laboratory testing on piping. In: Tenth International Conference on Soil Mechanics and Foundation Engineering, pp 517-520

Wittmann H, von Blanckenburg F, Kruesmann T, Norton KP, Kubik PW (2007) Relation between rock uplift and denudation from cosmogenic nuclides in river sediment in the Central Alps of Switzerland. Journal of Geophysical Research: Earth Surface, 112(F4)

Wörman A (1993) Seepage-induced mass wasting in coarse soil slopes. Journal of Hydraulic Engineering, 119(10):1155-1168

Wulf H, Bookhagen B, Scherler D (2010) Seasonal precipitation gradients and their impact on fluvial sediment flux in the Northwest Himalaya. Geomorphology, 118(1):13-21

Xu Q, Fan XM, Huang RQ, Van Westen C (2009) Landslide dams triggered by the Wenchuan Earthquake, Sichuan Province, south west China. Bulletin of engineering geology and the environment, 68(3):373-386

Xue-Cai F, An-ning G (1986) Principal characteristics of earthquake landslides in China. Geologiga Applicata e Idrogeologia Italy 21(2):2745

Yin A (2006) Cenozoic tectonic evolution of the Himalayan orogen as constrained by along-strike variation of structural geometry, exhumation history, and foreland sedimentation. Earth-Science Reviews, 76(1):1-131

Zasłavsky D, Kassiff G (1965) Theoretical formulation of piping mechanism in cohesive soils. Geotechnique, 15(3):305-316

Zeitler PK, Meltzer AS, Koons PO, Craw D, Hallet B, Chamberlain CP, Kidd WS, Park SK, Seeber L, Bishop M, Shroder J (2001) Erosion, Himalayan geodynamics, and the geomorphology of metamorphism. GSA Today, 11(1), pp.4-9

Zhang LM, Chen Q (2006) Seepage failure mechanism of the Gouhou rockfill dam during reservoir water infiltration. Soils and Foundations, 46(5):557-568.